NONLINEAR FLUTTER OF COMPOSITE SHEAR-DEFORMABLE PANELS IN A HIGH-SUPERSONIC FLOW

by

Naresh K. Chandiramani

Dissertation submitted to the faculty of the

Virginia Polytechnic Institute and State University

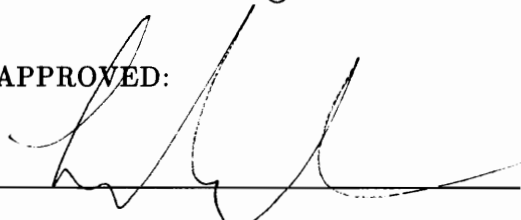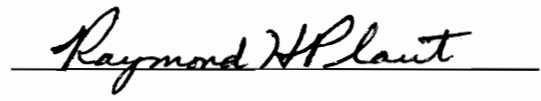in partial fulfillment of the requirements for the degree of

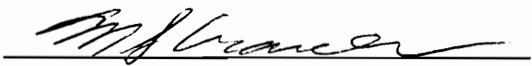## DOCTOR OF PHILOSOPHY

in

Engineering Mechanics

APPROVED:

_____
Dr. Liviu I. Librescu, Co-chairman
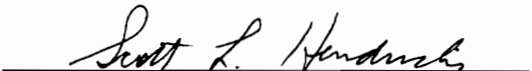
_____
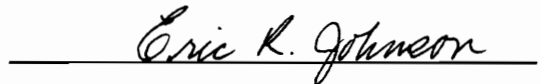Dr. Raymond H. Plaut, Co-chairman

_____
Dr. Mark S. Cramer

_____
Dr. Robert A. Heller

_____
Dr. Scott L. Hendricks

_____
Dr. Eric R. Johnson

July, 1993

Blacksburg, Virginia

NONLINEAR FLUTTER OF COMPOSITE SHEAR-DEFORMABLE PANELS IN A HIGH-SUPERSONIC FLOW

by

Naresh K. Chandiramani

Committee Co-chairmen:

Dr. Liviu I. Librescu

Department of Engineering Science and Mechanics

and

Dr. Raymond H. Plaut

The Charles Edward Via, Jr. Department of Civil Engineering

(ABSTRACT)

The nonlinear dynamical behavior of a laterally compressed, flat, composite panel subjected to a high supersonic flow is analyzed. The structural model considers a higher-order shear deformation theory which also includes the effect of the transverse normal stress and satisfies the traction-free condition on both faces of the panel. The possibility of small initial imperfections and in-plane edge restraints are also considered. Aerodynamic loads based on the third-order piston theory are used and the panel flutter equations are derived via Galerkin's method. Periodic solutions and their bifurcations are obtained by using a predictor-corrector type of numerical integration method, i.e., the Shooting Method, in conjunction with the Arclength Continuation Method for the static solution. For the perfect panel, the amplitudes and frequency of flutter obtained by the Shooting Method are shown to compare well with results from the Method of Multiple Scales when linear aerodynamics is considered and compressive loads are absent. It is seen that the presence of aerodynamic nonlinearities could result in the hard flutter phenomenon, i.e., a violent transition from the undisturbed equilibrium state to that of finite motions which may occur for pre-critical speeds also. Results show that linear aerodynamics correctly predicts the immediate post-flutter behavior of thin panels only. When compressive edge loads or edge restraints are applied, in certain cases multiple periodic solutions are found to coexist with the stable

static solution, or multiple buckled states are possible. Thus it is seen that the panel may remain buckled beyond the flutter boundary, or it may flutter within the region where buckled states exist. Furthermore, the presence of edge restraints normal to the flow tends to stabilize the panel by decreasing the flutter amplitudes and the possibility of hard flutter. Nonperiodic motions (i.e., quasiperiodic and chaotic) of the buckled panel are found to exist, and their associated Lyapunov exponents are calculated. The effects of transverse shear flexibility, aerodynamic nonlinearities, initial imperfections, and in-plane edge restraints on the stability boundaries are also studied. It is observed that the classical plate theory overpredicts the instability loads, and only the shear deformation theory correctly models the panel which is flexible in transverse shear. When aerodynamic nonlinearities are considered, multiple flutter speeds may exist.

ACKNOWLEDGEMENTS

I would like to thank:

My co-advisors Dr. Liviu I. Librescu and Dr. Raymond H. Plaut for their constant guidance, encouragement, and invaluable support throughout the duration of my research work and graduate studies at Virginia Tech.

The members of my graduate committee, i.e., Dr. Mark S. Cramer and Dr. Eric R. Johnson for the many useful discussions and suggestions, and Dr. Robert A. Heller and Dr. Scott L. Hendricks for serving on the committee.

All my teachers at the Indian Institute of Technology (New Delhi) and Virginia Tech.

Dr. Balakumar Balachandran and Dr. Tony J. Anderson for many helpful discussions.

Mr. Ravi Shankar Boppe for staying awake many nights to help me with the typing of the manuscript and eventually putting it all together.

Mr. Weiquing Lin, Mr. Anand V. N. Rau, Mrs. Anuradha Rau and Mr. Suresh Subramanian for helping me with the manuscript and the presentation, and most of all for the moral support when I needed it the most.

Mr. Duane Taylor and Mr. Tim Tomlin, who run the ESM computer lab, for helping me out with the computers on which all of this work was done.

The Engineering Science and Mechanics Department for its continued financial support.

All my friends in India and the USA for their friendship and moral support, especially those at the ESM computer lab, i.e., Mr. Vikas Juneja, Mr. Reza Karkehabadi, Dr. Gustavo O. Maldonado, Mr. Mohammad S. Rohanimanesh, and Mr. Madhu K. Sreedhar.

And last but not the least, my parents, grandmother, and family for their constant support, understanding and encouragement without which this goal could never have been achieved.

TABLE OF CONTENTS

LIST OF FIGURES

LIST OF TABLES

Chapter 1
INTRODUCTION

The dynamic behavior of laminated composite structures is currently a topic of widespread research. This is largely due to the fact that such composites have been successfully used in secondary aircraft structures and hence are likely to play a significant role in the development of the next generation of aeronautical and aerospace structures.

Composite material systems are preferred in design applications requiring maximum strength and stiffness with minimum weight. However, in contrast to their metallic counterparts, these advanced composite structures are characterized by weak rigidities in transverse shear. This necessitates the inclusion of transverse shear deformation effects when modelling their dynamic behavior.

Another important aspect of the problem is the effect, on the response, of nonlinearities arising from the modelling of the aerodynamic loads. These aerodynamic nonlinearities are more pronounced at high supersonic speeds ($M \gg 1$) and are generally of the hard type, i.e., they having a destabilizing effect (which increases with the flow speed) as opposed to the geometric nonlinearities which tend to stabilize the structure. Thus the presence of these aerodynamic nonlinearities could, in certain cases, result in a violent transition from the undisturbed equilibrium state to that of finite motions, and this could occur for flow speeds (M) lower than the critical (flutter) velocity (M_F). This phenomenon is known as hard flutter. It should be noted that so far only a few researchers have considered this refinement to the problem. However, since their effect would be more pronounced in the future generation of aircraft (e.g., the NASP flying at $M \geq 15$), these aerodynamic nonlinearities should be incorporated in the structural model.

Furthermore, the application of an in-plane compressive edge load (e.g., one resulting

1

from aerodynamic heating) can significantly alter the dynamic behavior of the panel, especially when the load is greater than the Euler buckling load. This could result in a transition to complicated motions, both periodic and non-periodic, for small variations of the control parameters (i.e., compressive load and flow speed). Moreover, multiple buckled and dynamic states of the structure are possible for certain combinations of the control parameters. A similar effect may result due to the edges being restrained from in-plane movement. Therefore, to correctly predict the complicated dynamics, and hence the fatigue life of the panel, any applied in-plane edge loads and existing edge restraints should be included in the structural model.

The presence of the unavoidable initial geometric imperfections (e.g., manufacturing defects) suggests that they also be incorporated in the analysis. These imperfections, along with the aerodynamic nonlinearities, have a pronounced effect (both qualitative and quantitative) on the stability and response characteristics of the structure.

In the present study, the nonlinear dynamical behavior of a flat composite panel subjected to a high supersonic gas flow of arbitrary orientation is analyzed. For flow speeds in excess of the critical (flutter) velocity predicted by the linear theory, membrane forces are induced. These forces tend to limit the amplitude of oscillation, and thus the flutter speed can be exceeded without immediate failure of the plate. Thus the need for a nonlinear analysis arises. The analysis considered herein includes the effects of aerodynamic and geometric nonlinearities, transverse shear flexibility, in-plane edge loads and edge restraints, and small initial geometric imperfections.

The literature review in Chapter II serves as a background for the present study. From this, we see that even though the nonlinear panel flutter problem has been widely researched, very few studies incorporate aerodynamic nonlinearities and in-plane edge restraint conditions in their structural model. Notable among these are the works of Bolotin (e.g., [1]), which contains the first published results regarding the hard flutter phenomenon for flat panels. As for the presence of initial imperfections and transverse shear deformations, presently there are no publications available that include these in the structural model when analyz-

ing the post-flutter behavior. Furthermore, a few recent analyses of the flutter of buckled panels (having infinite span length) reveal limited results concerning the complicated dynamics and onset of non-periodic motions. Moreover, it appears that these results have been arrived at by straightforward numerical integration methods without much emphasis on a systematic investigation of the bifurcation behavior. Finally, an overview of relevant concepts from nonlinear dynamics is also presented in the latter part of this chapter.

Chapter III presents the formulation of the panel flutter problem. Here, the governing equations are derived on the basis of a higher-order shear deformation theory. This also accounts for the transverse normal stress and satisfies the in-plane traction-free conditions on both faces of the panel. The case of a simply supported, symmetrically laminated panel composed of transversely isotropic layers is considered. The equations describing the evolution of the transverse displacement coordinate u_3, which appear in their uncoupled form, are considered along with the Galerkin method, and the panel flutter equations are obtained.

In Chapter IV the time-dependent modal amplitudes are represented in terms of their static and dynamic components, and the associated equations describing the static buckled state and motions about it are derived. The static solution is obtained using the Arclength Continuation Method which is described in Chapter IV. Periodic solutions are obtained by using a numerical integration technique—called the Shooting Method—which consists of an augmented initial value problem (the predictor) and a Newton-Raphson iteration procedure (the corrector). Floquet theory is then used to obtain the stability of these periodic solutions, and hence bifurcations to new solutions (periodic and non-periodic) can be predicted. A straightforward numerical integration of the original initial value problem is considered when non-periodic motions are sought. A number of tools, such as Poincaré sections and Lyapunov exponents, are used to characterize the various types of motion. Periodic solutions for the perfect panel are also obtained by a perturbation method, i.e., the Method of Multiple Scales, and results are compared with those obtained by the Shooting Method whenever possible (see Chapter V). However, this method has inherent limitations

CHAPTER 1. INTRODUCTION

which are discussed within this chapter.

Chapter V presents results and discussions concerning the stability boundaries and the effects of aerodynamic nonlinearities and in-plane edge loads and edge restraints on the post-flutter behavior of perfect and imperfect panels. Comparison of results obtained using the higher-order shear deformation theory and the classical plate theory is also presented, whenever possible. Finally, conclusions and recommendations for future research are presented in Chapter VI.

Chapter 2

LITERATURE REVIEW

2.1 Panel Flutter

It is well known that a steady wind blowing over a flexible elastic structure can induce and maintain large-amplitude oscillations. This phenomenon is easily observed as flutter of flags, galloping of ice-coated power cables, and flutter of aircraft wings. The destruction of the Tacoma Narrows suspension bridge was caused by flutter oscillations of the superstructure.

Most of the voluminous theoretical literature on this problem is focussed on the study of these flutter (limit cycle) oscillations that could eventually lead to structural failure. However, a few publications on the complicated dynamics associated with this phenomenon occurring for the broader class of self-excited systems are also available. Among the first studies concerning the flutter of panels were those of Bolotin et al. [1] , Bolotin [2] and Makarov [3]. In [1], a simply supported isotropic panel with a steady supersonic flow past its upper surface was analyzed. Quadratic nonlinearities arising from unsymmetric aerodynamic forces (i.e., for flow past one surface only) are neglected since the authors consider that in a self-excited system such as this, the primary effect of nonlinearities manifests itself through cubic terms. The ordinary differential equations (ODE's) describing modal amplitudes are solved by the Harmonic Balance Method (HBM) considering single-mode flutter. Results are obtained for a two-dimensional panel of infinite span. They indicate that for immovable edges (i.e., in-plane motion restrained) parallel to the span direction, soft flutter oscillations occur for $M > M_F$ (M = Mach number, M_F = Mach number at flutter) as compared to hard flutter when those edges are movable. However,

since only a two-mode approximation was used during spatial discretization, the amplitudes of hard flutter oscillation could not be obtained.

In [2] Bolotin included the effect of a temperature field which remains uniform through the thickness of the panel. Equations governing small but finite oscillations about the thermally buckled static state are derived. Numerical results for the amplitude of flutter are obtained via a perturbation solution (similar to the Linstedt-Poincaré Method) for the non-thermal problem. However, due to an inconsistency in the ordering of the modal amplitudes, the effect of quadratic aerodynamic nonlinearities is completely lost (even quantitatively) while cubic nonlinearities appear in the first order perturbation equations. The variation of M_F with the plate aspect ratio is presented and the qualitative nature of this flutter boundary (i.e., whether dangerous or benign) is also discussed. Makarov [3] extended the analysis of [2] to include boundary conditions where all four edges are fixed and where two opposite edges are fixed and the other two are simply supported. He concluded that a higher limit cycle amplitude exists for the latter case of boundary conditions. Similarly, the case of movable edges yielded higher amplitudes of oscillation when compared to that of immovable edges.

The role played by aerodynamic nonlinearities is described by Bolotin [4]. In this monograph he states that their effect is in general destabilizing and it becomes more pronounced as the flow speed increases. Thus in certain cases when M_F is high enough their effect may be such that undamped oscillations (i.e., divergent modes of static equilibrium) may exist for $M < M_F$. In such cases M_F as determined by the linear theory is only an upper bound for the actual critical flow speed. This results in hard (dangerous) flutter when M_F is exceeded. It corresponds to a sub-critical Hopf bifurcation of the modal-amplitude solution (i.e., a reversed pitchfork bifurcation of the limit-cycle amplitude solution). In a related work, Librescu [5,6] determined the nature of the flutter boundary (described in the M_F versus aspect-ratio plane). The analysis was carried out by using a method due to Bautin (see Bautin [7], Malkin [8]) based on Lyapunov's Direct Method. The results obtained agree well with those of [2,4], while providing a better insight into the specific problem

of determining the nature of flutter . In both [5,6] an orthotropic, laminated composite panel was considered, and in [6] the effects of initial curvature, physical nonlinearities, and different boundary conditions were also included. These results were also incorporated in Librescu's monograph [9].

Ventres and Dowell [11] analyzed the effects of in-plane edge restraints on the flutter behavior of plates exposed to transverse pressure loadings or buckled by uniform thermal expansion. It was shown that the stability boundaries of low aspect ratio plates without edge-restraints are more sensitive to pressure loads than are those when complete edge restraints are considered. Furthermore, for panels with aspect ratio less than unity, the boundary support flexibility decreases the stabilizing effect of the pressure load (i.e., lowers the critical speed). The opposite behavior is exhibited by panels with aspect ratio larger than unity. For unloaded plates it was concluded that the ratio of limit cycle amplitudes for plates with and without in-plane edge restraint decreases as the aspect ratio increases, this ratio always being greater than unity (see Bolotin [1]). Numerical results were also presented for the existence of sustained flutter motions below the linear stability boundary for a clamped, thermally buckled, pressure loaded plate.

The effect of aerodynamic damping on the flutter of thin panels was analyzed by Voss and Dowell [10]. They point out that when the panel is exposed to a flow at an arbitrary angle, a certain range of values of the flow angle exists which yields flutter involving modes of nearly identical frequency but weak aerodynamic coupling. This results in the aerodynamic damping having a pronounced effect on the stability boundary.

The problem of a panel subjected to air flow and constant in-plane edge loads has been studied by various authors. Fralich [12] presented a supersonic flutter analysis for a simply supported, rectangular panel subjected either to specified in-plane compressive edge loads or to specified total in-plane end shortenings and a uniform temperature field. Linear, static aerodynamic strip theory was used and linearized equations governing small motions about the static (buckled) equilibrium state were obtained . Hence the analysis, which yields a complete picture of the flutter and buckling boundaries, cannot be used to study the flutter

7

oscillations.

Analytical studies of the flutter of buckled, simply-supported panels were presented by Kobayashi [13]. It was shown that the relationship between streamwise and spanwise stress components has a significant influence on the flutter boundary of square panels. For most cases considered, the addition of spanwise tension to a bi-axial, equal, uniform compression (due to aerodynamic heating alone) lowers the critical speed. In the case of bi-axial, equal, uniform compression alone, the boundary above which no buckled equilibrium exists is not represented by a constant flow speed (i.e., independent of the streamwise compression), but instead rises along with the streamwise compression. This result is different when compared to that for the two-dimensional panel. Thus a given region of dynamic instability of the linearized system (i.e., flutter oscillations) occurs only between two values of streamwise compression, i.e., two values of temperature. This means that as the aerodynamic heating is increased the flutter motion would start and then cease. Kobayashi [14] obtained simplified approximations of the amplitude and frequency of steady flutter motion for thermally compressed two-dimensional panels, under the assumption of small damping. It was observed that for small flow speeds and moderate streamwise compression, a buckled equilibrium co-existed with flutter motion around the flat state (see Holmes[49]). This indicates that the buckled equilibrium may not be stable in the large. Periodic motion about the buckled configuration was not obtained for any combination of the loading parameters. For moderate flow speed and compressive load the motion was non-simple harmonic (see also Dowell [45,22] and Shiau and Lu [48]). For large compressive loads, the buckled equilibrium (for small flow speeds) is stable in the large, whereas the periodic vibrations (for moderate to large flow speeds) are of the breathing type . In a subsequent paper, Kobayashi [15] considered a clamped panel with initial geometric imperfections and a static pressure differential. It was shown that the initial geometric imperfections do not always raise the flutter boundary. In particular, the case of imperfections in the second mode yielded a new type of flutter boundary, defining a region of dynamic instability (of all obtained equilibria) enclosed by the region of buckled states. This new flutter boundary occurs well below the more traditional

flutter boundary that separates static configurations from periodic motions. The existence of this region was further clarified through experiments in which steady periodic motions of small amplitude were measured at comparatively small flow speeds. The amplitudes and frequencies of flutter were obtained by the HBM.

Kobayashi [16] studied the bending-torsion flutter of wings subjected to thermal stresses at high supersonic speeds. Linear piston theory aerodynamics, including the effect of an angle of attack, was considered along with a linear bending mode and a nonlinear torsional mode. The HBM was used to obtain periodic solutions around the flat and deformed (buckled) equilibria. The angle of attack, the effect of which is similar to a constant pressure load, was shown to have a significant influence on the stability boundaries.

Voss [17] considered the flutter of thin cylindrical shells using Goldenveizer's equations. It was determined that the tangential inertia forces are important particularly when considering small values of circumferential and axial mode numbers − i.e., in membrane-type flutter.

Evensen and Olson [18, 19] considered the flutter of a circular cylindrical shell subjected to a constant, axial, in-plane edge load which is lower than the static buckling load. Two types of limit cycle solutions are obtained by the HBM: (a) two-mode standing-wave flutter and (b) four-mode circumferentially travelling-wave flutter. For the type (b) solution the analysis indicates that flutter oscillations can occur for $M < M_F$. This implies that a nonlinear structural shell model with linear aerodynamic loading could exhibit the same softening behavior as is produced by nonlinear aerodynamic loading for flat panels (e.g., also Bolotin[4]). Moreover, the type (a) solution was found to be very sensitive to small amounts of structural damping. In an earlier work, a pressure differential was also included by Olson and Fung [20]. They used Donnell's equations and obtained a two-mode standing-wave solution for the flutter oscillations by the Krylov-Bogoliubov method. The results indicate that for practical purposes flutter in a standing-wave mode does not occur below the critical speed. Regarding the influence of the internal pressure differential on the stability boundary, it was noted that among the various aerodynamic theories considered, piston

theory yielded results that were closest to experimental observations.

Gordon and Atluri [21] reconsidered the problem presented in [19], performing the analysis using the Method of Multiple Scales (MMS). However, their assumed spatial mode shapes only satisfy, exactly, the simply-supported boundary conditions on the normal displacement, while the continuity (periodicity) condition on the circumferential displacement is fulfilled in an integral-average sense. This yielded discrepancies in their results when compared with those of Evensen and Olson [19]. An interesting conclusion from their MMS analysis is that the quadratic nonlinearities only have a secondary effect on the limit cycle amplitudes, and they decrease the hardening effect of the cubic nonlinearities.

Dowell [22] considered the problem of two and three-dimensional plates undergoing limit cycle oscillations. The effects of constant in-plane edge loads and a static pressure differential are also included in this analysis. Limit cycle amplitudes are determined using the NIM for a prescribed edge load (considered greater than the classical Euler buckling load). The results indicate a buckling branch for lower M and a flutter branch for higher M. Non-simple harmonic (but periodic) and symmetry broken solutions were also obtained. The stability boundaries obtained are in close agreement with [12] and they also include an additional region where non-simple harmonic oscillations exist. For a prescribed M $(> M_F)$ and in-plane edge load, the variation of the dynamic component of the limit cycle amplitude with static presure differential is also presented. Convergence studies indicate that 4 to 6 chordwise modes are required for quantitative accuracy of the results. The analysis in [22] considered linear, quasi-steady aerodynamics since it assumed that: (1) M_F would be of the order of one, and (2) the plate amplitudes are limited to a few plate thicknesses. However, when either of the conditions (1) or (2) is invalid, the effect of aerodynamic nonlinearities becomes important and should be included in the analysis. Furthermore, if the flutter occurs in the transonic–low supersonic ($M < 1.5$) regime, then quasi-steady aerodynamic theory cannot be considered and one must re-consider the problem using the full linearized (inviscid, potential flow) theory which retains the effects of memory and three-dimensionality of the flow. This was done by Dowell [23]. Further details on the applicability of different

aerodynamic theories can be found in Librescu [9] and Dowell [24,25] . In both [24,25], results concerning the regimes of flutter (i.e., single-mode flutter, coupled-mode flutter, travelling-wave flutter, and divergence or low-frequency flutter) are presented in the M versus ϕ (plate aspect ratio) plane.

Dowell [26] considered the shallow shell equations (von Karman) to study the flutter of a two-dimensional plate with streamwise curvature. It was shown that the static aerodynamic loading due to streamwise curvature has a detrimental effect both in lowering the speed at which flutter begins and in increasing the amplitude of the ensuing motion. The flutter amplitudes obtained were of the order of the rise height of the plate. It was also demonstrated that the static aerodynamic loading and aerodynamic damping must be considered in order to avoid obtaining the unrealistic result of zero critical speed for certain values of streamwise curvature. An important observation made here was that for large curvatures, i.e., when the product of Mach number and rise-height/length exceeds 0.1, nonlinear aerodynamic effects would become important. In a subsequent paper, Dowell [27] analyzed a three-dimensional curved panel where it was concluded that three-dimensional plates with streamwise curvature are more significantly affected by pre-flutter static deformations than two-dimensional ones. Furthermore, the degree of in-plane edge restraints has a pronounced effect on the stability boundaries and subsequent flutter oscillations of three-dimensional curved plates with spanwise curvature.

Eastep [28] presented a variational analysis for the problem of a panel under the influence of both random excitation (turbulent boundary layer) and aerodynamic loading. Linear piston theory aerodynamics was considered and the spatial discretization was done using a Rayleigh-Ritz modal approximation. Random excitation in the form of a pressure with known spatial and temporal correlations was introduced. The forced response was calculated by using Fourier-transform techniques and the method of equivalent linearization for flow speeds below and above the flutter speed. The supercritical response was obtained from a numerical integration of the derived coupled homogeneous Mathieu equations. When the effect of the random load is neglected and applied in-plane edge loads are considered,

11

the results obtained by the HBM are similar to those of [12] and [22] . An interesting conclusion obtained in [12] but emphasized by Eastep [28] is that for a buckled (initially flat) panel, flutter occurs at a critical speed for which the only static equilibrium state is the dynamically unstable flat panel. Thus aerodynamic forces cause a sudden flattening of the panel, which for any increase of M represents the static configuration about which flutter motion will occur. In a related study, Eastep and McIntosh [29] analyzed a simply supported two-dimensional panel with aerodynamic loads obtained from the nonlinear second order piston theory. This included a nonlinear aerodynamic damping effect. The limit cycle amplitudes obtained by the NIM indicate a symmetry broken solution due to the presence of quadratic nonlinearities. The effect of aerodynamic nonlinearity on the stability boundary was investigated and the 'nonlinear stability boundary' was obtained. This represents the lowest flow speed $(< M_F)$ for which limit cycle oscillations are possible for a prescribed edge load. The method used in [29], first suggested by Dimantha and Roorda [30], is based on calculating an upper bound on the total energy of the system such that any initial conditions producing a greater energy would yield an unstable motion. McIntosh [31] investigated the effects of hypersonic nonlinear (second-order) aerodynamic loading on panel flutter. By introducing a single interaction parameter which represents the importance of the nonlinear aerodynamic terms in comparison with the geometric nonlinearities, it is concluded that the presence of in-plane edge restraints could result in amplitude-sensitive instability similar to that caused by aerodynamic nonlinearities (see also Eastep and McIntosh[29]).

Friedmann and Hanin [32] studied the flutter of a simply supported, orthotropic panel subjected to a coplanar air flow of arbitrary orientation using a quasi-steady, linear aerodynamic theory. However, when performing the spatial discretization by the Galerkin method, only two chordwise modes were considered. The amplitude of flutter oscillations was determined by the NIM and results concerning the effects of the flow orientation and aerodynamic damping on M_F were presented. Dzygadlo [33] considered the harmonically forced vibration of a two-dimensional panel subjected to air flow. The primary forcing-flutter resonance was examined and the aerodynamic forces were considered on the basis of a second order

potential theory for supersonic flow. Limit cycle amplitudes were obtained by using the Method of Averaging. The detailed analysis was done after neglecting quadratic and integral terms (i.e., reduction to linear piston theory aerodynamics). Therefore the results are not affected by this seemingly incorrect application of the Method of Averaging which cannot handle quadratic nonlinearities. Frequency response curves near primary resonance were obtained and it was concluded that for $M > M_F$, the forcing-flutter interaction was the cause of the new bubble-shaped solutions. The presence of material damping resulted in a softening-type behavior for a system with hardening elastic characteristics.

Morino [34] considered the flutter of a curved panel using linear quasi-steady aerodynamics and used the MMS to obtain the flutter amplitude. In that paper it was concluded that if exceptional cases (e.g., autoparametric resonance) are disregarded, quadratic nonlinearities do not have a qualitative effect on the solution. A similar conclusion was obtained by Smith and Morino [35], where the state equations are solved by the MMS and general conclusions regarding the conditions for dangerous and benign flutter in autonomous systems are re-derived. Steady-state solutions obtained by the MMS are shown to compare well with solutions obtained by the HBM. It is also shown that MMS can handle the case of zero frequency at M_F (i.e., a non-oscillating system).

Kuo et al. [36] studied the problem of nonlinear panel flutter with quasi-steady, linear aerodynamics using the MMS, HBM and NIM. Results obtained by these three methods compared well with each other for both simply supported two-dimensional and clamped three-dimensional plates. The stability analysis of limit cycle solutions was done by considering slowly varying disturbances only. It was also concluded that aerodynamic damping stabilizes the panel by reducing the amplitude of flutter, while in-plane compressive loads and viscous and hysteretic structural damping destabilize the panel by increasing the amplitude of flutter, thus making it more dangerous. Morino and Kuo [37] extended the MMS analysis of [36] to study the problem considered by Evensen and Olson [19] which contains fifth-order geometric nonlinearities. This refined analysis revealed an unstable, bent-back, high-branch curve of limit cycle amplitude versus M, thus indicating that fifth-order ge-

ometric nonlinearities have a destabilizing effect. The analysis in [37] also includes the problem of flutter-buckling interaction. The case of zero flutter frequency (which occurs at the intersection of the flutter and buckling stability boundaries) was studied. Furthermore, the problem of small damping coefficients was also analyzed by the MMS. Kuo et al. [38] considered the forcing-flutter interaction for two-dimensional panels using the HBM. It was found that the flutter speed is higher if forcing excitation is present. Thus pure forced response may exist well above the pure flutter stability boundary, i.e., M_F. Beyond the flutter stability boundary, coexistence of pure forced response and forcing-flutter interaction response was observed. Eslami and Ibrahim [39] reconsidered the problem presented in [36] for the case of orthotropic panels and used the HBM for their analysis. Conclusions similar to those in [36] were realized.

Sipcic and Morino [40] presented a Lagrangian Mechanics formulation for the aeroelastic analysis of a maneuvering aircraft, by modelling it as a fluttering two-dimensional plate undergoing a pull-up maneuver. Linear quasi-steady aerodynamics and geometric nonlinearities, as well as coupling between rigid body rotation and the elastic degrees of freedom, were included in the formulation, and the solutions were obtained by the NIM. The effects of a maneuver load factor, in-plane compressive load, and static pressure differential were studied. A new type of limit cycle representing snap-through buckling and oscillations around four equilibrium states was obtained. It was shown that chaotic motions could occur during a maneuver for system parameters in the actual flight range. The presence of a maneuver load factor could transform the response from the fixed point to a periodic or even a chaotic state, and vice versa. The case of a time-dependent maneuver (i.e., angular velocity is not constant) was also analyzed. Further studies on this problem were done by Sipcic [41]. By increasing the maneuver load factor, chaotic motions were observed via the well known routes of Intermittency, Torus-Bifurcation (Ruelle-Takens scenario), and Period-Doubling. An uncommon route to chaos was also observed. This involves a sequence of period doubling, followed by a sequence of period demultiplying bifurcations, and culminating in a sudden transition ('jump') to a chaotic state.

14

Yuen and Lau [42] analyzed the effects of in-plane compressive loads on the limit cycle motion of a fluttering plate by considering linear quasi-steady aerodynamics. They used the Incremental Harmonic Balance Method to obtain the amplitudes of flutter oscillations. The amplitude versus M curves indicated various loops, which was the main discovery of the study. This indicates that a multitude of stable and unstable limit cycles coexist at a particular M. Aperiodic and chaotic motions were also observed using the NIM.

Weiliang and Dowell [43] were the first to study the oscillations of a fluttering cantilevered plate. They considered linear, quasi-steady aerodynamics and used the Rayleigh-Ritz method for spatial discretization. Convergence studies indicated that the chord-to-length ratio has a great effect on the flutter amplitude obtained by the NIM. As this ratio increases, the number of chordwise modes required to accurately predict the flutter amplitude increases.

Dowell [44] reconsidered the problem of flutter of a buckled plate [22]. He observed certain regions in the parameter space of M versus in-plane compressive load where chaotic motions occur. By increasing the static pressure differential, chaotic motion is suppressed, then re-appears, and finally the limit-cycle degenerates to a point and all motions cease. An intuitive explanation suggests that the interaction of the two parameters (i.e., M and in-plane compressive load) which govern the two instabilities, flutter (Hopf bifurcation) and buckling (static bifurcation), causes chaotic motions. Limit cycle plots, Poincaré maps, and power spectra were obtained to verify the type of motion. In a subsequent work, by increasing the in-plane compressive load for a fixed flow speed, Dowell [45] observed the following route to chaos: the static solution undergoes a Hopf bifurcation and a periodic solution is born; this then undergoes a period-doubling bifurcation yielding a period-2 solution; then it undergoes a secondary Hopf bifurcation creating a quasi-periodic solution composed of incommensurable frequencies (bifurcation to a T^2 torus, see Seydel [46]); the frequencies become commensurable once again (frequency locking) and the period-2 solution is recovered; another period doubling occurs and a period-4 solution exists; and chaotic motions alternate with periodic motions which finally prevail. While comparing

this phenomenon of chaos to the one occurring in the Lorenz model, Dowell conjectures that chaos appears to be the result of all equilibria (static and dynamic) being unstable to infinitesimal perturbations; nevertheless, the global solutions are still bounded. What remains to be done, however, is to determine whether chaos appears directly after this type of local instability. Among the many scenarios of chaos discussed in Seydel [46] and Thompson and Stewart [47], the one observed by Dowell [45] appears to be a combination of the Torus-Breakdown and Period-Doubling routes.

Shiau and Lu [48] studied the effects of aerodynamic damping, anisotropic properties (i.e., fiber orientation and elastic modulus ratio), static pressure differential, and in-plane compressive load on the flutter amplitudes of a two-dimensional, simply supported, composite laminated plate. The effect of these parameters on modal convergence characteristics and spatial location of the maximum limit cycle amplitude were obtained by direct numerical integration. Periodic motions were obtained for moderate to high flow speeds and moderate in-plane edge loads. It was revealed that chaotic motions could occur for moderate flow speeds and high in-plane edge loads (see also Dowell [44])

Holmes [49] studied the behavior of a two-dimensional fluid-loaded panel subjected to compressive loads. The model considered nonlinear structural damping, and the Galerkin method was used for spatial discretization. The modal equations thus obtained were analyzed qualitatively, by way of a center manifold reduction, to obtain the local behavior about the Bogdanov-Takens bifurcation point (i.e., double zero eigenvalues where the flutter and divergence boundaries intersect). The most interesting result here is the existence of two contiguous regions, in the control parameter space, in which the panel can either remain buckled or flutter about its flat configuration. Furthermore, two contiguous regions where non-sinusoidal oscillations exist (Dowell[22]) have been clearly demarcated and it is shown that the transition from a buckled state to these regions, or vice-versa, occurs through a sudden jump. This is in contrast to the smooth onset of flutter when crossing the flutter boundary. In a subsequent paper, Holmes and Marsden [50] considered the infinite dimensional analysis of this problem by applying the center manifold reduction technique

directly to the governing partial differential equations. Holmes [51] reconsidered this problem by studying two cases in which divergence and flutter are coupled. For the first case, which involves the Bogdanov-Takens bifurcation (Holmes [49]), application of the center manifold theorem shows that the coupling is qualitatively captured locally by reduction to a two-dimensional essential model i.e., a single-degree-of-freedom nonlinear oscillator. The Method of Normal Forms was then employed to simplify the nonlinear terms. The second case involves a Simple and Hopf bifurcation (i.e., one zero and two purely imaginary eigenvalues). For this case, the same techniques show that the essential model is now three-dimensional, and quasi-periodic as well as chaotic motions can occur.

Dowell and Virgin [52] reconsidered the flutter of a buckled, two-dimensional panel by investigating the region in control parameter space where chaotic motions occur. As this region is entered, a loss of temporal correlation occurs, i.e., temporal chaos. When the region is penetrated deeper, by increasing the compressive edge load, more higher modes become increasingly prominent, resulting in a loss of spatial correlation also. Thus it was proposed that for systems with temporally chaotic but spatially deterministic modes, low-dimensional ones exhibit temporal chaos only, whereas higher dimensional ones exhibit spatial and temporal chaos (i.e., turbulence or displacement localization).

Zhao and Yang [53] analyzed the chaotic motions of a linearly viscous-damped, two-dimensional airfoil with cubic pitching stiffness in an incompressible flow. The boundaries demarcating buckling and different types of flutter motion (i.e., simple harmonic, general periodic, and chaotic) were obtained in the parameter space of flow speed versus elastic-axis/focus-distance ratio. It was observed that chaotic motions occur in a narrow parameter range, through a sequence of period-doubling bifurcations, and only when the flow speed is higher than the linear divergence speed. It was also concluded that a buckled panel in a supersonic flow is more susceptible to chaos than an airfoil in an incompressible flow.

Mei and Dixon [54] developed a finite element formulation to study the large-amplitude flutter of arbitrarily laminated, anisotropic composite, thin plates. The equations of motion were solved by linearizing the nonlinear stiffness matrix. They considered cross-ply

laminates with various number of layers as well as three layered angle-ply laminates with varying ply angles. The effects of simply supported and clamped boundary conditions were also examined. Gray et al. [55] considered the finite element approach to determine the nonlinear panel flutter characteristics of two-dimensional panels using third-order piston theory aerodynamics (which included second-order aerodynamic damping terms as well). Comparison between the first-, second-, and third-order piston theory revealed that the quadratic, gradient term has the most significant influence. Results also showed that the third-order piston theory aerodynamics produces a destabilizing effect. Dixon and Mei [56] studied large-amplitude panel flutter of arbitrarily laminated composite plates subjected to a uniform temperature change, by using the finite element method. The temperature effects were modelled by applying the quasi-static thermal-stress theory. The equations were solved by employing a Newton Raphson procedure for the static component and a Linearized Updated Mode with Nonlinear Time Function approximation for the dynamic component of transverse displacement. Immovable in-plane boundary conditions were considered, and it was observed that the limit cycle amplitudes are higher in the presence of the thermal loads.

Tezak et al. [57] considered the response of a nonlinear multi-degree-of-freedom system having a repeated natural frequency and subjected to a parametric excitation. The study was applied to a panel flutter problem in which frequency-coalescence flutter occurs due to aeroelastic coupling when the damping is assumed small. Here the Jordan form of the linearized system is non-diagonalizable (i.e, non-semisimple 1:1 resonance). The modal equations were solved using the MMS with special attention to the ordering of the various terms. The main feature of the analysis is that the modal amplitudes are ordered differently since it is expected that one of them (i.e., the one which is linearly coupled) is of a higher magnitude than the remaining ones. Different cases of auto-parametric (e.g., 3:1) and parametric (e.g., 1:1) resonance are studied (see Tezak [58]). However, a detailed study of this work reveals that the ordering scheme imposes certain restrictions on the magnitudes of coefficients associated with nonlinear terms, and it appears that the physical applications

of this method would be limited (e.g., restricted to moderately thick plates with thickness ratios between 50 and 100).

Fu and Nemat-Nasser [59] were the first to analyze the response of a lightly-damped, parametrically-excited nonlinear dynamical system for the special case when the corresponding autonomous linearization has a non-diagonalizable Jordan form. Two cases of parametric resonance were considered and the method of Krylov, Bogoliubov, and Mitropolsky was used to show that certain steady-state solutions exist, whose description involves fractional powers of the small (perturbation) parameter.

Recently, Namachchivaya and Malhotra [60] studied the effect of periodic parametric excitations on a four-dimensional system exhibiting a Hopf bifurcation with 1:1 internal resonance along with subharmonic parametric resonance. The linear operator was assumed to have a generic non-semisimple structure. They investigated the stability and local bifurcational behavior of the trivial and nontrivial equilibrium solutions obtained from the reduced normal form equations (these equilibria correspond to periodic solutions of the original normal form system). Various bifurcations were located, i.e., Simple (divergence), Hopf, Bogdanov-Takens (Simple+Hopf), Double Hopf, Simple and Hopf, and Bogdanov-Takens and Hopf. Their numerical results indicate a sequence of period-doubling bifurcations leading to chaotic behavior.

2.2 Nonlinear Dynamics

2.2.1 Dimension of attractors

It is well known that for dissipative systems an infinitesimally small volume of initial conditions gets mapped onto an even smaller volume as time progresses (e.g., Eckmann [61], Moon[62]). Moreover, if for a given initial condition the long-time evolution of the phase trajectory confines itself to a bounded set of points, the motion is said to have converged to an attractor. Hence, we may define an attractor as a closed set, A, having an open neighborhood such that almost every trajectory starting in this neighborhood ends up in

19

A and passes arbitrarily close to every point in *A*. Other more formal definitions of an attractor and its properties may be found in Eckmann [61] and Seydel [46]. A chaotic attractor experiences contraction in some directions and expansion in at least one direction. Since the attractor, by definition, is bounded, this results in a stretching and folding of the attractor, as time unfolds, into a sheet-like, unfamiliar, complex structure called a strange attractor.

Farmer et al. [63] review various definitions of the dimension of an attractor (i.e., capacity, Hausdorff, information, pointwise, correlation, and Lyapunov) and discuss various aspects regarding their numerical computation (see also Parker and Chua [64]). These definitions fall into two categories, i.e., those that depend on metric properties of the attractor and those that depend on the frequency with which a trajectory visits different regions of the attractor. Generally, all dimensions obtained using the former definition take on the same value called the fractal dimension, and those based on the latter definition take on a common value termed the dimension of natural measure. The Lyapunov dimension, defined in terms of dynamical properties, does not fall into either of these two categories. Its definition, due to a conjecture presented by Kaplan and Yorke [65], uses the Lyapunov exponents and is the one considered in this thesis. Starting with the definition of the capacity dimension, Farmer et al. [63] provide a heuristic plausibility argument supporting the Kaplan-Yorke conjecture (see also Parker and Chua [64]). The Lyapunov dimension is generally the most feasible to compute, whereas the numerical algorithms for the remaining ones, although more straightforward, are impractical for all except low-dimensional attractors. Grassberger and Procaccia [66] conducted an extensive study of the correlation dimension. They proposed an efficient algorithm for its computation from experimental data obtained as a time series of a single variable. This is based on the embedding procedure for phase space reconstruction (Packard et al. [67]). They also pointed out the relationship between the capacity, correlation, and information dimensions.

Froehling et al. [68] gave a physical interpretation of the fractal dimension of a chaotic attractor, i.e., it measures how 'closely packed' the sheets of the attractor are. However, it

should be noted that this topic is as yet an active research area and relationships between, and physical meaning of, the different definitions of dimension are as yet unclear. Moreover, it has been shown that in addition to the dimensions discussed here, there exists a countably infinite set of dimensions called the Renyi dimensions (Parker and Chua [64]).

One of the main uses of dimensions is to quantify the complexity of an attractor, i.e., to measure its strangeness. The dimension of an attractor also provides a lower bound on the number of state variables needed to accurately describe the dynamics of an attractor. Hence, when obtained using experimental data, the dimension can serve as an estimate of the minimum number of degrees of freedom required to correctly model the physical phenomenon. Strange attractors usually have a fractal dimension, whereas non-strange attractors always have an integer dimension. However, merely calculating the dimension of an attractor is not sufficient to classify it as chaotic. Other tools, e.g., Lyapunov exponents, Poincaré sections, and frequency spectra, must also be considered.

2.2.2 Lyapunov exponents

Goldhirsch et al. [69] demonstrated that, under certain assumptions, the real parts of the stability exponents (i.e., eigenvalues of the stability matrix appearing in the variational equation) equal the corresponding Lyapunov exponents plus an error that decreases with increasing simulation time. This observation yields a method of extrapolation which has been used to obtain Lyapunov exponents from finite amounts of data. The above conclusion was verified in their numerical applications wherein it was also noted that the Lyapunov dimension (Kaplan-Yorke) converges much faster than the individual exponents. This technique (see also Berge et al. [70]) was employed by Aboudi et al. [71] to study the dynamic stability of homogenous, viscoelastic plates subjected to periodic in-plane loads. There the stability was determined by calculating the largest Lyapunov exponent.

Wolf et al. [72] presented two methods and accompanying Fortran codes for determining the Lyapunov spectrum. The first one, used in this thesis, is based on the technique developed independently by Shimada and Nagashima [73] and Benettin et al. [74] which

uses the phase-space plus tangent-space approach. Here a primary trajectory is defined by integrating the nonlinear equations of motion for some initial condition. Neighboring trajectories evolving from points on the surface of an infinitesimal hypersphere surrounding the initial condition are defined by the action of the variational equations. The points on the hypersphere (i.e., initial conditions for the variational system) are chosen to represent an orthonormal set of basis vectors. This ensures the generation of principal axes defined by the evolution via the variational equations. The stretching or contraction along the principal directions is then computed at each specified Lyapunov time step, thus yielding the Lyapunov spectrum. Then a Gram-Schmidt re-orthonormalization of the principal axes is carried out to prevent divergence in their magnitudes. These are then used as the new set of orthonormal basis vectors for the next Lyapunov time step.

The second method developed by the authors in [72] is used for estimating all non-negative Lyapunov exponents from an experimental time series. In this method the long-term exponential growth rate of small hyper-volume elements in an m-dimensional recon-structed attractor (obtained by using the concept of delay coordinates advanced by Packard et al. [67]) is monitored. Here m (an input parameter) is an estimated relevant dimension of the infinite-dimensional system. For the largest positive exponent, λ_1, the evolution of a single pair of nearby reconstructed orbits is monitored. Whenever their separation be-comes large, a Gram-Schmidt re-orthonormalization is done, and the primary and newly reconstructed secondary trajectory are monitored from there on. At the end of a specified Lyapunov time step, the exponential growth rate of the line element separating the orbits is calculated, thus yielding an estimate of λ_1. Similarly the exponential growth rate of an area element, defined by monitoring points on three reconstructed orbits, provides the estimate for the sum of the first two exponents, i.e., $\lambda_1 + \lambda_2$. Although it seems that the process could be repeated analogously to obtain the remaining non-negative exponents (Wolf et al. [72]), numerical problems inherent in this method limit its use to the determination of the largest two exponents only (Parker and Chua [64]). It is worthwhile mentioning that Packard et al. [67] showed that the method of phase space reconstruction preserves the

Lyapunov exponents.

Pezeshki and Dowell [75] used the two methods described above to calculate the Lyapunov exponents for the one-, two-, three-, and four-mode approximations of a magnetically-buckled cantilevered beam that is parametrically excited at the support. By obtaining convergence of the Lyapunov dimension for the two- and three-mode analyses when chaotic motions exist, they infer that modal convergence has occurred. The concept of using the Lyapunov dimension as an estimate of the number of necessary modes required for modal convergence was successfully tested. The effect of the forcing amplitude on the Lyapunov exponents was also studied. The monographs of Parker and Chua [64], Moon [62], and Seydel [46] provide further details and discussions on Lyapunov exponents and their calculations.

2.2.3 Routes to chaos

When varying the control parameter (e.g., edge load, flow velocity) in a dynamical system, the solution may undergo a bifurcation and hence a transition from one attracting state to another. The appearance of a chaotic attractor is usually preceded by a sequence of such bifurcations which can be considered as a route to chaos. Some of the frequently encountered routes are outlined here (Seydel [46], Berge et al. [70], Eckmann[61], and Swinney [76]). However, we note that there is no unique set of ways in which chaos ensues, and other routes may exist.

In the Torus-Bifurcation route, proposed by Newhouse, Ruelle, and Takens [77], it is conjectured that only two bifurcations precede the onset of chaos. These are a Hopf bifurcation, yielding periodic motion, followed by a secondary Hopf (or Niemark) bifurcation, resulting in quasi-periodic motion on a two-frequency torus (2-torus). As the control parameter is varied further, the system undergoes a transition to an unstable 3-torus with the simultaneous appearance of a (bounded) strange attractor. However, Grebogi et al. [78] have shown through numerical experiments that chaotic attractors rarely appear along with a 3-torus for systems with moderate nonlinearity. They reason that this may be due to the fact that the theorem of Newhouse, Ruelle, and Takens [77] considers a very specific type of

23

small perturbation to show instability of the 3-torus. An alternative theory regarding this scenario is that the appearance of wrinkles on the 2-torus is a sign of impending chaos (see Swinney [76]).

In the Period-Doubling route the periodic state undergoes a sequence of period-doubling bifurcations as the control parameter is varied. This process accumulates at a critical value of the parameter beyond which the motion becomes chaotic, with infinite period and a broadbanded freqency spectrum. A universal number, known as the Feigenbaum number, exists which describes asymptotically the ratio of successive intervals (expressed in terms of the control parameter) between bifurcation points.

Chaos through Intermittency, also known as the Pomeau-Maneville scenario (Seydel [46]), is characterized by the transition to chaotic behavior occurring through repeated intervals of periodic and chaotic motions. As the chaotic regime is penetrated deeper (by varying the control parameter), the periodic intervals decrease, making it more and more difficult and finally impossible to recognize the periodic motion. This scenario occurs at a turning point where a stable and unstable fixed point collide.

The Torus-Breakdown route is characterized by the transition from a 2-torus quasi-periodic state (i.e., motion described by two incommensurate frequencies) to a frequency-locked state (i.e., periodic motion with one basic frequency). This implies that a breakdown of the torus has occurred. Then, as the control parameter is varied further, the frequency-locked periodic solution undergoes a well-defined transition to a chaotic state.

Another scenario for chaos (see Swinney [76] and references therein) arises due to a phenomenon known as Soft Mode Instability. This occurs as a result of the nonlinear competition between a symmetry-breaking linear instability and an oscillatory instability, i.e., coexistence of symmetry-broken- and symmetric- unstable solutions. In general it is not possible to classify the motion resulting from this nonlinear competition when the number of unstable modes is greater than or equal to three. This then could result in chaotic behavior for systems of dimension equal to three or more.

Chapter 3

PROBLEM FORMULATION

3.1 Governing Equations

Consider a rectangular flat panel (l_1 x l_2) of uniform thickness h, symmetrically laminated with $2l + 1$ transversely isotropic layers. It is assumed that the plane of isotropy at each point is parallel to the reference plane (selected as the mid-plane of the laminate). The points of the undeformed reference plane ($x_3 = 0$) are referred to a set of Cartesian orthogonal axes x_ω ($\omega = 1,\ 2$), with the x_3 axis normal to the reference plane (see Fig. 3.1). Throughout this work the Einsteinian summation convention is implied unless otherwise stated, with Greek indices ranging from 1 to 2 and Latin indices ranging from 1 to 3.

3.1.1 Strain-displacement equations

The higher-order representation for the displacement field (Reddy [79]) is given as,

$$
\begin{aligned}
V_\alpha[x_\omega, x_3, t] &= u_\alpha[x_\omega, t] + x_3 \psi_\alpha[x_\omega, t] + x_3^2 \eta_\alpha[x_\omega, t] + x_3^3 \zeta_\alpha[x_\omega, t] \\
V_3[x_\omega, x_3, t] &= u_3[x_\omega, t]
\end{aligned}
\tag{3.1}
$$

Within the framework of the von Kármán theory for the large deflection of plates, only the nonlinearities associated with the transverse displacement (and its gradients) are retained. Hence the Lagrangian strain tensor e_{ij} is written as,

$$
2e_{ij} = V_{i,j} + V_{j,i} + V_{3,i}V_{3,j}
\tag{3.2}
$$

The above representation of e_{ij} can be shown to correspond to the small linear strain and moderate rotation concept (Librescu and Schmidt [80]). Following Reddy [79] and Librescu

and Stein [81], the exact fulfillment of the tangential static conditions on the bounding planes $x_3 = \pm\frac{h}{2}$, in the absence of tangential surface loads, requires that,

$$p_\alpha \equiv \left[s_{\alpha3}\right]_{-h/2}^{+h/2} = 0 \quad , \quad \tilde{p}_\alpha \equiv \left[s_{\alpha3}x_3\right]_{-h/2}^{+h/2} = 0 \tag{3.3}$$

Here $s_{\alpha3}$ denotes the transverse shear components of the symmetric second Piola-Kirchhoff stress tensor s_{ij}, while p_α, $\tilde{p}_\alpha$ denote the tangential surface loads and load couple components, respectively. Substitution of (3.1), (3.2) into the constitutive equation for $s_{\alpha3}$, i.e.,

$$s_{\alpha3} = 2E_{\alpha3\omega3}e_{\omega3} \tag{3.4}$$

considered in conjunction with conditions (3.3) and the symmetry of the laminate, yields

$$\eta_\alpha = 0 \quad , \quad \zeta_\alpha = -\frac{4}{3h^2}(u_{3,\alpha} + \psi_\alpha) \tag{3.5}$$

Here, $e_{\alpha3}$ denotes the transverse shear strain components and $E_{\alpha3\omega3}$ denotes the transverse shear components of the elastic moduli tensor E_{ijmn}.

Thus it is observed that the dependent variables in the displacement field when considering the higher-order transverse shear deformation theory (HSDT) are the same as those appearing within a first-order transverse shear deformation theory (FSDT) formulation, i.e., u_3, u_α and ψ_α. Substitution of (3.1), (3.5) into (3.2) yields the following expressions for the components of the strain tensor,

$$e_{\alpha\beta} = \varepsilon_{\alpha\beta} + x_3\kappa_{\alpha\beta} + x_3^3\zeta_{\alpha\beta} \quad , \quad e_{\alpha3} = \varepsilon_{\alpha3} + x_3^2\eta_{\alpha3} \tag{3.6}$$

where the strain measures are defined as,

$$2\varepsilon_{\alpha\beta} \equiv u_{\alpha,\beta} + u_{\beta,\alpha} + u_{3,\alpha}u_{3,\beta} \quad , \quad 2\kappa_{\alpha\beta} \equiv \psi_{\alpha,\beta} + \psi_{\beta,\alpha}$$

$$2\varepsilon_{\alpha3} \equiv \psi_\alpha + u_{3,\alpha} \quad , \quad 2\eta_{\alpha3} \equiv -\delta_h\frac{4}{h^2}(\psi_\alpha + u_{3,\alpha}) \tag{3.7}$$

$$2\zeta_{\alpha\beta} \equiv -\delta_h\frac{4}{3h^2}(2u_{3,\alpha\beta} + \psi_{\alpha,\beta} + \psi_{\beta,\alpha})$$

The tracer δ_h assumes the value one or zero according to whether the HSDT or FSDT is being considered. The specialization for the classical plate theory (CPT, based on Kirchhoff-Love constraints) is obtained by considering $\psi_\alpha = -u_{3,\alpha}$ and $\delta_h = 0$.

26

3.1.2 Constitutive equations

The 3D constitutive equations for a monoclinic elastic material are,

$$s_{\alpha\beta} = \tilde{E}_{\alpha\beta\omega\rho}e_{\omega\rho} + \delta_A \frac{E_{\alpha\beta33}}{E_{3333}}s_{33} \quad , \quad s_{\alpha3} = 2E_{\alpha3\omega3}e_{\omega3} \tag{3.8}$$

where,

$$\tilde{E}_{\alpha\beta\omega\rho} = E_{\alpha\beta\omega\rho} - \frac{E_{\alpha\beta33}E_{33\omega\rho}}{E_{3333}} \tag{3.9}$$

Using the third equation of motion from 3D elasticity theory (i.e., $(3.16)_3$) along with the displacement representation (3.1), and integrating over the transverse dimension x_3, we obtain the transverse normal stress component as,

$$s_{33} = -\int \Big\{ s_{\alpha3,\alpha} + (s_{\alpha\beta}V_{3,\beta})_{,\alpha} + (s_{3\alpha}V_{3,\alpha})_{,3} - \rho\ddot{V}_3\delta_B \Big\}dx_3 \quad + \quad K[x_\omega] \tag{3.10}$$

Here the tracers δ_A and δ_B identify the overall and dynamic-only contributions brought by s_{33}, respectively, with $\rho[x_3]$ being the mass density of the panel. When performing the above integral equations, (3.1), (3.6), (3.7) and (3.4) are used, and following the von Kármán concept, nonlinearities involving the in-plane displacement field quantities u_α or ψ_α are neglected. The elastic moduli tensor components and mass density are constant for each homogeneous laminate, hence they are represented by a superposition of weighted step functions in the x_3 coordinate. Furthermore, an order of magnitude analysis shows that the contribution due to the third term in the integral may be neglected in comparison with the remaining terms. The constant $K[x_\omega]$ is determined from conditions on the upper and lower bounding planes of the panel. Thus the transverse normal stress component may be expressed as,

$$s_{33} = s_{33}^{(1)}x_3 + s_{33}^{(2)}x_3^2 + s_{33}^{(3)}x_3^3 + K[x_\omega] \tag{3.11}$$

27

where,

$$s_{33}^{(1)} = -E_{\alpha3\omega3}^{<k>}(\psi_{\omega,\alpha} + u_{3,\omega\alpha}) + \delta_B \rho_{<k>} \ddot{u}_3 \quad , \quad s_{33}^{(2)} = E_{\alpha3\omega3}^{<k>} \delta_h \frac{4}{h^2} u_{3,\omega} u_{3,\alpha}$$

$$s_{33}^{(3)} = E_{\alpha3\omega3}^{<k>} \delta_h \frac{4}{3h^2}(\psi_{\omega,\alpha} + u_{3,\omega\alpha}) \quad , \quad K[x_\omega] = Z_1 - \left(\frac{h}{2}\right)^2 s_{33}^{(2)<1>}$$

$$Z_1 = \frac{p_3^+ + p_3^-}{2} \quad , \quad p_3^\pm \equiv s_{33}\Big|_{x_3 = \pm h/2} \tag{3.12}$$

Here the symbol $< k >$ implies that the material property is evaluated for the kth layer. Furthermore, an order of magnitude analysis shows that the term Z_1, appearing in (3.12), may be neglected from here on.

The stress-resultants are defined as the moment of order zero of the in-plane and transverse-shear-stress components, whereas the stress-couples are defined by the first order moment of the in-plane stress components. For a symmetric laminate these are given as,

$$L_{\alpha\beta} \equiv \sum_{r=1}^{2m+1} \int_{h_{<r-1>}}^{h_{<r>}} s_{\alpha\beta}^{<r>} dx_3 = 2\int_0^{h_{<m+1>}} s_{\alpha\beta}^{<m+1>} dx_3 + 2\sum_{r=1}^{m} \int_{h_{<r+1>}}^{h_{<r>}} s_{\alpha\beta}^{<r>} dx_3$$

$$Q_{\alpha3} \equiv \sum_{r=1}^{2m+1} \int_{h_{<r-1>}}^{h_{<r>}} s_{\alpha3}^{<r>} dx_3 = 2\int_0^{h_{<m+1>}} s_{\alpha3}^{<m+1>} dx_3 + 2\sum_{r=1}^{m} \int_{h_{<r+1>}}^{h_{<r>}} s_{\alpha3}^{<r>} dx_3 \tag{3.13}$$

$$M_{\alpha\beta} \equiv \sum_{r=1}^{2m+1} \int_{h_{<r-1>}}^{h_{<r>}} s_{\alpha\beta}^{<r>} x_3 dx_3 = 2\int_0^{h_{<m+1>}} s_{\alpha\beta}^{<m+1>} x_3 dx_3 + 2\sum_{r=1}^{m} \int_{h_{<r+1>}}^{h_{<r>}} s_{\alpha\beta}^{<r>} x_3 dx_3$$

Equation (3.13) considered in conjunction with (3.8), (3.6), (3.7), (3.11) and (3.12) yields the following expressions for the stress-resultants and stress-couples:

$$L_{\alpha\beta} = \frac{1}{2} F_{\alpha\beta\omega\rho}\left(u_{\omega,\rho} + u_{\rho,\omega} + u_{3,\omega} u_{3,\rho}\right) + \delta_A \delta_H \frac{4}{h^2} K_{\alpha\beta\omega\rho} u_{3,\omega} u_{3,\rho}$$
$$+ 2\delta_A K[x_\omega] Q_{\alpha\beta33}$$

$$Q_{\alpha3} = \left[R_{\alpha3\omega3} - \delta_h \frac{4}{h^2} P_{\alpha3\omega3}\right]\left(\psi_\omega + u_{3,\omega}\right) \tag{3.14}$$

$$M_{\alpha\beta} = \left[\frac{1}{2} D_{\alpha\beta\omega\rho} - \delta_h \frac{2}{3h^2} S_{\alpha\beta\omega\rho}\right]\left(\psi_{\omega,\rho} + \psi_{\rho,\omega}\right) - \delta_h \frac{4}{3h^2} S_{\alpha\beta\omega\rho} u_{3,\omega\rho}$$
$$- \delta_A \left[K_{\alpha\beta\omega\rho} - \delta_h \frac{4}{3h^2} N_{\alpha\beta\omega\rho}\right]\left(\psi_{\rho,\omega} + u_{3,\omega\rho}\right) + \delta_A \delta_B I_{\alpha\beta33} \ddot{u}_3$$

28

The expressions for the rigidity quantities $F_{\alpha\beta\omega\rho}$, $K_{\alpha\beta\omega\rho}$, $D_{\alpha\beta\omega\rho}$, $S_{\alpha\beta\omega\rho}$, $N_{\alpha\beta\omega\rho}$, $Q_{\alpha\beta33}$, $I_{\alpha\beta33}$, $R_{\alpha3\omega3}$ and $P_{\alpha3\omega3}$ are defined by equations (A.1) in Appendix A.

3.1.3 Governing equations of motion

For a 3D continuum, after neglecting body forces, the equations of motion are expressed as,

$$[s_{jk}(\delta_{ik} + V_{i,k})]_{,j} = \rho\ddot{V}_i \tag{3.15}$$

Here δ_{ik} denotes the Kronecker delta. Neglecting nonlinearities containing the in-plane displacements V_α (i.e., the von Kármán concept) and using the displacement representation (3.1) for the transverse displacement V_3, the three equations of motion are written as,

$$s_{\beta\alpha,\beta} + s_{3\alpha,3} = \rho\ddot{V}_\alpha$$
$$s_{33,3} + s_{\alpha3,\alpha} + (s_{\alpha\beta}V_{3,\beta})_{,\alpha} + (s_{3\alpha}V_{3,\alpha})_{,3} = \rho\ddot{V}_3 \tag{3.16}$$

The governing equations are derived by taking moments of order zero of the equations of motion (3.16), and moments of order one of $(3.16)_{1,2}$. Considering (3.1), (3.5), (3.13) and neglecting tangential inertia terms (i.e., those containing $\ddot{u}_\alpha$), the five governing equations for a symmetric laminate, in the absence of tangential surface loads, are obtained in terms of the five unknowns u_α, ψ_α and u_3 as,

$$L_{\alpha\beta,\beta} = 0$$
$$Q_{\alpha3,\alpha} + L_{\alpha\beta}u_{3,\alpha\beta} + p_3 - m_0\ddot{u}_3 = 0 \tag{3.17}$$
$$M_{\alpha\beta,\beta} - Q_{\alpha3} - \delta_C\left[m_2\ddot{\psi}_\alpha - m_4\frac{4}{3h^2}(\ddot{u}_{3,\alpha} + \ddot{\psi}_\alpha)\right] = 0$$

It should be noted that $(3.17)_1$ is considered when deriving $(3.17)_2$. Here $p_3(\equiv p_3^+ - p_3^-)$ represents the transverse normal surface load, i.e., the aerodynamic load in this thesis. The tracer δ_C identifies the effect of the rotary inertia terms, i.e., all inertia terms arising from the first order moment of in-plane inertias $\ddot{V}_\alpha$. It takes on the values one or zero according to whether the contribution of rotary inertias is considered or disregarded. The reduced mass quantities m_0, m_2, m_4 are defined by equation (A.2) in Appendix A.

3.1.4 A mixed formulation of governing equations

The governing equations are now specialized for the case of a composite panel with transversely isotropic constituent laminae. For this case the expressions for the reduced elastic moduli in terms of the engineering quantities are (Librescu [9]),

$$
\begin{aligned}
\tilde{E}_{\alpha\beta\omega\rho} &= \frac{E}{1+\mu}\Big[\frac{1}{2}(\delta_{\alpha\omega}\delta_{\beta\rho} + \delta_{\alpha\rho}\delta_{\beta\omega}) + \frac{\mu}{1-\mu}\delta_{\alpha\beta}\delta_{\omega\rho}\Big] \\
\frac{E_{\omega\rho33}}{E_{3333}} &= \frac{\mu'E}{E'(1-\mu)}\delta_{\omega\rho} \quad , \qquad E_{\alpha3\omega3} = G'\delta_{\alpha\omega}
\end{aligned}
\tag{3.18}
$$

Here E and μ represent the Young's modulus and Poisson ratio in the plane of isotropy, respectively, whereas E', μ' and G' are the Young's modulus, Poisson ratio and shear modulus in the planes normal to the plane of isotropy, respectively. Substituting (3.18), $(3.7)_1$ and $(3.12)_{4,2}$ into $(3.14)_1$, and using the fact that Z_1 may be neglected on the basis of an order of magnitude analysis, we obtain the result,

$$
L_{\alpha\beta} = b\varepsilon_{\alpha\beta} + c\delta_{\alpha\beta}\varepsilon_{\omega\omega} + \delta_A\delta_H\frac{4}{h^2}d\delta_{\alpha\beta}u_{3,\omega}u_{3,\omega}
\tag{3.19}
$$

The coefficients b, c, and d are defined by (A.3) in Appendix A. Performing a contraction on (3.19) to obtain $\varepsilon_{\omega\omega}$ and using this result when inverting (3.19) to solve for $\varepsilon_{\alpha\beta}$ results in,

$$
\varepsilon_{\alpha\beta} = \tilde{b}L_{\alpha\beta} + \tilde{c}\delta_{\alpha\beta}L_{\omega\omega} + \delta_A\delta_H\tilde{d}\delta_{\alpha\beta}u_{3,\omega}u_{3,\omega}
\tag{3.20}
$$

The coefficients $\tilde{b}$, $\tilde{c}$ and $\tilde{d}$ are defined by (A.4) in Appendix A.

The in-plane stress-resultants, $L_{\alpha\beta}$, are expressed in terms of a stress function $C[x_\omega, t]$ as,

$$
L_{\alpha\beta} = \epsilon_{\alpha\omega}\epsilon_{\beta\rho}C_{,\omega\rho}
\tag{3.21}
$$

thus implying that the first two governing equations, i.e., $(3.17)_{1,2}$, are identically satified. Here $\epsilon_{\alpha\omega}$ denotes the 2D permutation symbol. For the remaining three governing equations $(3.17)_{3,4,5}$ we proceed as follows. Substituting (3.21), $(3.14)_3$, (3.18), (A.1) and $(3.14)_{2,3}$,

(3.18), (A.1) into $(3.17)_3$ and $(3.17)_{4,5}$ respectively, we obtain,

$$\epsilon_{\alpha\omega}\epsilon_{\beta\rho}C_{,\omega\rho}u_{3,\alpha\beta} + B_4(\psi_{\omega,\omega} + u_{3,\omega\omega}) + p_3 - m_0\ddot{u}_3 = 0$$

$$B_2\psi_{\beta,\alpha\beta} + B_3\psi_{\alpha,\beta\beta} - B_1 u_{3,\alpha\beta\beta} - \delta_A B_5(\psi_{\beta,\alpha\beta} + u_{3,\alpha\beta\beta}) \qquad (3.22)$$
$$-B_4(\psi_\alpha + u_{3,\alpha}) + (\delta_A\delta_B B_6 + \delta_C m_4 \frac{4}{3h^2})\ddot{u}_{3,\alpha} - \delta_C(m_2 - m_4\frac{4}{3h^2})\ddot{\psi}_\alpha = 0$$

The coefficients $B_1 - B_6$ are given by (A.5) in Appendix A. Thus the reduced governing system (3.22) consists of three equations expressed in terms of the four unknowns ψ_α, u_3 and C. The fourth equation is obtained by considering the compatibility equation in terms of the in-plane strain components, obtained from $(3.7)_1$ as,

$$\epsilon_{\alpha\omega}\epsilon_{\beta\rho}\left[\varepsilon_{\alpha\beta,\omega\rho} + \frac{1}{2}u_{3,\alpha\beta}u_{3,\omega\rho}\right] = 0 \qquad (3.23)$$

Within a displacement formulation, equation (3.23) as well as the remaining compatibility equations are identically satisfied by virtue of the strain-displacement equations (3.7). However, for the mixed formulation the in-plane mid-surface displacements, u_α, have been eliminated from the reduced governing system (3.22) and hence (3.23) should be explicitly satisfied by any solution which satisfies the reduced governing system. Therefore, upon substituting (3.20) and (3.21) into (3.23) we obtain,

$$(\bar{b} + \bar{c})C_{,\omega\omega\pi\pi} + \frac{1}{2}(u_{3,\omega\omega}u_{3,\pi\pi} - u_{3,\omega\pi}u_{3,\omega\pi}) + 2\delta_A\delta_H\bar{d}(u_{3,\pi\omega\omega}u_{3,\pi} + u_{3,\pi\omega}u_{3,\pi\omega}) = 0 \quad (3.24)$$

Equations $(3.22)_{1,2,3}$ and (3.24) in the four unknowns ψ_α, u_3 and C govern the large-deflection theory of shear-deformable flat panels, symmetrically laminated with transversely isotropic layers. They incorporate the effects of transverse shear deformations and the transverse normal stress, and fulfill the static conditions on the bounding planes of the plate. Their FSDT conterpart is obtained by considering $\delta_A = \delta_H = 0$ and $G'_{<r>} \to K^2 G'_{<r>}$, where K^2 denotes a transverse shear correction factor. The von Kármán equations for a symmetrically laminated composite with isotropic laminae are obtained, within the framework of the CPT, by specializing their FSDT conterpart for $K^2 \to \infty$, $\psi_\alpha \to -u_{3,\alpha}$.

31

3.1.5 Alternative representation of governing equations

Following the procedure considered by Librescu and Stein [81], Librescu and Reddy [82], and Librescu and Chang [83, 84], an alternative form of the governing system, i.e, $(3.22)_{1,2,3}$ and (3.24), is derived. Introducing (3.21) into $(3.22)_1$, $\psi_{\omega\omega}$ is expressed as,

$$\psi_{\omega\omega} = -\frac{1}{B_4}L_{\omega\rho}u_{3,\omega\rho} + \frac{1}{B_4}(m_0\ddot{u}_3 - p_3) - u_{3,\omega\omega} \tag{3.25}$$

Equation $(3.22)_2$ can be re-written as,

$$(B_2 + B_3)\psi_{\beta,\alpha\beta} + B_3(\psi_{\alpha,\beta\beta} - \psi_{\beta,\alpha\beta}) - B_1 u_{3,\alpha\beta\beta} - \delta_A B_5(\psi_{\beta,\alpha\beta} + u_{3,\alpha\beta\beta}) \tag{3.26}$$
$$-B_4(\psi_\alpha + u_{3,\alpha}) + (\delta_A\delta_B B_6 + \delta_C m_4\frac{4}{3h^2})\ddot{u}_{3,\alpha} - \delta_C(m_2 - m_4\frac{4}{3h^2})\ddot{\psi}_\alpha = 0$$

Defining, without loss of generality, the potential function $\Phi[x_\omega, t]$ as,

$$\epsilon_{\alpha\beta}\Phi_{,\beta} \equiv \frac{B_3}{B_4}\epsilon_{\alpha\beta}\epsilon_{\omega\rho}\psi_{\omega,\beta\rho} = \frac{B_3}{B_4}(\psi_{\alpha,\beta\beta} - \psi_{\beta,\alpha\beta}) \tag{3.27}$$

results in a system of five equations, i.e., $(3.22)_{1,2,3}$, (3.24) and (3.27) in the five unknowns ψ_α, u_3, C and Φ. The remainder of the procedure consists of eliminating the two unknowns ψ_α from the governing system. Towards this end we solve for ψ_α by introducing (3.25) and (3.27) into (3.26) and considering a harmonic time dependency of the form $\psi_\alpha[x_\omega, t] = \hat{\psi}_\alpha[x_\omega]e^{i\hat{\omega}t}$. The result is,

$$\psi_\alpha(B_4 + \delta_C\hat{m}_1\hat{\omega}^2) = \left(\frac{B_2 + B_3}{B_4} - \delta_A\frac{B_5}{B_4}\right)\left[m_0\ddot{u}_{3,\alpha} - p_{3,\alpha} - (L_{\omega\rho}u_{3,\omega\rho})_{,\alpha}\right] - B_4\epsilon_{\beta\alpha}\Phi_{,\beta} \tag{3.28}$$
$$-(B_1 + B_2 + B_3)u_{3,\omega\omega\alpha} - B_4 u_{3,\alpha} + (\delta_A\delta_B B_6 + \delta_C m_4\frac{4}{3h^2})\ddot{u}_{3,\alpha}$$

Substitution of (3.28) into $(3.22)_1$ considered in conjunction with (3.21) and the above harmonic time dependency for u_3 yields the result,

$$Du_{3,\omega\omega\alpha\alpha} - \epsilon_{\alpha\omega}\epsilon_{\beta\rho}\left[C_{,\omega\rho}u_{3,\alpha\beta} - S(C_{,\omega\rho}u_{3,\alpha\beta})_{,\pi\pi}\right] - (p_3 - Sp_{3,\alpha\alpha})$$
$$+m_0(\ddot{u}_3 - T\ddot{u}_{3,\alpha\alpha}) + \delta_C\left[\frac{\hat{m}_1 m_0}{B_4}\dddot{u}_3 - (m_4\frac{4}{3h^2} + \hat{m}_1)\ddot{u}_{3,\alpha\alpha} - \frac{\hat{m}_1}{B_4}\ddot{p}_3\right] = 0 \tag{3.29}$$

The coefficients $\hat{m}_1$, D, S and T are given by (A.6) in Appendix A. Introducing (3.25), (3.28) into (3.26) and considering the above harmonic time dependency for ψ_ω and Φ, we obtain,

$$\Phi - \frac{B_3}{B_4}\Phi_{,\lambda\lambda} - \delta_C \frac{\hat{m}_1}{B_4}\ddot{\Phi} = 0 \tag{3.30}$$

Thus the governing system $(3.22)_{1,2,3}$ and (3.24) has been transformed into a system containing two coupled equations in the variables u_3 and C, and a third uncoupled equation expressed in terms of a potential function Φ, i.e., equations ((3.24), (3.29)) and (3.30), respectively. This tenth-order system of partial differential equations (PDE's) governs the large motions of a shear deformable composite panel made up of transversely isotropic laminae, subjected to constant in-plane edge loads and a transverse load. Its FSDT and CPT counterparts can be obtained by the procedure described in the previous section. The CPT related equations derived in this way coincide with von Kármán's results. We note that equation (3.30) defines the boundary layer effect on the overall solution, this effect diminishing away from the edges of the panel (e.g., Librescu and Stein [81]).

3.2 Boundary Conditions

For a simply supported panel, the five boundary conditions associated with the tenth-order governing system, represented by (3.22) and (3.24), are:

Case A : Edges $x_\alpha = 0, l_\alpha$ freely movable in the in-plane direction normal to the edge, and subjected to biaxial compressive loads $\tilde{L}_\alpha$:

$$u_3 = \psi_\beta = M_{\alpha\alpha} = L_{\alpha\beta} = 0 \quad , \quad L_{\alpha\alpha} = -\tilde{L}_\alpha \quad \text{where,} \quad \sum_\alpha \tag{3.31}$$

Case B : Edges $x_\alpha = 0, l_\alpha$ immovable in the in-plane direction normal to the edge, and unloaded:

$$u_3 = \psi_\beta = M_{\alpha\alpha} = L_{\alpha\beta} = 0 \quad , \quad u_\alpha = 0 \quad \text{where,} \quad \sum_\alpha \tag{3.32}$$

In equations (3.31) and (3.32), and henceforth where applicable, the symbol $\sum_\alpha$ means that summation over the index α is not implied, and the index β is chosen different from α.

Moreover, the underlined terms are associated with the out-of-plane boundary conditions.

Considering equations $(3.14)_2$ in conjunction with (3.18), (A.1) and (A.5), we obtain the result,

$$
\begin{aligned}
M_{\alpha\beta} &= B_3(\psi_{\alpha,\beta} + \psi_{\beta,\alpha}) + \Big[\delta_{\alpha\beta}\{B_2 - B_3\} - \delta_{\alpha\beta}\delta_A B_5\Big]\psi_{\omega,\omega} \\
&\quad + 4B_7 u_{3,\alpha\beta} + [2\delta_{\alpha\beta}B_8 - \delta_{\alpha\beta}\delta_A B_5]u_{3,\omega\omega} + \delta_{\alpha\beta}\delta_A\delta_B B_6\ddot{u}_3 \qquad (3.33)
\end{aligned}
$$

The coefficients B_7 and B_8 are defined by (A.5) in Appendix A. Representing the unknowns u_3, ψ_1 and ψ_2 as,

$$
\begin{aligned}
u_3 &= \sum_{m=1}^{\infty}\sum_{n=1}^{\infty} A_{mn}(t)\sin\gamma_m x_1 \sin\beta_n x_2 \\
\psi_1 &= \sum_{m=1}^{\infty}\sum_{n=1}^{\infty} B_{mn}(t)\cos\gamma_m x_1 \sin\beta_n x_2 \qquad (3.34) \\
\psi_2 &= \sum_{m=1}^{\infty}\sum_{n=1}^{\infty} C_{mn}(t)\sin\gamma_m x_1 \cos\beta_n x_2
\end{aligned}
$$

where $\gamma_m = \frac{m\pi}{l_1}$ and $\beta_n = \frac{n\pi}{l_2}$, and considering (3.33), it is verified that the out-of-plane boundary conditions in (3.31) or (3.32) are satisfied. The in-plane boundary conditions are satisfied in an integral-average sense (see Section 3.3).

As regards the tenth-order transformed governing system, i.e., (3.24), (3.29) and (3.30), we note that the potential function Φ, although uncoupled in the governing equations, remains coupled with the other two variables, u_3 and C, via the boundary conditions. However, as noted earlier, the solution of (3.30) represents a boundary layer effect which can be neglected when dealing with global problems such as vibration and stability (e.g., [81, 82, 83, 84]). Therefore, in the forthcoming analysis we neglect the equation (3.30) and consider only the eighth-order transformed governing system (3.24) and (3.29).

3.3 Derivation of the Panel Flutter Equations

Introducing the effect of viscous structural damping, i.e., c, and initial geometric imper-
fections into equations (3.24) and (3.29), neglecting the contribution of rotary inertia, and
based on discussions in Sections {3.1.5} and {3.2}, the relevant equations describing flutter
of an imperfect panel subjected to a high-supersonic coplanar airflow are,

$$
\begin{aligned}
Du_{3,\omega\omega\alpha\alpha} - \epsilon_{\alpha\omega}\epsilon_{\beta\rho}\Big[C_{,\omega\rho}\{u_{3,\alpha\beta} + \hat{u}_{3,\alpha\beta}\} - S(C_{,\omega\rho}\{u_{3,\alpha\beta} + \hat{u}_{3,\alpha\beta}\})_{,\pi\pi}\Big] & \\
-(p_3 - Sp_{3,\alpha\alpha}) + m_0\Big[\ddot{u}_3 + c\dot{u}_3 - T(\ddot{u}_{3,\alpha\alpha} + c\dot{u}_{3,\alpha\alpha})\Big] & = 0
\end{aligned}
$$

$$(3.35)$$

$$
\begin{aligned}
(\tilde{b} + \tilde{c})C_{,\omega\omega\pi\pi} + \frac{1}{2}(u_{3,\omega\omega}u_{3,\pi\pi} + 2u_{3,\omega\omega}\hat{u}_{3,\pi\pi} - u_{3,\omega\pi}u_{3,\omega\pi} - 2u_{3,\omega\pi}\hat{u}_{3,\omega\pi}) & \\
+2\delta_A\delta_H\tilde{d}(u_{3,\pi\omega\omega}u_{3,\pi} + u_{3,\pi\omega\omega}\hat{u}_{3,\pi} + \hat{u}_{3,\pi\omega\omega}u_{3,\pi} + u_{3,\pi\omega}u_{3,\pi\omega} + 2u_{3,\pi\omega}\hat{u}_{3,\pi\omega}) & = 0
\end{aligned}
$$

Here, $\hat{u}_3$ represents an initially unstressed, geometrically imperfect state of the panel, which
is measured from the flat configuration. Its magnitude is small compared to the motion of
the panel, i.e., u_3, which is measured from the imperfect state. Therefore, consistent with
the small imperfection assumption, in the following derivations we discard quadratic and
higher-order terms in $\hat{u}_3$. For a simply supported panel, we can express $\hat{u}_3$ as,

$$
\hat{u}_3 = \sum_{m=1}^{\infty} \sum_{n=1}^{\infty} \hat{A}_{mn} \sin \gamma_m x_1 \sin \beta_n x_2 \tag{3.36}
$$

The transverse load due to aerodynamic forces is given by the quasi-steady, third-order
piston theory (Ashley and Zartarian [85]). This theory gives the aerodynamic load on a
panel by relating the local pressure generated by the panel motion to the local normal
component of fluid velocity. In general, piston theory may be employed for large supersonic
Mach numbers, whenever the flow angle of attack is not too large. Furthermore, for high-
supersonic flows the effects of viscous forces can be neglected. Thus, the transverse load,

p_3, is expressed in terms of the aerodynamic operator, i.e., $\mathcal{A}[.]$ as,

$$p_3 = \mathcal{A}[u_3 + \hat{u}_3]$$

(3.37)

$$\mathcal{A}[.] = -\chi p_\infty \hat{\delta}_f \left\{ \frac{1}{c_\infty} \left[\frac{\partial [.]}{\partial t} + U_\infty \cos \Lambda \frac{\partial [.]}{\partial x_1} + U_\infty \sin \Lambda \frac{\partial [.]}{\partial x_2} \right] \right.$$

$$+ \frac{\chi + 1}{4} \delta_f M^2 \left[\cos^2 \Lambda \left(\frac{\partial [.]}{\partial x_1} \right)^2 + \sin 2\Lambda \frac{\partial [.]}{\partial x_1} \frac{\partial [.]}{\partial x_2} + \sin^2 \Lambda \left(\frac{\partial [.]}{\partial x_2} \right)^2 \right]$$

$$+ \frac{\chi + 1}{12} \hat{\delta}_f M^3 \left[\cos^3 \Lambda \left(\frac{\partial [.]}{\partial x_1} \right)^3 + 3 \cos^2 \Lambda \sin \Lambda \left(\frac{\partial [.]}{\partial x_1} \right)^2 \frac{\partial [.]}{\partial x_2} \right.$$

$$\left. \left. + 3 \cos \Lambda \sin^2 \Lambda \frac{\partial [.]}{\partial x_1} \left(\frac{\partial [.]}{\partial x_2} \right)^2 + \sin^3 \Lambda \left(\frac{\partial [.]}{\partial x_2} \right)^3 \right] \right\}$$

In equation (3.37), χ is the polytropic gas coefficient, p_∞ the pressure of the undisturbed air, c_∞ the speed of sound through air at atmospheric pressure, U_∞ the flow speed, Λ the in-plane flow orientation (see Fig. 3.2), $M(= \frac{U_\infty}{c_\infty})$ the flight Mach number. Here $\delta_f, \hat{\delta}_f$ are the tracers identifying whether flow occurs past both upper and lower faces ($\delta_f = 0$, $\hat{\delta}_f = 2$), or whether it occurs past the upper face only ($\delta_f = \hat{\delta}_f = 1$).

Derivation of stress function, C

Based on $(3.35)_2$, we can write the solution of the stress function C as,

$$C[x_\omega, t] = \underbrace{C_1[x_\omega, t]}_{\text{particular soln.}} + \overbrace{\frac{1}{2}(\tilde{L}_1 x_2^2 + \tilde{L}_2 x_1^2)}^{\text{homogeneous soln.}}$$

(3.38)

We now satisfy the in-plane boundary conditions in an integral-average sense by imposing the following conditions on C_1:

$$\int_0^{l_2} C_{1,22} \Big|_{x_1=0,l_1} dx_2 = 0 \qquad \int_0^{l_1} C_{1,11} \Big|_{x_2=0,l_2} dx_1 = 0$$

(3.39)

$$\int_0^{l_2} C_{1,12} \Big|_{x_1=0,l_1} dx_2 = 0 \qquad \int_0^{l_1} C_{1,12} \Big|_{x_2=0,l_2} dx_1 = 0$$

Considering (3.38) along with (3.39) shows that $\tilde{L}_1$, $\tilde{L}_2$ acquire the meaning of average in-plane edge loads (considered positive in tension). These are given as,

$$\tilde{L}_1 = \frac{1}{l_2}\int_0^{l_2} C_{,22}\Big|_{x_1=0,l_1} dx_2 \quad , \quad \tilde{L}_2 = \frac{1}{l_1}\int_0^{l_1} C_{,11}\Big|_{x_2=0,l_2} dx_1 \tag{3.40}$$

Introducing $(3.34)_1$, (3.36) and (3.38) into $(3.35)_2$, C_1 may be expressed as,

$$\begin{aligned}
C_1 = \frac{1}{4}\frac{h^2}{\tilde{b}+\tilde{c}}\phi^2 \sum_{m=1}^{\infty}\sum_{n=1}^{\infty}\sum_{i=1}^{\infty}\sum_{j=1}^{\infty} \Big\{ & \lambda_{mnij}^{(1)}\kappa_{mnij}^{(1)}\cos[(\gamma_m-\gamma_i)x_1]\cos[(\beta_n-\beta_j)x_2] + \\
& \lambda_{mnij}^{(2)}\kappa_{mnij}^{(2)}\cos[(\gamma_m-\gamma_i)x_1]\cos[(\beta_n+\beta_j)x_2] + \\
& \lambda_{mnij}^{(3)}\kappa_{mnij}^{(3)}\cos[(\gamma_m+\gamma_i)x_1]\cos[(\beta_n-\beta_j)x_2] + \\
& \lambda_{mnij}^{(4)}\kappa_{mnij}^{(4)}\cos[(\gamma_m+\gamma_i)x_1]\cos[(\beta_n+\beta_j)x_2]\Big\} \times \\
& \big(a_{mn}a_{ij} + a_{mn}\hat{a}_{ij} + \hat{a}_{mn}a_{ij}\big)
\end{aligned} \tag{3.41}$$

Here, the coefficients $\lambda_{mnij}^{(1)}$, $\kappa_{mnij}^{(1)}$, etc. are defined by (B.1) in Appendix B; the non-dimensional quantities, i.e., modal- and imperfection- amplitudes, a_{mn} and $\hat{a}_{mn}$, and panel aspect ratio ϕ are defined in (B.2). It can be seen by inspection that C_1 as given by (3.41) fulfills the conditions (3.39).

In order to solve for the average in-plane edge loads $\tilde{L}_1$ and $\tilde{L}_2$, we define the average in-plane displacements between the edges as,

$$\Delta_1 = -\frac{1}{l_1 l_2}\int_0^{l_1}\int_0^{l_2} u_{1,1}\,dx_1 dx_2 = \frac{\tilde{L}_1}{\alpha_1} \quad , \quad \Delta_2 = -\frac{1}{l_1 l_2}\int_0^{l_1}\int_0^{l_2} u_{2,2}\,dx_1 dx_2 = \frac{\tilde{L}_2}{\alpha_2} \tag{3.42}$$

Depending on the level of in-plane restraint at the edges $x_1 = 0$, l_1, we take $\alpha_1 = 0$ or $\alpha_1 \longrightarrow \infty$ according to whether the edges are movable or immovable. For partially restrained edges α_1 takes on intermediate values which may be determined from experiments. Similar statements can be made regarding the edge conditions at $x_2 = 0$, l_2 and the coefficient α_2. The counterparts of $(3.7)_1$ and (3.20) for an imperfect panel are obtained by considering the replacement $u_3 \to u_3 + \hat{u}_3$ and the small imperfections assumption. These are then used along with (3.21) and (3.42) to obtain the result,

$$\begin{aligned}
\frac{\tilde{L}_1}{\alpha_1} = -\frac{1}{l_1 l_2}\int_0^{l_1}\int_0^{l_2}\Big[& (\tilde{b}+\tilde{c})C_{,22} + \tilde{c}C_{,11} + (\delta_A \tilde{d} - 0.5)(u_{3,1}+2u_{3,1}\hat{u}_{3,1}) \\
& \delta_A \tilde{d}(u_{3,2}+2u_{3,2}\hat{u}_{3,2})\Big]dx_1 dx_2 \quad , \quad 1\rightleftharpoons 2
\end{aligned} \tag{3.43}$$

CHAPTER 3. PROBLEM FORMULATION

Here and henceforth, usage of the symbol $\rightleftharpoons$ means that by interchanging the accompanying indices the second corresponding equation is obtained. Using $(3.34)_1$, (3.36), (3.38) and (3.41), and adding possible applied edge-loads (see Fig. 3.2), i.e., L_1^{**} and L_2^{**}, we obtain,

$$\frac{\tilde{L}_1}{\alpha_1} = -(\tilde{b}+\tilde{c})\tilde{L}_1 - \tilde{c}\tilde{L}_2 + \delta_{M1}\frac{L_1^{**}}{\alpha_1}$$

$$-\frac{\pi^2}{4}\frac{1}{l_1^2}\sum_{m=1}^{\infty}\sum_{n=1}^{\infty}\left\{(\delta_A\tilde{d}-0.5)m^2+\phi^2\delta_A\tilde{d}n^2\right\}\left(A_{mn}^2+2A_{mn}\hat{A}_{mn}\right)$$

$$\frac{\tilde{L}_2}{\alpha_2} = \quad \langle 1\rightleftharpoons2 \quad, \quad m\rightleftharpoons n \quad, \quad \phi\to\phi^{-1}\rangle \tag{3.44}$$

The tracer δ_{M1} assumes the values 1 or 0 according to whether the edges $x_1 = 0$, l_1 are movable or immovable/partially restrained, respectively. Similar statements can be made regarding the edge conditions at $x_2 = 0$, l_2 and the tracer δ_{M2}. Solving (3.44) for $\tilde{L}_1$ and $\tilde{L}_2$ results in,

$$\tilde{L}_1 = \frac{\pi^2 h^2 \tilde{\alpha}_1}{4l_1^2(\tilde{b}+\tilde{c})\left[1-\left(\frac{\tilde{c}}{\tilde{b}+\tilde{c}}\right)^2\tilde{\alpha}_1\tilde{\alpha}_2\right]}\mathcal{B}$$

$$\mathcal{B} = \tilde{\alpha}_2\frac{\tilde{c}}{\tilde{b}+\tilde{c}}\sum_{m=1}^{\infty}\sum_{n=1}^{\infty}\left\{\delta_A\tilde{d}m^2+\phi^2(\delta_A\tilde{d}-0.5)n^2\right\}\left(a_{mn}^2+2a_{mn}\hat{a}_{mn}\right)$$

$$-\sum_{m=1}^{\infty}\sum_{n=1}^{\infty}\left\{(\delta_A\tilde{d}-0.5)m^2+\phi^2\delta_A\tilde{d}n^2\right\}\left(a_{mn}^2+2a_{mn}\hat{a}_{mn}\right)$$

$$+\frac{4}{h}(\tilde{b}+\tilde{c})D\left(\frac{1-\tilde{\alpha}_1}{\tilde{\alpha}_1}\delta_{M1}L_1^* - \frac{\tilde{c}}{\tilde{b}+\tilde{c}}[1-\tilde{\alpha}_2]\delta_{M2}L_2^*\right)$$

$$\tag{3.45}$$

$$\tilde{L}_2 = \frac{\pi^2 h^2 \tilde{\alpha}_2}{4l_1^2(\tilde{b}+\tilde{c})\left[1-\left(\frac{\tilde{c}}{\tilde{b}+\tilde{c}}\right)^2\tilde{\alpha}_1\tilde{\alpha}_2\right]}\mathcal{C}$$

$$\mathcal{C} = \mathcal{B}\to\langle\tilde{\alpha}_1\rightleftharpoons\tilde{\alpha}_2 \quad, \quad m\rightleftharpoons\phi n \quad, \quad \delta_{M1}L_1^*\rightleftharpoons\delta_{M2}L_2^*\rangle$$

where,

$$\tilde{\alpha}_1 \equiv \frac{(\tilde{b}+\tilde{c})\alpha_1}{1+(\tilde{b}+\tilde{c})\alpha_1} \quad, \quad \tilde{\alpha}_2 \equiv \frac{(\tilde{b}+\tilde{c})\alpha_2}{1+(\tilde{b}+\tilde{c})\alpha_2}$$

and the non-dimensional applied edge loads L_1^* and L_2^* are defined by (B.2) in Appendix B. It is easily verifiable that $\tilde{\alpha}_1 = 0$, $\tilde{\alpha}_1 = 1$ and $0 < \tilde{\alpha}_1 < 1$ imply that the edges $x_1 = 0$, l_1

38

are movable, immovable and partially restrained, respectively. Similar statements can be made regarding the edge conditions at $x_2 = 0$, l_2 and the coefficient α_2.

Spatial Discretization Using Galerkin's Method

The aerodynamic load given by (3.37) and the stress function given by (3.38), (3.41), (3.45) are introduced into equation $(3.35)_1$ which describes the transverse motion of the panel. The assumed modal expansions $(3.34)_1$, (3.36) are substituted into the resulting non-dimensional equations (see (B.2) for definitions of the non-dimensional parameters) and the residual thus obtained is minimized by using $\sin r\pi\xi_1 \sin s\pi\xi_2$ as the weighting function and integrating over the area of the panel. Extending the procedure considered by Friedmann and Hanin [32], the resulting non-dimensional Galerkin equations derived for an arbitrary number of spanwise and chordwise modes are,

$$
\ddot{a}_{rs} + [\epsilon_S + \epsilon_A \mathcal{G}_{rs}]\dot{a}_{rs} + \mathcal{R}_{rs}a_{rs} - [\mathcal{P}_{rs}\delta_{\mathrm{M1}}L_1^* + \mathcal{Q}_{rs}\delta_{\mathrm{M2}}L_2^*](a_{rs} + \hat{a}_{rs}) -
$$

$$
\sum_{m=1}^{k}\sum_{n=1}^{l}[\mathcal{Z}_{rsmn} + \mathcal{Y}_{rsmn}](a_{rs}a_{mn}^2 + \hat{a}_{rs}a_{mn}^2 + 2a_{rs}a_{mn}\hat{a}_{mn}) -
$$

$$
\sum_{p=1}^{k}\sum_{q=1}^{l}\sum_{m=1}^{k}\sum_{n=1}^{l}\sum_{i=1}^{k}\sum_{j=1}^{l}\mathcal{D}_{rspqmnij}(a_{pq}a_{mn}a_{ij} + \hat{a}_{pq}a_{mn}a_{ij} + a_{pq}\hat{a}_{mn}a_{ij} + a_{pq}a_{mn}\hat{a}_{ij}) +
$$

$$
\delta_f\lambda\Big[\cos\Lambda\sum_{p=1}^{k}\mathcal{U}_{rsp}(a_{ps} + \hat{a}_{ps}) + \sin\Lambda\sum_{q=1}^{l}\mathcal{W}_{rsq}(a_{rq} + \hat{a}_{rq})\Big] +
$$

$$
\hat{\delta}_f\lambda^2\sum_{m=1}^{k}\sum_{n=1}^{l}\sum_{i=1}^{k}\sum_{j=1}^{l}\mathcal{E}_{rsmnij}(a_{mn}a_{ij} + \hat{a}_{mn}a_{ij} + a_{mn}\hat{a}_{ij}) +
$$

$$
\delta_f\lambda^3\sum_{p=1}^{k}\sum_{q=1}^{l}\sum_{m=1}^{k}\sum_{n=1}^{l}\sum_{i=1}^{k}\sum_{j=1}^{l}\mathcal{F}_{rspqmnij}(a_{pq}a_{mn}a_{ij} + \hat{a}_{pq}a_{mn}a_{ij} + a_{pq}\hat{a}_{mn}a_{ij} + a_{pq}a_{mn}\hat{a}_{ij})
$$

$$
= 0
$$

$$
\sum_{r,s} \quad , \quad r = 1 \longrightarrow k \quad , \quad s = 1 \longrightarrow l \quad (3.46)
$$

The coefficients $\mathcal{D}_{rspqmnij}$, $\mathcal{E}_{rsmnij}$, $\mathcal{F}_{rspqmnij}$, $\mathcal{G}_{rs}$, $\mathcal{R}_{rs}$, $\mathcal{P}_{rs}$, $\mathcal{Q}_{rs}$, $\mathcal{U}_{rsp}$, $\mathcal{W}_{rsq}$, $\mathcal{Z}_{rsmn}$, and $\mathcal{Y}_{rsmn}$ are defined in Appendix B. Here λ, ϵ_S, and ϵ_A are the non-dimensional flow speed,

structural- and aerodynamic- damping coefficients, respectively, which are defined in (B.2). The overdots denote differentiation with respect to the non-dimensonal time, τ, also defined in (B.2). However, for convenience in notation, henceforth we continue to use the symbol t in place of τ with the understanding that from here onwards t denotes the non-dimensional time.

Equations (3.46) represent a system of ordinary differential equations (ODE's) describing the motion of a fluttering, composite panel composed of transversely isotropic laminae. They incorporate the effects of aerodynamic nonlinearities, transverse shear deformations, applied in-plane edge loads and/or edge restraints and initial stress-free imperfections. Written in a compact form, they read as,

$$\ddot{a}_{rs} + \epsilon_T \dot{a}_{rs} + \Omega^2_{rs} a_{rs} + F_1[a_{ij}; \lambda, \lambda^2, L^*_\alpha, \hat{a}_{uv}] +$$
$$F_2[a_{ij}a_{pq}; \lambda^2, \lambda^3, \hat{a}_{uv}] + F_3[a_{ij}a_{pq}a_{mn}; \lambda^3] + F_0[\lambda, L^*_\alpha, \hat{a}_{uv}] = 0$$
$$\sum_{r,s} \quad , \quad r = 1 \longrightarrow k \quad , \quad s = 1 \longrightarrow l \qquad (3.47)$$

In equation (3.47), F_1, F_2, F_3 are linear, quadratic and cubic functions of the non-dimensional modal amplitudes, respectively ; F_0 is a constant term arising due to initial imperfections; and ϵ_T represents the total (aerodynamic and structural) damping. The detailed form of (3.47) was derived using *MACSYMA* by considering two cases of modal truncation ($k \times l$ where $k =$ number of chordwise modes and $l =$ number of spanwise modes), i.e., the (2×2) and (4×1) cases. Introducing the state vector $\mathbf{w}$ of dimension $2N$ ($N = kl$), we can write equation (3.47) as,

$$\dot{\mathbf{w}} = \mathbf{f}[\mathbf{w}; \lambda, L^*_\alpha] \qquad (3.48)$$

The components of $\mathbf{w}$ are the displacement amplitudes and their time derivative. For the two cases of modal truncation considered herein we have,

$$(4 \times 1)\,\text{case}\,:\,\, \mathbf{w} \equiv \{a_{11}, a_{21}, a_{31}, a_{41}, \dot{a}_{11}, \dot{a}_{21}, \dot{a}_{31}, \dot{a}_{41}\}^\mathrm{T}$$

$$(3.49)$$

$$(2 \times 2)\,\text{case}\,:\,\, \mathbf{w} \equiv \{a_{11}, a_{12}, a_{21}, a_{22}, \dot{a}_{11}, \dot{a}_{12}, \dot{a}_{21}, \dot{a}_{22}\}^\mathrm{T}$$

40

The 2N-dimensional vector **f** is a nonlinear function of **w**. λ and L_α^* are the control parameters of the system.
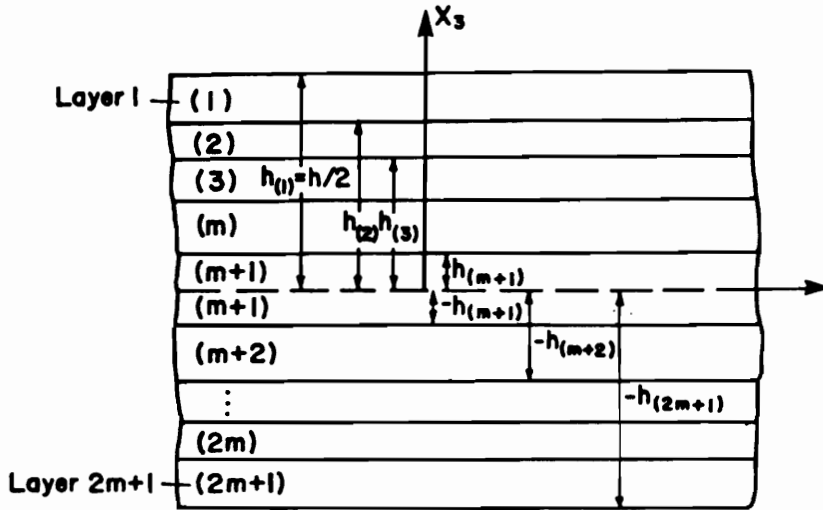
Figure 3.1: Cross-section of a symmetric laminate.
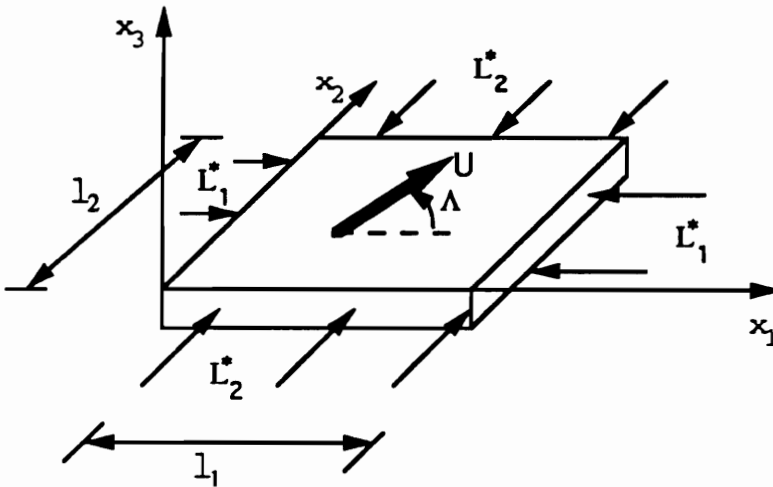
Figure 3.2: Panel with air flow and compressive edge loads.

Chapter 4

SOLUTION METHODOLOGY

As a first step towards obtaining a solution of the panel flutter equations (3.46) or (3.47), we write $a_{ij}[t]$ as,

$$a_{ij}[t] = \tilde{a}_{ij} + \bar{a}_{ij}[t] \tag{4.1}$$

where $\tilde{a}_{ij}$ and $\bar{a}_{ij}[t]$ represent the static and dynamic components of the displacement amplitudes, respectively. Considering the case of temporally constant edge loads, the static-buckling equations are derived from (3.46) as,

$$\begin{aligned}
&\mathcal{R}_{rs}\tilde{a}_{rs} - [\mathcal{P}_{rs}\delta_{\mathrm{M1}}L_1^* + \mathcal{Q}_{rs}\delta_{\mathrm{M2}}L_2^*](\tilde{a}_{rs} + \hat{a}_{rs}) - \\
&\sum_{m=1}^{k}\sum_{n=1}^{l}[\mathcal{Z}_{rsmn} + \mathcal{Y}_{rsmn}](\tilde{a}_{rs}\tilde{a}_{mn}^2 + \hat{a}_{rs}\tilde{a}_{mn}^2 + 2\tilde{a}_{rs}\tilde{a}_{mn}\hat{a}_{mn}) - \\
&\sum_{p=1}^{k}\sum_{q=1}^{l}\sum_{m=1}^{k}\sum_{n=1}^{l}\sum_{i=1}^{k}\sum_{j=1}^{l}\mathcal{D}_{rspqmnij}(\tilde{a}_{pq}\tilde{a}_{mn}\tilde{a}_{ij} + \hat{a}_{pq}\tilde{a}_{mn}\tilde{a}_{ij} + \tilde{a}_{pq}\hat{a}_{mn}\tilde{a}_{ij} + \tilde{a}_{pq}\tilde{a}_{mn}\hat{a}_{ij}) + \\
&\delta_f\lambda\Big[\cos\Lambda\sum_{p=1}^{k}\mathcal{U}_{rsp}(\tilde{a}_{ps} + \hat{a}_{ps}) + \sin\Lambda\sum_{q=1}^{l}\mathcal{W}_{rsq}(\tilde{a}_{rq} + \hat{a}_{rq})\Big] + \\
&\hat{\delta}_f\lambda^2\sum_{m=1}^{k}\sum_{n=1}^{l}\sum_{i=1}^{k}\sum_{j=1}^{l}\mathcal{E}_{rsmnij}(\tilde{a}_{mn}\tilde{a}_{ij} + \hat{a}_{mn}\tilde{a}_{ij} + \tilde{a}_{mn}\hat{a}_{ij}) + \\
&\delta_f\lambda^3\sum_{p=1}^{k}\sum_{q=1}^{l}\sum_{m=1}^{k}\sum_{n=1}^{l}\sum_{i=1}^{k}\sum_{j=1}^{l}\mathcal{F}_{rspqmnij}(\tilde{a}_{pq}\tilde{a}_{mn}\tilde{a}_{ij} + \hat{a}_{pq}\tilde{a}_{mn}\tilde{a}_{ij} + \tilde{a}_{pq}\hat{a}_{mn}\tilde{a}_{ij} + \tilde{a}_{pq}\tilde{a}_{mn}\hat{a}_{ij})
\end{aligned}$$

$$= 0$$

$$\sum_{r,s} \quad , \quad r = 1\longrightarrow k \quad , \quad s = 1\longrightarrow l \tag{4.2}$$

42

Introducing (4.1) into (3.46) considered in conjunction with (4.2), we obtain,

$$\ddot{\bar{a}}_{rs} + [\epsilon_S + \epsilon_A \mathcal{G}_{rs}]\dot{\bar{a}}_{rs} + \mathcal{R}_{rs}\bar{a}_{rs} - [\mathcal{P}_{rs}\delta_{M1}L_1^* + \mathcal{Q}_{rs}\delta_{M2}L_2^*]\bar{a}_{rs} -$$

$$\sum_{m=1}^{k}\sum_{n=1}^{l}[\mathcal{Z}_{rsmn} + \mathcal{Y}_{rsmn}](2\bar{a}_{mn}\tilde{a}_{mn}\tilde{a}_{rs} + 2\bar{a}_{mn}\hat{a}_{mn}\tilde{a}_{rs} + \bar{a}_{mn}^2\tilde{a}_{rs} + 2\bar{a}_{mn}\hat{a}_{rs}\tilde{a}_{mn} +$$

$$\bar{a}_{mn}^2\hat{a}_{rs} + \bar{a}_{rs}\tilde{a}_{mn}^2 + 2\bar{a}_{rs}\hat{a}_{mn}\tilde{a}_{mn} + 2\bar{a}_{mn}\bar{a}_{rs}\tilde{a}_{mn} +$$

$$2\bar{a}_{mn}\bar{a}_{rs}\hat{a}_{mn} + \bar{a}_{mn}^2\bar{a}_{rs}) -$$

$$\sum_{p=1}^{k}\sum_{q=1}^{l}\sum_{m=1}^{k}\sum_{n=1}^{l}\sum_{i=1}^{k}\sum_{j=1}^{l}\mathcal{D}_{rspqmnij}(\bar{a}_{ij}\tilde{a}_{mn}\tilde{a}_{pq} + \bar{a}_{ij}\hat{a}_{mn}\tilde{a}_{pq} + \bar{a}_{mn}\tilde{a}_{ij}\tilde{a}_{pq} + \bar{a}_{mn}\hat{a}_{ij}\tilde{a}_{pq} +$$

$$\bar{a}_{ij}\bar{a}_{mn}\tilde{a}_{pq} + \bar{a}_{ij}\hat{a}_{pq}\tilde{a}_{mn} + \bar{a}_{mn}\hat{a}_{pq}\tilde{a}_{ij} + \bar{a}_{ij}\bar{a}_{mn}\hat{a}_{pq} +$$

$$\bar{a}_{pq}\tilde{a}_{ij}\tilde{a}_{mn} + \bar{a}_{pq}\hat{a}_{ij}\tilde{a}_{mn} + \bar{a}_{ij}\bar{a}_{pq}\tilde{a}_{mn} + \bar{a}_{pq}\hat{a}_{mn}\tilde{a}_{ij} +$$

$$\bar{a}_{ij}\bar{a}_{pq}\hat{a}_{mn} + \bar{a}_{mn}\bar{a}_{pq}\hat{a}_{ij} + \bar{a}_{mn}\bar{a}_{pq}\hat{a}_{ij} + \bar{a}_{ij}\bar{a}_{mn}\bar{a}_{pq}) +$$

$$\delta_f\lambda\Big[\cos\Lambda\sum_{p=1}^{k}\mathcal{U}_{rsp}\bar{a}_{ps} + \sin\Lambda\sum_{q=1}^{l}\mathcal{W}_{rsq}\bar{a}_{rq}\Big] +$$

$$\hat{\delta}_f\lambda^2\sum_{m=1}^{k}\sum_{n=1}^{l}\sum_{i=1}^{k}\sum_{j=1}^{l}\mathcal{E}_{rsmnij}(\bar{a}_{ij}\tilde{a}_{mn} + \bar{a}_{ij}\hat{a}_{mn} + \bar{a}_{mn}\tilde{a}_{ij} + \bar{a}_{mn}\hat{a}_{ij} + \bar{a}_{ij}\bar{a}_{mn}) +$$

$$\hat{\delta}_f\lambda^3\sum_{p=1}^{k}\sum_{q=1}^{l}\sum_{m=1}^{k}\sum_{n=1}^{l}\sum_{i=1}^{k}\sum_{j=1}^{l}\mathcal{F}_{rspqmnij}(\bar{a}_{ij}\tilde{a}_{mn}\tilde{a}_{pq} + \bar{a}_{ij}\hat{a}_{mn}\tilde{a}_{pq} + \bar{a}_{mn}\tilde{a}_{ij}\tilde{a}_{pq} + \bar{a}_{mn}\hat{a}_{ij}\tilde{a}_{pq} +$$

$$\bar{a}_{ij}\bar{a}_{mn}\tilde{a}_{pq} + \bar{a}_{ij}\hat{a}_{pq}\tilde{a}_{mn} + \bar{a}_{mn}\hat{a}_{pq}\tilde{a}_{ij} + \bar{a}_{ij}\bar{a}_{mn}\hat{a}_{pq} +$$

$$\bar{a}_{pq}\tilde{a}_{ij}\tilde{a}_{mn} + \bar{a}_{pq}\hat{a}_{ij}\tilde{a}_{mn} + \bar{a}_{ij}\bar{a}_{pq}\tilde{a}_{mn} + \bar{a}_{pq}\hat{a}_{mn}\tilde{a}_{ij} +$$

$$\bar{a}_{ij}\bar{a}_{pq}\hat{a}_{mn} + \bar{a}_{mn}\bar{a}_{pq}\tilde{a}_{ij} + \bar{a}_{mn}\bar{a}_{pq}\hat{a}_{ij} + \bar{a}_{ij}\bar{a}_{mn}\bar{a}_{pq})$$

$$= 0$$

$$\sum_{r,s} \quad , \quad r = 1\longrightarrow k \quad , \quad s = 1\longrightarrow l \qquad (4.3)$$

Equation (4.3) can be writtten in compact form as,

$$\ddot{\bar{a}}_{rs} + \epsilon_T\dot{\bar{a}}_{rs} + \Omega_{rs}^2\bar{a}_{rs} + \bar{F}_1[\bar{a}_{ij}; \lambda, \lambda^2, \lambda^3, L_\alpha^*, \hat{a}_{uv}, \tilde{a}_{cd}]$$

$$+\bar{F}_2[\bar{a}_{ij}\bar{a}_{pq}; \lambda^2, \lambda^3, \hat{a}_{uv}, \tilde{a}_{cd}] + \bar{F}_3[\bar{a}_{ij}\bar{a}_{pq}\bar{a}_{mn}; \lambda^3] = 0$$

$$\sum_{r,s} \quad , \quad r = 1\longrightarrow k \quad , \quad s = 1\longrightarrow l \qquad (4.4)$$

43

Equation (4.3) (or its compact form (4.4)) describe the motion of the panel (represented by $\bar{a}_{r\,s}$) about the static buckled state (represented by $\tilde{a}_{r\,s}$). Introducing the state vectors **y** and **z** of dimension N and $2N$ respectively ($N = kl$), we can write equations (4.2), (4.3) as

$$\tilde{\mathbf{f}}[\mathbf{y}; \lambda, L_\alpha^*] = 0 \tag{4.5}$$

$$\dot{\mathbf{z}} = \bar{\mathbf{f}}[\mathbf{z}; \lambda, L_\alpha^*] \tag{4.6}$$

The components of **y** are the static component of the displacement amplitudes, i.e., $\tilde{a}_{r\,s}$, whereas those of **z** are the dynamic component of the displacement amplitudes and their time derivative. For the two cases of modal truncation considered, we have,

$$(4 \times 1)\,\text{case}: \quad \mathbf{y} \equiv \{\tilde{a}_{11}\,, \tilde{a}_{21}\,, \tilde{a}_{31}\,, \tilde{a}_{41}\}^{\mathrm{T}}$$
$$\mathbf{z} \equiv \{\bar{a}_{11}\,, \bar{a}_{21}\,, \bar{a}_{31}\,, \bar{a}_{41}\,, \dot{\bar{a}}_{11}\,, \dot{\bar{a}}_{21}\,, \dot{\bar{a}}_{31}\,, \dot{\bar{a}}_{41}\}^{\mathrm{T}}$$

$$(4.7)$$

$$(2 \times 2)\,\text{case}: \quad \mathbf{y} \equiv \{\tilde{a}_{11}\,, \tilde{a}_{12}\,, \tilde{a}_{21}\,, \tilde{a}_{22}\}^{\mathrm{T}}$$
$$\mathbf{z} \equiv \{\bar{a}_{11}\,, \bar{a}_{12}\,, \bar{a}_{21}\,, \bar{a}_{22}\,, \dot{\bar{a}}_{11}\,, \dot{\bar{a}}_{12}\,, \dot{\bar{a}}_{21}\,, \dot{\bar{a}}_{22}\}^{\mathrm{T}}$$

The N-dimensional vector $\tilde{\mathbf{f}}$ is a nonlinear function of **y** and the 2N-dimensional vector $\bar{\mathbf{f}}$ is a nonlinear function of **z**.

4.1 Determination of Static Displacement Amplitudes

The Arclength Continuation Method (ACM, e.g., Nayfeh and Balachandran [85]) is used to determine the solution of **y** from equation (4.5). By allowing for the variation of only one control parameter, e.g., λ, and using the arclength s along a solution branch as a parameter, we consider the functional dependencies $\mathbf{y} = \mathbf{y}[s]$ and $\lambda = \lambda[s]$. Thus we can write (4.5) as,

$$\tilde{\mathbf{f}}[\mathbf{y}[s]; \lambda[s]] = 0 \tag{4.8}$$

In order to solve (4.8) for the (N+1) unknowns, i.e., **y** and λ, we augment it with an additional equation, e.g., the Euclidean arclength normalization, which is written as,

$$\mathbf{y'}^{\mathrm{T}}\mathbf{y'} + \lambda'^2 = 1 \quad , \quad \text{where} \ \ ()' = \frac{d()}{ds} \tag{4.9}$$

Let $(\mathbf{y}^*, \lambda^*)$ and $(\mathbf{y}, \lambda)$ denote solutions for parameter values s^* and $s(= s^* + ds)$ respectively. Thus (4.9) can be rewritten as,

$$(y_1 - y_1^*)^2 + (y_2 - y_2^*)^2 + \cdots + (y_N - y_N^*)^2 + (\lambda - \lambda^*)^2 - ds^2 = 0 \qquad (4.10)$$

The continuation scheme is initiated by obtaining a solution of (4.5), i.e., $\mathbf{y}$ for a specified λ, and using it as the starting values of $\mathbf{y}^*$ and λ^*. Then, for a specified ds the system ((4.8), (4.10)) is solved for $(\mathbf{y}, \lambda)$ using the Newton-Raphson method. Thereafter we consider $\mathbf{y}^* = \mathbf{y}$ and $\lambda^* = \lambda$ for the next arclength step. In this manner the solution branch is generated for a specified number of arclength steps. The direction of continuation is dictated by the initial guess for any one unknown, e.g., λ, provided in the Newton-Raphson scheme. In general, a reasonably good initial guess for λ would be $\lambda^* \pm ds$ where the choice of the $+$ or $-$ sign would determine the direction of continuation. By monitoring and suitably altering the direction of continuation, turning points of the solution are easily negotiated.

At turning points and branch points, the Jacobian $\mathbf{J}_1$ defined as,

$$\mathbf{J}_1 = \nabla_{\mathbf{y}} \tilde{\mathbf{f}} \quad , \quad \text{where} \quad \nabla_{\mathbf{y}}(.) = \left[\frac{\partial(.)}{\partial y_1}, \frac{\partial(.)}{\partial y_2}, \cdots \cdots, \frac{\partial(.)}{\partial y_N} \right] \qquad (4.11)$$

is singular with rank $N - 1$ (Seydel [46]). Moreover the $(N + 1) \times N$ 'augmented matrix' $\tilde{\mathbf{A}}$ defined as,

$$\tilde{\mathbf{A}} = \left[\nabla_{\mathbf{y}} \tilde{\mathbf{f}} \,\middle|\, \tilde{\mathbf{f}}_\lambda \right] \quad , \quad \text{where} \quad \tilde{\mathbf{f}}_\lambda \equiv \frac{\partial \tilde{\mathbf{f}}}{\partial \lambda} \qquad (4.12)$$

has rank N at a turning point and rank $< N$ at a branch point. Therefore, by monitoring the eigenvalues of $\mathbf{J}_1$, the passing of a turning point or branch point can be detected. Similarly by monitoring the eigenvalues of the matrices formed by eliminating the ith column $(i = 1 \longrightarrow N)$ of $\tilde{\mathbf{A}}$, we can differentiate between the passing of a turning point or branch point. For all cases considered herein, no branch points were detected.

After the static equilibrium solution $(\mathbf{y}, \lambda)$ is obtained by the ACM, its stability (in the small) is determined by examining the eigenvalues of the Jacobian $\mathbf{J}_2$ defined as,

$$\mathbf{J}_2 = \nabla_{\mathbf{z}} \bar{\mathbf{f}} \Big|_{\mathbf{z}=0} \qquad (4.13)$$

When all eigenvalues of $\mathbf{J_2}$ possess negative real parts, the static equilibrium is asymptotically stable, whereas if any eigenvalue possesses a positive real part, the static equilibrium is unstable. If, for a solution $(\mathbf{y_0}, \lambda_0)$ the Jacobian $\mathbf{J_2}$ has a simple pair of purely imaginary eigenvalues which exhibit a transverse crossing of the imaginary axis as the control parameter (or arclength parameter) is varied, and no other eigenvalue of $\mathbf{J_2}$ has zero real part, a Hopf bifurcation occurs. This results in the static equilibrium state losing its stability beyond the bifurcation point and the birth of a periodic solution at the bifucation point. A supercritical Hopf bifurcation occurs when a stable periodic solution exists beyond the bifurcation point, which results in soft (or benign) flutter. When an unstable periodic solution exists before the bifurcation point, a subcritical Hopf bifurcation occurs, resulting in hard (or dangerous) flutter oscillations. The values of the control parameters at the Hopf bifurcation are henceforth referred to as the critical- or flutter- values.

4.2 Dynamic Solutions Using the Method of Multiple Time Scales (MMS)

The MMS is used to obtain the amplitudes of flutter oscillations about the static equilibrium state, i.e., the solution of $\bar{a}_{r_s}$ from (4.4) after obtaining $\tilde{a}_{r_s}$ by the ACM. We note that the MMS, being a perturbation method, is applicable only to the class of weakly-nonlinear systems, which in effect implies the assumption of small-but-finite motions in its usage. Hence its applicability is restricted to the region (in control parameter space) in the vicinity of the flutter boundary as defined by the critical values. However, the static displacement amplitudes are not necessarily small-but-finite near the flutter boundary and hence the MMS cannot be applied directly to equations (3.47). For convenience in notation we define the N-dimensional vector $\mathbf{a}$, with components $\bar{a}_{r_s}$, as (see (4.7)),

$$\mathbf{a} \equiv \{z_1, z_2, \cdots, z_N\}^{\mathrm{T}} \tag{4.14}$$

Following Nayfeh [86], we consider an asymptotic expansion for $\mathbf{a}$ in terms of unknown functions (denoted by the N-dimensional vectors $\mathbf{v}^{(i)}$) of multiple time scales T_i $(= \epsilon^i t)$, where ϵ is an arbitrarily small parameter denoting the order of $\bar{a}_{r_s}$. Consistent with the

small-but-finite motions and small imperfections assumptions, we consider $\bar{a}_{r_s} = O(\epsilon)$ and $\hat{a}_{r_s} = O(\epsilon^2)$ when ordering terms. For the total damping coefficient we consider $\epsilon_T = O(1)$. Moreover, due to the fact that (4.4) contains quadratic and cubic nonlinearities in $\bar{a}_{r_s}$, in order to obtain its first-order approximate solution the asymptotic expansion takes the form,

$$\mathbf{a}[t;\epsilon] = \sum_{i=1}^{3} \epsilon^i \mathbf{v}^{(i)}[T_0, T_1, T_2] \; + \; \text{higher order terms (} H.O.T. \text{)} \tag{4.15}$$

Similarly, the control parameter which is varied, e.g., λ, and differential operators are expanded as,

$$\lambda = \sum_{i=0}^{2} \epsilon^i \lambda_i + H.O.T$$

$$D(.) \equiv \frac{d(.)}{dt} = \sum_{i=0}^{2} \epsilon^i D_i(.) + H.O.T \quad ; \quad D_i(.) \equiv \frac{d(.)}{dT_i} \tag{4.16}$$

$$D^2(.) \equiv \frac{d^2(.)}{dt^2} = D_0^2(.) + 2\epsilon D_0 D_1(.) + \epsilon^2 D_1^2(.) + 2\epsilon^2 D_0 D_2(.) + H.O.T.$$

In equations (3.10), λ_0 is the critical flutter speed (λ_F) corresponding to a Hopf bifurcation of the eigenvalues of $\mathbf{J_2}$. Upon substituting (4.13) and (4.14) into (4.4) and following [86], the corresponding equations of $O(\epsilon)$, $O(\epsilon^2)$, and $O(\epsilon^3)$ are obtained. The detailed form of these equations was obtained using *MACSYMA* and will not be displayed here. In what follows, only the essential features of the method are discussed.

The $O(\epsilon)$ system

The $O(\epsilon)$ system may be represented as,

$$O(\epsilon) \; : \qquad \mathbf{M}\ddot{\mathbf{v}}^{(1)} + \mathbf{C}\dot{\mathbf{v}}^{(1)} + (\mathbf{K} + \mathbf{H})\mathbf{v}^{(1)} = 0 \tag{4.17}$$

Here $\mathbf{M}$, $\mathbf{C}$, $\mathbf{K}$ and $\mathbf{H}$ are the $N \times N$ mass-, damping-, stiffness- and circulatory- matrices respectively. $\mathbf{M}$ is equal to the identity matrix, $\mathbf{I}$, and $\mathbf{C}$ is diagonal. $\mathbf{K}$ and $\mathbf{H}$ represent geometric- and aerodynamic- linear terms. However, although $\mathbf{K}$ and $\mathbf{H}$ represent terms which are linear in $\mathbf{v}^{(1)}$ (and hence in $\bar{a}_{r_s}$), they contain nonlinear geometric- and

47

aerodynamic- terms in $\tilde{a}_{r_s}$. Upon introducing,

$$\left\{ \begin{array}{c} \dot{\mathbf{v}}^{(1)} \\ \mathbf{v}^{(1)} \end{array} \right\} = \mathbf{v}_0 e^{\iota \omega t} \quad , \quad \iota = \sqrt{-1} \tag{4.18}$$

into (4.17), and considering the resulting generalized eigenvalue problem (EVP), i.e.,

$$\left[\begin{array}{cc} -\mathbf{M}^{-1}\mathbf{C} & -\mathbf{M}^{-1}(\mathbf{K}+\mathbf{H}) \\ \mathbf{I} & \mathbf{0} \end{array} \right] \mathbf{v}_0 = \iota \omega \mathbf{v}_0 \tag{4.19}$$

the complex eigenfrequencies and eigenmodes are obtained. By varying the control parameter (e.g., λ), its flutter value (e.g., λ_0) and corresponding eigensolution (henceforth termed the critical eigensolution) are obtained when the Hopf bifurcation condition is satisfied. At flutter, one of the eigenfrequencies, henceforth denoted as ω_1 ($= \omega_F$), is real while the remaining are complex with positive imaginary part. At this point we note that the eigensolution of the EVP defined by $\mathbf{J}_2$ (also equivalent to the EVP obtained after linearizing (4.6)) would also yield the flutter quantities. However, since the ordering scheme $\hat{a}_{r_s} = O(\epsilon^2)$ is implied in the EVP (4.18) it is not equivalent to the EVP defined by $\mathbf{J}_2$, i.e., the terms representing the influence of initial imperfections are absent in the former. Therefore, the solution of (4.18) yields true flutter quantities only in the case of perfect panels. In particular, for imperfect panels the value of λ_0 obtained through (4.18) is lower than its true value obtained from the EVP defined by $\mathbf{J}_2$, the difference increasing with the magnitude of $\hat{a}_{r_s}$. Further, using the true flutter quantities, obtained from the EVP defined by $\mathbf{J}_2$, in the perturbation solution would result in divergent solutions of the $O(\epsilon)$ problem. Hence the MMS is applied to perfect panels only.

Thus, the solution of (4.17) can be written as,

$$\mathbf{v}^{(1)}[T_0, T_1, T_2] = \sum_{i=1}^{N} \mathbf{c}_i[T_1, T_2] e^{\iota \omega_i T_0} + C.C. \tag{4.20}$$

where $\mathbf{c}_i$ is proportional to the (complex) eigenvector $\check{\mathbf{c}}_i$ associated with the eigenvalue ω_i, and C.C. denotes the complex conjugates of all preceding terms.

CHAPTER 4. SOLUTION METHODOLOGY

The $O(\epsilon^2)$ system

Substitution of (4.20), considered in conjunction with the critical eigensolution, into the $O(\epsilon^2)$ system yields,

$$O(\epsilon^2): \quad \mathbf{M}\ddot{\mathbf{v}}^{(2)} + \mathbf{C}\dot{\mathbf{v}}^{(2)} + (\mathbf{K} + \mathbf{H})\mathbf{v}^{(2)} \quad =$$

$$\underline{\sum_{i=1}^{N} \left[\lambda_1(\lambda_0^2\hat{\mathbf{h}}_i + \lambda_0\check{\mathbf{h}}_i + \grave{\mathbf{h}}_i)c_{i1} + \tilde{\mathbf{h}}_i D_1[c_{i1}]\right] e^{\iota\omega_i T_0}} +$$

$$\tilde{\mathbf{g}}_1 c_{41}\bar{c}_{41}\, e^{\iota(\omega_4 - \bar{\omega}_4)T_0} + \tilde{\mathbf{g}}_2 c_{31}\bar{c}_{41}\, e^{\iota(\omega_3 - \bar{\omega}_4)T_0} + \tilde{\mathbf{g}}_3 c_{21}\bar{c}_{41}\, e^{\iota(\omega_2 - \bar{\omega}_4)T_0} +$$

$$\tilde{\mathbf{g}}_4 c_{11}\bar{c}_{41}\, e^{\iota(\omega_1 - \bar{\omega}_4)T_0} + \tilde{\mathbf{g}}_5 c_{41}c_{31}\, e^{\iota(\omega_4 + \omega_3)T_0} + \tilde{\mathbf{g}}_6 c_{41}c_{21}\, e^{\iota(\omega_4 + \omega_2)T_0} +$$

$$\tilde{\mathbf{g}}_7 c_{41}c_{11}\, e^{\iota(\omega_4 + \omega_1)T_0} + \tilde{\mathbf{g}}_8 c_{31}\bar{c}_{31}\, e^{\iota(\omega_3 - \bar{\omega}_3)T_0} + \tilde{\mathbf{g}}_9 c_{21}\bar{c}_{31}\, e^{\iota(\omega_2 - \bar{\omega}_3)T_0} +$$

$$\tilde{\mathbf{g}}_{10} c_{11}\bar{c}_{31}\, e^{\iota(\omega_1 - \bar{\omega}_3)T_0} + \tilde{\mathbf{g}}_{11} c_{31}c_{21}\, e^{\iota(\omega_3 + \omega_2)T_0} + \tilde{\mathbf{g}}_{12} c_{31}c_{11}\, e^{\iota(\omega_3 + \omega_1)T_0} +$$

$$\tilde{\mathbf{g}}_{13} c_{21}\bar{c}_{21}\, e^{\iota(\omega_2 - \bar{\omega}_2)T_0} + \tilde{\mathbf{g}}_{14} c_{11}\bar{c}_{21}\, e^{\iota(\omega_1 - \bar{\omega}_2)T_0} + \tilde{\mathbf{g}}_{15} c_{21}c_{11}\, e^{\iota(\omega_2 + \omega_1)T_0} +$$

$$\tilde{\mathbf{g}}_{16} c_{41}^2\, e^{2\iota\omega_4 T_0} + \tilde{\mathbf{g}}_{17} c_{31}^2\, e^{2\iota\omega_3 T_0} + \tilde{\mathbf{g}}_{18} c_{21}^2\, e^{2\iota\omega_2 T_0} + \tilde{\mathbf{g}}_{19} c_{11}^2\, e^{2\iota\omega_1 T_0} +$$

$$\tilde{\mathbf{g}}_{20} c_{11}\bar{c}_{11} \quad + \quad C.C.$$

where, \hfill (4.21)

$$\tilde{\mathbf{g}}_j \quad \equiv \quad \lambda_0^3\hat{\mathbf{g}}_j + \lambda_0^2\check{\mathbf{g}}_j + \grave{\mathbf{g}}_j \quad , \quad j = 1 \to 20$$

Here, the constant, N-dimensional vectors $\hat{\mathbf{h}}_i$, $\check{\mathbf{h}}_i$, $\grave{\mathbf{h}}_i$, $\tilde{\mathbf{h}}_i$ and $\hat{\mathbf{g}}_j$, $\check{\mathbf{g}}_j$, $\grave{\mathbf{g}}_j$ depend on the critical eigensolution and system coefficients. The coefficients $\hat{\mathbf{g}}_j$, $\grave{\mathbf{g}}_j$, and $\hat{\mathbf{h}}_i$ vanish for the case of a trivial static equilibrium, i.e., $\tilde{a}_{rs} = 0$, whereas $\check{\mathbf{h}}_i$ depends explicitly on the modal-damping coefficients. The explicit forms of these vectors are lengthy and hence they are not displayed herein. The operator $D_1[\ ]$ is defined in $(4.16)_3$ and the long overbars (-) denote the complex conjugate of the overbarred term.

The underlined quantity in (4.21) represent secular terms whereas the remaining terms on the r.h.s. are non-secular terms. In order to obtain a uniform expansion of the type (4.15) the secular terms are eliminated by deriving the solvability in the following manner. Pertaining to the secular terms in (4.21), we seek a particular solution of the form,

$$\mathbf{v}^{(2)}[T_0, T_1, T_2] = \sum_{i=1}^{N} \tilde{c}_i[T_1, T_2]e^{\iota\omega_i T_0} \quad + \quad C.C. \tag{4.22}$$

49

Inserting (4.22) into (4.21) considered without its non-secular terms, and equating coefficients of $e^{\iota\omega_i T_0}$ yields the systems of linear algebraic equations,

$$\mathbf{A}_i \tilde{\mathbf{c}}_i = \hat{\mathbf{c}}_i \quad , \quad i = 1 \rightarrow N$$

where, (4.23)

$$\mathbf{A}_i \equiv -\omega_i^2 \mathbf{M} + \iota\omega_i \mathbf{C} + (\mathbf{K} + \mathbf{H})$$

$$\hat{\mathbf{c}}_i \equiv (\lambda_0^2 \lambda_1 \hat{\mathbf{h}}_i + \lambda_0 \lambda_1 \check{\mathbf{h}}_i + \lambda_1 \grave{\mathbf{h}}_i) c_{i1} + \tilde{\mathbf{h}}_i D_1[c_{i1}]$$

Now, considering (4.20) and (4.17) it is easily verified that for non-trivial solutions of (4.17) the $\mathbf{A}_i$ must be singular. Let $\mathbf{B}_i$ denote the $N \times (N + 1)$ augmented coefficient matrix of the system $(4.23)_1$, obtained by augmenting $\mathbf{A}_i$ with the column vector $\hat{\mathbf{c}}_i$. A well-known result from linear algebra states that a necessary and sufficient condition for $(4.23)_1$ to possess a solution is that $\mathbf{A}_i$ and $\mathbf{B}_i$ should have the same rank. Using this result, the solvability conditions are obtained by replacing the kth column of $\mathbf{A}_i$ with $\hat{\mathbf{c}}_i$ and then imposing the condition that the resulting matrix be singular. Since $i = 1 \rightarrow N$ we obtain N solvability conditions, each of which is unique for any choice of $k : 1 \leq k \leq N$ (except in certain cases involving repeated frequencies—see Appendix C for further discussion on this point and a more formal derivation of the solvability condition for linear algebraic systems). The solvability conditions obtained in this manner are,

$$\frac{dc_{i1}}{dT_1} = \lambda_1 k_i c_{i1} \quad , \quad i = 1 \rightarrow N \tag{4.24}$$

where k_i are complex constants depending on the system coefficients, critical eigensolution and λ_0. In order to obtain a bounded but non-trivial solution of the form (4.20), which implies a bounded but non-trivial solution for c_{11}, based on (4.24) we conclude that,

$$\lambda_1 = 0 \quad \Longrightarrow \quad \frac{d}{dT_1} = 0 \tag{4.25}$$

CHAPTER 4. SOLUTION METHODOLOGY

Introducing (4.25) into (4.21), the solution for $\mathbf{v}^{(2)}$ may be expressed as,

$$
\begin{aligned}
\mathbf{v}^{(2)}[T_0, T_2] &= \Big[-(\omega_4 - \overline{\omega}_4)^2 \mathbf{M} + \iota(\omega_4 - \overline{\omega}_4)\mathbf{C} + (\mathbf{K} + \mathbf{H}) \Big]^{-1} \tilde{\mathbf{g}}_1 c_{41} \overline{c}_{41} \, e^{\iota(\omega_4 - \overline{\omega}_4)T_0} \\
&\quad + \cdots\cdots + \Big[-(2\omega_1)^2 \mathbf{M} + \iota(2\omega_1)\mathbf{C} + (\mathbf{K} + \mathbf{H}) \Big]^{-1} \tilde{\mathbf{g}}_{19} c_{11}^2 \, e^{2\iota\omega_1 T_0} \\
&\quad + \Big[\mathbf{K} + \mathbf{H} \Big]^{-1} \tilde{\mathbf{g}}_{20} c_{11} \overline{c}_{11} \quad + \quad C.C.
\end{aligned}
\tag{4.26}
$$

We note that in writing the solution for $\mathbf{v}^{(2)}$ the homogeneous solution has been omitted since it has the same form as (4.20), hence it can be absorbed into $\mathbf{v}^{(1)}$.

The $O(\epsilon^3)$ system

Following the same procedure as for the $O(\epsilon^2)$ problem, i.e., after introducing (4.20), (4.25), (4.26) and the critical eigensolution into the $O(\epsilon^3)$ system, we obtain,

$$
\begin{aligned}
O(\epsilon^3): \quad \mathbf{M}\ddot{\mathbf{v}}^{(3)} &+ \mathbf{C}\dot{\mathbf{v}}^{(3)} + (\mathbf{K} + \mathbf{H})\mathbf{v}^{(3)} = \\
&\sum_{i=1}^{N} \Big[\lambda_2(\lambda_0^2 \hat{\mathbf{h}}_i + \lambda_0 \breve{\mathbf{h}}_i + \dot{\mathbf{h}}_i)c_{i1} + + \tilde{\mathbf{h}}_i D_2[c_{i1}] + (\lambda_0^3 \tilde{\mathbf{l}}_i + \lambda_0^2 \hat{\mathbf{l}}_i + \breve{\mathbf{l}}_i)c_{i1} + \\
&\quad (\lambda_0^3\{\tilde{\mathbf{t}}_i + \hat{\mathbf{t}}_i\} + \lambda_0^2 \breve{\mathbf{t}}_i + \acute{\mathbf{t}}_i + \grave{\mathbf{t}}_i)c_{11}\overline{c}_{11}c_{i1} \Big] e^{\iota\omega_i T_0} + C.C. + N.S.T.
\end{aligned}
\tag{4.27}
$$

where N.S.T. denotes the nonsecular terms appearing in the $O(\epsilon^3)$ system. Their explicit form is not required for a first-order approximate solution. The constant, N-dimensional vectors $\tilde{\mathbf{t}}_i, \hat{\mathbf{t}}_i, \breve{\mathbf{t}}_i, \acute{\mathbf{t}}_i, \grave{\mathbf{t}}_i, \tilde{\mathbf{l}}_i, \hat{\mathbf{l}}_i,$ and $\breve{\mathbf{l}}_i$, whose explicit forms are not displayed herein, depend on the critical eigensolution and system coefficients. The coefficients $\hat{\mathbf{l}}_i$ vanish when considering a perfect panel, whereas $\tilde{\mathbf{l}}_i$ and $\breve{\mathbf{l}}_i$ vanish when a trivial static equilibrium exists and/or when considering a perfect panel. The operator $D_2[\ ]$ is defined in $(4.16)_3$.

Following a procedure similar to that used for the $O(\epsilon^2)$ system, the secular terms in (4.27) are eliminated and the resulting solvability conditions are,

$$
\frac{dc_{i1}}{dT_2} = \lambda_2 \hat{k}_i c_{i1} + \breve{k}_i \overline{c}_{11} c_{11} c_{i1} \quad , \qquad i = 1 \to N
\tag{4.28}
$$

At this stage it is worth mentioning that the fact that the critical eigenfrequencies ω_i $(i \neq 1)$ are complex does not allow us to conclude that the asymptotic behavior (i.e., whether growth

51

or decay) of the modal components of $\mathbf{v}^{(1)}$ is the same as that obtained for the c_{i1} solution through a linearization of (4.28). Introducing the representation,

$$c_{i1}[T_2] = \Upsilon_i[T_2]e^{\iota\vartheta_i[T_2]} \quad , \quad i = 1 \rightarrow N \tag{4.29}$$

into (4.28), we obtain the following equations describing the evolution of the phase ϑ_i and amplitude Υ_i pertaining to the modal components of $\mathbf{v}^{(1)}$:

$$\frac{d\Upsilon_i}{dT_2} = \lambda_2 \check{k}_i \Upsilon_i + \acute{k}_i \Upsilon_1^2 \Upsilon_i$$
$$\Upsilon_i \frac{d\vartheta_i}{dT_2} = \lambda_2 \bar{k}_i \Upsilon_i + \grave{k}_i \Upsilon_1^2 \Upsilon_i \quad , \quad i = 1 \rightarrow N \tag{4.30}$$

The complex constants $\hat{k}_i$, $\tilde{k}_i$ and real constants $\check{k}_i$, $\acute{k}_i$, $\bar{k}_i$, $\grave{k}_i$ appearing in (4.28) and (4.30), respectively, depend on the system coefficients, critical eigensolution, λ_0, and implicitly $\tilde{a}_{r_\bullet}$. Hence, at each value of the control parameter λ the solution of (4.30) is obtained after determining $\tilde{a}_{r_\bullet}$ by the ACM. However, as noted previously the MMS is consistent only when applied to cases involving perfect panels, for which numerical results reveal that flutter oscillations occur about the trivial equilibrium only. In such cases equations (4.28) or (4.30) independently describe the amplitude and frequency of the ensuing flutter motion in terms of λ.

Solution of the Evolution Equations

Equation $(4.30)_1$ with $i = 1$ reads as,

$$\frac{d\Upsilon_1}{dT_2} = \lambda_2 \check{k}_1 \Upsilon_1 + \acute{k}_1 \Upsilon_1^2 \Upsilon_1 \tag{4.31}$$

The fixed point solutions of (4.31) are,

$$\Upsilon_1^2 = 0 \quad , \quad -\frac{\check{k}_1}{\acute{k}_1}\lambda_2 \tag{4.32}$$

For convenience we shall denote the trivial and non-trivial fixed points as $\{0\}$ and $\{\pm1\}$, respectively. Further, assuming that the onset of flutter occurs as λ increases, i.e., $\lambda_2 > 0$ (this is usually the case for flat panels), we conclude from (4.31) that $\check{k}_1 > 0$. Upon

considering the variational equation derived from (4.31), the stability of the fixed point solutions is ascertained. For the $\{0\}$ solution we conclude that it is stable or unstable according to whether $\lambda_2 < 0$ or $\lambda_2 > 0$. For the $\{\pm 1\}$ solution two cases arise. These represent the supercritical (subcritical) Hopf bifurcation for which we consider $\acute{k}_1 < 0$ ($\acute{k}_1 > 0$) and hence obtain real fixed point solutions only when $\lambda_2 > 0$ ($\lambda_2 < 0$) which are stable (unstable). As regards the remaining modes, using the result (4.32) we conclude that only trivial fixed point solutions exist for Υ_i $(i = 2 \to N)$.

The solution of Υ_1 is obtained from (4.31) as,

$$\Upsilon_1^2[T_2] = \frac{\Upsilon_1^2[0]}{e^{-2\check{k}_1\lambda_2 T_2} - \Upsilon_1^2[0]\frac{\acute{k}_1}{\lambda_2\check{k}_1}(1 - e^{-2\check{k}_1\lambda_2 T_2})} \tag{4.33}$$

Based on the solution (4.33) and considering non-trivial initial conditions, i.e., $\Upsilon_1[0] \neq 0$, we conclude the following for the four cases involving $\check{k}_1 > 0$:

$$\underline{\acute{k}_1 < 0\,,\,\lambda_2 > 0} \;:\; \lim_{t\to\infty} \Upsilon_1^2 = -\frac{\check{k}_1}{\acute{k}_1}\lambda_2$$

$$\underline{\acute{k}_1 < 0\,,\,\lambda_2 < 0} \;:\; \lim_{t\to\infty} \Upsilon_1^2 = 0 \tag{4.34}$$

$$\underline{\acute{k}_1 > 0\,,\,\lambda_2 > 0} \;:\; \text{at}\;\; \epsilon^2 t = -\frac{1}{2\check{k}_1\lambda_2}\ln\left[\frac{\Upsilon_1^2[0]\acute{k}_1}{\Upsilon_1^2[0]\acute{k}_1 - \lambda_2\check{k}_1}\right]\;,\;\; \Upsilon_1^2 \to \infty$$

$$\underline{\acute{k}_1 > 0\,,\,\lambda_2 < 0} \;:\; \text{if}\;\; \Upsilon_1^2[0]\frac{\acute{k}_1}{\lambda_2\check{k}_1} > 1 \;\; \text{then at}\;\; \epsilon^2 t = -\frac{1}{2\check{k}_1\lambda_2}\ln\left[\frac{\Upsilon_1^2[0]\acute{k}_1}{\Upsilon_1^2[0]\acute{k}_1 - \lambda_2\check{k}_1}\right]\;,\;\; \Upsilon_1^2 \to \infty$$

$$\text{if}\;\; \Upsilon_1^2[0]\frac{\acute{k}_1}{\lambda_2\check{k}_1} < 1 \;\; \text{then}\;\; \lim_{t\to\infty} \Upsilon_1^2 = 0$$

We see that only the first case shown above admits a non-trivial steady state solution for Υ_1, this being identical to its stable, non-trivial fixed point solution. Thus, only fixed point solutions of Υ_1 need be considered in future.

Considering $(4.30)_2$ written for $i = 1$ in conjunction with the non-trivial fixed point solution for Υ_1, we obtain,

$$\vartheta_1[T_2] = \left(\bar{k}_1 - \frac{\acute{k}_1\check{k}_1}{\acute{k}_1}\right)\lambda_2 T_2 \tag{4.35}$$

Similarly, considering $(4.30)_{1,2}$ for $i = 2 \to N$, and using the non-trivial solution (4.32) we

obtain,

$$\Upsilon_i[T_2] = \Upsilon_i[0]e^{\left(k_i - k_i\frac{k_1}{k_1}\right)\lambda_2 T_2}$$

$$\vartheta_i = \left(\bar{k}_i - k_i\frac{\check{k}_1}{k_1}\right)\lambda_2 T_2 \quad , \quad i = 2 \to N \qquad (4.36)$$

Finally, introducing the non-trivial solutions (4.32), (4.35) and (4.36) into (4.29) and considering (4.15) in conjunction with (4.20), we obtain the first-order approximation for a as,

$$\mathbf{a} = \check{c}_1\sqrt{-\frac{\check{k}_1\hat{\lambda}}{\hat{k}_1}}e^{\iota\tilde{\omega}_1 t} + \epsilon\sum_{i=2}^{N}\check{c}_i\Upsilon_i[0]e^{\iota\tilde{\omega}_i t} \quad + \quad C.C.$$

where, $\qquad\qquad\qquad\qquad\qquad\qquad\qquad\qquad\qquad\qquad\qquad\qquad (4.37)$

$$\hat{\lambda} \equiv \epsilon^2\lambda_2 = \lambda - \lambda_F$$

$$\tilde{\omega}_1 \equiv \left(\bar{k}_1 - k_1\frac{\check{k}_1}{k_1}\right)\hat{\lambda} + \omega_1$$

$$\tilde{\omega}_i \equiv \left(\bar{k}_i - k_i\frac{\check{k}_1}{k_1} - \iota\left\{\check{k}_i - k_i\frac{\check{k}_1}{k_1}\right\}\right)\hat{\lambda} + \omega_i \quad , \quad i = 2 \to N$$

For small absolute values of $\hat{\lambda}$, i.e., confining the analysis to the region near the flutter boundary, it is observed that the imaginary parts of $\tilde{\omega}_i$ ($i = 2 \to N$) are positive. In that case the steady state modal amplitudes of the flutter component of motion are given by discarding the summation term in $(4.37)_1$.

At this point it is worthwhile to make the following remarks concerning MMS analysis as carried out herein:

- The MMS can be used to predict the modal ampitudes of the flutter component of motion only when flutter ensues as a result of a Hopf bifurcation.

- Since the MMS is a perturbation method, results obtained by it are accurate only in the region (defined in control parameter space) near the flutter boundary.

- Based on the present analysis, a Hopf bifurcation cannot occur for the system of evolution equations (this corrresponds to a secondary Hopf bifurcation of the system (4.6)).

Hence periodic solutions of the evolution quantities which would yield non-periodic motions (i.e., solutions of z or a) cannot be obtained by the MMS as considered herein.

- The case of negligible total damping has not been considered. In this case the $O(\epsilon)$ system (4.17) is free of damping, thus yielding real eigenfrequencies and flutter due to frequency coalescence. For certain special values of the system parameters, e.g., h, Λ, ϕ, etc., this could result in certain commensurability relations being satisfied between the eigenfrequencies at flutter, hence giving rise to the phenomenon of autoparametric resonance. Upon examining (4.21), we see that in the presence of an autoparametric resonance some of the quadratic, non-secular terms would then become small-divisor-producing terms and hence the solvability condition (4.24) (hence (4.25)) would no longer be valid.

4.3 Dynamic Solutions Using the Numerical Integration Method (NIM)

After obtaining the static equilibrium state $\tilde{a}_{r_s}$ by the ACM, the amplitudes of flutter oscillation about the static equilibrium, i.e., $\tilde{a}_{r_s}$, are obtained by numerically integrating (4.6). The first method used here is the usual one that considers the initial value problem (IVP), defined by (4.6) and some well chosen initial conditions, which is then numerically integrated for a sufficiently long time until transients have decayed. Henceforth, we term this as NIM1. The drawback of this method is that the convergence to steady state may be very slow. Moreover, depending upon whether the choice of initial conditions lies within the basin of attraction of the solution sought, we may or may not converge to it. The second method considered here is the shooting technique originally proposed by Aprille and Trick [87]. This is more efficient and applicable only when limit cycle (periodic) solutions are sought. This method is henceforth termed NIM2 and is described in the following sub-section.

4.3.1 Shooting technique to obtain periodic solutions (NIM2)

In order to obtain a periodic solution (i.e., the state and period) of the autonomous system (4.6), we seek an initial condition $\boldsymbol{\nu}$ (a $2N$-dimensional vector) that lies on the limit cycle. Denoting the period of the solution as T, and imposing the periodicity condition, the IVP is transformed into the following two-point boundary value problem (BVP):

$$\dot{\mathbf{z}} = \bar{\mathbf{f}}[\mathbf{z}\,;\,\lambda\,,\,L_\alpha^*]$$

$$\mathbf{z}[0\,;\,\boldsymbol{\nu}] = \boldsymbol{\nu} \quad , \quad \mathbf{z}[T\,;\,\boldsymbol{\nu}] = \boldsymbol{\nu} \tag{4.38}$$

where, $\qquad\qquad \mathbf{z} = \mathbf{z}[t\,;\,\boldsymbol{\nu}]$

The algorithm to solve the BVP (4.38) is initiated by providing initial guesses $\boldsymbol{\nu}_0$ and T_0 for $\boldsymbol{\nu}$ and T, respectively. Then we seek corrections $\delta\boldsymbol{\nu}$ and δT by requiring that the periodicity condition be satisfied, i.e.,

$$\mathbf{z}[T_0 + \delta T\,;\,\boldsymbol{\nu}_0 + \delta\boldsymbol{\nu}] = \boldsymbol{\nu}_0 + \delta\boldsymbol{\nu} \tag{4.39}$$

Performing a Taylor series expansion of (4.39) and retaining only linear terms, we obtain,

$$\frac{\partial \mathbf{z}}{\partial t}[T_0\,;\,\boldsymbol{\nu}_0]\delta T + \Big[\nabla_{\boldsymbol{\nu}}\mathbf{z}\,[T_0\,;\,\boldsymbol{\nu}_0] - \mathbf{I}\Big]\delta\boldsymbol{\nu} = \boldsymbol{\nu}_0 - \mathbf{z}[T_0\,;\,\boldsymbol{\nu}_0] \tag{4.40}$$

where, due to (4.38)$_1$, we have,

$$\frac{\partial \mathbf{z}}{\partial t}[T_0\,;\,\boldsymbol{\nu}_0] = \bar{\mathbf{f}}[\mathbf{z}[T_0\,;\,\boldsymbol{\nu}_0]\,;\,\lambda, L_\alpha^*] \tag{4.41}$$

Here I is the $2N \times 2N$ identity matrix and $\nabla_{\boldsymbol{\nu}}\mathbf{z}$ is the $2N \times 2N$ Jacobian matrix of the state taken with respect to the initial condition we seek. Equation (4.40) represents a system of $2N$ linear algebraic equations in terms of the $2N + 1$ unknown corrections $\delta\boldsymbol{\nu}$ and δT. In order to solve the system (4.40) for the $2N + 1$ unknowns, the criterion of Mees [88] is considered. This requires that $\delta\boldsymbol{\nu}$ be normal to $\bar{\mathbf{f}}$, i.e.,

$$\bar{\mathbf{f}}^{\mathbf{T}}[\mathbf{z}[T_0\,;\,\boldsymbol{\nu}_0]\,;\,\lambda, L_\alpha^*]\,\delta\boldsymbol{\nu} = 0 \tag{4.42}$$

It should be noted that other criteria for augmenting (4.40) with an additional equation exist (e.g., arbitrarily setting one of the corrections $\delta\nu_i = 0$; see Nayfeh and Balachandran [85] for further details)

The components of $\nabla_{\boldsymbol{\nu}}\mathbf{z}$, required in the corrector, are obtained by differentiating $(4.38)_1$ with respect to $\boldsymbol{\nu}$ in conjunction with the functional dependency indicated in $(4.38)_4$. Thus we obtain a system of linear ODE's in $\frac{\partial z_i}{\partial \nu_j}$, i.e.,

$$\nabla_{\boldsymbol{\nu}}\dot{\mathbf{z}} = \nabla_{\boldsymbol{\nu}}\bar{\mathbf{f}} \quad \Longrightarrow \quad \frac{d}{dt}(\nabla_{\boldsymbol{\nu}}\mathbf{z}) = \nabla_{\mathbf{z}}\bar{\mathbf{f}}\,\nabla_{\boldsymbol{\nu}}\mathbf{z} \qquad (4.43)$$

Further, using the initial condition given by $(4.38)_2$ and integrating $(4.38)_1$, the state can be expressed as,

$$\mathbf{z}[t\,;\boldsymbol{\nu}] = \boldsymbol{\nu} + \int_0^t \bar{\mathbf{f}}\,dt^* \qquad (4.44)$$

from which we obtain the result,

$$\nabla_{\boldsymbol{\nu}}\mathbf{z} = \mathbf{I} + \int_0^t \nabla_{\mathbf{z}}\bar{\mathbf{f}}\,\nabla_{\boldsymbol{\nu}}\mathbf{z}\,dt^* \quad \Longrightarrow \quad \nabla_{\boldsymbol{\nu}}\mathbf{z}\,[0\,;\boldsymbol{\nu}] = \mathbf{I} \qquad (4.45)$$

The algorithm for obtaining a periodic solution can now be stated as follows:

Step 1 : Obtain $\mathbf{z}[T_0\,;\boldsymbol{\nu}_0]$ and $\nabla_{\boldsymbol{\nu}}\mathbf{z}\,[T_0\,;\boldsymbol{\nu}_0]$ by numerically integrating the augmented IVP defined by the $(2N)^2+2N$ ODE's $(4.38)_1$ and $(4.43)_2$ subject to the initial conditions $(4.45)_2$ and $(4.38)_2$ (evaluated for the initial guess $\boldsymbol{\nu}_0$), i.e., $\mathbf{z}[0] = \boldsymbol{\nu}_0$ and $\nabla_{\boldsymbol{\nu}}\mathbf{z}\,[0] = \mathbf{I}$. This numerical integration scheme constitutes the predictor part of the algorithm.

Step 2 : Using $\mathbf{z}[T_0\,;\boldsymbol{\nu}_0]$ and $\nabla_{\boldsymbol{\nu}}\mathbf{z}\,[T_0\,;\boldsymbol{\nu}_0]$, and (4.41), solve the system $((4.40)\,,(4.42))$ to obtain the corrections $\delta\boldsymbol{\nu}$ and δT.

Step 3 : If the absolute values of the corrections are below a specified tolerance, then we accept $\boldsymbol{\nu}_0$ and T_0 as $\boldsymbol{\nu}$ and T, respectively, i.e., we have converged onto the limit cycle. Otherwise, we consider the new initial guesses as $\delta\boldsymbol{\nu}+\boldsymbol{\nu}_0 \to \boldsymbol{\nu}_0$ and $\delta T+T_0 \to T_0$ and repeat the above procedure. This Newton-Raphson iteration procedure constitutes the corrector part of the algorithm.

Regarding the NIM, the following points should be noted:

- Unlike the straightforward integration method (NIM1), the shooting technique (NIM2) can also be used to converge onto unstable limit cycles. In fact even in the case of stable limit cycles the rate of convergence is much faster when using the NIM2.

- The NIM2 cannot be used when non-periodic solutions are sought. Moreover its convergence characteristics are very sensitive to the initial guesses and step size of numerical integration, especially when multiple solutions co-exist. Hence, when seeking periodic solutions, the NIM usually consists of applying the NIM1 to get onto the solution branch and then the NIM2 to continue on that branch. Non-periodic (i.e., quasi-periodic or chaotic) motions are obtained by using the NIM1.

- Stability and bifurcation behavior of the solution is obtained as a by-product when using the NIM2. This is discussed in the following sub-section.

- Unlike the MMS, the NIM is not restricted to the class of weakly-nonlinear systems and hence it is applied in the deep post-flutter range also.

The relevant derivations for the NIM, i.e., obtaining the explicit forms of (4.5), (4.6) and the associated Jacobian matrices were done using *MACSYMA*. These expressions are not displayed herein. The numerical integration was carried out using the fifth and sixth order Runge-Kutta-Verner method (*IMSL–DVERK*). Further discussions of algorithms for shooting methods and continuation methods to obtain dynamic solutions appear in, e.g., Seydel [46] and Nayfeh and Balachandran [85].

4.3.2 Stability and bifurcation behavior of periodic solutions

After a limit cycle solution $\tilde{z}[t]$ ($= \tilde{z}[t + T]$) and its period T are obtained by the shooting technique, its stability is ascertained using Floquet theory (see Appendix C). Comparing $(4.43)_2$, $(4.45)_2$ with $(C.8)_{1,2}$, respectively, and considering $(C.5)$, we see that the monodromy matrix $\tilde{\Phi}$ is identical to $\nabla_{\boldsymbol{\nu}} z[T; \boldsymbol{\nu}_0]$. Hence, after the shooting technique

has converged to a periodic solution we can determine its stability as a by-product by obtaining the Floquet multipliers, i.e., $\tilde{\lambda}_j$ $(j = 1 \rightarrow 2N)$, which are the eigenvalues of $\nabla_{\boldsymbol{\nu}}\boldsymbol{z}[T \,;\, \boldsymbol{\nu}_0]$.

As the control parameter is varied, bifurcations of the periodic solution $\tilde{\boldsymbol{z}}$ (see Appendix C) occur for certain control parameter values (henceforth referred to as bifurcation values). These bifurcations are determined based on how the critical Floquet multiplier λ_k leaves the unit circle in the complex plane (see Fig. 4.1) as the control parameter is varied. This in turn determines—at the bifurcation values—the nature of the non-decaying (oscillatory) disturbance $\boldsymbol{z}^*$ which, when superimposed on $\tilde{\boldsymbol{z}}$, results in a bifurcating solution $\boldsymbol{z}$ $(= \tilde{\boldsymbol{z}} + \boldsymbol{z}^*)$ The various bifurcations encountered are:

Symmetry Breaking Bifurcation : For a stable limit cycle possessing inversion symmetry, i.e., $\tilde{\boldsymbol{z}}[t] = -\tilde{\boldsymbol{z}}[t + \frac{T}{2}]$, a symmetry breaking bifurcation occurs when λ_k leaves the unit circle through $+1$. Stable, symmetry broken (unsymmetric) limit cycles co-exist with the unstable, symmetric limit cycle beyond the bifurcation point. The period of these solutions is preserved, locally, beyond the bifurcation point.

Tangent Bifurcation : When the stable limit cycle is symmetric (unsymmetric), a tangent bifurcation occurs when λ_k leaves the unit circle through -1 $(+1)$. A branch of unstable limit cycles meets the branch of stable limit cycles at the bifurcation point. This is also known as a cyclic-fold bifurcation and the bifurcation points are called turning points. Beyond the bifurcation point the solution jumps to another periodic or non-periodic state. For the case when periodic solutions exist beyond the bifurcation point, the period and symmetry are locally preserved.

Period-Doubling Bifurcation : When the stable limit cycle is unsymmetric, a period-doubling bifurcation occurs when λ_k leaves the unit circle through -1. Stable, period-doubled solutions co-exist with the unstable, periodic solution beyond the bifurcation point. The period-doubled solutions have a period that is, locally, equal to twice that of the unstable periodic solution.

Secondary Hopf or Neimark Bifurcation : As discussed earlier, a Hopf bifurcation of a fixed point solution yields a periodic bifurcating solution containing a new (non-zero) frequency. Similarly, a Hopf bifurcation of a stable periodic solution introduces an additional frequency into the bifurcating solution. Depending on whether the two frequencies, i.e., the newly introduced frequency and the frequency of the periodic solution prior to the bifurcation, are commensurate or incommensurate, the bifurcating solution is periodic (i.e., phase-locked) or two-period quasi-periodic (QPM), respectively. Phase-locked motions are rare and were not observed in this study. This bifurcation is also called a Neimark bifurcation and occurs when two complex conjugate Floquet multipliers leave the unit circle transversely. Since quasi-periodic motions are non-periodic, only the NIM1 can be used to obtain them. Beyond the bifurcation point, the original periodic solution branch is unstable, whereas the QPM (also known as motion on a T^2 torus) is stable.

4.4 Characterization of Motion

The various types of dynamic solutions obtained, i.e., periodic (symmetric, symmetry broken, period-doubled), and non-periodic (i.e., quasi-periodic and chaotic), are characterized by obtaining phase trajectories, frequency spectra, Poincaré sections, Lyapunov exponents and associated Lyapunov dimension.

Phase Trajectories

These are obtained for the periodic solutions in the z_1–z_5 plane. The symmetric, symmetry broken and period-doubled (up to period-4 motion) solutions are clearly distinguishable.

Frequency spectra

These are obtained using the Fast Fourier Transform (FFT) routine in the software *IGOR*. For a symmetric limit cycle the frequency components are the fundamental (flutter) frequency and its higher harmonics. The unsymmetric solution is characterized by the ap-

pearance of an additional zero-frequency component (DC component) and the period-doubled solution contains additional sub-harmonics of the fundamental frequency and its higher harmonics. The QPM contains additional sidebands around the fundamental frequency, its sub-harmonics and higher harmonics, whereas chaotic motion is characterized by a broadband frequency spectrum.

Poincaré Sections

These are defined by holding z_i constant (e.g., zero as considered herein) and $\dot{z}_i > 0$ (or $\dot{z}_i < 0$). For most applications the sections were defined using $i = 6$.

Lyapunov Exponents and Lyapunov Dimension

The Lyapunov exponents measure the average exponential rates of divergence or convergence of nearby phase space trajectories. The Lyapunov exponents corresponding to an initial condition $\mathbf{z}_0$ are defined as (Parker and Chua [64]),

$$\hat{\lambda}_j = \lim_{t \to \infty} \frac{1}{t} \ln | \hat{\mu}_j[t] | \quad , \quad j = 1 \longrightarrow 2N \tag{4.46}$$

where $\hat{\mu}_j[t]$ are the eigenvalues of the fundamental matrix solution $\mathbf{Z}^*[t]$ obtained by integrating the IVP (C.8) with $\hat{\mathbf{A}}[t; \lambda, L_\alpha^*] = \nabla_\mathbf{z} \bar{\mathbf{f}} \big|_{\mathbf{z}=\mathbf{z}_0}$. As shown earlier, the $\hat{\mu}_j[t]$ are also the eigenvalues of $\nabla_{\boldsymbol{\nu}} \mathbf{z}[t; \boldsymbol{\nu}_0]$ which is obtained by integrating the IVP defined by $(4.38)_1$ and $(4.43)_2$ subject to the initial conditions $\mathbf{z}[0] = \mathbf{z}_0$ and $\nabla_{\boldsymbol{\nu}} \mathbf{z}[0] = \mathbf{I}$.

Another equivalent definition (e.g., Wolf et al. [72]), used in computational algorithms, considers the evolution of an infinitesimal $2N$-dimensional sphere of initial conditions. As time evolves, the sphere expands or contracts along its $2N$ principal directions and gets transformed into a $2N$-dimensional ellipsoid. The jth Lyapunov exponent is defined in terms of the length of the jth principal axis of the ellipsoid, i.e., $d_j[t]$, as,

$$\hat{\lambda}_j = \lim_{t \to \infty} \frac{1}{t} \log_2 \frac{d_j[t]}{d_j[0]} \quad , \quad j = 1 \longrightarrow 2N \tag{4.47}$$

The algorithm and program by Wolf et al. [72] was used for calculating the Lyapunov exponents. The value of $\hat{\lambda}_j$ depends upon input parameters such as the Lyapunov time

step and Runge-Kutta integration time step. Moreover, since $\hat{\lambda}_j$ is a statistical property we need to integrate $(4.38)_1$ and $(4.43)_2$ over a long time to obtain an acceptable value for it (Moon [62]). Due to these reasons, for some cases, the Lyapunov exponents oscillate about a mean value instead of converging.

For an autonomous system (e.g., (4.6)), one Lyapunov exponent is always zero, except in the case of a stable equilibrium point. Moreover, since (4.6) is a dissipative system, contraction of an attractor must outweigh its expansion and hence the sum of the exponents must be negative. For a stable equilibrium point all exponents are negative. Periodic solutions are characterized by one zero exponent, the remaining $2N-1$ being negative. When K exponents are zero and the remaining $2N-K$ are negative, the motion is K-period quasi-periodic (i.e., K incommensurate frequencies are involved). Chaotic attractors possess at least one positive exponent (say $\hat{\lambda}_i$) which indicates an exponential expansion in the corresponding principal direction (say $d_i[t]$). Since, by definition, an attractor is bounded, this implies that a folding process occurs in the principal directions corresponding to the positive exponents. Thus, each positive exponent represents a principal direction along which we have a repeated stretching and folding process that decorrelates nearby states on the attractor. This implies an exponential loss of correlation between two orbits initially separated by an infinitesimal distance, i.e., sensitivity to initial conditions.

The Lyapunov dimension of the attractor was determined according to the following procedure due to Kaplan and Yorke [65]. We order the Lyapunov exponents of the attractor as $\hat{\lambda}_1 \geq \hat{\lambda}_2 \geq \cdots \cdots \geq \hat{\lambda}_{2N}$ and define m as the largest integer which satisfies the relation $\hat{\lambda}_1 + \hat{\lambda}_2 + \cdots \cdots + \hat{\lambda}_m \geq 0$. Then, the Lyapunov dimension is defined as,

$$d_L \equiv m + \frac{\hat{\lambda}_1 + \hat{\lambda}_2 + \cdots \cdots + \hat{\lambda}_m}{|\hat{\lambda}_{m+1}|} \tag{4.48}$$

If no such m exists, as is the case for a stable equilibrium point, we have $d_L \equiv 0$. Thus, it can be easily shown that $d_L = 0$ for a point attractor, $d_L = 1$ for a periodic attractor and $d_L = K$ for a K-periodic attractor. A chaotic attractor has a non-integer d_L.
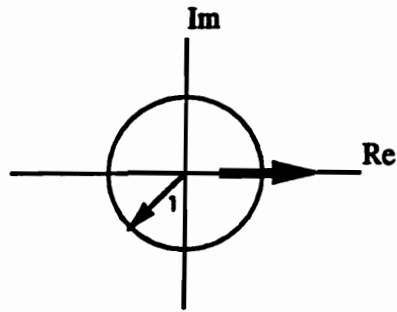
Symmetry Breaking Bifurcation ; Tangent Bifurcation
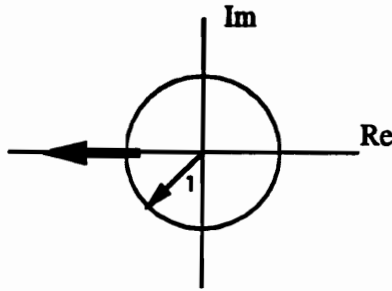
Period - Doubling Bifurcation ; Tangent Bifurcation
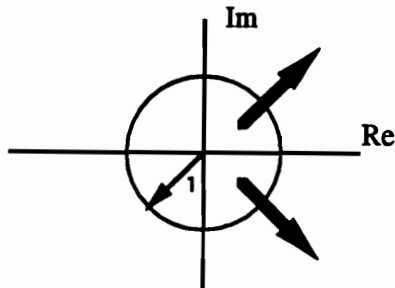
Secondary Hopf (Neimark) Bifurcation

Figure 4.1: Bifurcation behavior determined by how Floquet multiplier leaves the unit circle.

Chapter 5

NUMERICAL RESULTS AND DISCUSSIONS

The numerical applications considered herein are for a composite panel made up of three layers ($i = 1, 2, 3$) with the indices 1 and 3 representing the outer layers. The following data are common to all the cases considered:

Pressure of still air (i.e., atmospheric pressure) : $p_\infty = 14.63$ psi

Speed of sound at sea level: $\qquad\qquad\qquad c_\infty = 1082.5$ ft.sec^{-1}

Polytropic gas coefficient : $\qquad\qquad\qquad \chi = 1.4$

Structural damping (assumed) : $\qquad\qquad\quad \varepsilon_S = 0.1\varepsilon_A$

Relative thickness of layers : $\qquad\qquad\quad h_{<1>} = h_{<3>} = 0.5h_{<2>}$

Total thickness of panel : $\qquad\qquad\qquad h = 1$ in

Nondimensional imperfection considered : $\quad \hat{a}_{11} = 0.2$ (unless stated otherwise)

Mass density of panel layers : $\qquad\qquad\quad \rho_{<i>} = 0.00013$ lbf.sec^2.in^{-4}

In-plane Young's moduli of panel layers : $\quad E_{<1>} = E_{<3>} = 20.83 \times 10^6$ psi ; $E_{<2>} = \frac{E_{<1>}}{10}$

Transverse Young's moduli of panel layers : $\quad E'_{<i>} = \frac{E_{<i>}}{5}$

Transverse shear moduli of panel layers : $\quad G'_{<i>} = \frac{E_{<i>}}{40}$ (unless stated otherwise)

In-plane, transverse Poisson's ratio of panel layers $\mu_{<i>} = \mu'_{<i>} = 0.25$

5.1   Stability Boundaries

A 4 × 1 mode analysis was performed for a square panel with thickness ratio $\frac{l_1}{h} = 50$, subjected to a uniaxial compressive edge load L_1^*, and flow past both faces ($\delta_f = 0$, $\hat{\delta}_f = 2$) in the x_1 direction ($\Lambda = 0^o$). Unless stated otherwise, aerodynamic nonlinearities were included in the simulations.

CHAPTER 5. NUMERICAL RESULTS AND DISCUSSIONS

Perfect panel

The stability of the trivial static equilibrium {0} was analyzed and the associated stability boundaries were obtained by following the eigenvalues of $\mathbf{J_2}$ (eqn. (4.13)). Depending on the number of real and complex eigenvalues residing in the right-half complex plane, denoted R and C, respectively, the λ–L_1^* plane is divided into regions I–IX on the basis of $[R, C]$ (see Fig. 5.1 for details).

Figs. 5.1 and 5.2 display the stability boundaries obtained for a panel with movable edges, within the framework of the CPT and HSDT, respectively. The {0} solution is stable in I and loses its stability by divergence when going across the divergence boundary into II, and by flutter when going across the flutter boundary into IV. When going across into IV flutter occurs as the result of a Hopf bifurcation. However, as will be seen later, this is not the only mechanism for flutter. Stable non-trivial (buckled) equilibria {±1} exist in regions II and III. The critical buckling load for the CPT, obtained for $\lambda = 0$, is 4 (i.e., the classical Euler buckling load).

Results obtained by the CPT and HSDT for various values of $\frac{E_{<i>}}{G'_{<i>}}$ are compared in Fig. 5.3 where only the principal stability boundaries are shown. We see that the CPT overpredicts both instability loads (i.e., divergence and flutter), and is not sensitive to variations in the transverse shear flexibility of the panel. Furthermore, in contrast to the CPT results, those obtained by the HSDT show that an increase in the transverse shear flexibility of the panel (i.e., higher $\frac{E_{<i>}}{G'_{<i>}}$) yields lower instability loads. This behavior conforms to physical expectations. Figs. 5.4 and 5.5 obtained for the CPT and HSDT, respectively, show the effect of in-plane edge restraints applied along the edges $x_2 = 0, l_2$. We see that for a given λ, divergence occurs for lower values of $-L_1^*$ when the edges are immovable. This is due to the fact that the edge restraint induces in-plane compressive loads in the x_2 direction, thus causing the panel to buckle at a lower $-L_1^*$. Furthermore, the flow speed required to return a buckled panel to its flat stable configuration is higher when the edges are immovable. For this case, where the induced edge load is normal to the flow direction, the edge restraints have no visible effect on the flutter boundary.

CHAPTER 5. NUMERICAL RESULTS AND DISCUSSIONS

Imperfect panel

Figs. 5.6–5.9 show that for low values of $-L_1^*$ the (non-trivial) equilibrium becomes unstable as the result of a Hopf bifurcation and flutter ensues. For high values of $-L_1^*$, the loss of stability results in a jump either to flutter or a new buckled state (snap-through). This region is marked with dots in Figs. 5.6–5.9. Results obtained by the HSDT in Fig. 5.6 show that for a given flow speed the compressive load at which instability occurs is higher for a panel possessing greater transverse shear rigidity. As in the case of perfect panels, the CPT predicts the highest instability loads and does not model the effect of variations in transverse shear rigidity. An interesting feature is that for a certain range of L_1^* three distinct flutter speeds exist.

Fig. 5.7 shows that for low values of compressive loads (< 4.0) the flutter speeds are slightly lower when the panel is restrained along the edges parallel to the flow. This is in contrast to the results obtained for the perfect panel for which the edge restraints had no visible effect on the flutter boundary. The effect of aerodynamic nonlinearities are displayed in Fig. 5.8. Here we see that for small edge loads the inclusion of aerodynamic nonlinearities yields higher flutter speeds. However, for high edge loads, as the flow speed is increased, the flutter speed predicted by the aerodynamically nonlinear model is lower than that obtained using linear aerodynamics. Moreover, the aerodynamically linear model does not yield multiple flutter speeds. These may occur when considering the aerodynamic nonlinearities in which case, starting from different stable points in the λ–L_1^* plane for a given compressive load and then varying the flow speed could result in more than one speed at which flutter instability occurs. This is physically possible, e.g., when starting from various values of the flow speed which are held constant while the edge load is varied upto a certain common value and subsequently varying only the flow speed for each case. Fig. 5.9 shows that as the flow speed is increased, a panel with a greater imperfection (in the first mode) flutters at a lower speed when the compressive load is small to moderate (except, for the HSDT case, within a small region of L_1^*, i.e., between the leftmost points of vertical tangency of the two curves). For higher edge loads this trend is reversed, with marginal differences in

the instability speeds.

5.2 Effect of Aerodynamic Nonlinearities on Post-Flutter Behavior

The amplitudes and frequency of flutter were obtained by using the HSDT model for a panel with movable edges. Unless stated otherwise, the results discussed within this section pertain to a nonlinear aerodynamic model of a perfect, rectangular panel ($\phi = 0.5$) without edge loads. The amplitudes and frequency of flutter obtained by the MMS (eqn. $(4.37)_{1,2,3}$) are compared with those obtained by the NIM2. Henceforth, in the discussions, figures, and tables the flutter amplitude is loosely referred to as z_1.

The results shown in Figs. 5.10–5.21 were obtained using a 2×2 mode analysis, an aerodynamically linear theory with flow past both faces, flow orientation $\Lambda = 30^o$, and $\frac{l_1}{h} = 24$. Upon comparing the results obtained by the NIM2 and MMS, displayed in Figs. 5.10 and 5.11, we see that the NIM2 yields higher amplitudes and lower frequency of flutter. This conforms to the work of Morino and Kuo [37] wherein the flutter amplitudes obtained by a 5th-order perturbation analysis (which, just like the NIM2, is more accurate) are higher than those obtained via a 3rd-order analysis. Moreover, as λ increases, the non-linearity becomes stronger, thus yielding bigger differences in the results predicted by the two methods. In Fig. 5.11 the frequency variation predicted by the NIM2 is almost linear whereas the MMS result is exactly linear. This trend seems typical for flat panels exposed to a supersonic flow (see Dowell [22], Kuo et al. [36]) but not for shells (see Gordon and Atluri [21]). Since bifurcations of the periodic solution cannot be predicted by the MMS for the problem considered herein, the comparison between the two methods is terminated at the symmetry breaking bifurcation point.

The results displayed in Figs. 5.12–5.21 were obtained by the NIM2. Fig 5.12 shows the z_1 versus λ curve, going into the deep post-flutter range. Flutter oscillations start at $\lambda_F = 57.9410$ at which point the trivial equilibrium **y** undergoes a Hopf bifurcation and a symmetric limit cycle **z** is born. At $\lambda = 68.3410$ a symmetry breaking bifurcation

occurs with the stable symmetric solution (SS) losing its stability to a stable symmetry broken (SB) solution. Fig. 5.13 shows the phase trajectories of typical SS and SB solutions. Fig. 5.14 shows that the frequency spectrum of the SB solution includes the fundamental frequency (≈ 3.0079 Hz) and its second harmonic. We note that the frequency spectrum also includes the higher harmonics which do not appear in Fig. 5.14 due to the frequency range considered therein. A small DC (zero frequency) component is also present but this is only visible when the amplitudes in the frequency spectrum are plotted in the logarithmic scale (not shown here). At $\lambda = 78.9410$ a period-doubling bifurcation occurs with the SB solution losing its stability to a period-doubled (P2) solution. Figs. 5.15 and 5.16 show the phase trajectory and frequency spectrum for a typical P2 motion. The frequency spectrum contains the fundamental frequency, its sub- and higher- harmonics, and the DC component which is more pronounced now.

At $\lambda = 81.365497$ the P2 solution loses its stability as the result of a transverse crossing of the unit circle (in the complex plane) by two complex conjugate Floquet multipliers, and quasiperiodic motion (QPM) ensues. Thus we revert to the NIM1 in order to obtain the QPM. The Poincaré sections and frequency spectrum of typical QPM's are shown in Figs. 5.17–5.19. Fig. 5.17 shows the transition from P2 motion to QPM, i.e., the transformation of two discrete points into two closed loops. Fig. 5.19 shows that the frequency spectrum for QPM contains sidebands around the fundamental frequency and its higher- and sub- harmonics, thus indicating the presence of additional, incommensurable frequencies. The Lyapunov exponents and associated dimension, shown in Table 5.46, indicate that the motion is 2-period quasiperiodic, i.e., motion on a T^2 torus.

Continuing along the unstable symmetric solution (US) that exists beyond the symmetry breaking bifurcation point, we see that it regains its stability at $\lambda = 92.6404$ which is the second symmetry breaking bifurcation point. For a reverse sweep of λ, at $\lambda = 92.5410$ the NIM2 converges to the US solution only. However, the NIM1 yields a phase trajectory (not shown) which shows bounded, non-periodic motion between the US and two neighboring unstable symmetry broken (USB) limit cycles. Figs. 5.20 and 5.21 show a Poincaré section

and frequency spectrum for this case. The Poincaré section has a pattern emerging and the frequency spectrum is broad-banded. Furthermore, the Lyapunov exponents and associated dimension shown in Table 5.46 indicate the motion to be chaotic. This type of chaos conforms to the conjecture advanced by Dowell [45], which states that chaotic motion could emerge when all coexisting equilibria (static or dynamic) are unstable.

Results displayed in Figs. 5.22–5.24 pertain to the 4×1 mode analysis of a panel with flow orientation $\Lambda = 0°$. Fig. 5.22 shows the variation of nondimensional flutter speed (λ_0) with thickness ratio $(\frac{l_1}{h})$ for the cases of flow past the upper face and flow past both faces. We note that even though λ_0 increases with $\frac{l_1}{h}$ the actual dimensional flutter speed decreases (see $(B.2)_4$). The coefficient $\frac{k_1}{k_1}$, appearing in the MMS solution $(4.37)_1$, is shown in Fig. 5.23 for flow past the upper face, and Fig. 5.24 for flow past both faces. Based on discussions in Section 4.2, the regimes of hard (soft) flutter are demarcated on the basis of whether $\frac{k_1}{k_1}$ is positive (negative) which corresponds to a subcritical (supercritical) Hopf bifurcation. Fig. 5.23 shows that hard flutter is only possible for $\frac{l_1}{h} \leq 15$. A comparison of the aerodynamically linear and nonlinear theories presented in Fig. 5.24 indicates that linear aerodynamics does not yield the hard flutter phenomenon, whereas the aerodynamically nonlinear model yields hard flutter for $\frac{l_1}{h} \leq 75$. As $\frac{l_1}{h}$ increases, the difference in $\frac{k_1}{k_1}$ predicted by the aerodynamically linear and nonlinear models diminishes. This implies that the aerodynamically linear model correctly predicts the immediate post-flutter behavior of thin panels only. The result that thick panels experience hard flutter was also obtained by Librescu [5,6] based on a method due to Bautin [7].

Figs. 5.25–5.27 show the corresponding results for a 2×2 mode analysis of a panel with flow orientation $\Lambda = 30°$. Comparing Figs. 5.25 and 5.22, we see that for thin panels the variation of λ_0 with $\frac{l_1}{h}$ is small when $\Lambda = 0°$, but quite large when $\Lambda = 30°$. Fig. 5.27 shows that for flow past the upper face, hard flutter occurs only within the range $45 \leq \frac{l_1}{h} \leq 55$.

The flutter amplitude and bifurcation behavior, obtained by the NIM2, for a 2×2 mode analysis with $\Lambda = 30°$ are shown in Figs. 5.28–5.30. Figs. 5.28 and 5.30 pertain to the case of flow past both faces for panels with thickness ratio 100 and 50, respectively.

Fig. 5.28 shows that a supercritical Hopf bifurcation occurs at $\lambda = \lambda_0 = 84.25$; the resulting SS solution undergoes a symmetry breaking bifurcation at $\lambda = 139.45$; and the resulting SB solution undergoes a secondary Hopf bifurcation at $\lambda = 148.15$, yielding QPM. The US solution regains its stability at $\lambda = 155.65$, which is the second symmetry breaking bifurcation point, and the resulting SS solution appears to approach a turning point at $\lambda \approx 160.45$. However, the continuation of this branch around the turning point could not be obtained. Fig. 5.30 shows that a subcritical Hopf bifurcation occurs at $\lambda = \lambda_0 = 74.49$ prior to which US motions coexist with the stable $\{0\}$ state. This implies that hard flutter motion occurs for $\lambda > \lambda_0$, although the steady state solution describing it could not be obtained by either the NIM1 or NIM2. However, we see that if the $\{0\}$ state is appropriately disturbed, violent motions could occur for pre-critical speeds, i.e., for $\lambda < \lambda_0$. This is in contrast to the results obtained when the similar case is analyzed using linear aerodynamics, in which case hard flutter motion is not possible.

Fig. 5.29 reconsiders the case presented in Fig. 5.28 for flow past the upper face of the panel. Soft flutter, i.e., stable nonsymmetric (SN) periodic motion, ensues as the result of a supercritical Hopf bifurcation occurring at $\lambda = 161.03$. A period-doubling bifurcation occurs at $\lambda = 195.13$ and the resulting P2 solution undergoes a secondary Hopf bifurcation at $\lambda = 202.83$, thus yielding QPM. Continuing on the unstable nonsymmetric solution past the period-doubling bifurcation, we see that it approaches a turning point at $\lambda \approx 202.83$, i.e., the same value as that at which the secondary Hopf bifurcation occurs on the P2 solution. However, both the NIM1 and NIM2 did not yield a continuation of this branch around the turning point, nor could they yield any periodic states for $\lambda > 202.83$.

Fig. 5.31 presents a comparison of results obtained by a 2×1 and 4×1 mode analysis of flow past both faces with $\Lambda = 0°$ and $\frac{l_y}{l_x} = 50$. Both analyses indicate that hard flutter motion occurs, although the steady state solution describing it could not be obtained. An interesting result of the 4×1 mode analysis is that, for $67.11 \leq \lambda \leq 99.81$, a secondary US branch coexists with the primary one that starts from $\lambda = \lambda_0 = 170.89$. Unstable limit cycles for $\lambda = 90.09$, obtained by integrating from initial conditions on the primary and

secondary US branches, are shown in the insets.

Results for a 4×1 mode analysis of a square, imperfect panel, with $\frac{l_1}{h} = 50$, subjected to flow past both its faces in the x_1 direction and an in-plane compressive load $L_1^* = -5.3$, were obtained using nonlinear and linear aerodynamics. For the aerodynamically linear model a supercritical Hopf bifurcation occurs at $\lambda = 39.980088$ with $y_1 = 0.1164$. The corresponding result obtained by using nonlinear aerodynamics will be seen in Fig. 5.43. The results for the ensuing motion using nonlinear and linear aerodynamics are summarized in Tables 5.11 and 5.17, respectively. For both cases the motion starts off as stable nonsymmetric (SN) and then goes through a sequence of period-doublings. Although a true comparison of flutter amplitudes cannot be made, since the flutter speeds are different for the two cases, it appears that the aerodynamically nonlinear model yields higher amplitudes.

5.3 Effect of In-plane Edge Loads and Flutter of Buckled Panels.

Unless stated otherwise, the results discussed in this section pertain to a 4×1 mode, aerodynamically nonlinear analysis of a square panel with movable edges and $\frac{l_1}{h} = 50$, subjected to flow past both faces (with $\Lambda = 0^o$) and a unidirectional compressive edge load L_1^*. Both perfect and imperfect panels were analyzed using the CPT and HSDT, and results were obtained by the NIM2 and NIM1.

Imperfect panel

The region in the $\lambda - L_1^*$ plane where the transition from Hopf-bifurcation instability to jump-type instability occurs was studied (i.e., transition to the region marked with dots in Fig. 5.6).

CPT results

Fig. 5.32 shows the static equilibrium state of the panel as λ is varied, with $L_1^* = -6.1$. As the flow speed is increased, the panel tends to flatten out until a Hopf bifurcation (H) occurs, resulting in soft flutter oscillations about the non-trivial static equilibrium. The periodic motion starts off as stable nonsymmetric (SN) and undergoes a

sequence of period-doubling bifurcations, yielding period-2 (P2) up to period-32 (P32) motion. These results are summarized in Table 5.1. Fig. 5.33 shows phase trajectories for typical P1 up to P8 motions, and Fig. 5.34 shows the corresponding frequency spectra. Fig. 5.35 shows a Poincaré section for a value of λ just beyond the P32 motion value, and Fig. 5.36 shows the corresponding frequency spectrum which is broad-banded. The Lyapunov exponents and associated dimension for this case are shown in Table 5.46. Based on these results, it appears that chaotic motion has resulted after a sequence of period-doublings. Fig. 5.37 shows the static solution for $L_1^* = -6.3$. Motion about TP1 and motion past H, summarized in Tables 5.2 and 5.3, respectively, show that multiple periodic solutions and the static solution coexist within the range $40.4544 \leq \lambda \leq 41.0225$. Holmes [49] made similar observations when analyzing the cylindrical bending of a perfect panel. He concluded that a region in the λ–L_1^* plane exists in which multiple attracting solutions coexist, i.e., the panel can remain buckled or flutter. Fig. 5.38 shows phase trajectories for nonsymmetric motion about TP1.

The static solution for $\lambda = 35$ with L_1^* varying is shown in Fig. 5.39. Table 5.4 summarizes the UN motion obtained prior to H1, thus indicating that violent flutter motions are possible. Table 5.5 summarizes the motion prior to H2, which starts off as SN before bifurcating to QPM. Table 5.6 summarizes the motion past H3, which undergoes a sequence of period-doublings. An interesting feature is that UN motion about H3, summarized in Table 5.7, was found to coexist with the stable motions in Table 5.6. Bounded motions about TP1 could not be obtained. Fig. 5.40 shows the static solutions for $\lambda = 37$ and 43. For $\lambda = 37$, motion past H and motion about TP1 are summarized in Tables 5.8 and 5.9, respectively. Table 5.10 shows that the motion past H, for $\lambda = 43$, undergoes a sequence of period-doublings as L_1^* is increased. A Poincaré section for a value of L_1^* which is well past the P8 motion value is shown in Fig. 5.41. Fig. 5.42 shows the associated frequency spectrum which is broad-banded. Based on these results and the Lyapunov exponents and associated dimension shown in Table 5.46, it appears that the motion is chaotic.

HSDT results

Fig. 5.43 shows the static solution for $L_1^* = -5.3$ and -5.4 with λ varying. The motion past H for these two cases, summarized in Tables 5.11 and 5.12, undergoes a sequence of period-doubling bifurcations. Furthermore, for $L_1^* = -5.4$, when going past TP1 the solution obtained by the NIM1 was the same as that obtained for motion past H. The static solution for $\lambda = 32$ and 42 with L_1^* varying is shown in Fig. 5.44. For $\lambda = 32$, the motions past H and TP1 are summarized in Tables 5.13 and 5.14, respectively. For $\lambda = 42$ the motion past H is summarized in Table 5.15. A comparison of the numerical data pertaining to Fig. 5.40 ($\lambda = 43$) and Fig. 5.44 ($\lambda = 42$) shows that, as L_1^* is increased, the CPT yields larger stable static equilibrium solutions than the HSDT. However, it appears that the HSDT predicts higher amplitudes of flutter oscillations past TP1 than the CPT (compare Tables 5.9 and 5.14).

With $L_1^* = 0$, as λ is increased a supercritical Hopf bifurcation occurs for $y = \{-0.3914, -0.0561, 0.0065, -0.0166\}^T$ at $\lambda = 281.0285$, resulting in SN periodic motion which undergoes a period-doubling bifurcation. The results are summarized in Table 5.16.

Perfect panel

The region in the $\lambda - L_1^*$ plane where the divergence and flutter boundaries meet was studied (see Fig. 5.3). The motivation for this choice of parameter space is the work of Holmes [49], wherein it was noted that complex dynamic solutions may coexist with buckled equilibria in this region.

CPT results

Fig. 5.45 shows the static and dynamic solution (y, z_1) for $L_1^* = -5.5$ as λ is varied. We see that the buckled panel becomes flat, following which SS periodic motion occurs about the flat configuration. The static solutions for $L_1^* = -5.8$ and -6.2 are shown in Fig. 5.46. For $L_1^* = -5.8$, a Hopf bifurcation occurs for the $\{0\}$ solution. The resulting SS solution undergoes a sequence of period-doublings (summarized in Table 5.18). The motion past TP was obtained for $\lambda = 36.8456$ and $\lambda = 36.9456$. For $\lambda = 36.8456$, the

CHAPTER 5. NUMERICAL RESULTS AND DISCUSSIONS

Poincaré section, frequency spectrum, and phase trajectory (shown in Figs. 5.47, 5.49, and 5.50, respectively) indicate that the motion is periodic. The limit cycle shown in Fig. 5.50 indicates the existence of multiple unstable equilibria (i.e., the trivial and other non-trivial fixed points) about which motion occurs. Similar limit cycles were obtained by Sipcic and Morino [40] and Dowell [44]. For $\lambda = 36.9456$, the Poincaré section, frequency spectrum, and Lyapunov exponents and associated dimension (shown in Figs. 5.48, 5.51, and Table 5.46, respectively) indicate that the motion is chaotic. A similar transition from periodic to chaotic motion was observed by Dowell [44]. Furthermore, comparing the value of λ at TP (≈ 36.7, see Fig. 5.45) with the value at which the Hopf bifurcation for $\{0\}$ occurs (≈ 35.11, see Fig. 5.3), we see that a stable non-trivial static equilibrium state exists beyond the flutter boundary. For $L_1^* = -6.2$, the motion past TP was obtained for $\lambda = 34.8739$. The Poincaré section, frequency spectrum, and Lyapunov exponents and associated dimension (shown in Fig. 5.52, 5.53 and Table 5.46, respectively) indicate that the motion is chaotic.

The static solution for $\lambda = 25$ with L_1^* varying is shown in Fig. 5.54. The motion past H1, H2 and H3 is summarized in Tables 5.19, 5.20 and 5.21, respectively. However, these results are of academic interest only, since the values of L_1^* required to cause flutter are too high. Bounded motions about TP1 could not be obtained. For $\lambda = 34$, the static solution is shown in Fig. 5.55. For the motion past TP1, the Poincaré section, frequency spectrum, and Lyapunov exponents and associated dimension (shown in Figs. 5.56, 5.57, and Table 5.46, respectively) indicate that the motion is chaotic. The motion past the supercritical Hopf bifurcation point for the trivial solution (i.e., H$\{0\}$), summarized in Table 5.22, starts off as SS and subsequently undergoes a symmetry breaking and period-doubling bifurcation. These results indicate that the panel could remain buckled or flutter beyond H$\{0\}$. For $\lambda = 39$, only the $\{0\}$ static solution exists. Motion about H$\{0\}$ is summarized in Table 5.23.

CHAPTER 5. NUMERICAL RESULTS AND DISCUSSIONS

HSDT results

Fig. 5.58 shows the static solution for $L_1^* = -4.7, -4.8, -4.9$, and -5.0 when λ is varied. It also shows the motion past H{0} for $L_1^* = -4.7, -4.8$, and -4.9. The motion past H{0} for $L_1^* = -5.0$ is summarized in Table 5.24. In contrast to the motion past H{0} for the other three values of L_1^*, in this case the motion undergoes a sequence of period-doublings. We see that for $L_1^* = -4.9$ and -5.0 there exists a range of λ for which the panel can either stay buckled or flutter.

A comparison of flutter amplitude and frequency, obtained by the MMS and NIM2 for motion about H{0} when $L_1^* = -4.8$, is presented in Figs. 5.59 and 5.60, respectively. Even though the basic trend, i.e., NIM2 predicting higher amplitudes and lower frequencies, remains the same as that obtained for the aerodynamically linear model without compressive loads (see Figs. 5.10 and 5.11), the quantitative differences are large except in the immediate post-flutter range. Moreover, the frequency variation predicted by the NIM2 is nonlinear. We see that the NIM2 yields an inexplicable discontinuity at $\lambda = 36.8480$, i.e., a sudden drop (rise) in amplitude (frequency). However, there is no reason to doubt these results since convergence to a periodic solution was obtained, albeit after a larger-than-usual number of iterations.

The solution past TP for $L_1^* = -4.8$ gets attracted to {0}, whereas for $L_1^* = -4.9$ it gets attracted to the corresponding branch originating from H{0}. For $L_1^* = -5.0$, the motion past the TP was obtained for $\lambda = 26.8543$ and 26.9443. For $\lambda = 26.8543$ the Poincaré section, frequency spectrum, and Lyapunov exponents and associated dimension (shown in Figs. 5.61, 5.63, and Table 5.46, respectively) indicate that the motion is chaotic. Periodic motion about multiple unstable equilibria occurs when $\lambda = 26.9443$, as indicated by the Poincaré section, frequency spectrum, and phase trajectory, shown in Figs. 5.62, 5.64, and 5.65, respectively.

For $\lambda = 18$ with L_1^* varying, the static solution is shown in Fig. 5.66. No bounded motion past TP1 could be obtained. However, when investigating the dynamics prior to TP2 the solution converged to a new static configuration. This result was then used as a

starting point in the ACM which yielded the isolas shown in Fig. 5.67. This result implies that multiple buckled configurations of the panel are possible, i.e., the primary one of Fig. 5.66 and the secondary one of Fig. 5.67. Hence, as $-L_1^*$ is increased the panel would snap-through to the secondary configuration. Thereafter, decreasing $-L_1^*$ would make it snap back to the primary state, whereas increasing $-L_1^*$ would lead to flutter about H1 (see Fig. 5.67). However, the motion about the Hopf bifurcation points and turning points in Fig. 5.67 was not studied due to the large compressive loads involved which would yield results of little practical importance.

The static solution for $\lambda = 24$ is shown in Fig. 5.68. The motion past the supercritical Hopf bifurcation point at $\{0\}$ is summarized in Table 5.25. This indicates that for a certain range of the compressive load, the panel can remain buckled or flutter about $\{0\}$. Hard flutter oscillations are possible about H1, H2, and H3. The UN motions prior to H1, and H3, and past H2, are summarized in Tables 5.26, 5.29, and 5.28, respectively. Stable motions that occur prior to H4 are summarized in Table 5.30. The numerical data indicate that for a small region prior to TP1, the panel could stay buckled or flutter as shown in Table 5.30.

Using the NIM1, quasiperiodic motions representing hard flutter were obtained about H1. These are shown in Figs. 5.69 and 5.70 for values of compressive loads past and prior to H1, respectively. Continuing past H1 on this branch of QPM's, as $-L_1^*$ is increased the motion becomes periodic (SN). As $-L_1^*$ is increased further, the NIM2 yields a sequence of period-doubling bifurcations followed by a secondary Hopf bifurcation that results in QPM once again. These results are summarized in Table 5.27. An interesting feature is the appearance of wrinkles in the Poincaré sections (see Fig. 5.69), which is indicative of impending chaos via the Torus-Bifurcation route (see Swinney [76]). However, chaotic motions were not obtained in this case. Continuing prior to H1 on the branch of QPM's, as $-L_1^*$ is decreased the Poincaré section reduces in size until all motion ceases, i.e., the fluttering panel snaps back to the buckled equilibrium. Comparing the numerical data pertaining to the buckled solution shown in Fig. 5.54 ($\lambda = 25$)

with that of Fig. 5.68 ($\lambda = 24$), it appears that as L_1^* is increased the CPT yields larger displacements than the HSDT (a similar observation was made when comparing Fig. 5.40 with 5.44).

Fig. 5.71 shows the static solution for $\lambda = 27$ and L_1^* varying. The motion past the Hopf bifurcation point at $\{0\}$ is summarized in Table 5.31. This reveals that the buckled state and flutter motion coexist for certain compressive loads. Poincaré sections pertaining to the motion past TP were obtained for $L_1^* = -4.9652$ and -4.9752. They have the same structure as that in Fig. 5.48, thus indicating that chaotic motions exist past TP.

5.4 Effect of In-plane Edge Restraints on Post-flutter Behavior.

Unless stated otherwise, the cases considered in this section are for a 4×1 mode analysis of a square panel with $\frac{l}{h} = 50$, subjected to flow past both faces (with $\Lambda = 0$) and unidirectional compressive edge loads L_1^*, using the aerodynamically nonlinear model.

Fig. 5.72 shows the flutter amplitudes for a perfect panel with the edges $x_1 = 0\,, l_1$ considered either movable or immovable. For all cases, the edges $x_2 = 0\,, l_2$ are movable. Various values of $\frac{l_1}{h}$ (i.e., 50, 75, and 100) were considered, with $L_1^* = 0$. The results show that the amplitudes of soft flutter motion are higher when the edges $x_1 = 0\,, l_1$ are unrestrained (see results for $\frac{l_1}{h} = 100$). Furthermore, hard flutter motion for pre-critical speeds appears to result from smaller disturbances (of the flat state) when the edges are unrestrained rather than restrained (see results for $\frac{l_1}{h} = 50$). For the intermediate value of $\frac{l_1}{h} = 75$, hard flutter motion is possible only in the case of movable edges. Similar observations were made by Bolotin [1] when analyzing a two-dimensional panel of infinite span, undergoing cylindrical bending. Hence, we can conclude that panels with movable edges exhibit higher amplitudes of soft flutter (as λ is increased) and are more susceptible to hard flutter motion.

The remaining results discussed in this section are for a panel with edges $x_2 = 0\,, l_2$ being either movable or immovable and edges $x_1 = 0\,, l_1$ being movable.

Imperfect panel

CPT results

Fig. 5.73 shows the static solution when $-L_1^* = -5.8$ with λ varying. The motion past H is summarized in Tables 5.32 and 5.33 for the case of movable and immovable edges, respectively. The static solution when $\lambda = 48$ with $-L_1^*$ varying is shown in Fig. 5.74. We see that the static displacements (i.e., stable static solutions) are larger when the edges are immovable. Tables 5.34 and 5.35 summarize the motion past H for the case of movable and immovable edges, respectively.

HSDT results

For $-L_1^* = -4.9$ with λ varying, Fig. 5.75 shows the static solution, and Tables 5.36 and 5.37 summarize the motion past H for the case of movable and immovable edges, respectively. The static solution for $\lambda = 46$ with $-L_1^*$ varying, and associated motion past H for the movable and immovable cases, are shown in Fig. 5.76, and Tables 5.38 and 5.39, respectively. We see that the static displacements are larger for the panel with immovable edges (same as was obtained using the CPT). For the case of movable edges, the results indicate the existence of a turning point in the dynamic solutions. This implies that stable and unstable periodic motions coexist for a certain range of λ.

The results for imperfect panels appear to indicate that as λ is varied with L_1^* held constant, the panel with movable edges exhibits larger amplitudes of flutter. The converse is true when L_1^* is varied with λ held constant. However, these comparisons are not exact since the point at which flutter occurs differs for the two edge conditions.

Perfect panel

CPT results

Fig. 5.77 shows the static and dynamic solution for $L_1^* = -5.2$ with λ varying. We see that, as in the case of imperfect panels, the buckled state is lower when the edges are movable. For this case where the induced edge load is normal to the flow, the edge restraints have no visible effect on the critical speed and amplitudes of US motion that exists for pre-critical speeds (i.e., prior to the subcritical Hopf bifurcation H{0}.)

Tables 5.40 and 5.41 summarize the motions past H1 and prior to H2, respectively. The data shows that these two dynamic solution branches merge into each other. This implies that for the present case with immovable edges, as λ is increased, the buckled panel starts to flutter about the unstable non-trivial static equilibrium (i.e., the panel flutters in region II of Fig. 5.4 — see Holmes [49]). The amplitudes of flutter gradually increase and then decrease until flutter ceases and the buckled state is recovered. Increasing λ further would eventually lead to hard flutter oscillations about $\{0\}$. However, since hard flutter oscillations may occur prior to H$\{0\}$, we see that there exists a range of λ for which hard flutter motion about the flat state coexists with the buckled state or with soft flutter motion about the non-trivial equilibrium.

Fig. 5.78 shows the static solution for $\lambda = 50$ with L_1^* varying. We see that in the case of movable edges the panel remains flat prior to the subcritical Hopf bifurcation point H$\{0\}$. The amplitudes of US motion prior to H$\{0\}$ are summarized in Tables 5.42 and 5.43 for the case of movable and immovable edges, respectively, whereas those for motions past H1 and prior to H2 are summarized in Tables 5.44 and 5.45, respectively. From Tables 5.43 and 5.45, we see that there exists a range of L_1^* for which hard flutter motion about the flat state coexists with soft flutter motion about the non-trivial equilibrium.

HSDT results

Fig. 5.79 shows the static and dynamic solutions for $L_1^* = -4.5$ with λ varying. Once again we obtain a lower buckled state for movable edges. Fig. 5.80 shows the static and dynamic solutions for $\lambda = 40$ with L_1^* varying. For the case of movable edges the panel remains flat prior to experiencing flutter. For the cases pertaining to Figs. 5.79 and 5.80 no motion (i.e., $\{0\}$ solution) was obtained past TP. Furthermore, in the immediate post-flutter region the flutter amplitudes are not affected by edge restraints.
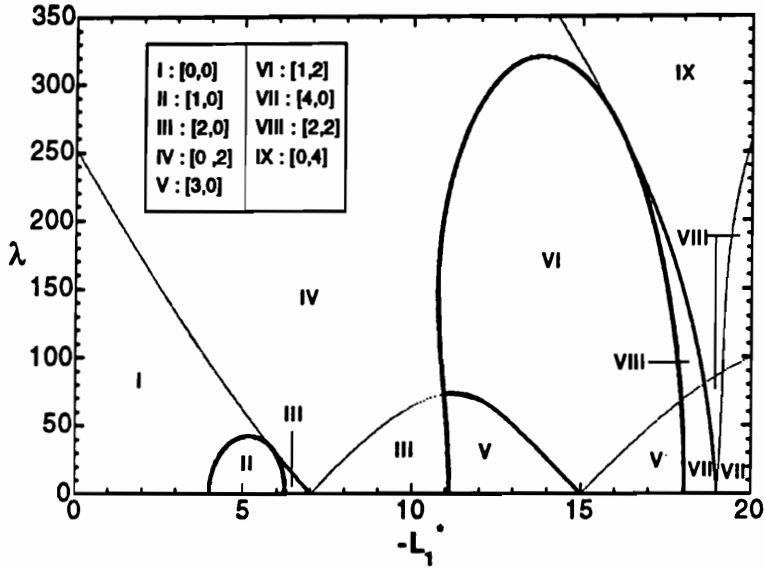
Figure 5.1: Stability boundaries for perfect panel; CPT; all edges movable ($\tilde{\alpha}_1 = \tilde{\alpha}_2 = 0$, $\delta_{M1} = \delta_{M2} = 1$).
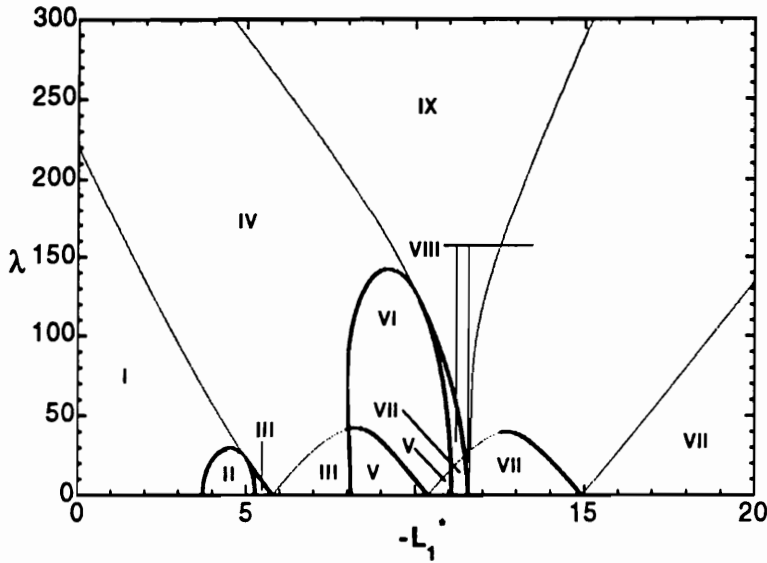

Figure 5.2: Stability boundaries for perfect panel; HSDT; $E_i/G'_i = 40$; all edges movable ($\delta_{M1} = \delta_{M2} = 1$, $\tilde{\alpha}_1 = \tilde{\alpha}_2 = 0$).
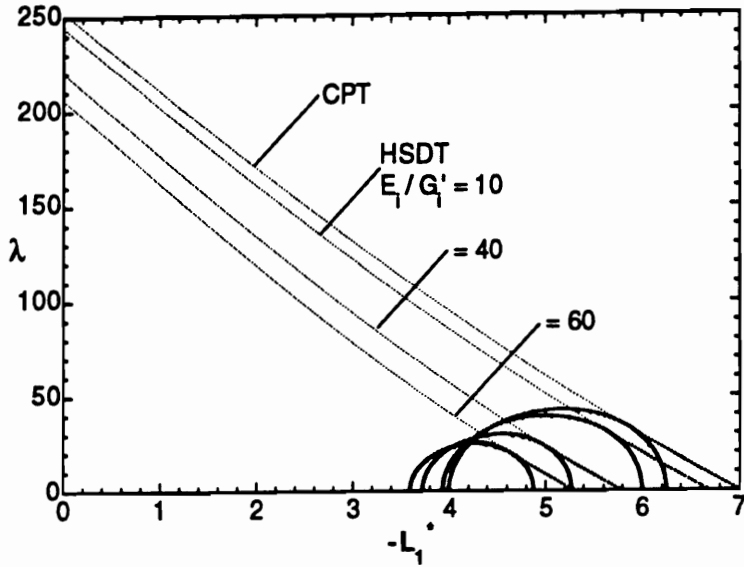
Figure 5.3: Effect of transverse shear flexibility on stability boundaries for perfect panel; all edges movable ($\delta_{M1} = \delta_{M2} = 1$, $\tilde{\alpha}_1 = \tilde{\alpha}_2 = 0$).
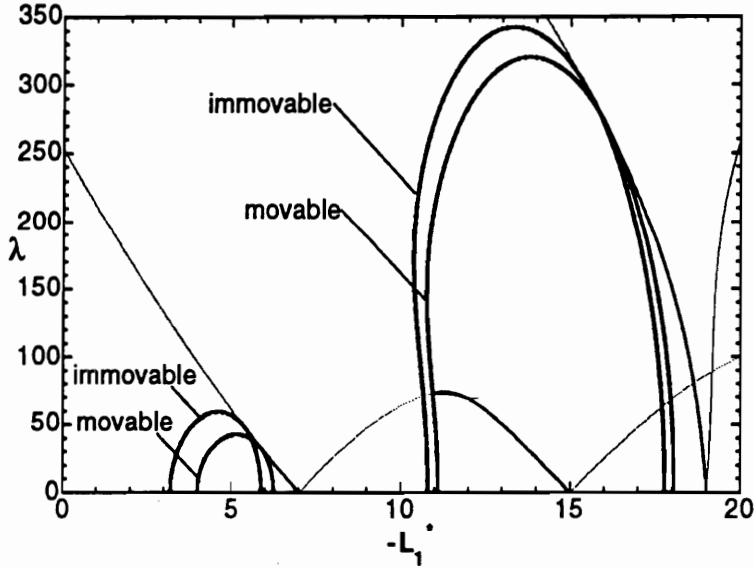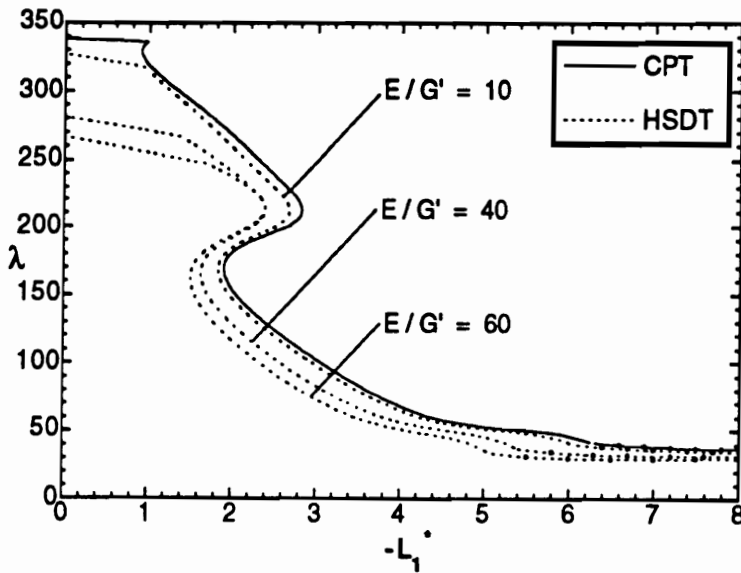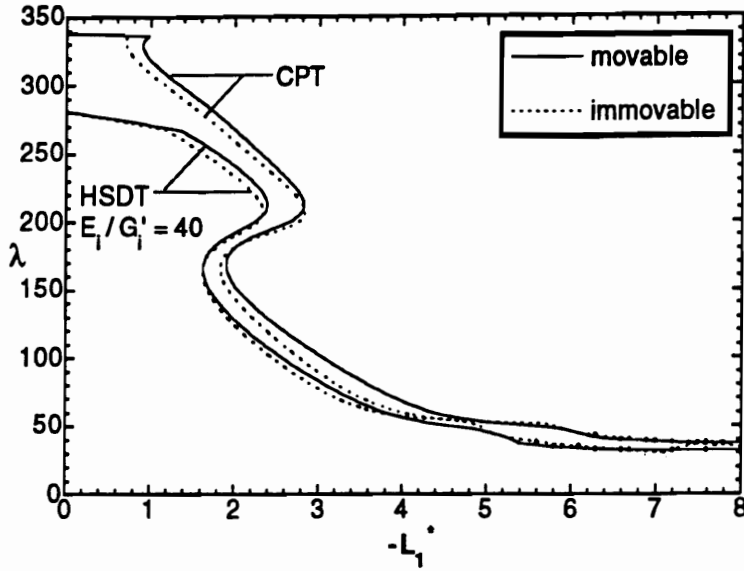

Figure 5.4: Effect of edge restraint on stability boundaries for perfect panel; CPT; edges $x_1 = 0$, l_1 movable ($\delta_{M1} = 1$, $\tilde{\alpha}_1 = 0$), edges $x_2 = 0$, l_2 movable ($\delta_{M2} = 1$, $\tilde{\alpha}_2 = 0$) or immovable ($\delta_{M2} = 0$, $\tilde{\alpha}_2 = 1$).

81
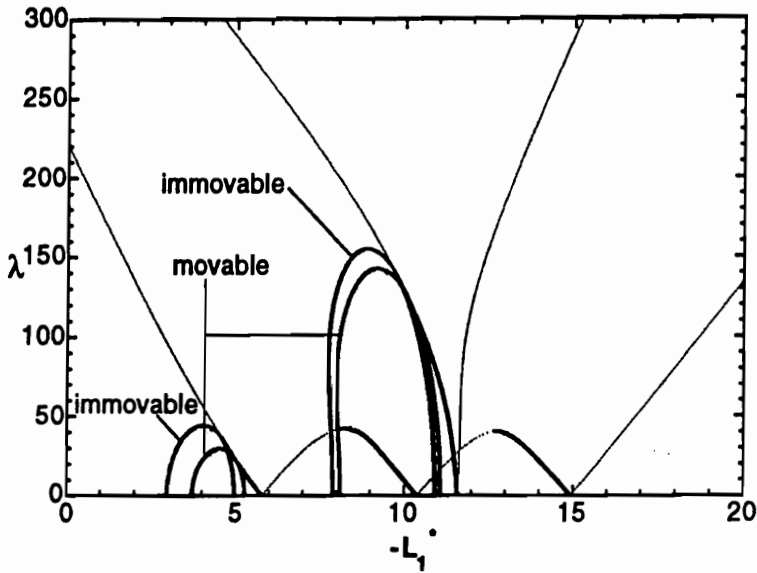
Figure 5.5: Effect of edge restraint on stability boundaries for perfect panel; HSDT; $E_i/G'_i = 40$; edges $x_1 = 0$, l_1 movable ($\delta_{M1} = 1$, $\tilde{\alpha}_1 = 0$), edges $x_2 = 0$, l_2 movable ($\delta_{M2} = 1$, $\tilde{\alpha}_2 = 0$) or immovable ($\delta_{M2} = 0$, $\tilde{\alpha}_2 = 1$).

Figure 5.6: Effect of transverse shear flexibility on stability boundaries for imperfect panel ($\hat{a}_{11} = 0.2$); all edges movable ($\delta_{M1} = \delta_{M2} = 1$, $\tilde{\alpha}_1 = \tilde{\alpha}_2 = 0$).

Figure 5.7: Effect of edge restraint on stability boundaries for imperfect panel ($\hat{a}_{11} = 0.2$); edges $x_1 = 0$, l_1 movable ($\delta_{M1} = 1$, $\tilde{\alpha}_1 = 0$), edges $x_2 = 0$, l_2 movable ($\delta_{M2} = 1$, $\tilde{\alpha}_2 = 0$) or immovable ($\delta_{M2} = 0$, $\tilde{\alpha}_2 = 1$).
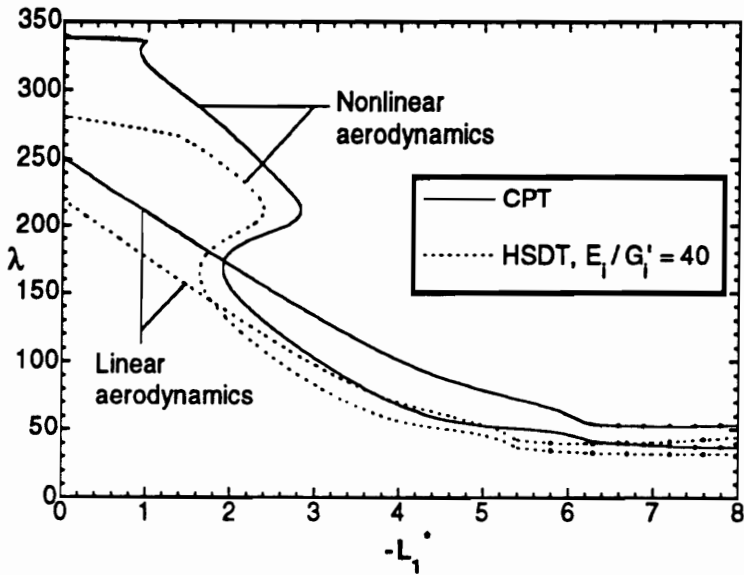

Figure 5.8: Effect of aerodynamic nonlinearities on the stability boundaries for imperfect panel ($\hat{a}_{11} = 0.2$); all edges movable ($\delta_{M1} = \delta_{M2} = 1$, $\tilde{\alpha}_1 = \tilde{\alpha}_2 = 0$).
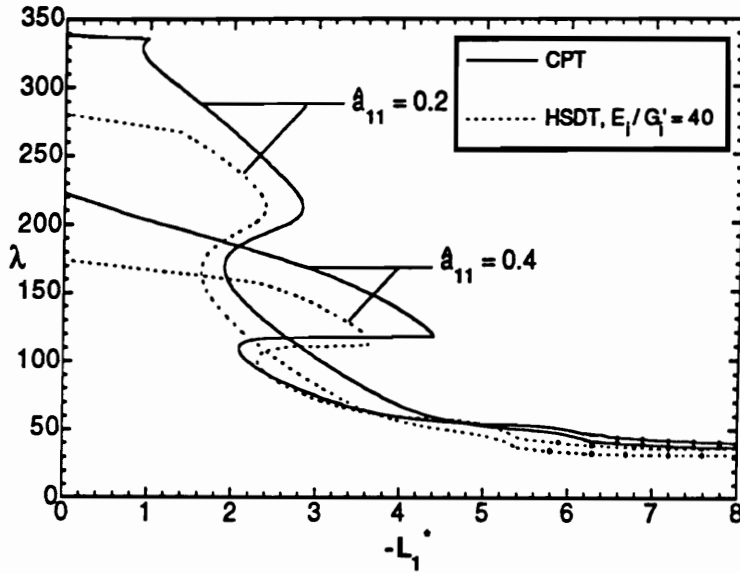
Figure 5.9: Effect of imperfections on the stability boundaries; all edges movable $(\delta_{M1} = \delta_{M2} = 1 \, , \, \tilde{\alpha}_1 = \tilde{\alpha}_2 = 0)$.
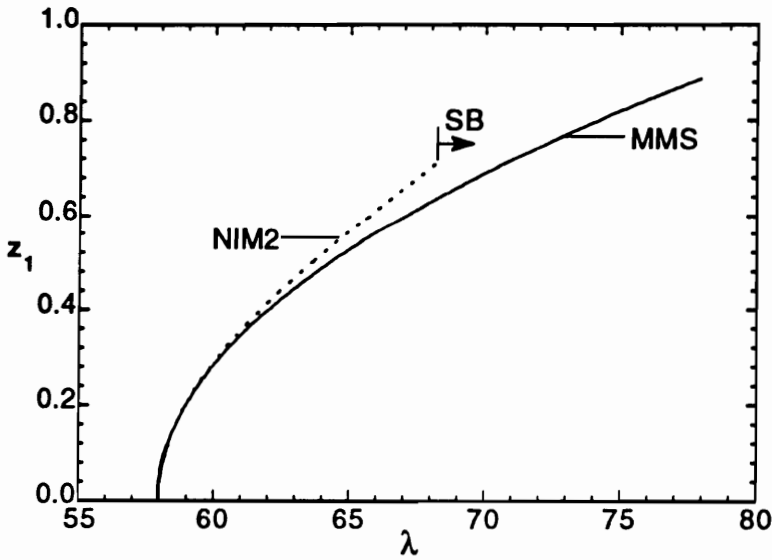

Figure 5.10: Comparison of flutter amplitude for perfect panel obtained by MMS and NIM2; flow past both faces $(\delta_F = 0 \, , \, \hat{\delta}_F = 2)$; linear aerodynamics; SB–symmetry broken periodic motion.
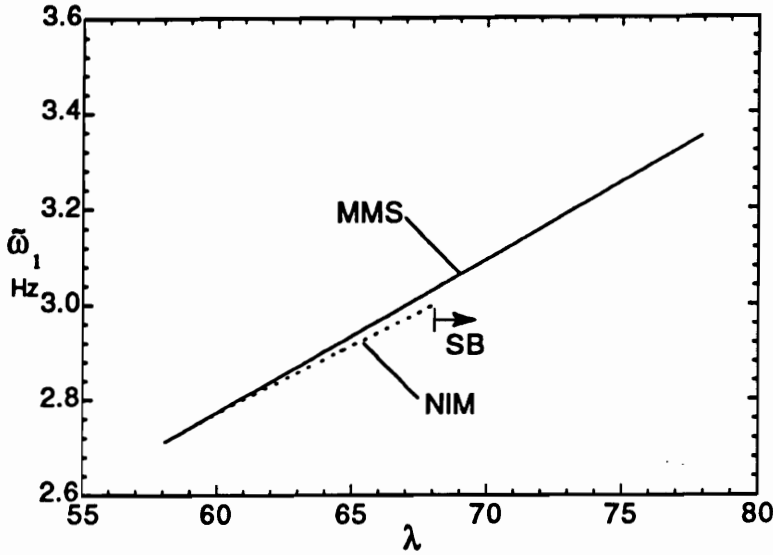
84

Figure 5.11: Comparison of flutter frequency for perfect panel obtained by MMS and NIM2; flow past both faces ($\delta_F = 0$, $\hat{\delta}_F = 2$); linear aerodynamics; SB–symmetry broken periodic motion.
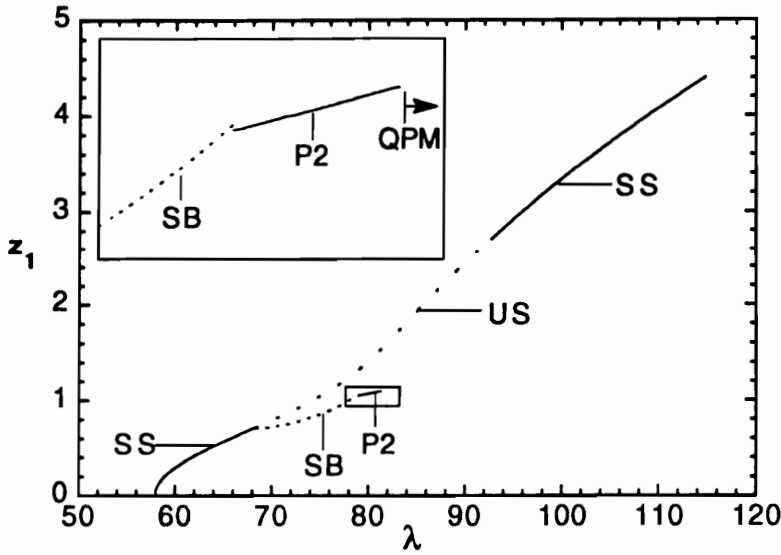

Figure 5.12: Flutter amplitude and bifurcation behavior for perfect panel; flow past both faces ($\delta_F = 0$, $\hat{\delta}_F = 2$); linear aerodynamics; stable periodic motions are: SS (stable symmetric), SB (symmetry broken), P2 (period-2); US–unstable symmetric; QPM–quasiperiodic motion.
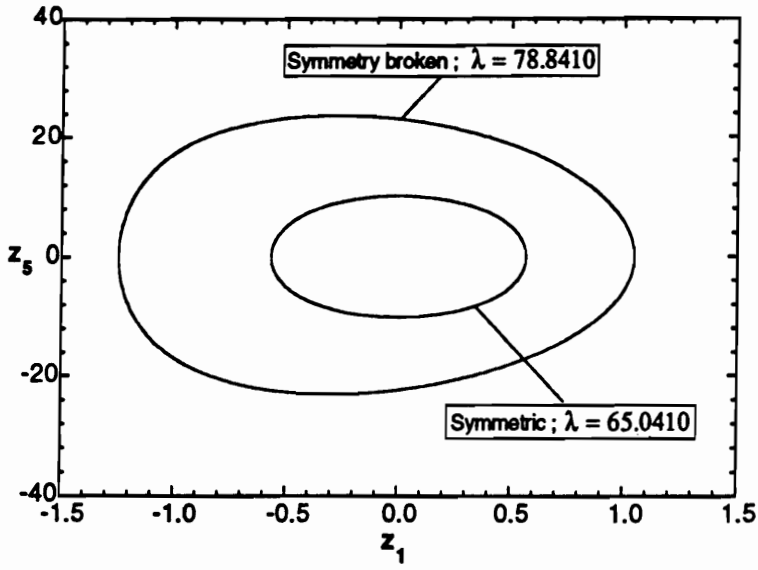
Figure 5.13: Phase trajectories: symmetric and symmetry broken limit cycles.
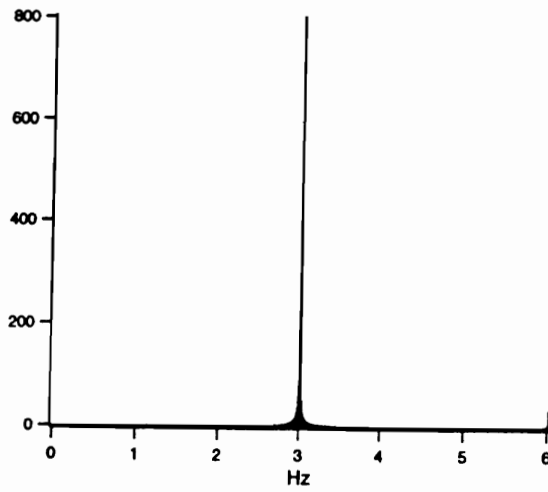
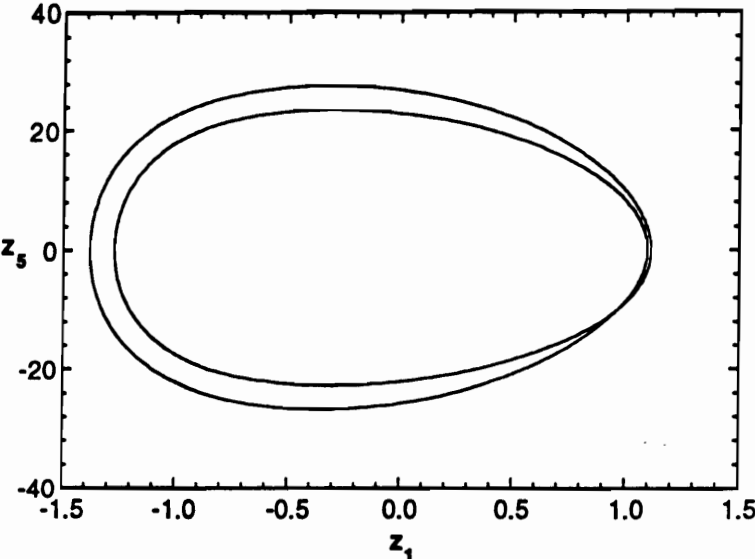Figure 5.14: Frequency spectrum of z_1 for symmetry broken motion ($\lambda = 78.8410$).

Figure 5.15: Phase trajectories: period-2 limit cycle ($\lambda = 81.3410$).
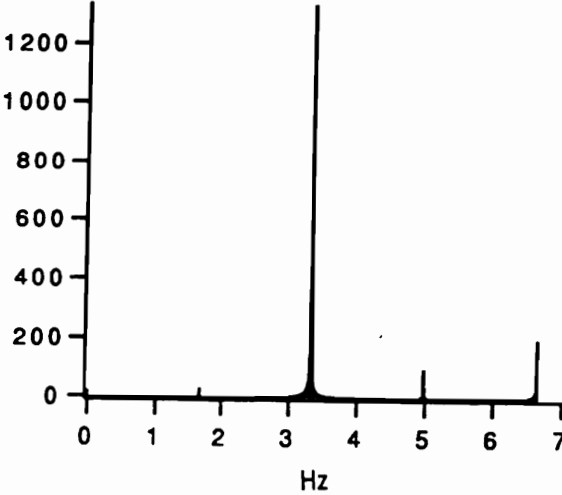
Figure 5.16: Frequency spectrum of z_1 for period-2 motion ($\lambda = 81.3410$).
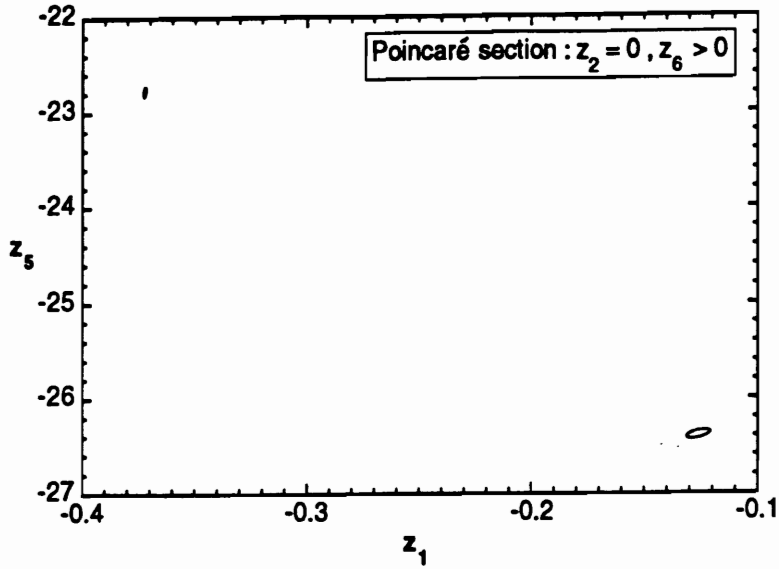
87

Figure 5.17: Poincaré section showing quasiperiodic motion ($\lambda = 81.365498$).
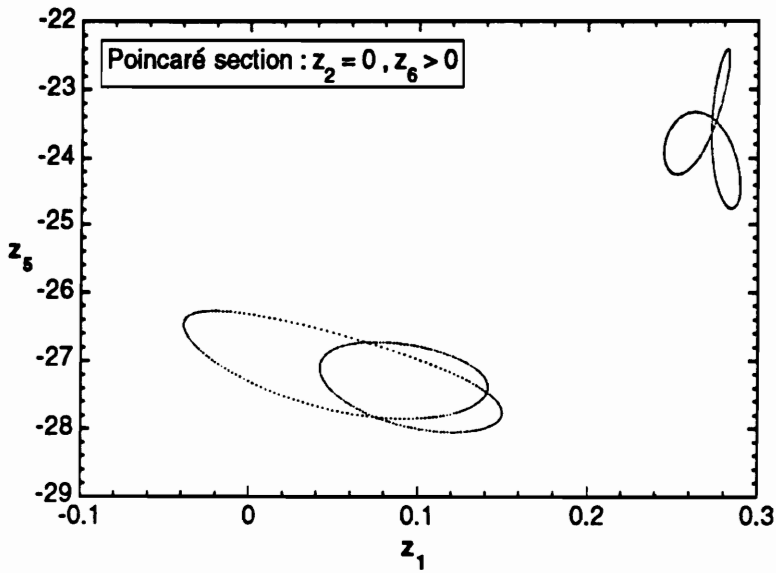
Figure 5.18: Poincaré section showing quasiperiodic motion ($\lambda = 81.365507$).

Figure 5.19: Frequency spectrum of z_1 for quasiperiodic motion ($\lambda = 81.365507$).
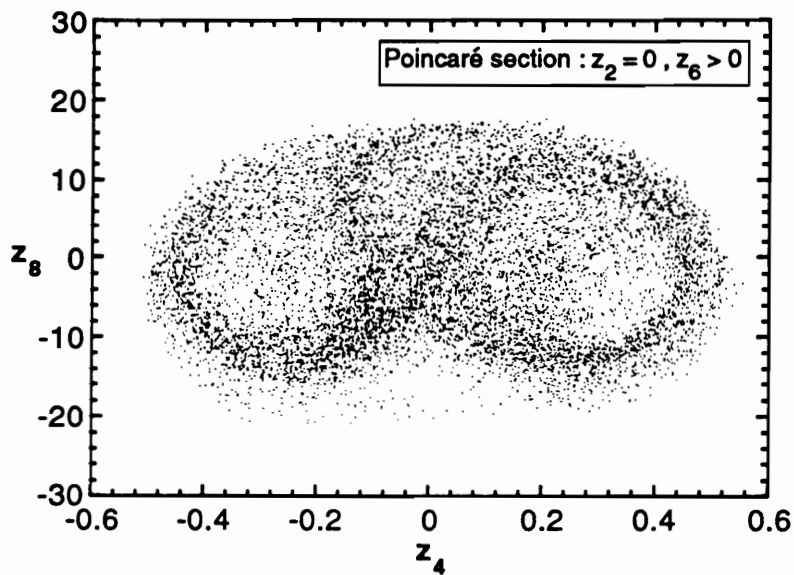
Figure 5.20: Poincaré section showing existence of strange attractor (chaotic motion) for $\lambda = 92.5410$.

89
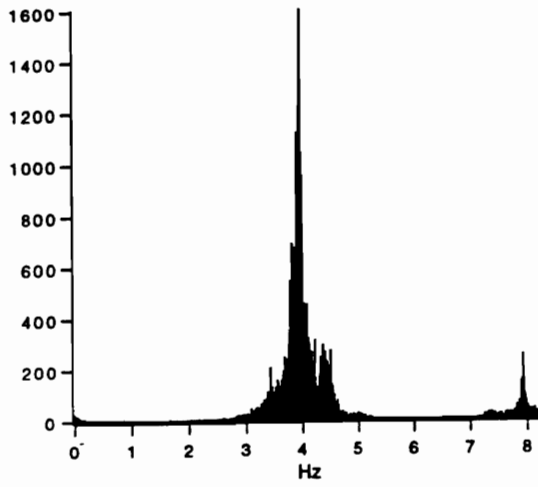
Figure 5.21: Frequency spectrum of z_1 for chaotic motion ($\lambda = 92.5410$).
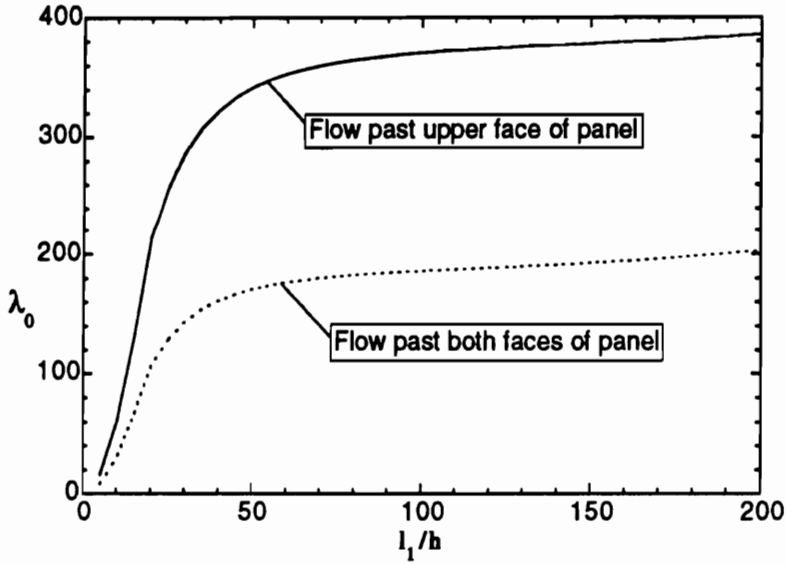
Figure 5.22: Variation of non-dimensional flutter speed with thickness ratio; perfect panel; $\Lambda = 0°$; 4×1 mode analysis.
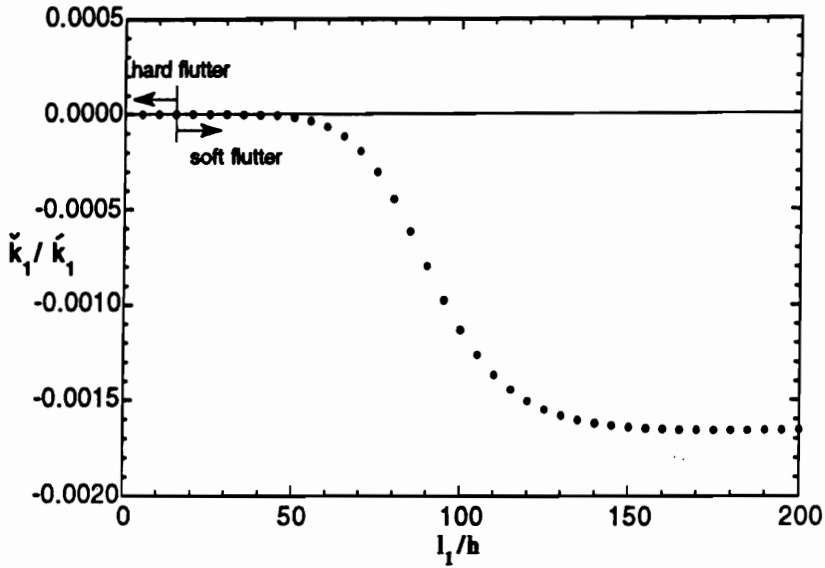
Figure 5.23: $\check{k}_1/\acute{k}_1$ for various thickness ratios—shows that aerodynamic nonlinearities may yield hard flutter; flow past upper face $(\delta_F = \hat{\delta}_F = 1)$; perfect panel; $\Lambda = 0$; 4×1 mode analysis.
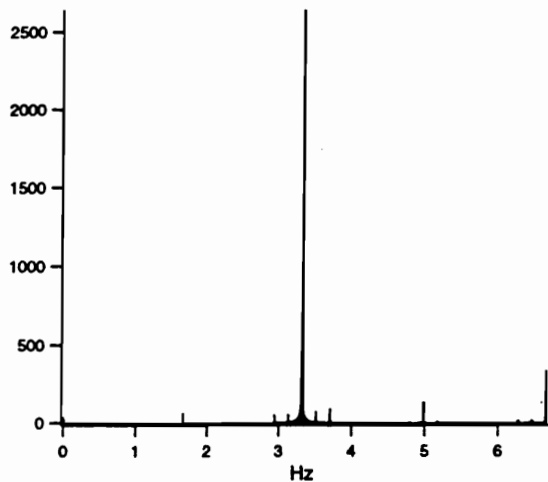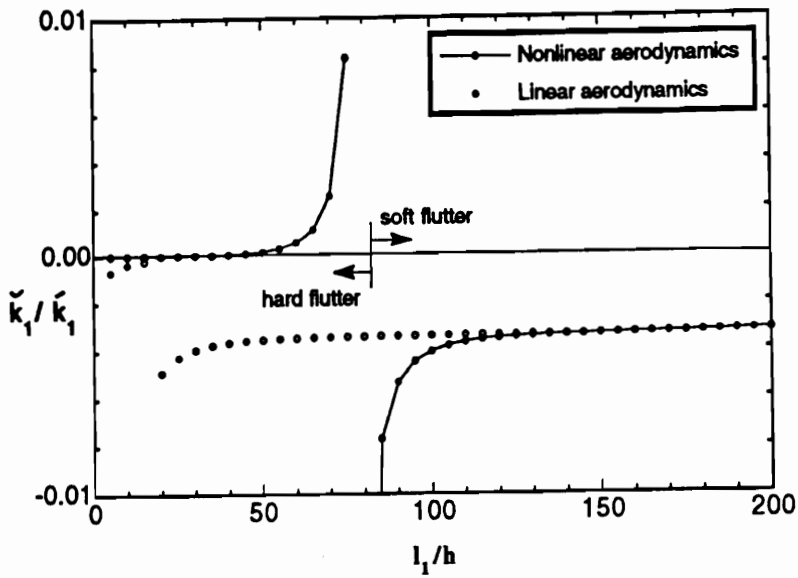

Figure 5.24: $\check{k}_1/\acute{k}_1$ for various thickness ratios—shows that only aerodynamic nonlinearities may yield hard flutter motion; flow past both faces $(\delta_F = 0$, $\hat{\delta}_F = 2)$; perfect panel; $\Lambda = 0$; 4×1 mode analysis.
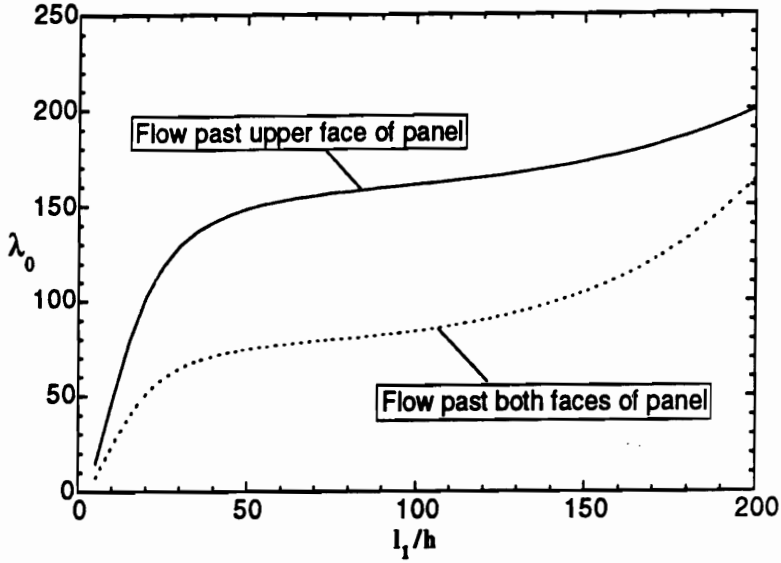
Figure 5.25: Variation of non-dimensional flutter speed with thickness ratio; perfect panel; $\Lambda = 30°$; 2×2 mode analysis.
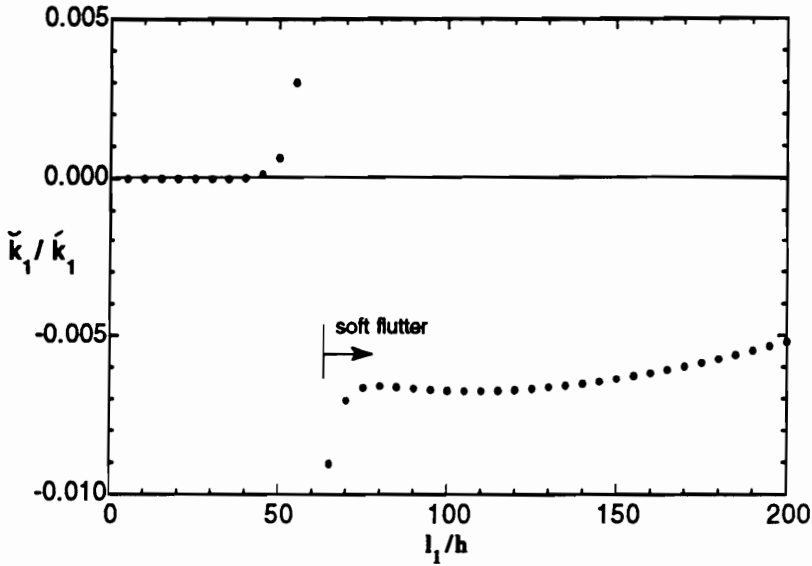
Figure 5.26: $\check{k}_1/\acute{k}_1$ for various thickness ratios—shows that aerodynamic nonlinearities may yield hard flutter; flow past upper face ($\delta_F = \hat{\delta}_F = 1$); perfect panel; $\Lambda = 30°$; 2×2 mode analysis.
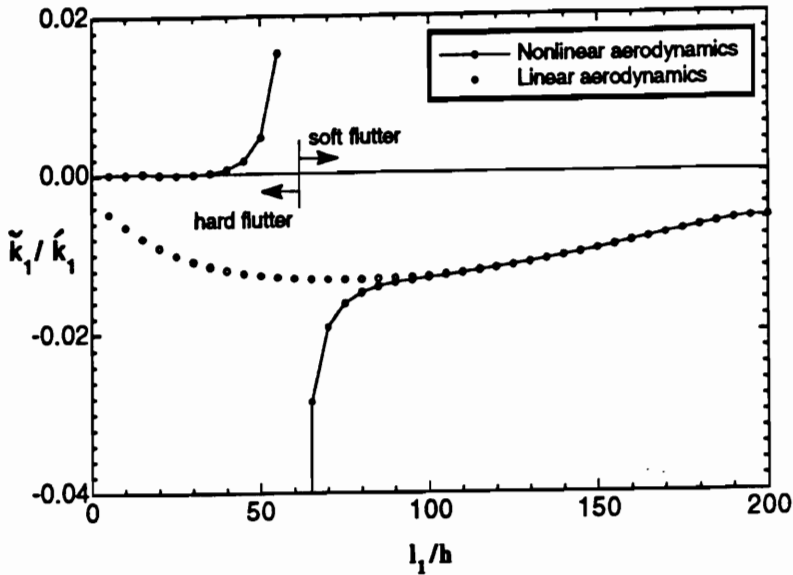
Figure 5.27: $\check{k}_1/\acute{k}_1$ for various thickness ratios—shows that aerodynamic nonlinearities may yield hard flutter; flow past both faces ($\delta_F = 0$, $\hat{\delta}_F = 2$); perfect panel; $\Lambda = 30°$; 2×2 mode analysis.
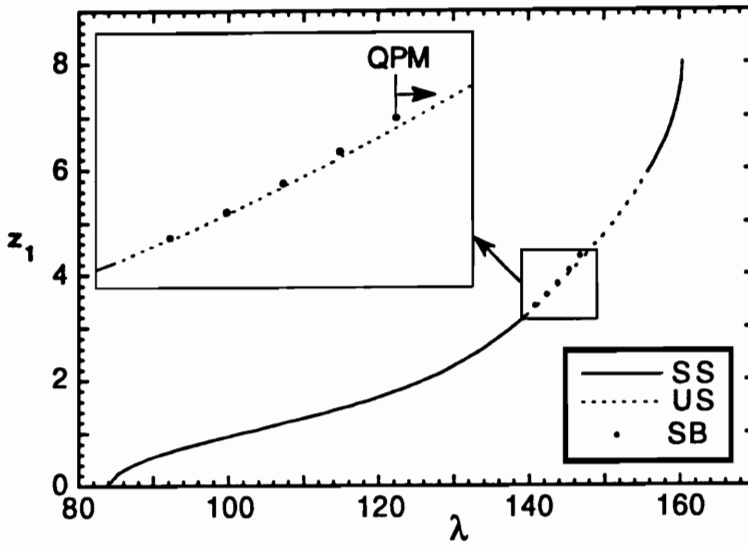
Figure 5.28: Flutter amplitude and bifurcation behavior for perfect panel; flow past both faces ($\delta_F = 0$, $\hat{\delta}_F = 2$); nonlinear aerodynamics; $\Lambda = 30°$; 2×2 mode analysis; $l_1/h = 100$; stable periodic motions are: SS (stable symmetric), SB (symmetry broken); US–unstable symmetric; QPM–quasiperiodic motion.
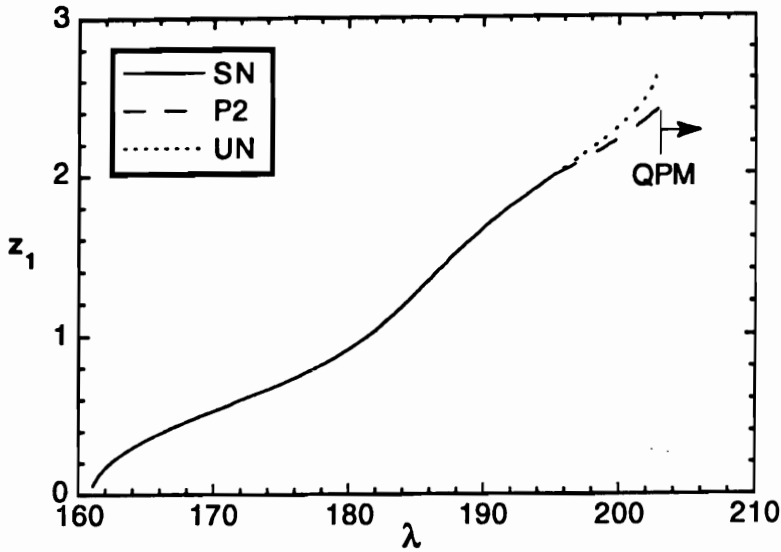
Figure 5.29: Flutter amplitude and bifurcation behavior for perfect panel; flow past upper face $(\delta_F = \hat{\delta}_F = 1)$; nonlinear aerodynamics; $\Lambda = 30^o$; 2×2 mode analysis; $l_1/h = 100$; stable periodic motions are: SN (stable nonsymmetric), P2 (period-2); UN–unstable nonsymmetric; QPM–quasiperiodic motion.
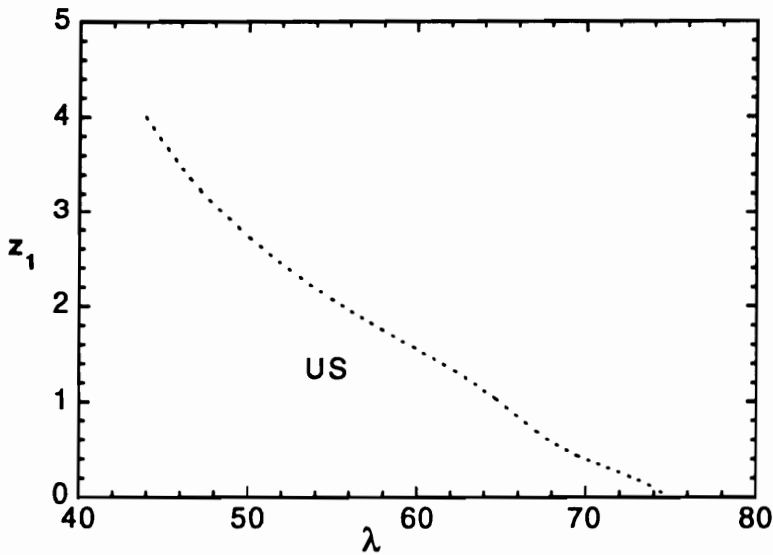
Figure 5.30: Flutter amplitude for perfect panel—subcritical Hopf bifurcation and resulting unstable symmetric (US) periodic motion; flow past both faces $(\delta_F = 0 , \hat{\delta}_F = 2)$; nonlinear aerodynamics; $\Lambda = 30^o$; 2×2 mode analysis; $l_1/h = 50$.
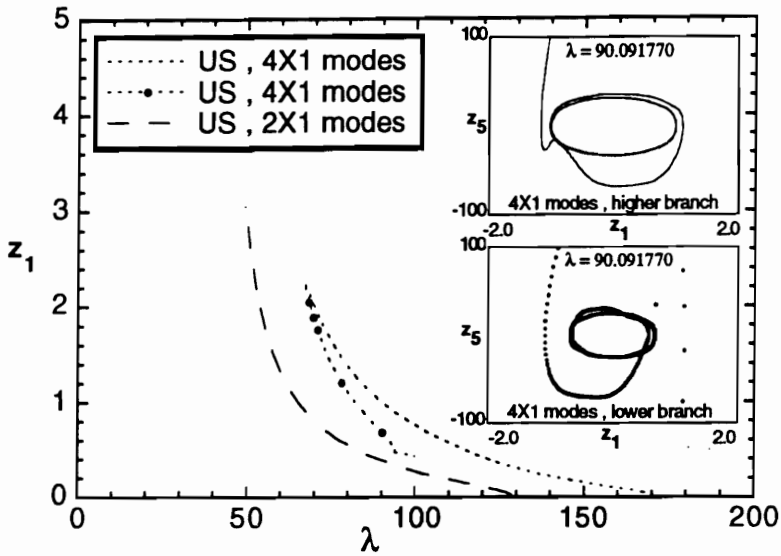
Figure 5.31: Flutter amplitude for perfect panel—subcritical Hopf bifurcation and resulting unstable symmetric (US) periodic motion (insets); flow past both faces ($\delta_F = 0$, $\hat{\delta}_F = 2$); nonlinear aerodynamics; $\Lambda = 0°$; $l_1/h = 50$.
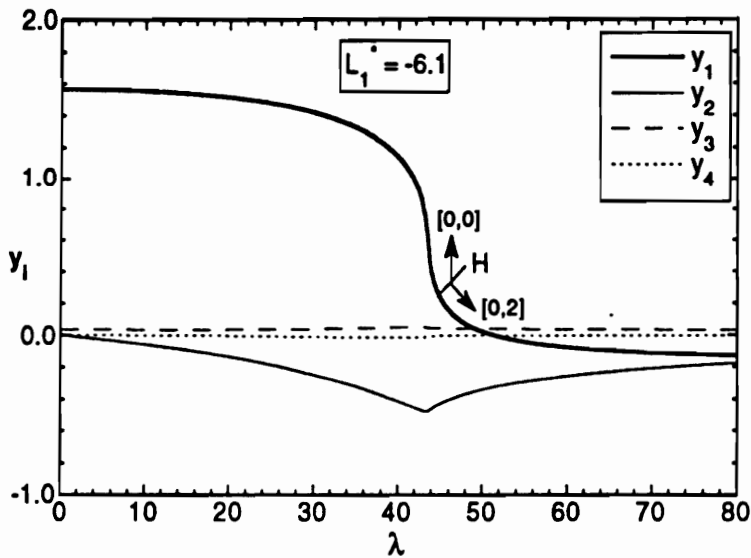
Figure 5.32: Static displacement modal amplitudes; CPT; imperfect panel ($\hat{a}_{11} = 0.2$); H–supercritical Hopf bifurcation point.
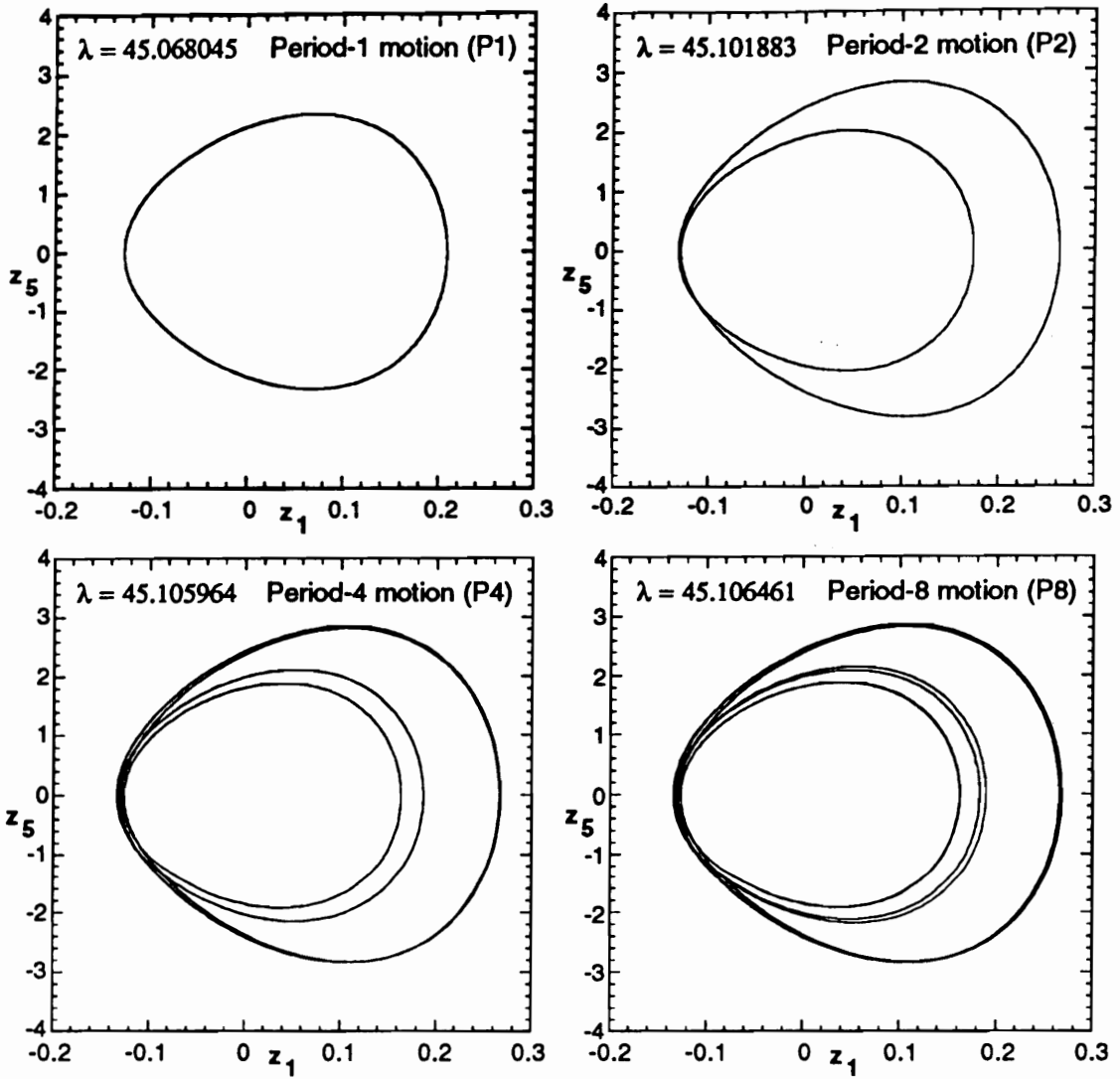
Figure 5.33: Phase trajectories: period-1 up to period-8 motions that exist beyond supercritical Hopf bifurcation point (cf. Fig. 5.32).
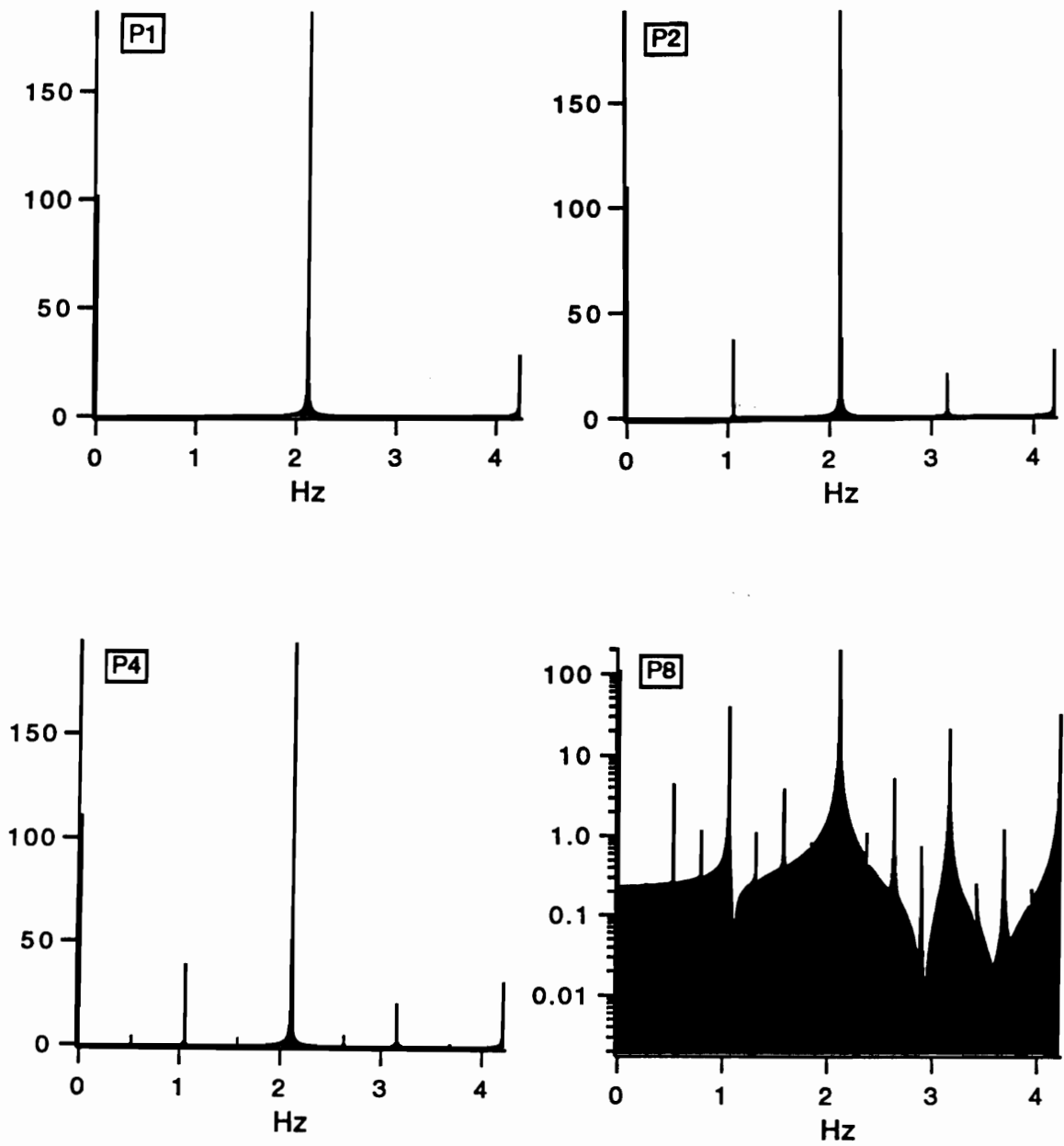
Figure 5.34: Frequency spectra of z_1 for period-1 up to period-8 motions that exist beyond supercritical Hopf bifurcation point (cf. Fig. 5.32).
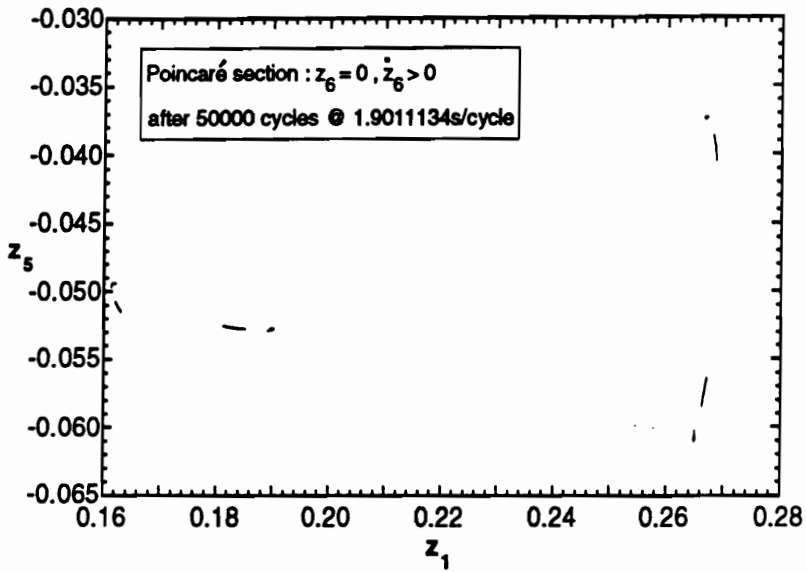
Figure 5.35: Motion beyond region of period-32 motion (cf. Figs. 5.32, 5.33); Poincaré section for $\lambda = 45.106600$ showing existence of strange attractor (chaotic motion following period-doubling sequence).
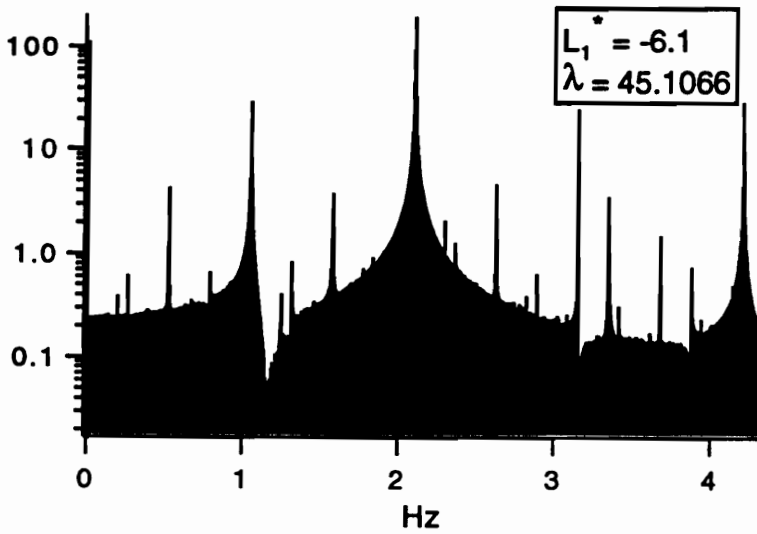
Figure 5.36: Frequency spectrum of z_1 for chaotic motion ($\lambda = 45.106600$, cf. Fig. 5.35).
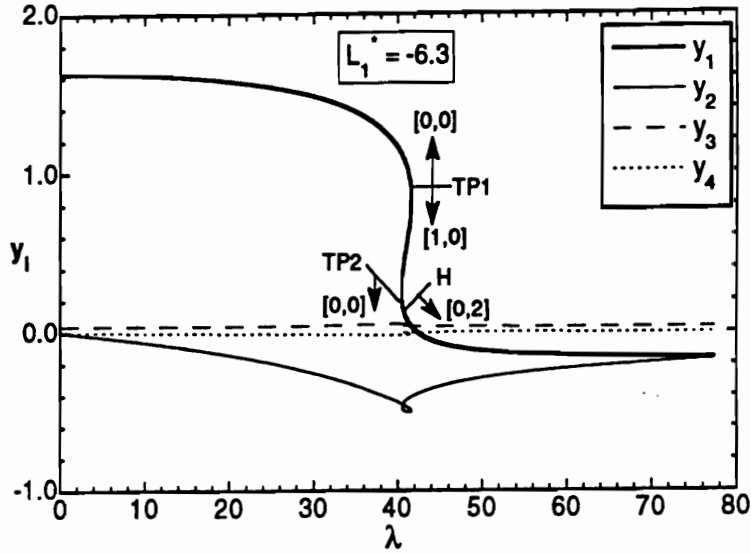
Figure 5.37: Static displacement modal amplitudes; CPT; imperfect panel ($\hat{a}_{11} = 0.2$); H–supercritical Hopf bifurcation point; TP1–, TP2– turning point.
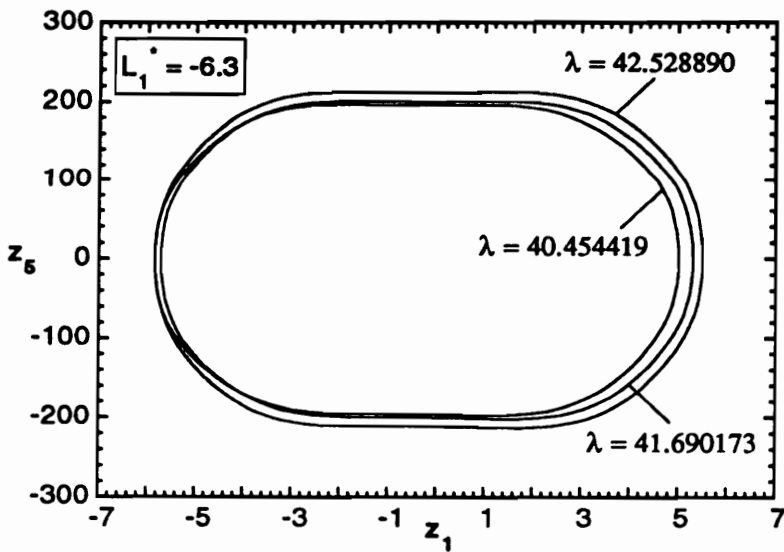
Figure 5.38: Phase trajectories: Nonsymmetric periodic motion about TP1 (cf. Fig. 5.37).
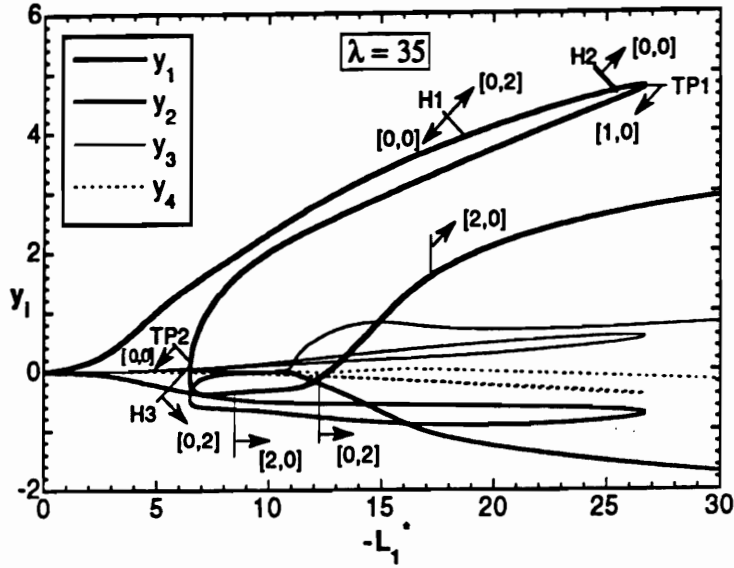
Figure 5.39: Static displacement modal amplitudes; CPT; imperfect panel ($\hat{a}_{11} = 0.2$); H1(subcritical)–, H2(supercritical)–, H3(supercritical)–Hopf bifurcation point; TP1–, TP2–turning point.
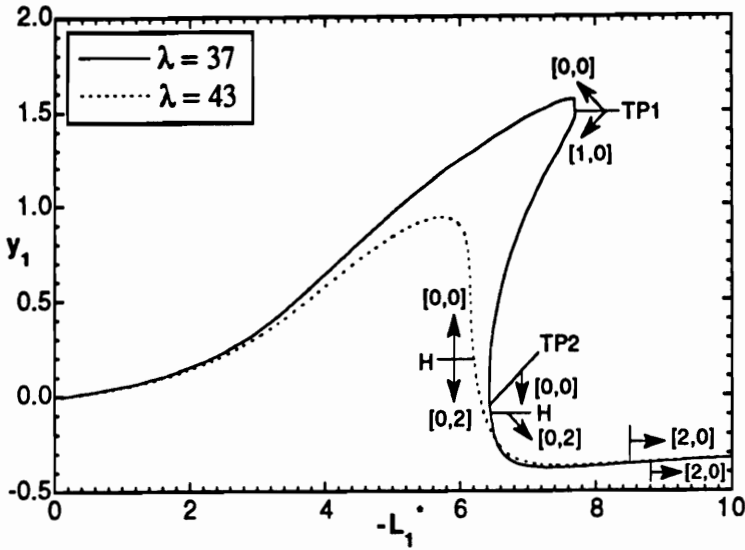
Figure 5.40: Static displacement modal amplitude (y_1); CPT; imperfect panel ($\hat{a}_{11} = 0.2$); H–supercritical Hopf bifurcation point; TP1–, TP2– turning point.
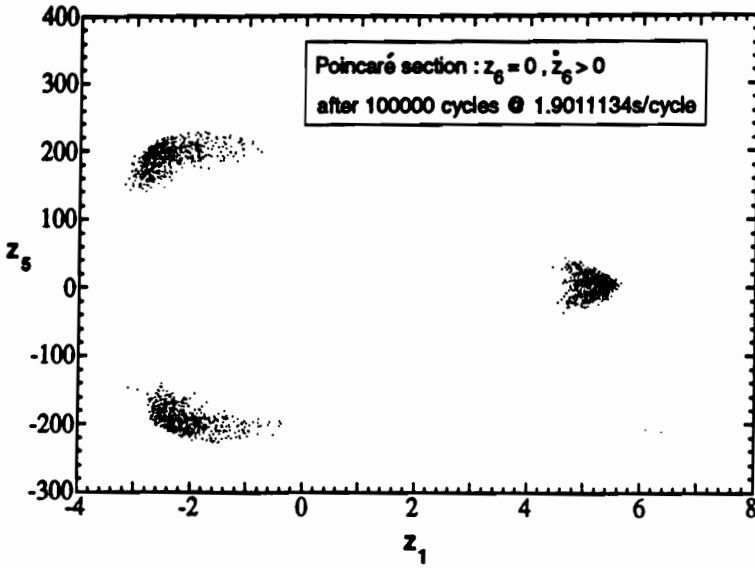
Figure 5.41: Motion beyond region of period-8 motion (cf. Fig. 5.40): Poincaré section for $\lambda = 43$, $L_1^* = -6.2353164$, showing existence of strange attractor (chaotic motion).
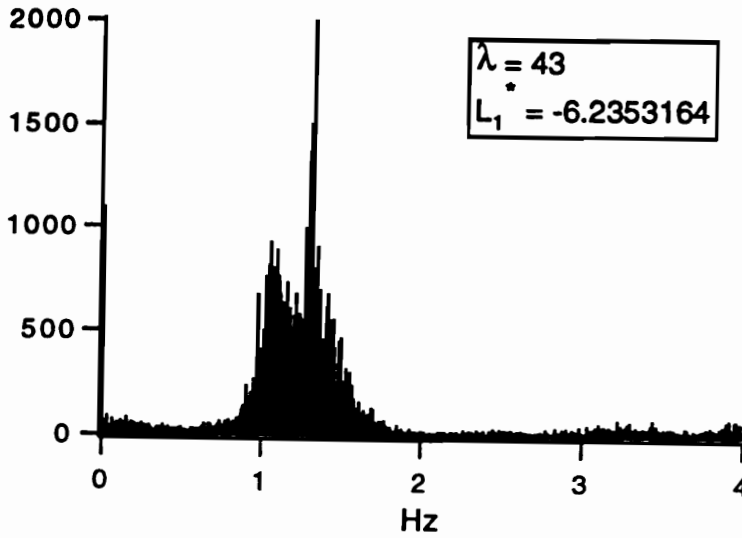
Figure 5.42: Frequency spectrum of z_1 for chaotic motion (cf. Fig. 5.40): $\lambda = 43$, $L_1^* = -6.2353164$.

101
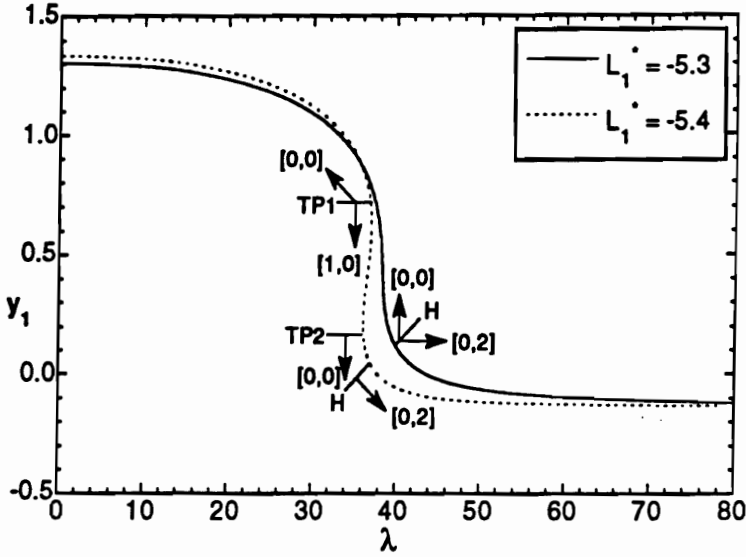
Figure 5.43: Static displacement modal amplitude (y_1); HSDT; imperfect panel ($\hat{a}_{11} = 0.2$); H–supercritical Hopf bifurcation point; TP1–, TP2– turning point.
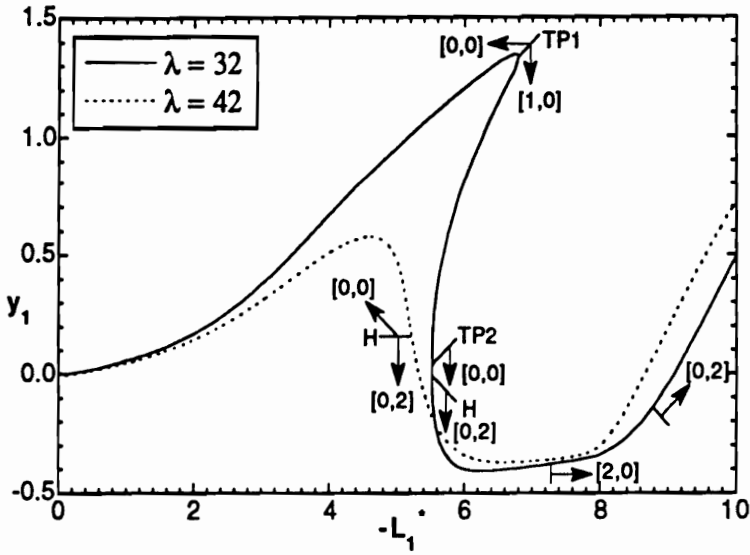
Figure 5.44: Static displacement modal amplitude (y_1); HSDT; imperfect panel ($\hat{a}_{11} = 0.2$); H–supercritical Hopf bifurcation point; TP1–, TP2– turning point.
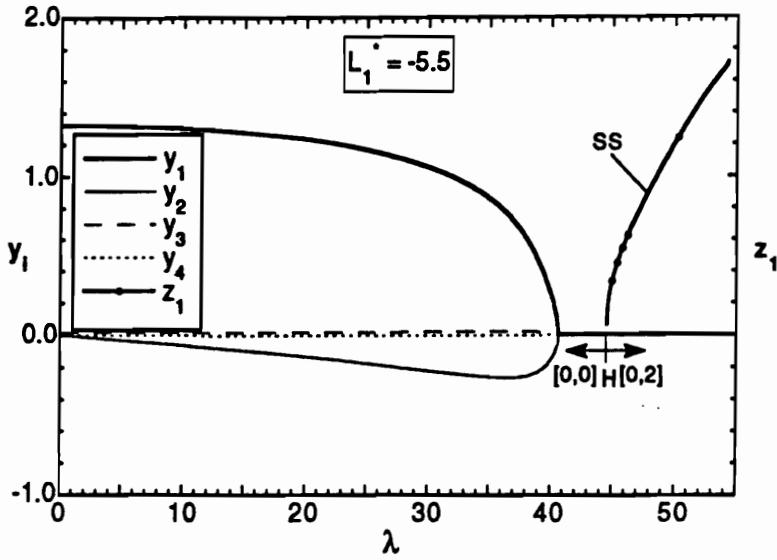
Figure 5.45: Static and dynamic displacement modal amplitudes; CPT; perfect panel; H–supercritical Hopf bifurcation point.
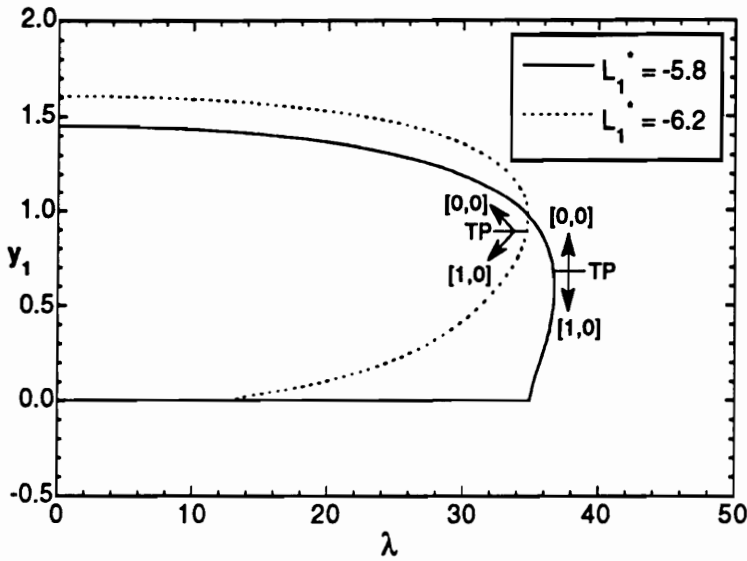
Figure 5.46: Static displacement modal amplitude (y_1); CPT; perfect panel; TP–turning point.
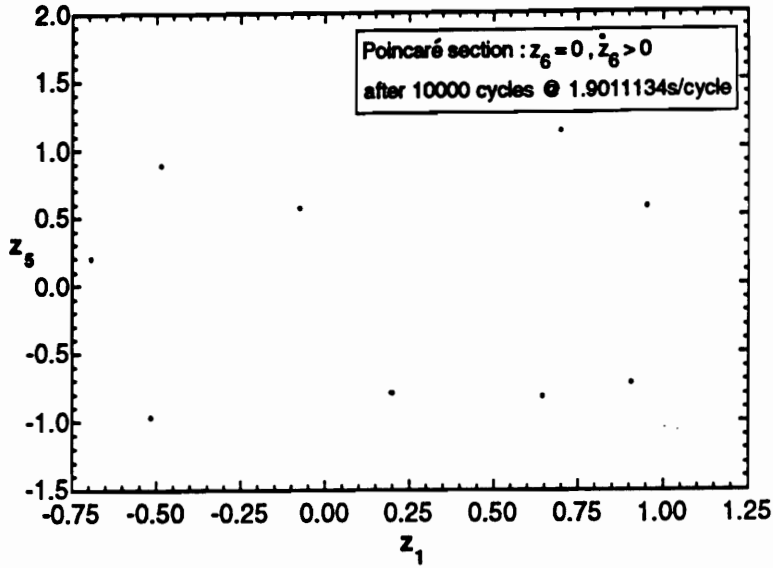
Figure 5.47: Motion past TP (cf. Fig. 5.46): Poincaré section for $\lambda = 36.845568$, $L_1^* = -5.8$, indicating periodic behavior.
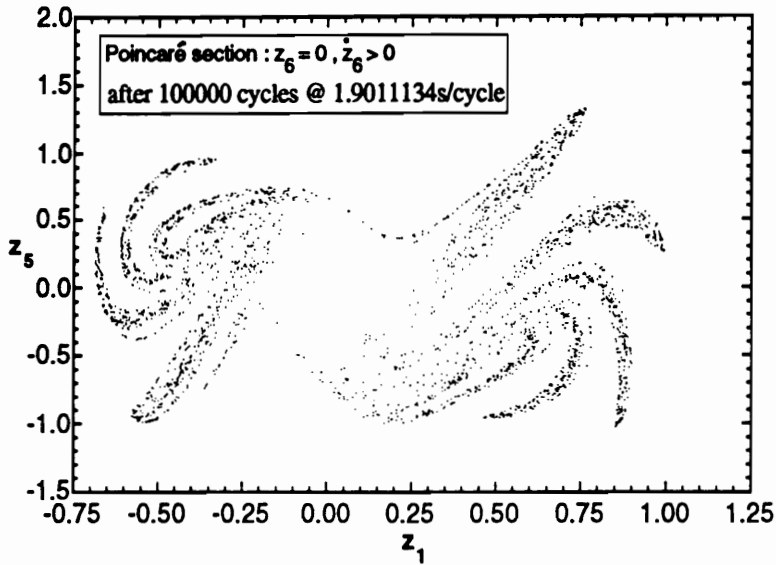
Figure 5.48: Motion past TP (cf. Fig. 5.46): Poincaré section for $\lambda = 36.945568$, $L_1^* = -5.8$, showing existence of strange attractor (chaotic motion).
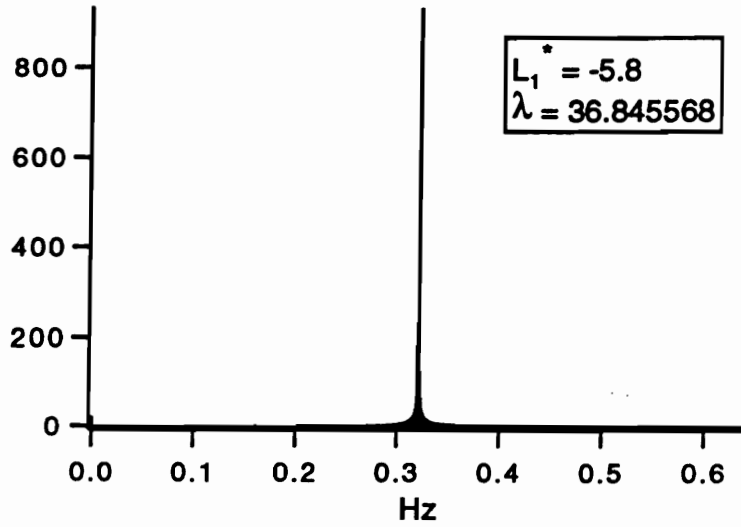
Figure 5.49: Frequency spectrum of z_1 for periodic motion past TP (cf. Fig. 5.46): $\lambda = 36.845568$, $L_1^* = -5.8$.
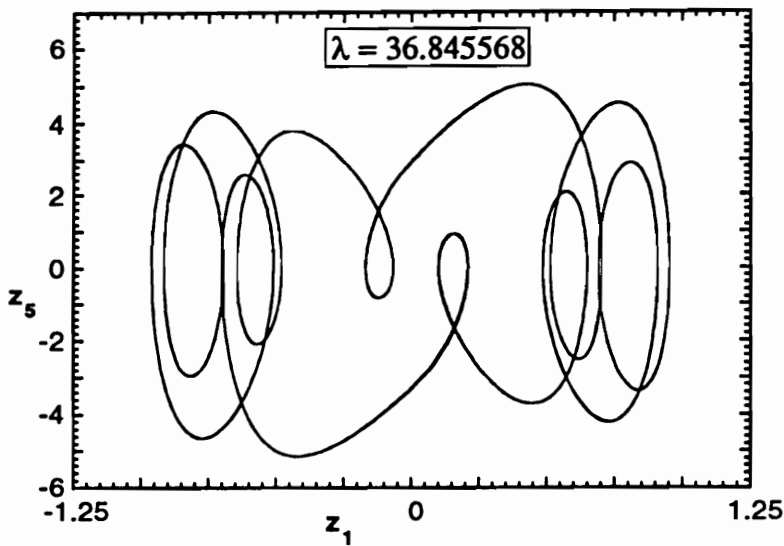
Figure 5.50: Phase trajectory: Periodic motion past TP (cf. Fig. 5.46): $\lambda = 36.845568$, $L_1^* = -5.8$.
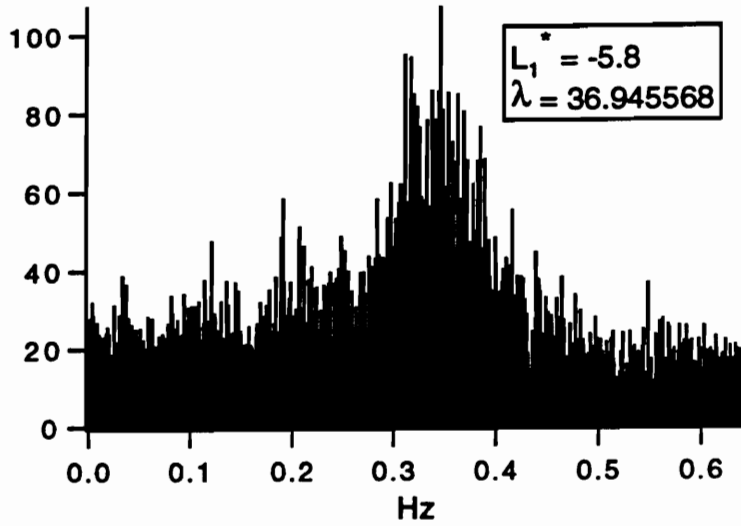
Figure 5.51: Frequency spectrum of z_1 for chaotic motion past TP (cf. Fig. 5.46): $\lambda = 36.945568$, $L_1^* = -5.8$.
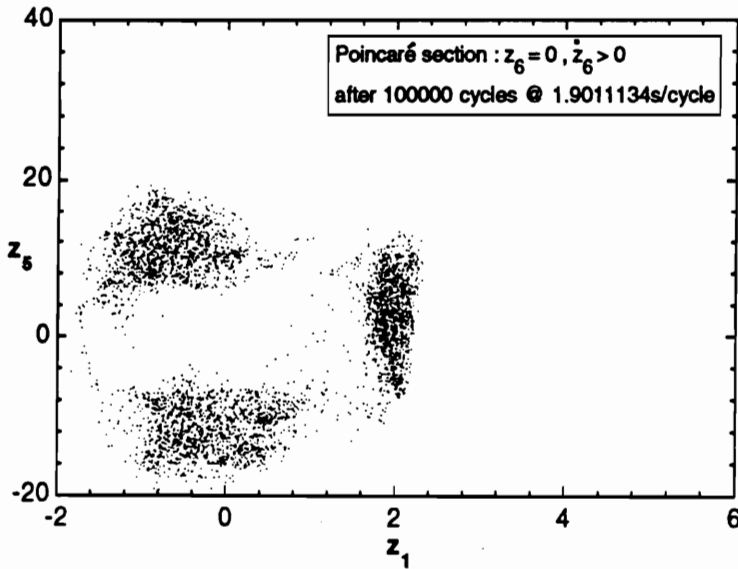
Figure 5.52: Motion past TP (cf. Fig. 5.46): Poincaré section for $\lambda = 34.873906$, $L_1^* = -6.2$, showing existence of strange attractor (chaotic motion).
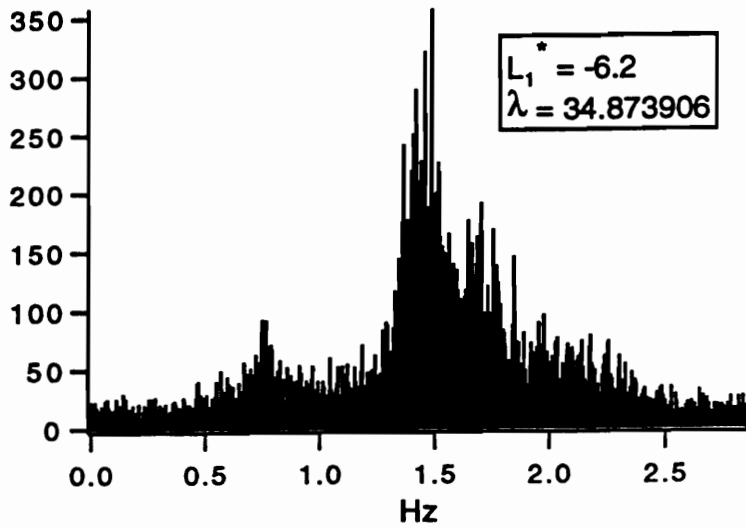
Figure 5.53: Frequency spectrum of z_1 for chaotic motion past TP (cf. Fig. 5.46): $\lambda = 34.873906$, $L_1^* = -6.2$.
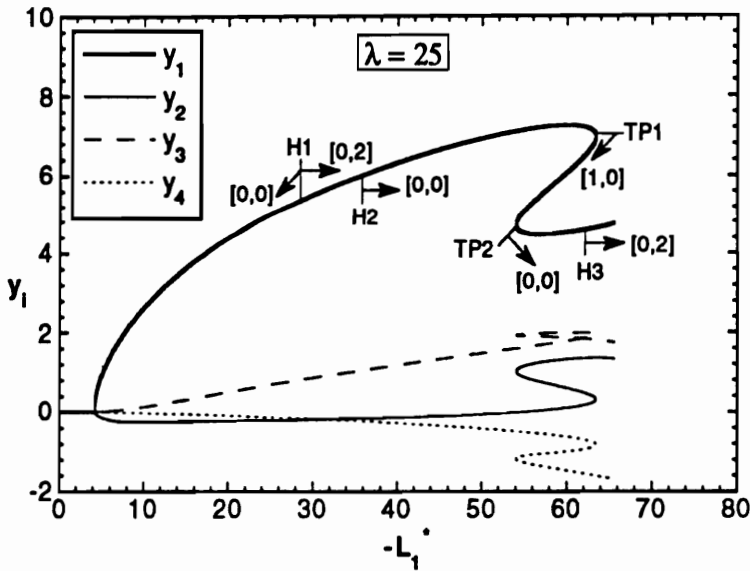
Figure 5.54: Static displacement modal amplitudes; CPT; perfect panel; H1(supercritical)–, H2(subcritical)–, H3(subcritical)–Hopf bifurcation point; TP1–, TP2– turning point.
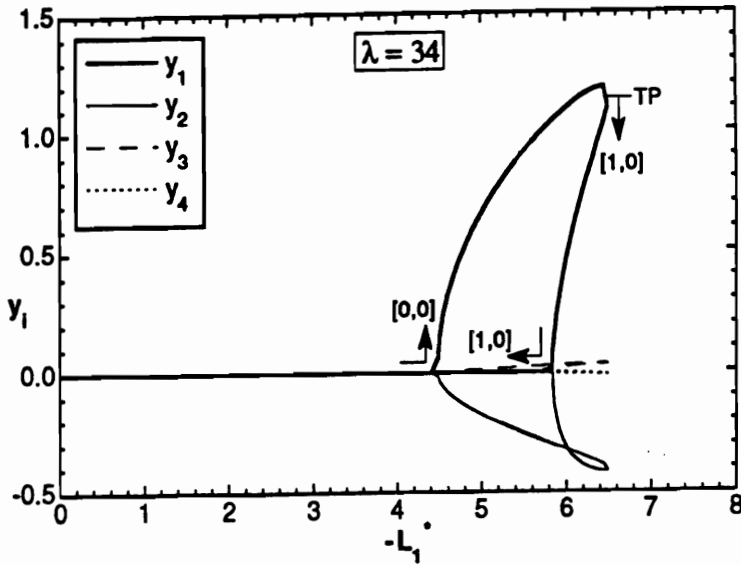
Figure 5.55: Static displacement modal amplitudes; CPT; perfect panel; TP–turning point.
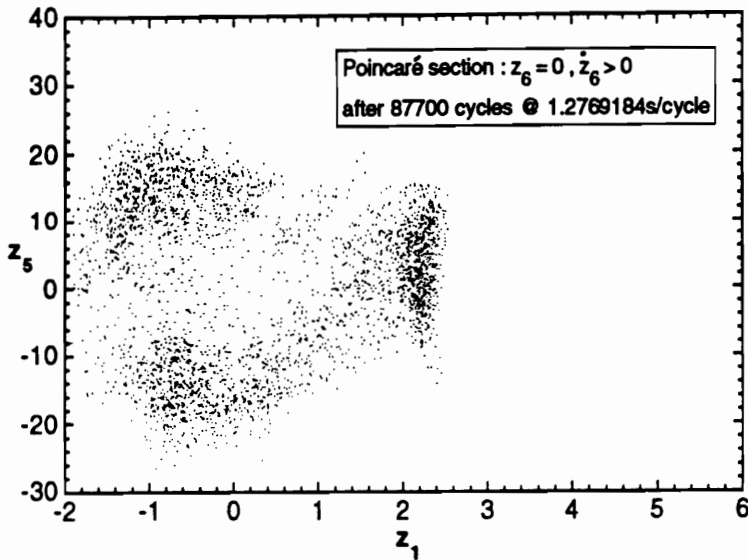
Figure 5.56: Motion past TP (cf. Fig. 5.55): Poincaré section for $\lambda = 34$, $L_1^* = -6.5155240$, showing existence of strange attractor (chaotic motion).

108
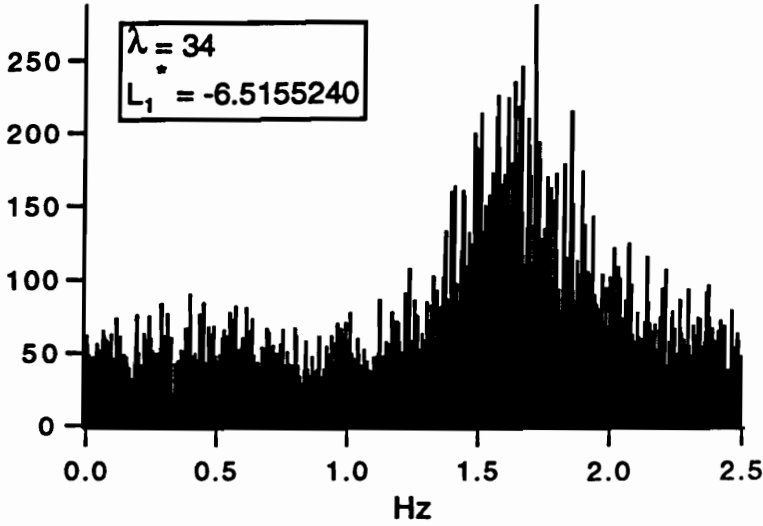
Figure 5.57: Frequency spectrum of z_1 for chaotic motion past TP (cf. Fig. 5.55): $\lambda = 34$, $L_1^* = -6.5155240$.
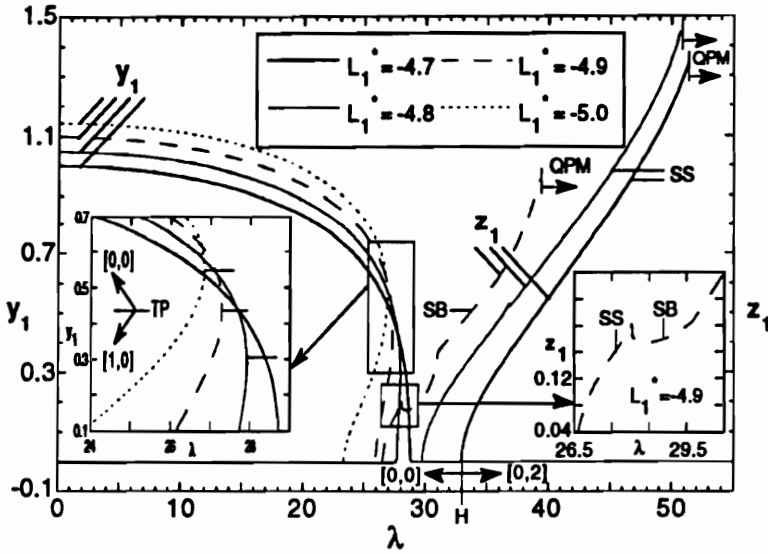
Figure 5.58: Static and dynamic displacement modal amplitude (y_1, z_1); HSDT; perfect panel; TP–turning point; stable periodic motions are: SS (stable symmetric), SB (symmetry broken); QPM–quasiperiodic motion.
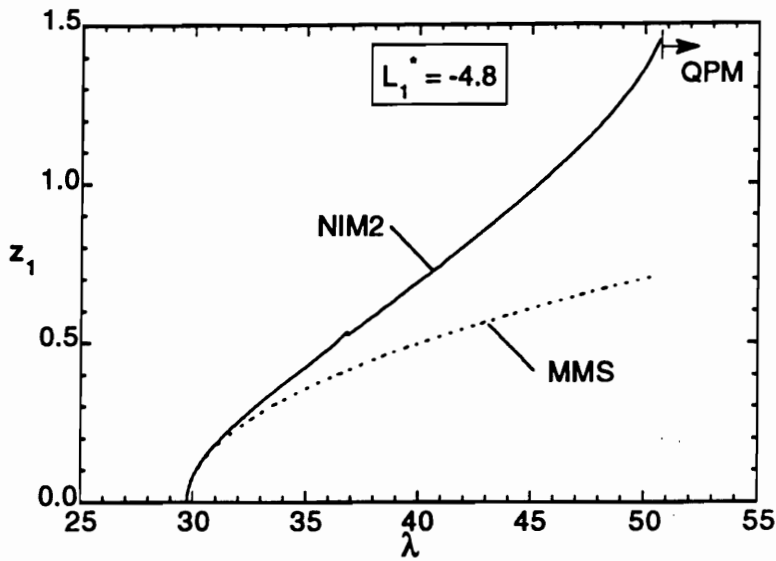
Figure 5.59: Comparison of flutter amplitude obtained by MMS and NIM2: HSDT; perfect panel; $L_1^* = -4.8$; SS–stable symmetric periodic motion; QPM–quasiperiodic motion.
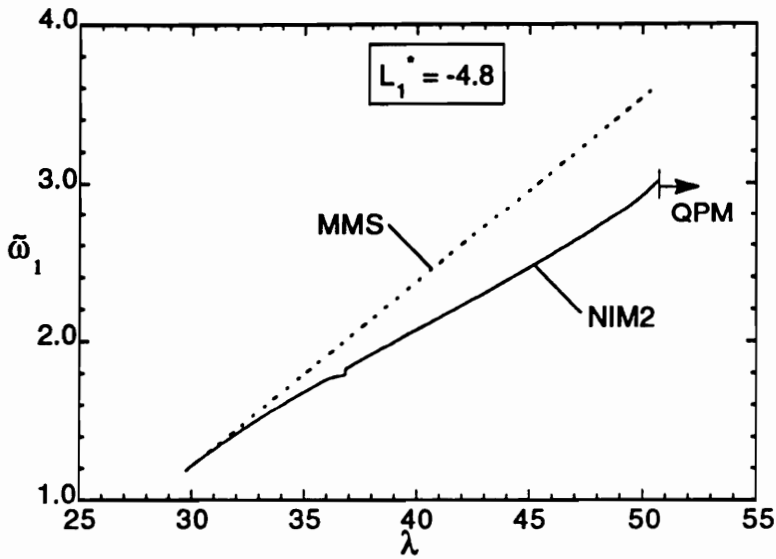
Figure 5.60: Comparison of flutter frequency obtained by MMS and NIM2: HSDT; perfect panel; $L_1^* = -4.8$; SS–stable symmetric periodic motion; QPM–quasiperiodic motion.
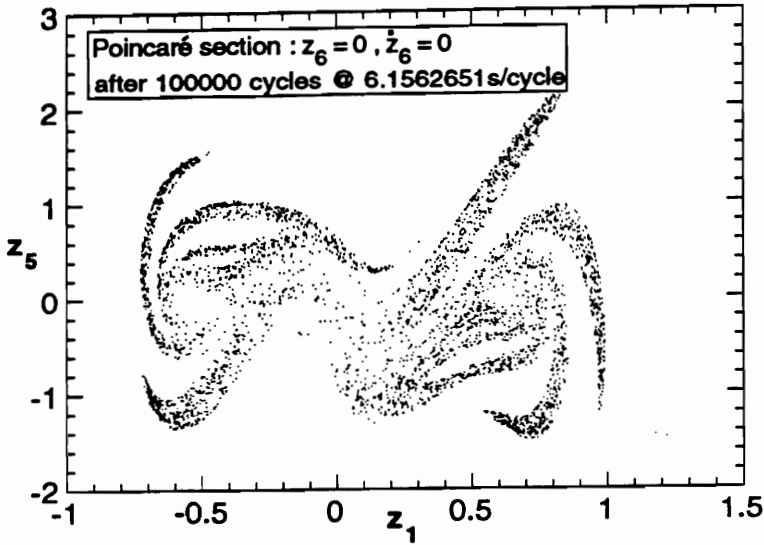
Figure 5.61: Motion past TP (cf. Fig. 5.58): Poincaré section for $\lambda = 26.854302$, $L_1^* = -5.0$, showing existence of strange attractor (chaotic motion).
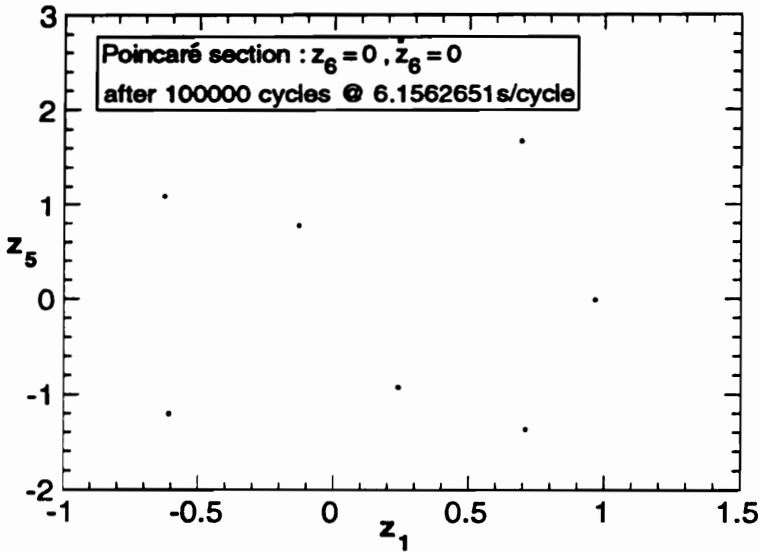
Figure 5.62: Motion past TP (cf. Fig. 5.58): Poincaré section for $\lambda = 26.944302$, $L_1^* = -5.0$, indicating periodic behavior.

111
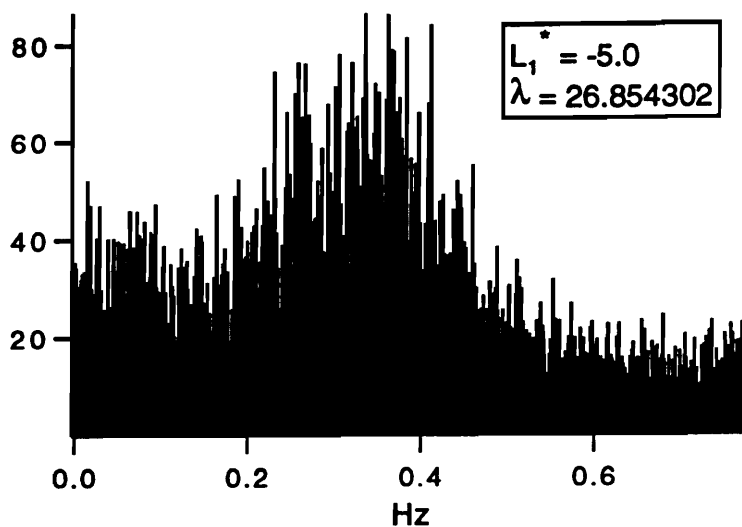
Figure 5.63: Frequency spectrum of z_1 for chaotic motion past TP (cf. Fig. 5.58): $\lambda = 26.854302$, $L_1^* = -5.0$.
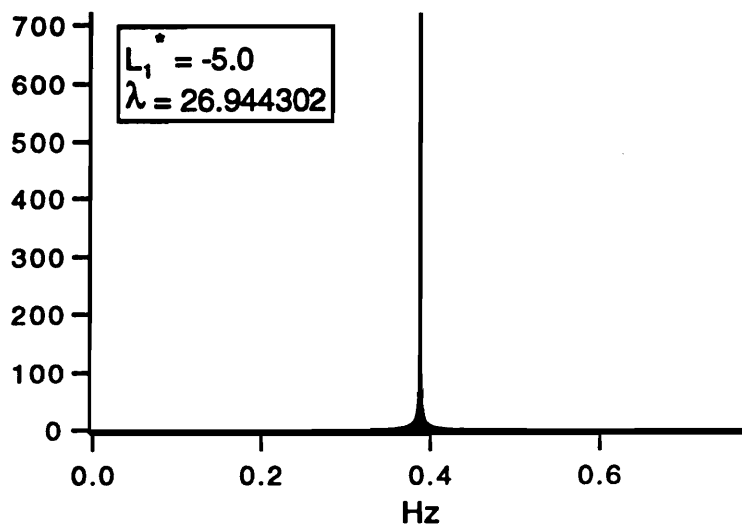
Figure 5.64: Frequency spectrum of z_1 for periodic motion past TP (cf. Fig. 5.58): $\lambda = 26.944302$, $L_1^* = -5.0$.

112
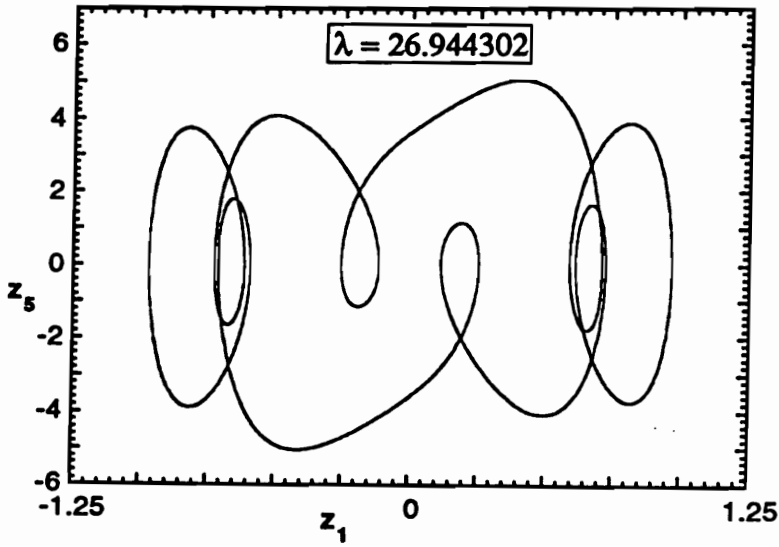
Figure 5.65: Phase trajectory: periodic motion past TP (cf. Fig. 5.58): $\lambda = 26.944302$, $L_1^* = -5.0$.
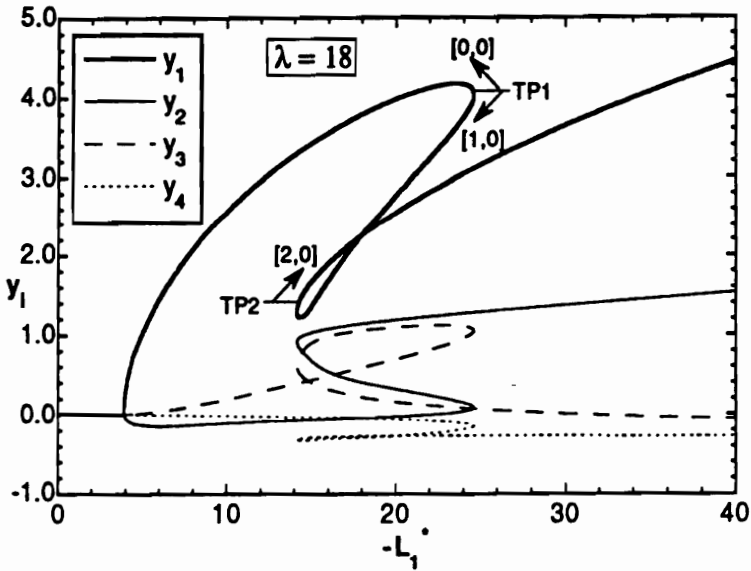
Figure 5.66: Static displacement modal amplitudes; HSDT; perfect panel; TP1–, TP2–turning point.

113
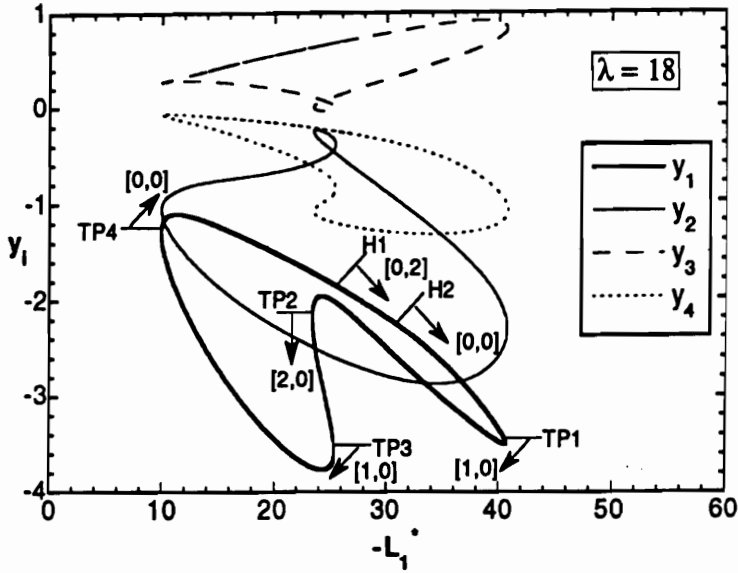
Figure 5.67: Static displacement modal amplitudes: co-existence of isolas with solution branch displayed in Fig. 5.66; H1-, H2- Hopf bifurcation point; TP1-, TP2-, TP3-, TP4- turning point.
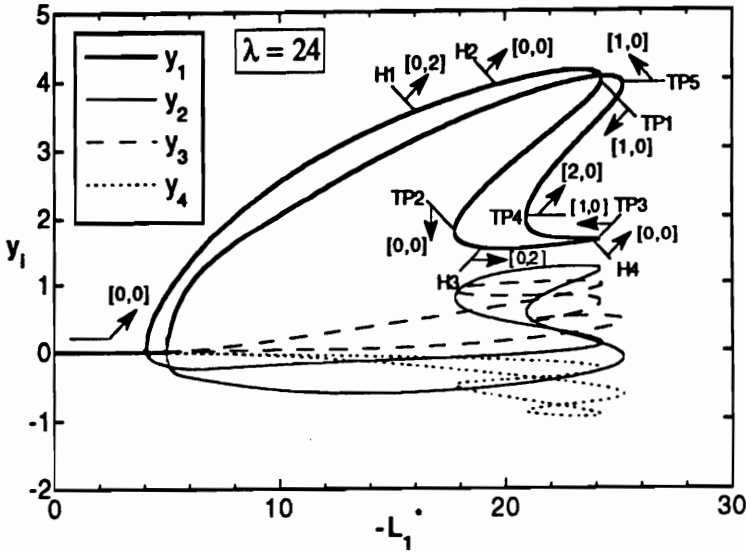
Figure 5.68: Static displacement modal amplitudes; HSDT; perfect panel; H1(subcritical)-, H2(subcritical)-, H3(subcritical)-, H4(supercritical)- Hopf bifurcation point; TP1-, TP2-, TP3-, TP4-, TP5- turning point.
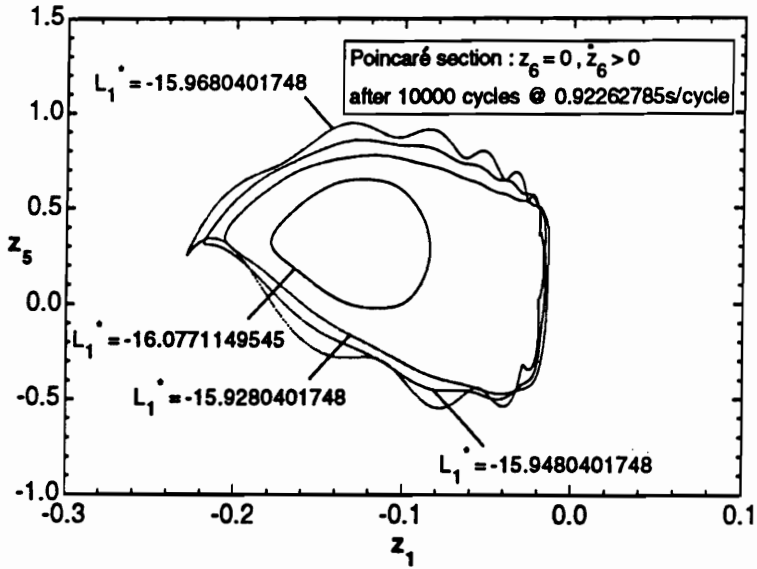
Figure 5.69: Hard flutter phenomenon: Poincaré sections indicating quasiperiodic motions past H1 (cf. Fig. 5.68).
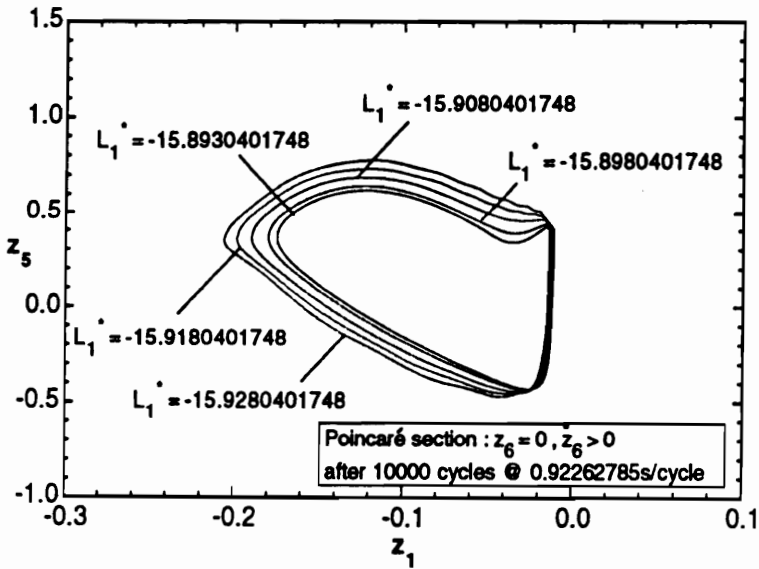
Figure 5.70: Hard flutter phenomenon: Poincaré sections indicating quasiperiodic motions prior to H1 (cf. Fig. 5.68).

115
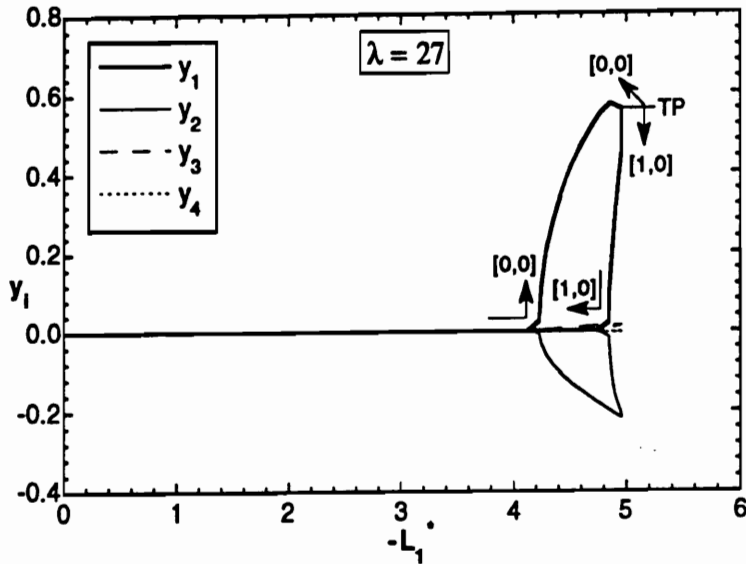
Figure 5.71: Static displacement modal amplitudes; HSDT; perfect panel; TP–turning point.
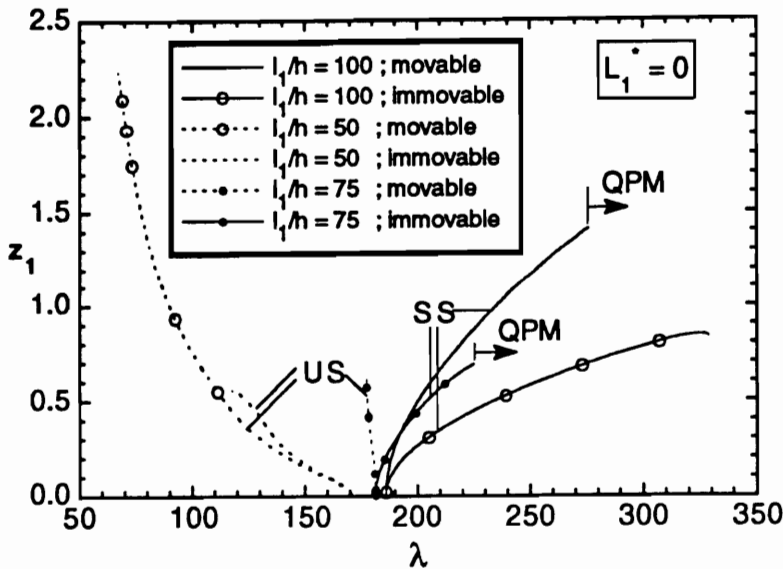
Figure 5.72: Effect of edge restraint on flutter amplitude and type of flutter (hard or soft): edges $x_2 = 0$, l_2 movable ($\delta_{M2} = 1$, $\tilde{\alpha}_2 = 0$), edges $x_1 = 0$, l_1 movable ($\delta_{M1} = 1$, $\tilde{\alpha}_1 = 0$) or immovable ($\delta_{M1} = 0$, $\tilde{\alpha}_1 = 1$); HSDT; perfect panel; periodic motions are: SS (stable symmetric), US (unstable symmetric); QPM–quasiperiodic motion.
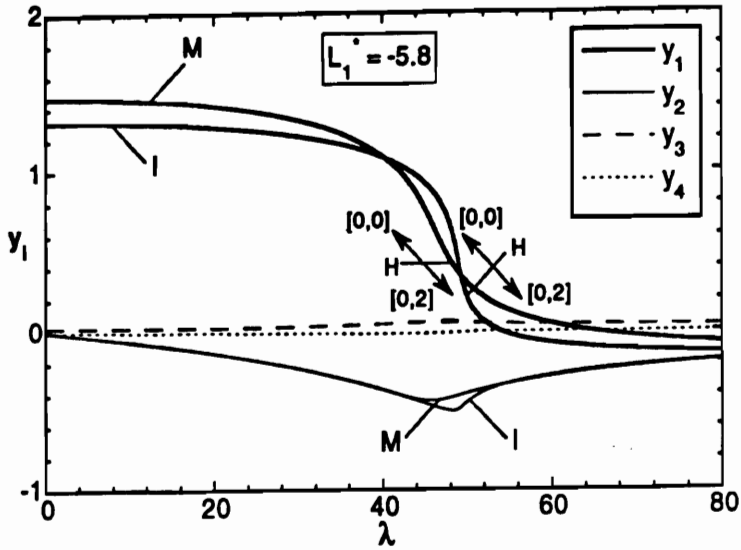
Figure 5.73: Static displacement modal amplitudes; CPT; imperfect panel ($\hat{a}_{11} = 0.2$); edges $x_1 = 0, l_1$ movable (M), edges $x_2 = 0, l_2$ movable (M) or immovable (I); H–supercritical Hopf bifurcation point.
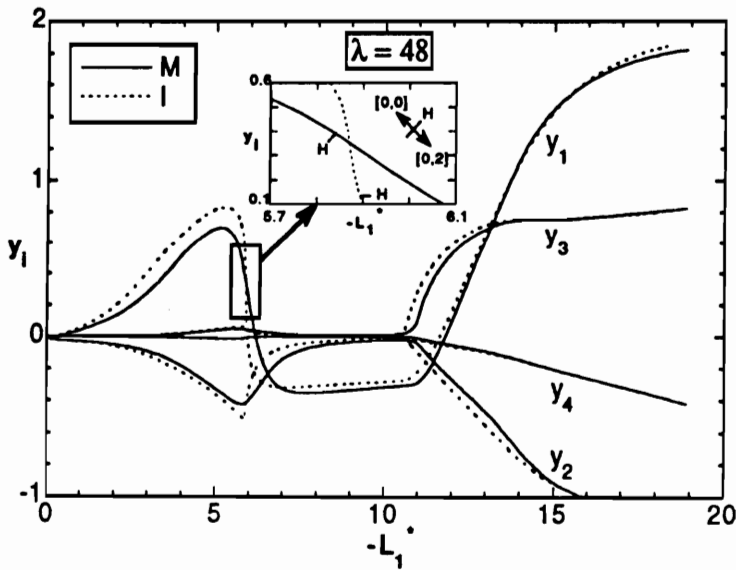
Figure 5.74: Static displacement modal amplitudes; CPT; imperfect panel ($\hat{a}_{11} = 0.2$); edges $x_1 = 0, l_1$ movable (M), edges $x_2 = 0, l_2$ movable (M) or immovable (I); H–supercritical Hopf bifurcation point.
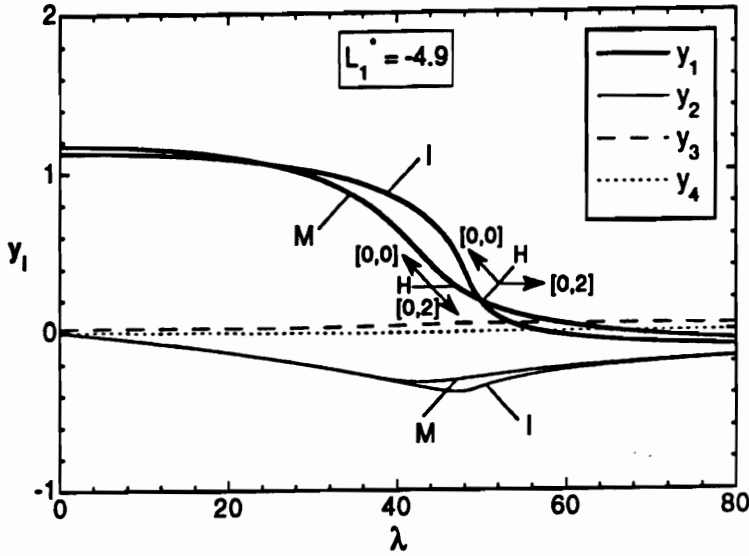
Figure 5.75: Static displacement modal amplitudes; HSDT; imperfect panel ($\hat{a}_{11} = 0.2$); edges $x_1 = 0, l_1$ movable (M), edges $x_2 = 0, l_2$ movable (M) or immovable (I); H–supercritical Hopf bifurcation point.
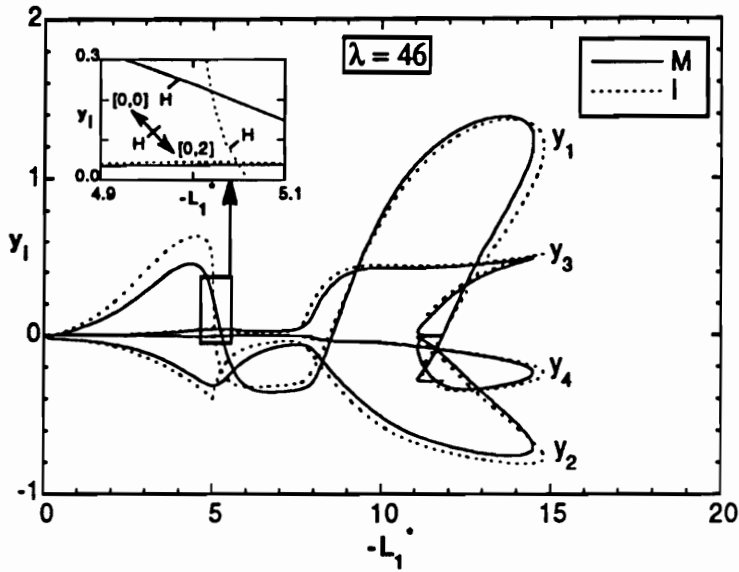
Figure 5.76: Static displacement modal amplitudes; HSDT; imperfect panel ($\hat{a}_{11} = 0.2$); edges $x_1 = 0, l_1$ movable (M), edges $x_2 = 0, l_2$ movable (M) or immovable (I); H–supercritical Hopf bifurcation point.
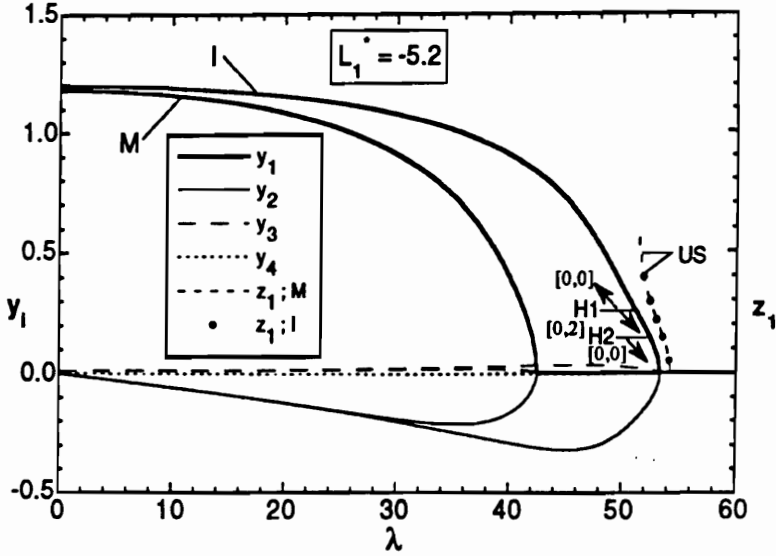
Figure 5.77: Static and dynamic displacement modal amplitudes; CPT; perfect panel; edges $x_1 = 0$, l_1 movable (M), edges $x_2 = 0$, l_2 movable (M) or immovable (I); H1-, H2- supercritical Hopf bifurcation point; US-unstable symmetric periodic motion.
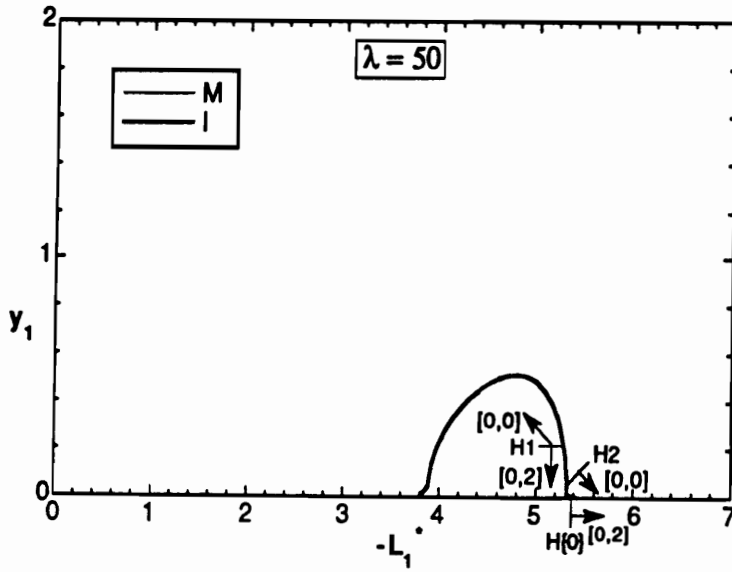
Figure 5.78: Static displacement modal amplitude (y_1); CPT; perfect panel; edges $x_1 = 0$, l_1 movable (M), edges $x_2 = 0$, l_2 movable (M) or immovable (I); H1(supercritical)-, H2(supercritical)-, H{0}(subcritical)- Hopf bifurcation point.
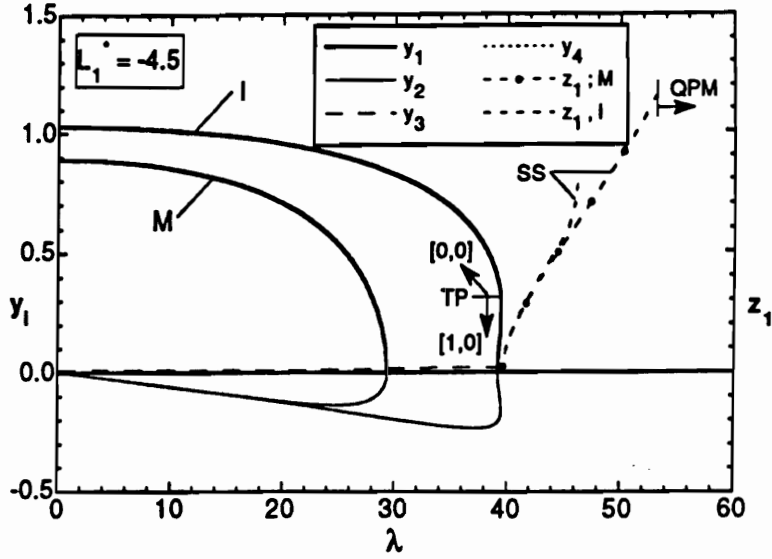
Figure 5.79: Static and dynamic displacement modal amplitudes; HSDT; perfect panel; edges $x_1 = 0$, l_1 movable (M), edges $x_2 = 0$, l_2 movable (M) or immovable (I); TP–turning point; SS–stable symmetric periodic motion; QPM–quasiperiodic motion.
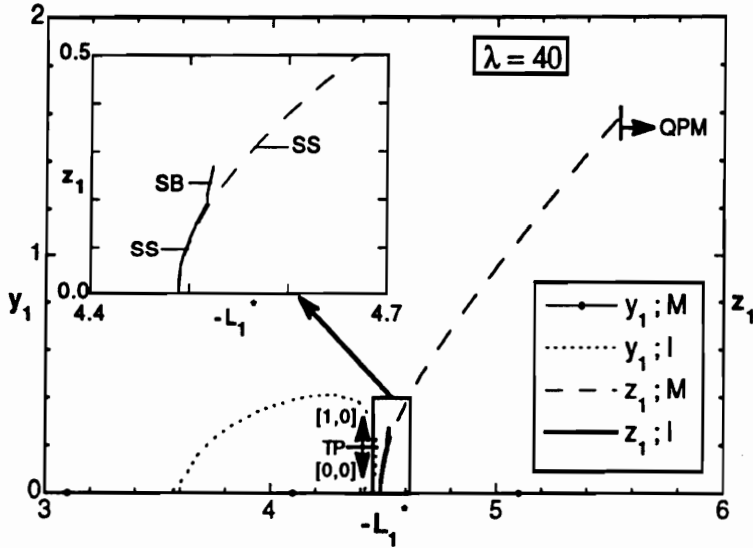
Figure 5.80: Static and dynamic displacement modal amplitude (y_1, z_1) ; HSDT; perfect panel; edges $x_1 = 0$, l_1 movable (M), edges $x_2 = 0$, l_2 movable (M) or immovable (I); TP–turning point; stable periodic motions are: SS (stable symmetric), SB (symmetry broken); QPM–quasiperiodic motion.

Table 5.1: Motion past H (cf. Fig. 5.32).

$\lambda(\uparrow)$	T	max z_1 : $z_5 = 0$	Motion type	Stability
.44869150E+02	.46438769E+00	.38164241E-01	SN	stable
.45077997E+02	.47284284E+00	.21532889E+00	UN	unstable
.45077997E+02	.94576682E+00	.20601160E+00	P2	stable
.45105864E+02	.95063955E+00	.26743826E+00	P2	unstable
.45105864E+02	.19010539E+01	.26693264E+00	P4	stable
.45106063E+02	.19011134E+01	.26707803E+00	P4	unstable
.45106063E+02	.38022305E+01	.26734630E+00	P8	stable
.45106481E+02	.38025139E+01	.26826008E+00	P8	unstable
.45106481E+02	.76050264E+01	.26830890E+00	P16	stable
.45106551E+02	.76051153E+01	.26816345E+00	P16	unstable
.45106551E+02	.15210230E+02	.26846988E+00	P32	stable

Table 5.2: Motion about TP1 (cf. Fig. 5.37).

$\lambda(\uparrow)$	T	max z_1 : $z_5 = 0$	Motion type	Stability
.41690173E+02	.14674223E+00	.53032141E+01	SN	stable
.42548870E+02	.14175458E+00	.55130582E+01	UN	unstable
.42548870E+02			QPM	
$\lambda(\downarrow)$	T	max z_1 : $z_5 = 0$	Motion type	Stability
.41690173E+02	.14674223E+00	.53032141E+01	SN	stable
.41670221E+02	.14679947E+00	.53001344E+01	SN	stable
.40454419E+02	.14901721E+00	.50118265E+01	SN	stable

Table 5.3: Motion past H (cf. Fig. 5.37).

$\lambda(\uparrow)$	T	$\max z_1 : z_5 = 0$	*Motion type*	*Stability*
.40906308E+02	.54559788E+00	.20795220E-03	SN	stable
.41011267E+02	.55339957E+00	.10365322E+00	UN	unstable
.41011267E+02	.11074027E+01	.92148183E-01	P2	stable
.41021192E+02	.11112766E+01	.12582815E+00	P2	unstable
.41021192E+02	.22224569E+01	.12587073E+00	P4	stable
.41022284E+02	.22231401E+01	.12672274E+00	P4	unstable
.41022284E+02	.44462831E+01	.12681876E+00	P8	stable
.41022503E+02	.44466073E+01	.12730508E+00	P8	unstable

Table 5.4: Motion prior to H1 (cf. Fig. 5.39).

$-L_1^*(\downarrow)$	T	$\max z_1 : z_5 = 0$	*Motion type*	*Stability*
.18744727E+02	.12005298E+00	.26747620E-01	UN	unstable
.17538763E+02	.12073563E+00	.64164044E+00	UN	unstable

Table 5.5: Motion prior to H2 (cf. Fig. 5.39).

$-L_1^*(\downarrow)$	T	$\max z_1 : z_5 = 0$	*Motion type*	*Stability*
.25363203E+02	.12244570E+00	.61199071E-02	SN	stable
.22828150E+02	.12388885E+00	.29854028E+00	UN	unstable
.22828150E+02			QPM	

Table 5.6: Motion past H3 (cf. Fig. 5.39).

$-L_1^*(\uparrow)$	T	$\max z_1 : z_5 = 0$	*Motion type*	*Stability*
.648416646810E+01	.75877913E+00	.88366768E-04	SN	stable
.648464349177E+01	.76733867E+00	.28763125E-01	UN	unstable
.648464349177E+01	.15350455E+01	.26576941E-01	P2	stable
.648469702835E+01	.15403858E+01	.23026538E-01	P2	unstable
.648469702835E+01	.30807199E+01	.23650810E-01	P4	stable
.648470420000E+01	.30818594E+01	.35666556E-01	P4	unstable
.648470420000E+01	.61637271E+01	.35708451E-01	P8	stable
.648470545808E+01	.61642039E+01	.35859140E-01	P8	unstable

Table 5.7: Coexisting unstable motion about H3 (cf. Fig. 5.39).

$-L_1^*(\uparrow)$	T	max z_1 : $z_5 = 0$	*Motion type*	*Stability*
.64841666E+01	.11228076E+01	.33379227E-01	UN	unstable
.64872083E+01	.89659804E+00	.91244961E-01	UN	unstable
$-L_1^*(\downarrow)$	T	max z_1 : $z_5 = 0$	*Motion type*	*Stability*
.64841666E+01	.11228068E+01	.33379818E-01	UN	unstable
.64832136E+01	.11513977E+01	.13268620E-01	UN	unstable

Table 5.8: Motion past H ($\lambda = 37$, cf. Fig. 5.40).

$-L_1^*(\uparrow)$	T	max z_1 : $z_5 = 0$	*Motion type*	*Stability*
.643286189708E+01	.66045592E+00	.13502372E-03	SN	stable
.643415379073E+01	.67029534E+00	.51112414E-01	UN	unstable
.643415379073E+01	.13433266E+01	.39683186E-01	P2	stable
.643418162838E+01	.13444783E+01	.38833094E-01	P2	unstable
.643418162838E+01	.26888523E+01	.59654888E-01	P4	stable
.643419557365E+01	.26897397E+01	.60120256E-01	P4	unstable
.643419557365E+01	.53794840E+01	.60174020E-01	P8	stable
.643419840529E+01	.53799105E+01	.60421536E-01	P8	unstable

Table 5.9: Motion about TP1 (cf. Fig. 5.40).

$-L_1^*(\uparrow)$	T	max z_1 : $z_5 = 0$	*Motion type*	*Stability*
.771248430000E+01	.27745235E+00	.55990937E+00	SN	stable
.791221752197E+01	.27072663E+00	.69340328E+00	UN	unstable
.791221752197E+01			QPM	
$-L_1^*(\downarrow)$	T	max z_1 : $z_5 = 0$	*Motion type*	*Stability*
.771248430000E+01	.27745235E+00	.55990937E+00	SN	stable
.760268308664E+01	.28398192E+00	.52515844E+00	UN	unstable
.760268308664E+01			QPM	

Table 5.10: Motion past H ($\lambda = 43$, cf. Fig. 5.40).

$-L_1^*(\uparrow)$	T	max $z_1 : z_5 = 0$	*Motion type*	*Stability*
.620518218889E+01	.50058650E+00	.25023776E-03	SN	stable
.621268025521E+01	.51175794E+00	.87581411E-01	UN	unstable
.621268025521E+01	.10239027E+01	.15611906E+00	P2	stable
.621338826743E+01	.10283543E+01	.17596841E+00	P2	unstable
.621338826743E+01	.20566988E+01	.17604639E+00	P4	stable
.621349002276E+01	.20577813E+01	.17770197E+00	P4	unstable
.621349002276E+01	.41155628E+01	.17773998E+00	P8	stable

Table 5.11: Motion past H ($L_1^* = -5.3$, cf. Fig. 5.43).

$\lambda(\uparrow)$	T	max $z_1 : z_5 = 0$	*Motion type*	*Stability*
.399800887691E+02	.50942077E+00	.58574840E-03	SN	stable
.402714420357E+02	.51737969E+00	.15019151E+00	UN	unstable
.402714420357E+02	.10347665E+01	.15181899E+00	P2	stable
.403067898132E+02	.10398989E+01	.18595873E+00	P2	unstable
.403067898132E+02	.20797946E+01	.18588311E+00	P4	stable
.403112433994E+02	.20808586E+01	.18670910E+00	P4	unstable
.403112433994E+02	.41617187E+01	.18660764E+00	P8	stable
.403118824661E+02	.41620801E+01	.18892821E+00	P8	unstable

Table 5.12: Motion past H ($L_1^* = -5.4$, cf. Fig. 5.43).

$\lambda(\uparrow)$	T	max $z_1 : z_5 = 0$	*Motion type*	*Stability*
.369517622638E+02	.55858597E+00	.57176982E-03	SN	stable
.371390550241E+02	.56658003E+00	.10184718E+00	UN	unstable
.371390550241E+02	.11332288E+01	.98323347E-01	P2	stable
.371612101153E+02	.11382635E+01	.12546337E+00	P2	unstable
.371612101153E+02	.22765208E+01	.12551513E+00	P4	stable
.371640546192E+02	.22775710E+01	.12686657E+00	P4	unstable
.371640546192E+02	.45551427E+01	.12691297E+00	P8	stable
.371644886055E+02	.45555230E+01	.12748020E+00	P8	unstable

Table 5.13: Motion past H ($\lambda = 32$, cf. Fig. 5.44).

$-L_1^*(\uparrow)$	T	max z_1 : $z_5 = 0$	*Motion type*	*Stability*
.552581727289E+01	.65123105E+00	.34689776E-03	SN	stable
.552790522668E+01	.66214208E+00	.59111200E-01	UN	unstable
.552790522668E+01	.13243017E+01	.58163373E-01	P2	stable
.552817502353E+01	.13312123E+01	.73468115E-01	P2	unstable
.552817502353E+01	.26621734E+01	.73474477E-01	P4	stable
.552818919516E+01	.26627710E+01	.73791861E-01	P4	unstable
.552818919516E+01	.53255562E+01	.73905649E-01	P8	stable
.552819345561E+01	.53259764E+01	.74149908E-01	P8	unstable

Table 5.14: Motion about TP1 (cf. Fig. 5.44).

$-L_1^*(\uparrow)$	T	max z_1 : $z_5 = 0$	*Motion type*	*Stability*
.680658590000E+01	.24836834E+00	.25656915E+01	SN	stable
.700627577997E+01	.24279073E+00	.26397234E+01	UN	unstable
.700627577997E+01			QPM	
$-L_1^*(\downarrow)$	T	max z_1 : $z_5 = 0$	*Motion type*	*Stability*
.680658590000E+01	.24836834E+00	.25656915E+01	SN	stable
.677664087946E+01	.24922712E+00	.25542532E+01	UN	unstable
.677664087946E+01			QPM	

Table 5.15: Motion past H ($\lambda = 42$, cf. Fig. 5.44).

$-L_1^*(\uparrow)$	T	max z_1 : $z_5 = 0$	*Motion type*	*Stability*
.521708085045E+01	.47761951E+00	.75905771E-02	SN	stable
.523436265574E+01	.49210247E+00	.19741698E+00	UN	unstable
.523436265574E+01	.98454103E+00	.21092792E+00	P2	stable
.523610241579E+01	.99073338E+00	.24282863E+00	P2	unstable
.523610241579E+01	.19814114E+01	.24294207E+00	P4	stable
.523629725010E+01	.19826569E+01	.24480662E+00	P4	unstable
.523629725010E+01	.39653179E+01	.24506320E+00	P8	stable
.523632801815E+01	.39657528E+01	.24592788E+00	P8	unstable

Table 5.16: Motion past supercritical Hopf bifurcation point, i.e., motion beyond λ_F; HSDT; imperfect panel ($\hat{a}_{11} = 0.2$); $L_1^* = 0$ (cf. Fig. 5.9).

$\lambda(\uparrow)$	T	$\max z_1 : z_5 = 0$	*Motion type*	*Stability*
.281029450000E+03	.58877571E-01	.31771749E-03	SN	stable
.281204457172E+03	.58843665E-01	.38531796E-02	SN	stable
.281804454818E+03	.58737366E-01	.70789802E-02	SN	stable
.282504452053E+03	.58635004E-01	.85948481E-02	SN	stable
.282512822315E+03	.58633938E-01	.86063041E-02	UN	unstable

Table 5.17: Motion past supercritical Hopf bifurcation point, i.e., motion beyond λ_F; HSDT; imperfect panel ($\hat{a}_{11} = 0.2$); $L_1^* = -5.3$, linear aerodynamics (cf. Fig. 5.8).

$\lambda(\uparrow)$	T	$\max z_1 : z_5 = 0$	*Motion type*	*Stability*
.457982460000E+02	.51482314E+00	.15046569E-02	SN	stable
.461964177438E+02	.52184748E+00	.12109041E+00	UN	unstable
.461964177438E+02	.10441483E+01	.11027886E+00	P2	stable
.462383876952E+02	.10488966E+01	.95525294E-01	P2	unstable
.462383876952E+02	.20977540E+01	.97839594E-01	P4	stable
.462439840983E+02	.20987458E+01	.15076253E+00	P4	unstable

Table 5.18: Motion past H{0} ($L_1^* = -5.8$, cf. Fig. 5.46).

$\lambda(\uparrow)$	T	$\max z_1 : z_5 = 0$	*Motion type*	*Stability*
.351134850000E+02	.17528856E+01	.61232436E-02	SS	stable
.352254848801E+02	.16522372E+01	.63827358E-01	US	unstable
.352254848801E+02	.16522372E+01	.67686926E-01	SB	stable
.352494848505E+02	.16548883E+01	.54255185E-01	SB	unstable
.352494848505E+02	.33096252E+01	.53160279E-01	P2	stable
.352531832752E+02	.33097591E+01	.59084932E-01	P2	unstable
.352531832752E+02	.66195192E+01	.59161574E-01	P4	stable
.352539042249E+02	.66200360E+01	.60535712E-01	P4	unstable
.352539042249E+02	.13240069E+02	.60495503E-01	P8	stable
.352540549519E+02	.13240223E+02	.60787566E-01	P8	unstable
.352540549519E+02	.26480450E+02	.60765893E-01	P16	stable
.352540648408E+02	.26480475E+02	.60763029E-01	P16	stable

Table 5.19: Motion past H1 (cf. Fig. 5.54).

$-L_1^*(\uparrow)$	T	$\max z_1 : z_5 = 0$	*Motion type*	*Stability*
.287653655205E+02	.60100231E-01	.29585288E-02	SN	stable
.288847273777E+02	.60353622E-01	-.17459464E-01	UN	unstable
.288847273777E+02			QPM	

Table 5.20: Motion past H2 (cf. Fig. 5.54).

$-L_1^*(\uparrow)$	T	$\max z_1 : z_5 = 0$	*Motion type*	*Stability*
.357662929421E+02	.55096270E-01	.45471870E-02	UN	unstable
.450685866412E+02	.56313334E-01	.14779276E+00	UN	unstable

Table 5.21: Motion prior to H3 (cf. Fig. 5.54).

$-L_1^*(\downarrow)$	T	$\max z_1 : z_5 = 0$	*Motion type*	*Stability*
.620632687758E+02	.12769200E+00	.14306267E-02	UN	unstable
.618229085266E+02	.14104101E+00	.47054347E+00	UN	unstable

127

Table 5.22: Motion past H{0} (cf. Fig. 5.55).

$-L_1^*(\uparrow)$	T	$\max z_1 : z_5 = 0$	*Motion type*	*Stability*
.583586809154E+01	.34354155E+01	.22404979E-03	SS	stable
.583607906921E+01	.34210367E+01	.15118345E-01	US	unstable
.583607906921E+01	.34263391E+01	.16205688E-01	SB	stable
.583610914485E+01	.34519568E+01	.12346486E-01	SB	unstable
.583610914485E+01	.69018875E+01	.11772454E-01	P2	stable
.583611221860E+01	.69061196E+01	.13528078E-01	P2	unstable

Table 5.23: Motion past H{0} (supercritical), i.e., motion beyond λ_F; CPT; perfect panel; $\lambda = 39$ (cf. Fig. 5.1 or Fig. 5.3).

$-L_1^*(\uparrow)$	T	$\max z_1 : z_5 = 0$	*Motion type*	*Stability*
.567553046533E+01	.92705502E+00	.65967566E-03	SS	stable
.576737115399E+01	.76629962E+00	.41826169E+00	US	unstable
.576737115399E+01	.76647105E+00	.40865302E+00	SB	stable
.577254633910E+01	.81989149E+00	.56289669E+00	SB	unstable

Table 5.24: Motion past H{0} ($L_1^* = -5.0$, cf. Fig. 5.58).

$\lambda(\uparrow)$	T	$\max z_1 : z_5 = 0$	*Motion type*	*Stability*
.233421549911E+02	.61562651E+01	.15893916E-03	SS	stable
.233431449450E+02	.61337121E+01	.46803350E-02	US	unstable
.233431449450E+02	.61348561E+01	.48180423E-02	SB	stable
.233433431322E+02	.61845389E+01	.57743754E-02	SB	unstable
.233433431322E+02	.12368179E+02	.57348892E-02	P2	stable
.233433927211E+02	.12387630E+02	.59932932E-02	P2	unstable
.233433927211E+02	.24777157E+02	.60146850E-02	P4	stable
.233433943134E+02	.24778840E+02	.60210297E-02	P4	unstable
.233433943134E+02	.49557629E+02	.60211110E-02	P8	stable
.233433947377E+02	.49558433E+02	.59719604E-02	P8	stable

Table 5.25: Motion past H{0} (cf. Fig. 5.68).

$-L_1^*(\uparrow)$	T	$\max z_1 : z_5 = 0$	*Motion type*	*Stability*
.497915733685E+01	.24413151E+01	.74882528E-03	SS	stable
.498025189963E+01	.24350615E+01	.27779394E-01	US	unstable
.498025189963E+01	.24363591E+01	.27168439E-01	SB	stable
.498041232317E+01	.24552778E+01	.22986852E-01	SB	unstable
.498041232317E+01	.49098439E+01	.22248526E-01	P2	stable
.498043270743E+01	.49134351E+01	.24865734E-01	P2	unstable
.498043270743E+01	.98269053E+01	.25001475E-01	P4	stable
.498043782707E+01	.98292740E+01	.25442032E-01	P4	unstable
.498043782707E+01	.19658545E+02	.25425749E-01	P8	stable
.498043905023E+01	.19659561E+02	.25562331E-01	P8	unstable

Table 5.26: Unstable motion prior to H1 (cf. Fig. 5.68).

$-L_1^*(\downarrow)$	T	$\max z_1 : z_5 = 0$	*Motion type*	*Stability*
.159279401748E+02	.92265432E-01	.78683260E-03	UN	unstable
.158760342409E+02	.95135451E-01	-.48128206E-01	UN	unstable

Table 5.27: Motion past H1 (cf. Figs. 5.68, 5.69).

$-L_1^*(\uparrow)$	T	$\max z_1 : z_5 = 0$	*Motion type*	*Stability*
.160771148936E+02			QPM	
.160771148936E+02	.99221252E-01	-.12893554E+00	UN	unstable
.161762027628E+02	.99839226E-01	-.14013450E+00	SN	stable
.164735428013E+02	.10101666E+00	-.16493192E+00	UN	unstable
.164735428013E+02	.20218756E+00	-.14373765E+00	P2	stable
.168106621204E+02	.20559189E+00	-.13688439E+00	P2	unstable
.168106621204E+02	.41108671E+00	-.17927960E+00	P4	stable
.168304961206E+02	.41087612E+00	-.19686630E+00	P4	unstable
.168304961206E+02			QPM	

Table 5.28: Motion past H2 (cf. Fig. 5.68).

$-L_1^*(\uparrow)$	T	max z_1 : $z_5 = 0$	*Motion type*	*Stability*
.195338888295E+02	.85232367E-01	.30149467E-02	UN	unstable
.213403492042E+02	.92009075E-01	.14750902E+00	UN	unstable

Table 5.29: Motion prior to H3 (cf. Fig. 5.68).

$-L_1^*(\downarrow)$	T	max z_1 : $z_5 = 0$	*Motion type*	*Stability*
.189849159923E+02	.25309413E+00	.14248529E-02	UN	unstable
.188296730678E+02	.27846700E+00	.37291706E-01	UN	unstable

Table 5.30: Motion prior to H4 (cf. Fig. 5.68).

$-L_1^*(\downarrow)$	T	max z_1 : $z_5 = 0$	*Motion type*	*Stability*
.242286955037E+02	.31784759E+00	.15005867E-02	SN	stable
.242192340223E+02	.31853974E+00	.12301141E-01	UN	unstable
.242192340223E+02	.63703018E+00	.12959834E-01	P2	stable
.242182564054E+02	.63698724E+00	.14257783E-01	P2	unstable
.242182564054E+02	.12739835E+01	.14240090E-01	P4	stable
.242181437504E+02	.12740185E+01	.14342875E-01	P4	unstable
.242181437504E+02	.25480369E+01	.14345375E-01	P8	stable

Table 5.31: Motion past H{0} (cf. Fig. 5.71).

$-L_1^*(\uparrow)$	T	max z_1 : $z_5 = 0$	*Motion type*	*Stability*
.488486920729E+01	.11100582E+01	.74174260E-03	SS	stable
.491323041842E+01	.10891031E+01	.14845231E+00	US	unstable
.491323041842E+01	.10921903E+01	.16108722E+00	SB	stable
.491873041162E+01	.11327093E+01	.19775183E+00	SB	stable
.491883041150E+01	.11339287E+01	.19827104E+00	SB	unstable

Table 5.32: Motion past H (edges $x_2 = 0, l_2$ are movable, cf. Fig. 5.73).

$\lambda(\uparrow)$	T	max z_1 : $z_5 = 0$	Motion type	Stability
.483269600000E+02	.39466735E+00	.18795804E-01	SN	stable
.487306970353E+02	.40241242E+00	.75668799E+00	SN	stable

Table 5.33: Motion past H (edges $x_2 = 0, l_2$ are immovable, cf. Fig. 5.73).

$\lambda(\uparrow)$	T	max z_1 : $z_5 = 0$	Motion type	Stability
.498632650000E+02	.46810166E+00	.14646955E-01	SN	stable
.500136380310E+02	.48112640E+00	.22803843E+00	UN	unstable
.500136380310E+02	.96398701E+00	.18882884E+00	P2	stable
.500235439883E+02	.96842075E+00	.17371982E+00	P2	unstable
.500235439883E+02	.19367442E+01	.18047643E+00	P4	stable
.500253271527E+02	.19380611E+01	.27917738E+00	P4	unstable

Table 5.34: Motion past H (edges $x_2 = 0, l_2$ are movable, cf. Fig. 5.74).

$-L_1^*(\uparrow)$	T	max z_1 : $z_5 = 0$	Motion type	Stability
.583820990000E+01	.40161201E+00	.35502268E-03	SN	stable
.589551518192E+01	.42687591E+00	.57526358E+00	UN	unstable
.589551518192E+01	.85312197E+00	.66029033E+00	P2	stable
.590339115481E+01	.85634831E+00	.78313659E+00	P2	unstable
.590339115481E+01	.17130425E+01	.78386430E+00	P4	stable
.590550939334E+01	.17157773E+01	.80680880E+00	P4	unstable
.590550939334E+01	.34315162E+01	.80483689E+00	P8	stable
.590563041168E+01	.34318496E+01	.80808361E+00	P8	stable

Table 5.35: Motion past H (edges $x_2 = 0, l_2$ are immovable, cf. Fig. 5.74).

$-L_1^*(\uparrow)$	T	max z_1 : $z_5 = 0$	Motion type	Stability
.589311800000E+01	.54241695E+00	.16033122E-02	SN	stable
.589586603518E+01	.55373412E+00	.10172905E+00	UN	unstable
.589586603518E+01	.11079986E+01	.92015582E-01	P2	stable
.589612980567E+01	.11132346E+01	.12372178E+00	P2	unstable
.589612980567E+01	.22264449E+01	.12379433E+00	P4	stable
.589616864720E+01	.22277007E+01	.12500396E+00	P4	unstable

131

Table 5.36: Motion past H (edges $x_2 = 0, l_2$ are movable, cf. Fig. 5.75).

$\lambda(\uparrow)$	T	max z_1 : $z_5 = 0$	*Motion type*	*Stability*
.469855780000E+02	.39943785E+00	.21451899E-01	SN	stable
.470865036643E+02	.40252185E+00	.34125278E+00	SN	stable

Table 5.37: Motion past H (edges $x_2 = 0, l_2$ are immovable, cf. Fig. 5.75).

$\lambda(\uparrow)$	T	max z_1 : $z_5 = 0$	*Motion type*	*Stability*
.501491550000E+02	.46013451E+00	.26231751E-01	SN	stable
.505683978507E+02	.47213289E+00	.28716658E+00	UN	unstable
.505683978507E+02	.94458456E+00	.30224526E+00	P2	stable
.506556671928E+02	.98296494E+00	.46173414E+00	P2	stable

Table 5.38: Motion past H and past turning point of dynamic solution (edges $x_2 = 0, l_2$ are movable, cf. Fig. 5.76).

$-L_1^*(\uparrow)$	T	max z_1 : $z_5 = 0$	*Motion type*	*Stability*
.498203220000E+01	.41484348E+00	.29387420E-03	SN	stable
.503653244050E+01	.43867989E+00	.56612462E+00	SN	stable
.503719055016E+01	.43993564E+00	.57335584E+00	SN	stable
.503726367431E+01	.44216841E+00	.57502027E+00	UN	unstable
$-L_1^*(\downarrow)$	T	max z_1 : $z_5 = 0$	*Motion type*	*Stability*
.503726367431E+01	.44216841E+00	.57502027E+00	UN	unstable
.502956974521E+01	.44681857E+00	.51225250E+00	UN	unstable
.501480742759E+01	.44961017E+00	.41910746E+00	UN	unstable
.500960368164E+01	.45064050E+00	.39616661E+00	UN	unstable

132

Table 5.39: Motion past H (edges $x_2 = 0, l_2$ are immovable, cf. Fig. 5.76).

$-L_1^*(\uparrow)$	T	max z_1 : $z_5 = 0$	*Motion type*	*Stability*
.504005970000E+01	.56472612E+00	.11380982E-02	SN	stable
.504297809669E+01	.57439889E+00	.77476982E-01	UN	unstable
.504297809669E+01	.11495515E+01	.68436419E-01	P2	stable
.504325178669E+01	.11542966E+01	.60748731E-01	P2	unstable
.504325178669E+01	.23084510E+01	.58543923E-01	P4	stable
.504328156874E+01	.23092710E+01	.95146317E-01	P4	unstable
.504328156874E+01	.46150819E+01	.96999805E-01	P8	stable

Table 5.40: Motion past H1 (cf. Fig. 5.77).

$\lambda(\uparrow)$	T	max z_1 : $z_5 = 0$	*Motion type*	*Stability*
.511534830546E+02	.60202152E+00	.10997608E-02	SN	stable
.514320576100E+02	.64224457E+00	.47564696E-01	SN	stable
.515315576426E+02	.65514990E+00	.48647987E-01	SN	stable
.516310474850E+02	.66753784E+00	.48206916E-01	SN	stable
.524064434839E+02	.75268830E+00	.44375268E-02	SN	stable

Table 5.41: Motion prior to H2 (cf. Fig. 5.77).

$\lambda(\downarrow)$	T	max z_1 : $z_5 = 0$	*Motion type*	*Stability*
.524086699438E+02	.75291013E+00	.24989491E-02	SN	stable
.516253196321E+02	.66683696E+00	.48262887E-01	SN	stable
.515258291419E+02	.65442191E+00	.48633937E-01	SN	stable
.514263285553E+02	.64148339E+00	.47437267E-01	SN	stable
.511576363492E+02	.60268449E+00	.92346881E-02	SN	stable

Table 5.42: Motion prior to H{0} (edges $x_2 = 0, l_2$ are movable, cf. Fig. 5.78).

$-L_1^*(\downarrow)$	T	max z_1 : $z_5 = 0$	*Motion type*	*Stability*
.533024067895E+01	.53259108E+00	.36956387E-02	US	unstable
.528047859741E+01	.43898584E+00	.51207456E+00	US	unstable

133

Table 5.43: Motion prior to H{0} (edges $x_2 = 0, l_2$ are immovable, cf. Fig. 5.78).

$-L_1^*(\downarrow)$	T	max z_1 : $z_5 = 0$	*Motion type*	*Stability*
.532970184251E+01	.20364948E+01	.36766561E-02	US	unstable
.531574575203E+01	.12864481E+01	.17560471E+00	US	unstable

Table 5.44: Motion past H1 (cf. Fig. 5.78).

$-L_1^*(\uparrow)$	T	max z_1 : $z_5 = 0$	*Motion type*	*Stability*
.526327070295E+01	.63064575E+00	.28147974E-02	SN	stable
.527887413425E+01	.76285461E+00	.76421171E-01	UN	unstable
.527887413425E+01	.15253783E+01	.75879759E-01	P2	stable
.527997038313E+01	.15413996E+01	.75063319E-01	P2	unstable
.527997038313E+01	.30828648E+01	.75417105E-01	P4	stable
.528011070530E+01	.30874753E+01	.75900288E-01	P4	unstable

Table 5.45: Motion prior to H2 (cf. Fig. 5.78).

$-L_1^*(\downarrow)$	T	max z_1 : $z_5 = 0$	*Motion type*	*Stability*
.532744508951E+01	.18402358E+01	.76547166E-03	SN	stable
.532713746399E+01	.18227675E+01	.89896089E-02	UN	unstable
.532713746399E+01	.36455480E+01	.89492477E-02	P2	stable
.532708957692E+01	.36424322E+01	.94135601E-02	P2	unstable
.532708957692E+01	.72848609E+01	.94733674E-02	P4	stable
.532708088291E+01	.72839782E+01	.97287429E-02	P4	unstable

Table 5.46: Lyapunov exponents and Kaplan-Yorke dimension (d_L).

| Case cf. | $\hat{\lambda}_1$ | $\hat{\lambda}_2$ | $\hat{\lambda}_3$ | $\hat{\lambda}_4$ | Comment | d_L | Motion |
	$\hat{\lambda}_5$	$\hat{\lambda}_6$	$\hat{\lambda}_7$	$\hat{\lambda}_8$			
Fig. 5.18	.2187E-03	-.1688E-04	-.3989E-02	-.6216E-01	$\hat{\lambda}_1 \approx 0$,	≈ 2.00	QPM
	-.6230E-01	-.1028E+00	-.2415E+00	-.2415E+00	$\hat{\lambda}_2 \approx 0$		(T^2 torus)
Fig. 5.20	.8308E+00	.2289E-01	.4776E-04	-.3047E-01	$\hat{\lambda}_3 \approx 0$	7.36	chaotic
	-.7561E-01	-.1349E+00	-.2146E+00	-.1112E+01			
Fig. 5.35	.1448E+00	.1568E-03	-.4085E+00	-.4086E+00	$\hat{\lambda}_2 \approx 0$	2.36	chaotic
	-.4090E+00	-.4090E+00	-.8155E+00	-.9639E+00			
Fig. 5.41	.9138E+00	.3802E+00	.1059E-02	-.1167E+00	$\hat{\lambda}_3 \approx 0$	5.69	chaotic
	-.5223E+00	-.9506E+00	-.1205E+01	-.1769E+01			
Fig. 5.48	.1907E+01	-.1439E-05	-.4013E+00	-.4085E+00	$\hat{\lambda}_2 \approx 0$	6.38	chaotic
	-.4089E+00	-.4165E+00	-.7038E+00	-.2837E+01			
Fig. 5.52	.1579E+01	.5187E+00	.9115E-04	-.2209E+00	$\hat{\lambda}_3 \approx 0$	6.55	chaotic
	-.4286E+00	-.6644E+00	-.1415E+01	-.2638E+01			
Fig. 5.56	.3124E+01	.9493E+00	.1371E-02	-.5240E-01	$\hat{\lambda}_3 \approx 0$	7.16	chaotic
	-.4708E+00	-.8921E+00	-.2013E+01	-.3916E+01			
Fig. 5.61	.1967E+01	.2138E-03	-.3545E+00	-.4054E+00	$\hat{\lambda}_2 \approx 0$	6.54	chaotic
	-.4071E+00	-.4307E+00	-.6725E+00	-.2956E+01			
Fig. 5.69 $L_1^* = -15.928$	.2005E-03	-.1669E-04	-.3942E+00	-.3944E+00	$\hat{\lambda}_1 \approx 0$,	≈ 2.00	QPM
	-.4328E+00	-.4329E+00	-.8025E+00	-.8028E+00	$\hat{\lambda}_2 \approx 0$		(T^2 torus)
Fig. 5.69 $L_1^* = -15.968$	.6388E-03	.7795E-04	-.3956E+00	-.3958E+00	$\hat{\lambda}_1 \approx 0$,	≈ 2.00	QPM
	-.4359E+00	-.4360E+00	-.6264E+00	-.9703E+00	$\hat{\lambda}_2 \approx 0$		(T^2 torus)

Chapter 6

CONCLUSIONS AND FUTURE RESEARCH

6.1 Conclusions

The nonlinear dynamical behavior of a flat composite panel subjected to a high super-sonic gas flow of arbitrary orientation has been studied. The governing equations for a laterally compressed panel, possessing small initial imperfections and possible in-plane edge restraints, were derived using a higher-order shear deformation theory and third-order piston theory aerodynamics. The panel flutter equations obtained via Galerkin's method were solved using numerical integration in conjunction with the Arclength Continuation Method for the static solution. Periodic solutions were obtained by a predictor-corrector numerical integration technique (i.e., the NIM2) which also predicts the bifurcation of solutions. The amplitudes and frequency of flutter obtained by the NIM2 were compared with results from the Method of Multiple Scales. Based on the results obtained the following conclusions are drawn :

- In the case of both perfect and imperfect panels, the CPT yields larger instability loads (i.e., flow speeds and compressive edge loads) than the HSDT. Moreover, only the HSDT model is sensitive to variations in the transverse shear rigidity of the panel, i.e., it predicts lower instability loads for panels with greater transverse shear flexibility.

- As the imperfection (in the first mode) is increased, the flutter speeds are lowered when the compressive loads are small to moderate. For large compressive loads the behavior is imperfection insensitive.

136

- The compressive loads at which divergence occurs for perfect panels are lower when the edges parallel to the flow are restrained. However, such edge restraints have no visible effect on the flutter speeds. In the case of imperfect panels, the flutter speeds are slightly lower when the compressive load is small and the edges are restrained.

- When considering a nonlinear aerodynamic model, multiple flutter speeds exist for imperfect panels. For small values of the compressive load, the aerodynamically non-linear model predicts higher flutter speeds than its linearized counterpart. This trend is reversed for larger compressive loads.

- For perfect panels, the immediate post-flutter amplitudes and frequency obtained by the MMS and NIM2 compare well when an aerodynamically linear theory is considered and compressive loads are absent. For all cases studied, the NIM2 always predicts higher amplitudes and lower frequencies of flutter.

- The presence of aerodynamic nonlinearities could result in hard flutter oscillations, especially in the case of thick panels. In this regard, it may be noted that the aero-dynamically linear model correctly predicts the immediate post-flutter behavior of thin panels only. Furthermore, the results obtained by the MMS and NIM2 regarding the type of flutter (i.e., whether hard or soft flutter oscillations exist for post-flutter speeds) are always in agreement. This implies that the MMS can also be used to determine the character of the flutter boundary (see Librescu [5,6]).

- For an imperfect panel, it appears that the presence of aerodynamic nonlinearities yields higher amplitudes of soft flutter oscillations than those obtained when using linear aerodynamics. However, it may be argued that a true comparison of flutter amplitudes cannot be made since the flutter speeds predicted by the two theories are not the same.

- For both perfect and imperfect panels, it was observed that the onset of flutter is not always preceded by a Hopf bifurcation, i.e., a sudden jump from a stable static

equilibrium state to one of flutter is also possible. For the case of imperfect panels the region in the λ–L_1^* plane where the transition from Hopf-bifurcation instability to jump-type instability occurs was studied. Within this region, multiple periodic solutions (both stable and unstable) may be found to coexist with the stable static solution, i.e., the panel can remain buckled or flutter. Hard flutter motions are also possible within this region.

- For the case of perfect panels, the region in the λ–L_1^* plane where the divergence and flutter boundaries meet was studied. In this case, flutter about the trivial equilibrium may coexist with the buckled state or multiple buckled states may coexist, indicating that the panel could snap-through to a new buckled configuration and subsequently snap back or undergo flutter oscillations about this new buckled configuration. Hard flutter oscillations in the form of quasiperiodic and periodic motion were also obtained.

- For imperfect panels, chaotic motions appear after a sequence of period-doubling bifurcations as either λ or L_1^* is varied. For perfect panels, as the control parameter is varied beyond the turning point of the static solution, a transition from chaotic motions to periodic states (and vice-versa) occurs. Another scenario of chaotic motions was observed for perfect panels, i.e., one in which bounded non-periodic motion exists between three unstable periodic solutions.

- For the case of perfect panels without compressive edge loads, a panel with movable edges exhibits higher amplitudes of flutter oscillations and is more susceptible to hard flutter than when its edges normal to the flow are immovable.

- For the case of both perfect and imperfect panels, the static displacements are larger when the edges parallel to the flow are immovable than when all edges are movable. However, in the case of perfect panels the amplitudes of flutter oscillations in the immediate post-flutter region are not affected by edge restraints.

- For a perfect panel with its edges parallel to the flow restrained, as the flow speed is increased the buckled panel may experience soft flutter oscillations about the unstable non-trivial equilibrium. This behavior is not obtained when the edges are unrestrained (for which flutter always occurs about the trivial equilibrium). Furthermore, hard flutter motion about the flat state may coexist with either the buckled state or these soft flutter oscillations about the unstable non-trivial equilibrium.

6.2 Recommendations For Future Research

- A more sophisticated numerical integration method, e.g., one based on continuation techniques, should be considered so that turning points of the dynamic solution may be negotiated (see, e.g., Seydel[46] and Nayfeh and Balachandran[85]). This would yield amplitudes of hard flutter oscillations without having to resort to the straightforward integration method which may or may not converge to the hard flutter solution.

- The case of internal resonance arising for certain special values of the system parameters, e.g., h, Λ, ϕ, etc., when the total damping is negligible, needs to be examined.

- The effect of the modal truncations considered in the numerical examples should be examined (although the computations will become increasingly cumbersome as more terms are included in Galerkin's method).

- An aeroelastic tailoring analysis should be performed by considering other types of anisotropy for the laminate, e.g., one composed of angle-ply layers.

- Various other out-of-plane boundary conditions for the panel should also be considered for a more comprehensive study of the panel flutter problem.

- An additional refinement of the structural model may also be considered by fulfilling the static continuity conditions for the transverse shear stresses between contiguous layers of the laminate. Such a theory would allow one to predict, with greater accuracy, the failure of the panel in the post-flutter regime.

Appendix A

COEFFICIENTS IN GOVERNING EQUATIONS

A.1 Expressions of Rigidity Quantities

$$F_{\alpha\beta\omega\rho} = 2\tilde{E}_{\alpha\beta\omega\rho}^{<m+1>}h_{<m+1>} + 2\sum_{r=1}^{m}\tilde{E}_{\alpha\beta\omega\rho}^{<r>}(h_{<r>} - h_{<r+1>})$$

$$K_{\alpha\beta\omega\rho} = \frac{2}{3}\frac{E_{\alpha\beta33}^{<m+1>}}{E_{3333}^{<m+1>}}E_{\omega3\rho3}^{<m+1>}h_{<m+1>}^{3} + \frac{2}{3}\sum_{r=1}^{m}\frac{E_{\alpha\beta33}^{<r>}}{E_{3333}^{<r>}}E_{\omega3\rho3}^{<r>}(h_{<r>}^{3} - h_{<r+1>}^{3})$$

$$D_{\alpha\beta\omega\rho} = \frac{2}{3}\tilde{E}_{\alpha\beta\omega\rho}^{<m+1>}h_{<m+1>}^{3} + \frac{2}{3}\sum_{r=1}^{m}\tilde{E}_{\alpha\beta\omega\rho}^{<r>}(h_{<r>}^{3} - h_{<r+1>}^{3})$$

$$S_{\alpha\beta\omega\rho} = \frac{2}{5}\tilde{E}_{\alpha\beta\omega\rho}^{<m+1>}h_{<m+1>}^{5} + \frac{2}{5}\sum_{r=1}^{m}\tilde{E}_{\alpha\beta\omega\rho}^{<r>}(h_{<r>}^{5} - h_{<r+1>}^{5}) \tag{A.1}$$

$$N_{\alpha\beta\omega\rho} = \frac{2}{5}\frac{E_{\alpha\beta33}^{<m+1>}}{E_{3333}^{<m+1>}}E_{\omega3\rho3}^{<m+1>}h_{<m+1>}^{5} + \frac{2}{5}\sum_{r=1}^{m}\frac{E_{\alpha\beta33}^{<r>}}{E_{3333}^{<r>}}E_{\omega3\rho3}^{<r>}(h_{<r>}^{5} - h_{<r+1>}^{5})$$

$$Q_{\alpha\beta33} = \frac{E_{\alpha\beta33}^{<m+1>}}{E_{3333}^{<m+1>}}h_{<m+1>} + \sum_{r=1}^{m}\frac{E_{\alpha\beta33}^{<r>}}{E_{3333}^{<r>}}(h_{<r>} - h_{<r+1>})$$

$$I_{\alpha\beta\omega\rho} = \frac{2}{3}\frac{E_{\alpha\beta33}^{<m+1>}}{E_{3333}^{<m+1>}}\rho_{<m+1>}h_{<m+1>}^{3} + \frac{2}{3}\sum_{r=1}^{m}\frac{E_{\alpha\beta33}^{<r>}}{E_{3333}^{<r>}}\rho_{<r>}(h_{<r>}^{3} - h_{<r+1>}^{3})$$

$$R_{\alpha3\omega3} = 2E_{\alpha3\omega3}^{<m+1>}h_{<m+1>} + 2\sum_{r=1}^{m}E_{\alpha3\omega3}^{<r>}(h_{<r>} - h_{<r+1>})$$

$$P_{\alpha3\omega3} = \frac{2}{3}E_{\alpha3\omega3}^{<m+1>}h_{<m+1>}^{3} + \frac{2}{3}\sum_{r=1}^{m}E_{\alpha3\omega3}^{<r>}(h_{<r>}^{3} - h_{<r+1>}^{3})$$

APPENDIX A. COEFFICIENTS IN GOVERNING EQUATIONS

A.2   Reduced Mass Quantities

$$
\begin{aligned}
m_n &\equiv \sum_{r=1}^{2m+1} \int_{h_{<r-1>}}^{h_{<r>}} \rho_{<r>} x_3^n dx_3 \\
&= 2\int_0^{h_{<m+1>}} \rho_{<m+1>} x_3^n dx_3 + 2\sum_{r=1}^{m} \int_{h_{<r+1>}}^{h_{<r>}} \rho_{<r>} x_3^n dx_3 \\
&= \frac{2}{n+1}\Big[\rho_{<m+1>} h_{<m+1>}^{n+1} + \sum_{r=1}^{m} \rho_{<r>}(h_{<r>}^{n+1} - h_{<r+1>}^{n+1})\Big]
\end{aligned}
\tag{A.2}
$$

A.3   Expressions of Coefficients b, c, d, and $\tilde{b}$, $\tilde{c}$, $\tilde{d}$

$$
b = 2\frac{E_{<m+1>}}{1+\mu_{<m+1>}} h_{<m+1>} + 2\sum_{r=1}^{m} \frac{E_{<r>}}{1+\mu_{<r>}}(h_{<r>} - h_{<r+1>})
$$

$$
c = 2\frac{\mu_{<m+1>} E_{<m+1>}}{1-\mu_{<m+1>}^2} h_{<m+1>} + 2\sum_{r=1}^{m} \frac{\mu_{<r>} E_{<r>}}{1-\mu_{<r>}^2}(h_{<r>} - h_{<r+1>})
$$

$$
\begin{aligned}
d =\ & \frac{2}{3} \frac{\mu'_{<m+1>} E_{<m+1>}}{E'_{<m+1>}(1-\mu_{<m+1>})} G'_{<m+1>} h_{<m+1>}^3 \\
&+ \frac{2}{3} \sum_{r=1}^{m} \frac{\mu'_{<r>} E_{<r>}}{E'_{<r>}(1-\mu_{<r>})} G'_{<r>}(h_{<r>}^3 - h_{<r+1>}^3) \\
&- \frac{h^2}{2} G'_{<1>} \Big[\frac{\mu'_{<m+1>} E_{<m+1>}}{E'_{<m+1>}(1-\mu_{<m+1>})} h_{<m+1>} \\
&\qquad\qquad + \sum_{r=1}^{m} \frac{\mu'_{<r>} E_{<r>}}{E'_{<r>}(1-\mu_{<r>})}(h_{<r>} - h_{<r+1>})\Big]
\end{aligned}
\tag{A.3}
$$

$$
\tilde{b} = \frac{1}{b} \quad , \quad \tilde{c} = -\frac{c}{b(b+2c)} \quad , \quad \tilde{d} = -\frac{4}{h^2}\frac{d}{b+2c}
\tag{A.4}
$$

141

APPENDIX A. COEFFICIENTS IN GOVERNING EQUATIONS

A.4   Rigidity Coefficients for Symmetrically Laminated, Transversely Isotropic, Composite Panels

$$B_1 = \delta_H \frac{8}{15h^2}\left[\frac{E_{<m+1>}}{1-\mu^2_{<m+1>}}h^5_{<m+1>} + \sum_{r=1}^{m}\frac{E_{<r>}}{1-\mu^2_{<r>}}(h^5_{<r>}-h^5_{<r+1>})\right]$$

$$B_2 = \frac{1}{3}\frac{E_{<m+1>}}{1-\mu_{<m+1>}}h^3_{<m+1>} + \frac{1}{3}\sum_{r=1}^{m}\frac{E_{<r>}}{1-\mu_{<r>}}(h^3_{<r>}-h^3_{<r+1>})$$
$$-\delta_H\frac{4}{15h^2}\left[\frac{E_{<m+1>}}{1-\mu_{<m+1>}}h^5_{<m+1>} + \sum_{r=1}^{m}\frac{E_{<r>}}{1-\mu_{<r>}}(h^5_{<r>}-h^5_{<r+1>})\right]$$

$$B_3 = \frac{1}{3}\frac{E_{<m+1>}}{1+\mu_{<m+1>}}h^3_{<m+1>} + \frac{1}{3}\sum_{r=1}^{m}\frac{E_{<r>}}{1+\mu_{<r>}}(h^3_{<r>}-h^3_{<r+1>})$$
$$-\delta_H\frac{4}{15h^2}\left[\frac{E_{<m+1>}}{1+\mu_{<m+1>}}h^5_{<m+1>} + \sum_{r=1}^{m}\frac{E_{<r>}}{1+\mu_{<r>}}(h^5_{<r>}-h^5_{<r+1>})\right] \qquad (A.5)$$

$$B_4 = 2G'_{<m+1>}h_{<m+1>} + 2\sum_{r=1}^{m}G'_{<r>}(h_{<r>}-h_{<r+1>})$$
$$-\delta_H\frac{8}{3h^2}\left[G'_{<m+1>}h^3_{<m+1>} + \sum_{r=1}^{m}G'_{<r>}(h^3_{<r>}-h^3_{<r+1>})\right]$$

$$B_5 = \frac{2}{3}\left\{\frac{\mu'_{<m+1>}E_{<m+1>}}{E'_{<m+1>}(1-\mu_{<m+1>})}G'_{<m+1>}h^3_{<m+1>}\right.$$
$$+\sum_{r=1}^{m}\frac{\mu'_{<r>}E_{<r>}}{E'_{<r>}(1-\mu_{<r>})}G'_{<r>}(h^3_{<r>}-h^3_{<r+1>})$$
$$-\delta_H\frac{4}{5h^2}\left[\frac{\mu'_{<m+1>}E_{<m+1>}}{E'_{<m+1>}(1-\mu_{<m+1>})}G'_{<m+1>}h^5_{<m+1>}\right.$$
$$\left.\left.+\sum_{r=1}^{m}\frac{\mu'_{<r>}E_{<r>}}{E'_{<r>}(1-\mu_{<r>})}G'_{<r>}(h^5_{<r>}-h^5_{<r+1>})\right]\right\}$$

$$B_6 = \frac{2}{3}\frac{\mu'_{<m+1>}E_{<m+1>}}{E'_{<m+1>}(1-\mu_{<m+1>})}\rho_{<m+1>}h^3_{<m+1>}$$
$$+\frac{2}{3}\sum_{r=1}^{m}\frac{\mu'_{<r>}E_{<r>}}{E'_{<r>}(1-\mu_{<r>})}\rho_{<r>}(h^3_{<r>}-h^3_{<r+1>})$$

APPENDIX A. COEFFICIENTS IN GOVERNING EQUATIONS

$$B_7 = -\delta_H \frac{2}{15h^2} \left[\frac{E_{<m+1>}}{1 + \mu_{<m+1>}} h^5_{<m+1>} + \sum_{r=1}^{m} \frac{E_{<r>}}{1 + \mu_{<r>}} (h^5_{<r>} - h^5_{<r+1>}) \right]$$

$$B_8 = -\delta_H \frac{4}{15h^2} \left[\frac{E_{<m+1>} \mu_{<m+1>}}{1 - \mu^2_{<m+1>}} h^5_{<m+1>} + \sum_{r=1}^{m} \frac{E_{<r>} \mu_{<r>}}{1 - \mu^2_{<r>}} (h^5_{<r>} - h^5_{<r+1>}) \right]$$

A.5   Coefficients Appearing in Equation (3.29)

$$\hat{m}_1 = m_4 \frac{4}{3h^2} - m_2 \qquad , \qquad D = B_1 + B_2 + B_3$$

$$S = \frac{B_2 + B_3}{B_4} - \delta_A \frac{B_5}{B_4} \qquad , \qquad T = S + \delta_A \delta_B \frac{B_6}{m_0} \qquad\qquad \text{(A.6)}$$

Appendix B

COEFFICIENTS IN PANEL FLUTTER EQUATIONS

B.1   Expressions of Coefficients Appearing in C_1 Solution

$$\lambda^{(1)}_{mnij} = \left[(m-i)^2 + \phi^2(n-j)^2\right]^{-2} \quad , \quad = 0 \quad \text{if} \quad m=i \quad \text{and} \quad n=j$$

$$\lambda^{(2)}_{mnij} = \left[(m-i)^2 + \phi^2(n+j)^2\right]^{-2} \quad , \quad \lambda^{(3)}_{mnij} = \left[(m+i)^2 + \phi^2(n-j)^2\right]^{-2}$$

$$\lambda^{(4)}_{mnij} = \left[(m+i)^2 + \phi^2(n+j)^2\right]^{-2}$$

$$\text{(B.1)}$$

$$\kappa^{(1)}_{mnij} = mj(ni - mj) + 2\delta_A \frac{\tilde{d}}{\phi^2}\left\{[m^2 + \phi^2 n^2][mi + \phi^2 nj] - [mi + \phi^2 nj]^2\right\}$$

$$\kappa^{(2)}_{mnij} = mj(ni + mj) + 2\delta_A \frac{\tilde{d}}{\phi^2}\left\{[m^2 + \phi^2 n^2][-mi + \phi^2 nj] + [-mi + \phi^2 nj]^2\right\}$$

$$\kappa^{(3)}_{mnij} = mj(ni + mj) + 2\delta_A \frac{\tilde{d}}{\phi^2}\left\{[m^2 + \phi^2 n^2][mi - \phi^2 nj] + [mi - \phi^2 nj]^2\right\}$$

$$\kappa^{(4)}_{mnij} = mj(ni - mj) + 2\delta_A \frac{\tilde{d}}{\phi^2}\left\{-[m^2 + \phi^2 n^2][mi + \phi^2 nj] - [mi + \phi^2 nj]^2\right\}$$

APPENDIX B. COEFFICIENTS IN PANEL FLUTTER EQUATIONS

B.2 Definitions of Non-dimensional Quantities

$$L_1^* \equiv \frac{L_1^{**} l_1^2}{\pi^2 D} \quad , \quad L_2^* \equiv \frac{L_2^{**} l_1^2}{\pi^2 D} \quad , \quad \phi \equiv \frac{l_1}{l_2} \quad , \quad \lambda \equiv l_1^3 \frac{\chi p_\infty}{D} \frac{U_\infty}{c_\infty}$$

$$\xi_\alpha \equiv \frac{x_\alpha}{l_\alpha} \quad , \quad \tau \equiv \sqrt{\frac{D}{m_0 l_1^4}} \, t \quad , \quad a_{mn} \equiv \frac{A_{mn}}{h} \quad , \quad \hat{a}_{mn} \equiv \frac{\hat{A}_{mn}}{h} \qquad \text{(B.2)}$$

$$\mathcal{S} \equiv \frac{S}{l_1^2} \quad , \quad \mathcal{T} \equiv \frac{T}{l_1^2} \quad , \quad \varepsilon_S \equiv c \sqrt{\frac{m_0 l_1^4}{D}} \quad , \quad \varepsilon_A \equiv \frac{\chi p_\infty}{c_\infty} \frac{l_1^2}{\sqrt{m_0 D}}$$

B.3 Coefficients in Galerkin Equations

$$\begin{aligned}
\mathcal{F}_{rspqmnij} \equiv \; & K_4 \Big[(\cos^3\Lambda \, \Phi^{(1)}_{pmnij} + \cos\Lambda \, \sin^2\Lambda \, \phi^3 \Omega^{(2)}_{pnj} + \cos\Lambda \, \Omega^{(3)}_{pmnij}) H^{(3)}_{rpmi} I^{(1)}_{sqnj} + \\
& (-\cos^3\Lambda \, \Phi^{(1)}_{pmnij} - \cos\Lambda \, \sin^2\Lambda \, \phi^3 \Omega^{(2)}_{pnj} + \cos\Lambda \, \Omega^{(3)}_{pmnij}) H^{(3)}_{rpmi} I^{(2)}_{sqnj} + \\
& (-\cos^3\Lambda \, \Phi^{(2)}_{pmnij} - \cos\Lambda \, \sin^2\Lambda \, \phi^3 \Omega^{(2)}_{pnj} + \cos\Lambda \, \Omega^{(3)}_{pmnij}) H^{(4)}_{rpmi} I^{(1)}_{sqnj} + \\
& (\cos^3\Lambda \, \Phi^{(2)}_{pmnij} + \cos\Lambda \, \sin^2\Lambda \, \phi^3 \Omega^{(2)}_{pnj} + \cos\Lambda \, \Omega^{(3)}_{pmnij}) H^{(4)}_{rpmi} I^{(2)}_{sqnj} + \\
& (\sin^3\Lambda \, \phi^3 \Psi^{(1)}_{qnmji} + \cos^2\Lambda \, \sin\Lambda \, \Omega^{(2)}_{qmi} + \sin\Lambda \, \phi \Omega^{(3)}_{qnmji}) I^{(1)}_{rpmi} H^{(3)}_{sqnj} + \\
& (-\sin^3\Lambda \, \phi^3 \Psi^{(2)}_{qnmji} - \cos^2\Lambda \, \sin\Lambda \, \Omega^{(2)}_{qmi} + \sin\Lambda \, \phi \Omega^{(3)}_{qnmji}) I^{(1)}_{rpmi} H^{(4)}_{sqnj} + \\
& (-\sin^3\Lambda \, \phi^3 \Psi^{(1)}_{qnmji} - \cos^2\Lambda \, \sin\Lambda \, \Omega^{(2)}_{qmi} + \sin\Lambda \, \phi \Omega^{(3)}_{qnmji}) I^{(2)}_{rpmi} H^{(3)}_{sqnj} + \\
& (\sin^3\Lambda \, \phi^3 \Psi^{(2)}_{qnmji} + \cos^2\Lambda \, \sin\Lambda \, \Omega^{(2)}_{qmi} + \sin\Lambda \, \phi \Omega^{(3)}_{qnmji}) I^{(2)}_{rpmi} H^{(4)}_{sqnj} + \\
& \cos^2\Lambda \, \sin\Lambda \, (\delta^{(1)}_{pmnij} J^{(1)}_{rpmi} H^{(5)}_{sqnj} + \delta^{(2)}_{pmnij} J^{(1)}_{rpmi} H^{(6)}_{sqnj} + \\
& \qquad \delta^{(3)}_{pmnij} J^{(2)}_{rpmi} H^{(5)}_{sqnj} + \delta^{(4)}_{pmnij} J^{(2)}_{rpmi} H^{(6)}_{sqnj}) \\
& \cos\Lambda \, \sin^2\Lambda \, (\Theta^{(1)}_{qnmji} H^{(5)}_{rpmi} J^{(1)}_{sqnj} + \Theta^{(2)}_{qnmji} H^{(5)}_{rpmi} J^{(2)}_{sqnj} + \\
& \qquad \Theta^{(3)}_{qnmji} H^{(6)}_{rpmi} J^{(1)}_{sqnj} + \Theta^{(4)}_{qnmji} H^{(6)}_{rpmi} J^{(2)}_{sqnj}) \Big]
\end{aligned}$$

APPENDIX B. COEFFICIENTS IN PANEL FLUTTER EQUATIONS

$$
\begin{aligned}
\mathcal{D}_{rspqmnij} \;\equiv\; K_2\Big[& \lambda^{(1)}_{mnij}\kappa^{(1)}_{mnij}\eta^{(1)}_{pqmnij}I^{(1)}_{rpmi}I^{(1)}_{sqnj} + \lambda^{(2)}_{mnij}\kappa^{(2)}_{mnij}\eta^{(2)}_{pqmnij}I^{(1)}_{rpmi}I^{(2)}_{sqnj} + \\
& \lambda^{(3)}_{mnij}\kappa^{(3)}_{mnij}\eta^{(3)}_{pqmnij}I^{(2)}_{rpmi}I^{(1)}_{sqnj} + \lambda^{(4)}_{mnij}\kappa^{(4)}_{mnij}\eta^{(4)}_{pqmnij}I^{(2)}_{rpmi}I^{(2)}_{sqnj} + \\
& \lambda^{(1)}_{mnij}\kappa^{(1)}_{mnij}\zeta^{(1)}_{pqmnij}J^{(1)}_{rpmi}J^{(1)}_{sqnj} + \lambda^{(2)}_{mnij}\kappa^{(2)}_{mnij}\zeta^{(2)}_{pqmnij}J^{(1)}_{rpmi}J^{(2)}_{sqnj} + \\
& \lambda^{(3)}_{mnij}\kappa^{(3)}_{mnij}\zeta^{(3)}_{pqmnij}J^{(2)}_{rpmi}J^{(1)}_{sqnj} + \lambda^{(4)}_{mnij}\kappa^{(4)}_{mnij}\zeta^{(4)}_{pqmnij}J^{(2)}_{rpmi}J^{(2)}_{sqnj}\Big]
\end{aligned}
$$

$$
\begin{aligned}
\mathcal{E}_{rsmnij} \;\equiv\; K_3\Big[& (\cos^2\Lambda\,\beta^{(1)}_{mij} + \Omega^{(1)}_{mnij} + \sin^2\Lambda\,\phi^2\gamma^{(1)}_{nji})H^{(1)}_{rmi}H^{(1)}_{snj} + \\
& (-\cos^2\Lambda\,\beta^{(1)}_{mij} + \Omega^{(1)}_{mnij} - \sin^2\Lambda\,\phi^2\gamma^{(2)}_{nji})H^{(1)}_{rmi}H^{(2)}_{snj} + \\
& (-\cos^2\Lambda\,\beta^{(2)}_{mij} + \Omega^{(1)}_{mnij} - \sin^2\Lambda\,\phi^2\gamma^{(1)}_{nji})H^{(2)}_{rmi}H^{(1)}_{snj} + \\
& (\cos^2\Lambda\,\beta^{(2)}_{mij} + \Omega^{(1)}_{mnij} + \sin^2\Lambda\,\phi^2\gamma^{(2)}_{nji})H^{(2)}_{rmi}H^{(2)}_{snj} + \\
& \pi^2\phi\,\sin\Lambda\,\cos\Lambda\,(\tau^{(1)}_{mnij}J^{(3)}_{rmi}J^{(3)}_{snj} + \tau^{(2)}_{mnij}J^{(3)}_{rmi}J^{(4)}_{snj} + \\
& \qquad\qquad\qquad\quad \tau^{(3)}_{mnij}J^{(4)}_{rmi}J^{(3)}_{snj} + \tau^{(4)}_{mnij}J^{(4)}_{rmi}J^{(4)}_{snj})\Big]
\end{aligned}
$$

$$
\mathcal{G}_{rs} \equiv \frac{\Gamma^{(5)}_{rs}}{\Gamma^{(4)}_{rs}} \;,\quad \mathcal{R}_{rs} \equiv \pi^4\frac{\left(\Gamma^{(1)}_{rs}\right)^2}{\Gamma^{(4)}_{rs}} \;,\quad \mathcal{U}_{rsp} \equiv 2\Gamma^{(6)}_{ps}H_{rp} \;,\quad \mathcal{W}_{rsq} \equiv 2\Gamma^{(7)}_{rq}H_{sq}
$$

$$
\mathcal{P}_{rs} \;\equiv\; K_1\frac{4}{h}(\tilde{b}+\tilde{c})D\Big[\frac{\Gamma^{(2)}_{rs}}{\phi^2} - \Gamma^{(3)}_{rs}\frac{\tilde{\alpha}_2\tilde{c}}{\tilde{b}+\tilde{c}}\Big](1-\tilde{\alpha}_1)
$$

$$
\mathcal{Q}_{rs} \;\equiv\; K_1\frac{4}{h}(\tilde{b}+\tilde{c})D\Big[-\frac{\Gamma^{(2)}_{rs}}{\phi^2}\frac{\tilde{\alpha}_1\tilde{c}}{\tilde{b}+\tilde{c}} + \Gamma^{(3)}_{rs}\Big](1-\tilde{\alpha}_2)
$$

$$
\mathcal{Z}_{rsmn} \;\equiv\; K_1\frac{\Gamma^{(2)}_{rs}}{\phi^2}\tilde{\alpha}_1\Big[\tilde{\alpha}_2\frac{\tilde{c}}{\tilde{b}+\tilde{c}}\big\{\delta_A\tilde{d}m^2 + \phi^2(\delta_A\tilde{d}-0.5)n^2\big\} - (\delta_A\tilde{d}-0.5)m^2 - \phi^2\delta_A\tilde{d}n^2\Big]
$$

$$
\mathcal{Y}_{rsmn} \;\equiv\; K_1\Gamma^{(3)}_{rs}\tilde{\alpha}_2\Big[\tilde{\alpha}_1\frac{\tilde{c}}{\tilde{b}+\tilde{c}}\big\{\delta_A\tilde{d}\phi^2 n^2 + (\delta_A\tilde{d}-0.5)m^2\big\} - \phi^2(\delta_A\tilde{d}-0.5)n^2 - \delta_A\tilde{d}m^2\Big]
$$

146

APPENDIX B. COEFFICIENTS IN PANEL FLUTTER EQUATIONS

where,

$$\Gamma_{cd}^{(1)} \equiv c^2 + \phi^2 d^2 \quad , \quad \Gamma_{cd}^{(4)} \equiv 1 + \pi^2 T \Gamma_{cd}^{(1)} \quad , \quad \Gamma_{cd}^{(5)} \equiv 1 + \pi^2 S \Gamma_{cd}^{(1)}$$

$$\Gamma_{cd}^{(2)} \equiv -c^2 \Gamma_{cd}^{(5)} \quad , \quad \Gamma_{cd}^{(3)} \equiv -d^2 \Gamma_{cd}^{(5)} \quad , \quad \Gamma_{cd}^{(6)} \equiv c\Gamma_{cd}^{(5)} \quad , \quad \Gamma_{cd}^{(7)} \equiv d\Gamma_{cd}^{(5)}$$

$$\eta_{cdefgh}^{(1)} \equiv [c^2(f-h)^2 + d^2(e-g)^2][1 + \pi^2 S\{(e-g)^2 + \phi^2(f-h)^2 + c^2 + \phi^2 d^2\}]$$

$$\eta_{cdefgh}^{(2)} \equiv [c^2(f+h)^2 + d^2(e-g)^2][1 + \pi^2 S\{(e-g)^2 + \phi^2(f+h)^2 + c^2 + \phi^2 d^2\}]$$

$$\eta_{cdefgh}^{(3)} \equiv [c^2(f-h)^2 + d^2(e+g)^2][1 + \pi^2 S\{(e+g)^2 + \phi^2(f-h)^2 + c^2 + \phi^2 d^2\}]$$

$$\eta_{cdefgh}^{(4)} \equiv [c^2(f+h)^2 + d^2(e+g)^2][1 + \pi^2 S\{(e+g)^2 + \phi^2(f+h)^2 + c^2 + \phi^2 d^2\}]$$

$$\zeta_{cdefgh}^{(1)} \equiv -[2cd(e-g)(f-h)][1 + \pi^2 S\{(e-g)^2 + \phi^2(f-h)^2 + c^2 + \phi^2 d^2\}]$$

$$\zeta_{cdefgh}^{(2)} \equiv -[2cd(e-g)(f+h)][1 + \pi^2 S\{(e-g)^2 + \phi^2(f+h)^2 + c^2 + \phi^2 d^2\}]$$

$$\zeta_{cdefgh}^{(3)} \equiv -[2cd(e+g)(f-h)][1 + \pi^2 S\{(e+g)^2 + \phi^2(f-h)^2 + c^2 + \phi^2 d^2\}]$$

$$\zeta_{cdefgh}^{(4)} \equiv -[2cd(e+g)(f+h)][1 + \pi^2 S\{(e+g)^2 + \phi^2(f+h)^2 + c^2 + \phi^2 d^2\}]$$

$$\beta_{cde}^{(1)} \equiv cd[1 - 2\pi^2 S(cd - d^2 - \phi^2 e^2)] \quad , \quad \beta_{cde}^{(2)} \equiv cd[-1 - 2\pi^2 S(cd + d^2 + \phi^2 e^2)]$$

$$\gamma_{cde}^{(1)} \equiv cd[1 - 2\pi^2 S(\phi^2 cd - e^2 - \phi^2 d^2)] \quad , \quad \gamma_{cde}^{(2)} \equiv cd[-1 - 2\pi^2 S(\phi^2 cd + e^2 + \phi^2 d^2)]$$

$$\Omega_{cdef}^{(1)} \equiv -2\pi^2 S \phi^2 cdef \quad , \quad \Omega_{cde}^{(2)} \equiv -6\pi^2 S \phi cd^2 e^2 \quad , \quad \Omega_{cdefg}^{(3)} \equiv -6\pi^2 S \phi^2 cdefg$$

$$\tau_{cdef}^{(1)} \equiv cf[-1 - 2\pi^2 S(c-e)^2] + de[-1 - 2\pi^2 S\phi^2(d-f)^2]$$

$$\tau_{cdef}^{(2)} \equiv cf[-1 - 2\pi^2 S(c-e)^2] + de[1 + 2\pi^2 S\phi^2(d+f)^2]$$

$$\tau_{cdef}^{(3)} \equiv cf[1 + 2\pi^2 S(c+e)^2] + de[-1 - 2\pi^2 S\phi^2(d-f)^2]$$

$$\tau_{cdef}^{(4)} \equiv cf[1 + 2\pi^2 S(c+e)^2] + de[1 + 2\pi^2 S\phi^2(d+f)^2]$$

147

APPENDIX B. COEFFICIENTS IN PANEL FLUTTER EQUATIONS

$$\Phi^{(1)}_{cdefg} \equiv cdf[1 - 3\pi^2 S(2df - f^2 - \phi^2 g^2)]$$

$$\Phi^{(2)}_{cdefg} \equiv cdf[-1 - 3\pi^2 S(2df + f^2 + \phi^2 g^2)]$$

$$\Psi^{(1)}_{cdefg} \equiv cdf[1 - 3\pi^2 S(-g^2 + 2\phi^2 df - \phi^2 f^2)]$$

$$\Psi^{(2)}_{cdefg} \equiv cdf[-1 - 3\pi^2 S(g^2 + 2\phi^2 df + \phi^2 f^2)]$$

$$\delta^{(1)}_{cdefg} \equiv \phi[-3cdg - 3\pi^2 S(-4cdef^2 + 2cef^3 + cdgf^2 + \phi^2\{-4cdeg^2 + 2cefg^2 + cdg^3\})]$$

$$\delta^{(2)}_{cdefg} \equiv \phi[-3cdg - 3\pi^2 S(4cdef^2 - 2cef^3 + cdgf^2 + \phi^2\{4cdeg^2 - 2cefg^2 + cdg^3\})]$$

$$\delta^{(3)}_{cdefg} \equiv \phi[3cdg - 3\pi^2 S(4cdef^2 + 2cef^3 - cdgf^2 + \phi^2\{4cdeg^2 + 2cefg^2 - cdg^3\})]$$

$$\delta^{(4)}_{cdefg} \equiv \phi[3cdg - 3\pi^2 S(-4cdef^2 - 2cef^3 - cdgf^2 + \phi^2\{-4cdeg^2 - 2cefg^2 - cdg^3\})]$$

$$\Theta^{(1)}_{cdefg} \equiv \phi^2[-3cdg - 3\pi^2 S(phi^2\{-4cdef^2 + 2cef^3 + cdgf^2\} - 4cdeg^2 + 2cefg^2 + cdg^3)]$$

$$\Theta^{(2)}_{cdefg} \equiv \phi^2[3cdg - 3\pi^2 S(phi^2\{4cdef^2 + 2cef^3 - cdgf^2\} + 4cdeg^2 + 2cefg^2 - cdg^3)]$$

$$\Theta^{(3)}_{cdefg} \equiv \phi^2[-3cdg - 3\pi^2 S(phi^2\{4cdef^2 - 2cef^3 + cdgf^2\} + 4cdeg^2 - 2cefg^2 + cdg^3)]$$

$$\Theta^{(4)}_{cdefg} \equiv \phi^2[3cdg - 3\pi^2 S(phi^2\{-4cdef^2 - 2cef^3 - cdgf^2\} - 4cdeg^2 - 2cefg^2 - cdg^3)]$$

$$
\begin{aligned}
I_{uv} \equiv \int_0^1 \cos u\pi\xi_\alpha \cos v\pi\xi_\alpha d\xi_\alpha &= 1 \ \text{ if }\ u = v = 0 \\
&= \frac{1}{2} \ \text{ if }\ u = \pm v \neq 0 \\
&= 0 \ \text{ if }\ u \neq v
\end{aligned}
$$

$$
\begin{aligned}
J_{uv} \equiv \int_0^1 \sin u\pi\xi_\alpha \sin v\pi\xi_\alpha d\xi_\alpha &= \frac{1}{2} \ \text{ if }\ u = v \neq 0 \\
&= -\frac{1}{2} \ \text{ if }\ u = -v \neq 0 \\
&= 0 \ \text{ if }\ u \neq \pm v \ \text{ or }\ u = 0 \ \text{ or }\ v = 0
\end{aligned}
$$

APPENDIX B. COEFFICIENTS IN PANEL FLUTTER EQUATIONS

$$I^{(1)}_{uvwx} \equiv \int_0^1 \sin u\pi\xi_\alpha \sin v\pi\xi_\alpha \cos (w-x)\pi\xi_\alpha d\xi_\alpha = \frac{1}{2}[I_{(u-v)(w-x)} - I_{(u+v)(w-x)}]$$

$$I^{(2)}_{uvwx} \equiv \int_0^1 \sin u\pi\xi_\alpha \sin v\pi\xi_\alpha \cos (w+x)\pi\xi_\alpha d\xi_\alpha = \frac{1}{2}[I_{(u-v)(w+x)} - I_{(u+v)(w+x)}]$$

$$J^{(1)}_{uvwx} \equiv \int_0^1 \sin u\pi\xi_\alpha \cos v\pi\xi_\alpha \sin (w-x)\pi\xi_\alpha \ d\xi_\alpha = \frac{1}{2}[J_{(u+v)(w-x)} + J_{(u-v)(w-x)}]$$

$$J^{(2)}_{uvwx} \equiv \int_0^1 \sin u\pi\xi_\alpha \cos v\pi\xi_\alpha \sin (w+x)\pi\xi_\alpha d\xi_\alpha = \frac{1}{2}[J_{(u+v)(w+x)} + J_{(u-v)(w+x)}]$$

$$J^{(3)}_{uvw} \equiv \int_0^1 \sin u\pi\xi_\alpha \sin (v-w)\pi\xi_\alpha d\xi_\alpha = J_{(u)(v-w)}$$

$$J^{(4)}_{uvw} \equiv \int_0^1 \sin u\pi\xi_\alpha \sin (v+w)\pi\xi_\alpha d\xi_\alpha = J_{(u)(v+w)}$$

$$H_{uv} \equiv \pi \int_0^1 \sin u\pi\xi_\alpha \cos v\pi\xi_\alpha d\xi_\alpha = \frac{u}{u^2 - v^2}[1 - (-1)^{u+v}] \ \text{ if } \ u \neq v$$

$$= 0 \ \text{ if } \ u = \pm v$$

$$H^{(1)}_{uvw} \equiv \pi \int_0^1 \sin u\pi\xi_\alpha \cos (v-w)\pi\xi_\alpha d\xi_\alpha = H_{(u)(v-w)}$$

$$H^{(2)}_{uvw} \equiv \pi \int_0^1 \sin u\pi\xi_\alpha \cos (v+w)\pi\xi_\alpha d\xi_\alpha = H_{(u)(v+w)}$$

$$H^{(3)}_{uvwx} \equiv \pi \int_0^1 \sin u\pi\xi_\alpha \cos v\pi\xi_\alpha \cos (w-x)\pi\xi_\alpha d\xi_\alpha = \frac{1}{2}[H_{(u+v)(w-x)} + H_{(u-v)(w-x)}]$$

$$H^{(4)}_{uvwx} \equiv \pi \int_0^1 \sin u\pi\xi_\alpha \cos v\pi\xi_\alpha \cos (w+x)\pi\xi_\alpha d\xi_\alpha = \frac{1}{2}[H_{(u+v)(w+x)} + H_{(u-v)(w+x)}]$$

$$H^{(5)}_{uvwx} \equiv \pi \int_0^1 \sin u\pi\xi_\alpha \sin v\pi\xi_\alpha \sin (w-x)\pi\xi_\alpha d\xi_\alpha = \frac{1}{2}[H_{(w-x)(u-v)} - H_{(w-x)(u+v)}]$$

$$H^{(6)}_{uvwx} \equiv \pi \int_0^1 \sin u\pi\xi_\alpha \sin v\pi\xi_\alpha \sin (w+x)\pi\xi_\alpha d\xi_\alpha = \frac{1}{2}[H_{(w+x)(u-v)} - H_{(w+x)(u+v)}]$$

$$K_1 \equiv \frac{\phi^2}{D}\frac{\pi^4 h^2}{4(\bar{b} + \bar{c})\left[1 - \left(\frac{\bar{c}}{\bar{b}+\bar{c}}\right)^2 \tilde{\alpha}_1\tilde{\alpha}_2\right]} \quad , \quad K_2 \equiv \frac{\phi^4}{D}\frac{\pi^4 h^2}{\bar{b} + \bar{c}}$$

$$K_3 \equiv \frac{Dh}{l_1^4}\frac{1}{\chi p_\infty}\frac{\chi + 1}{4} \quad , \quad K_4 \equiv \pi^2\left(\frac{Dh}{l_1^4}\frac{1}{\chi p_\infty}\right)^2\frac{\chi + 1}{12}$$

149

Appendix C

RELEVANT LINEAR SYSTEMS THEORY

C.1 Solvability Conditions for Linear Algebraic Sytems

The systems of algebraic equations (4.23) are re-written as,

$$\mathbf{A}_i \tilde{\mathbf{c}}_i = \hat{\mathbf{c}}_i \quad , \quad i = 1 \to N \tag{C.1}$$

The solvability conditions for (C.1) are derived in the following manner (see, e.g., Nayfeh [86]). Pre-multiplying (C.1) by an arbitrary row vector $\overline{\mathbf{b}_i}^T$ and transposing the resulting equation, we obtain,

$$\tilde{\mathbf{c}}_i^T \overline{\mathbf{A}_i^* \mathbf{b}_i} = \hat{\mathbf{c}}_i^T \overline{\mathbf{b}_i}$$

where $\qquad \mathbf{A}_i^* \equiv \overline{\mathbf{A}_i}^T \quad$ (the adjoint of $\mathbf{A}_i$) $\tag{C.2}$

Here, the overbars denote the complex conjugate of the overbarred terms. Now if $\mathbf{A}_i$ is singular then so is $\mathbf{A}_i^*$. Thus, choosing $\mathbf{b}_i$ as the nontrivial solution of $\mathbf{A}_i^* \mathbf{b}_i = 0$ we obtain the following solvability condition (note that $\tilde{\mathbf{c}}_i$ is bounded):

$$\hat{\mathbf{c}}_i^T \overline{\mathbf{b}_i} = 0 \tag{C.3}$$

In most physical problems, the rank of $\mathbf{A}_i$ is $N - 1$. Thus $\mathbf{b}_i$ and hence the solvability conditions (C.3) are unique (up to a multiplicative constant). However, for certain special cases involving repeated frequencies, the rank of $\mathbf{A}_i$ could be less than $(N-1)$. In such cases $\mathbf{b}_i$ and hence (C.3) are non-unique (since they contain two or more arbitrary constants).

150

C.2   Stability of Linear Differential Systems with Periodic Coefficients— Floquet Theory

Consider the $2N$-dimensional ODE system $(4.38)_1$, i.e.,

$$\dot{\mathbf{z}} = \bar{\mathbf{f}}[\mathbf{z} \, ; \, \lambda \, , \, L_\alpha^*] \tag{C.4}$$

which has a periodic solution $\tilde{\mathbf{z}}$ with period T, i.e., $\tilde{\mathbf{z}}[t] = \tilde{\mathbf{z}}[t + T]$. The stability of the periodic solution is determined by applying a generalized perturbation $\mathbf{z}^*[t]$ to $\tilde{\mathbf{z}}[t]$ and determining how $\mathbf{z}^*[t]$ evolves with time. The solution $\tilde{\mathbf{z}}[t]$ is asymptotically stable (unstable) if $\mathbf{z}^*[t] \rightarrow 0$ ($\mathbf{z}^*[t] \rightarrow \infty$) as $t \rightarrow \infty$. Thus, introducing $\mathbf{z}[t] = \tilde{\mathbf{z}}[t] + \mathbf{z}^*[t]$ into (C.4) we obtain the linearized disturbance equations (i.e., for a local stability analysis),

$$\dot{\mathbf{z}}^*[t] = \hat{\mathbf{A}}[t \, ; \, \lambda \, , \, L_\alpha^*] \, \mathbf{z}^*[t]$$
$$\text{where} \qquad \hat{\mathbf{A}}[t \, ; \, \lambda \, , \, L_\alpha^*] = \nabla_{\mathbf{z}} \bar{\mathbf{f}} \Big|_{\mathbf{z} = \tilde{\mathbf{z}}} \tag{C.5}$$

Here, the $2N \times 2N$ matrix $\hat{\mathbf{A}}$ is periodic with period T_A, i.e.,

$$\hat{\mathbf{A}}[t \, ; \, \lambda \, , \, L_\alpha^*] = \hat{\mathbf{A}}[t + T_A, ; \, \lambda \, , \, L_\alpha^*] \tag{C.6}$$

where $T_A = T$ $(T_A = \frac{T}{2})$ when $\bar{\mathbf{f}}$ contains even nonlinearities, i.e., the limit cycle is unsymmetric, ($\bar{\mathbf{f}}$ contains only odd nonlinearities, and the limit cycle is symmetric). The symmetry referred to here is the inversion symmetry for which we have $\tilde{\mathbf{z}}[t] = -\tilde{\mathbf{z}}[t + \frac{T}{2}]$.

The fundamental matrix solution $\mathbf{Z}^*[t]$ is defined as,

$$\mathbf{Z}^*[t] = [\mathbf{z}_1^*[t] \, , \, \mathbf{z}_2^*[t] \, , \cdots\cdots , \, \mathbf{z}_{2N}^*[t]] \tag{C.7}$$

where the column vectors $\mathbf{z}_j^*$ $(j = 1 \rightarrow 2N)$ are linearly independent solutions of $\mathbf{z}^*$ obtained using the initial conditions, e.g., $z_i^*[0] = 0 \, \forall \, i \neq j$, $z_j^*[0] = 1$. Thus, from $(C.5)_1$ we have the matrix IVP that would yield one possible fundamental matrix solution, i.e.,

$$\dot{\mathbf{Z}}^* = \hat{\mathbf{A}}[t \, ; \, \lambda \, , \, L_\alpha^*] \, \mathbf{Z}^* \qquad , \qquad \mathbf{Z}^*[0] = \mathbf{I} \tag{C.8}$$

APPENDIX C. RELEVANT LINEAR SYSTEMS THEORY

where $\mathbf{I}$ is the $2N \times 2N$ identity matrix. By introducing the new variable $t^* \equiv t + T_A$ into $(C.5)_1$ and considering $(C.6)$, we conclude that if $\mathbf{Z}^*[t]$ is a fundamental matrix solution then so is $\mathbf{Z}^*[t + T_A]$. Further, knowing that every solution of the linear ODE system $(C.5)_1$ is expressible as a linear combination of any fundamental set of solutions, we can express $\mathbf{Z}^*[t + T_A]$ as,

$$\mathbf{Z}^*[t + T_A] = \mathbf{Z}^*[t]\, \boldsymbol{\Phi} \tag{C.9}$$

where $\boldsymbol{\Phi}$ is a constant $2N \times 2N$ matrix which depends on the fundamental matrix solution chosen (and hence on $\mathbf{Z}^*[0]$). For $\mathbf{Z}^*[0]$ as in $(C.8)_2$ and considering $(C.9)$, we obtain,

$$\widetilde{\boldsymbol{\Phi}} \equiv \boldsymbol{\Phi} = \mathbf{Z}^*[T_A] \tag{C.10}$$

where the unique, constant, $2N \times 2N$ matrix $\widetilde{\boldsymbol{\Phi}}$ is called the monodromy matrix.

Now, we consider the linear transformation,

$$\hat{\mathbf{Z}}[t]\, \mathbf{P}^{-1} = \mathbf{Z}^*[t] \tag{C.11}$$

where $\mathbf{P}$ is a constant, and as yet arbitrary, $2N \times 2N$ matrix. Considering $(C.11)$ in conjunction with $(C.9)$ and $(C.10)$, we obtain,

$$\hat{\mathbf{Z}}[t + T_A] = \hat{\mathbf{Z}}[t]\, \hat{\mathbf{J}} \qquad \text{where} \qquad \hat{\mathbf{J}} = \mathbf{P}^{-1}\widetilde{\boldsymbol{\Phi}}\mathbf{P} \tag{C.12}$$

Here, $\hat{\mathbf{J}}$ is a constant, $2N \times 2N$ matrix. If $\widetilde{\boldsymbol{\Phi}}$ has distinct eigenvalues $\tilde{\lambda}_j$, and we choose $\mathbf{P}$ comprising of columns which are the right eigenvectors of $\widetilde{\boldsymbol{\Phi}}$, then $\hat{\mathbf{J}}$ is the Jordan form of $\widetilde{\boldsymbol{\Phi}}$, i.e., $\hat{\mathbf{J}}$ is diagonal with $\tilde{\lambda}_j$ (known as the Floquet multipliers) as its elements. Hence, the components (i.e., column vectors) of $\hat{\mathbf{Z}}[t + T_A]$ are obtained as,

$$\hat{\mathbf{z}}_j[t + T_A] = \tilde{\lambda}_j \hat{\mathbf{z}}_j[t] \quad , \quad j = 1 \longrightarrow 2N$$
$$\hat{\mathbf{z}}_j[t + MT_A] = \tilde{\lambda}_j^M \hat{\mathbf{z}}_j[t] \tag{C.13}$$

From $(C.13)_2$ and $(C.11)$ we see that the periodic solution is asymptotically stable if $|\tilde{\lambda}_j| < 1$ for all $j = 1 \rightarrow 2N$, and unstable if $|\tilde{\lambda}_k| > 1$ for any $k = 1 \rightarrow 2N$.

152

APPENDIX C. RELEVANT LINEAR SYSTEMS THEORY

Differentiating the autonomous system (C.4) once with respect to t, we obtain,

$$\ddot{z} = \nabla_z \bar{f} \, \dot{z} \tag{C.14}$$

Comparing (C.5)$_1$ and (C.14), we conclude that $\dot{z}$ is a periodic solution of (C.5)$_1$, with period T. Hence, $\dot{z}$ can be expressed in terms of the fundamental matrix solution obtained from (C.8), as,

$$\dot{z}[t] = Z^*[t] \, \dot{z}[0] \tag{C.15}$$

Considering (C.10), (C.15) and the periodicity of $\dot{z}$, we obtain,

$$\underline{T_A = T} : \qquad \dot{z}[0] = \dot{z}[T] = \tilde{\Phi} \, \dot{z}[0]$$

$$\underline{T_A = T/2} : \qquad \dot{z}[0] = \dot{z}[T] = \tilde{\Phi}^2 \, \dot{z}[0] \tag{C.16}$$

Equation (C.16)$_1$ reveals that when $T_A = T$, i.e., for an unsymmetric limit cycle, one of the Floquet multipliers of an autonomous system, say $\tilde{\lambda}_i$, is $+1$. For $T_A = \frac{T}{2}$, (C.16)$_2$ implies that $\tilde{\lambda}_i^2 = 1$. Further, considering (C.13)$_1$ for $j = i$ along with the fact that the symmetry of the limit cycle $\tilde{z}$ is preserved only when $\hat{z}_i$ possesses inversion symmetry, we conclude that for $T_A = \frac{T}{2}$, i.e., for a symmetric limit cycle, $\tilde{\lambda}_i = -1$.

REFERENCES

1. Bolotin, V.V., Gavrilov, Iu.N., Makarov, B.P., and Shveiko, Iu.Iu., (1959). ' Nonlinear Problems of the Stability of Flat Panels at High Supersonic Velocities ', *Izvestia Akademiia Nauk USSR OTN, Mekhanika i Mashinostroenie* , No.3, pp. 59-64.

2. Bolotin, V.V., (1960). ' Nonlinear Flutter of Plates and Shells ', *Inzhenernyi Sbornik*, V.28 , pp. 55-75.

3. Makarov, B.P., (1961). ' Amplitudes of the Steady Flutter of Clamped Plates ', *Izvestia Vysshikh Uchebnykh Zavednii Mashinostroenie* 5, pp. 11-25.

4. Bolotin, V.V., (1963). *Nonconservative Problems of the Theory of Elastic Stability*, The Macmillan Company, New York.

5. Librescu, L., (1965). ' Aeroelastic Stability of Orthotropic Heterogeneous Thin Panels in the Vicinity of the Flutter Critical Boundary - Part I ', *Journal de Mécanique* , V.4, No.1, pp. 51-76.

6. Librescu, L., (1967). ' Aeroelastic Stability of Orthotropic Heterogeneous Thin Panels in the Vicinity of the Flutter Critical Boundary - Part II ', *Journal de Mécanique* , V.6, No.1, pp. 132-152.

7. Bautin, N.N. (1950). *The Behavior of Dynamic Systems in the Neighborhood of the Boundaries of the Region of Stability*, Gostekhizdat (in Russian).

8. Malkin, I.G., (1963). *Theory of Stability of Motion*, AEC-tr-3352.

9. Librescu, L., (1975). *Elastostatics and Kinetics of Anisotropic and Heterogeneous Shell Type Structures*, Noordhoff Int. Publ., Leyden, The Netherlands.

10. Voss, H.M., and Dowell, E.H., (1964). ' Effect of Aerodynamic Damping on Flutter of

Thin Panels ', *AIAA J.* , V.2, No.1, pp. 119-120.

11. Ventres, C. S., and Dowell, E.H., (1970). ' Comparison of Theory and Experiment for Nonlinear Flutter of Loaded Plates ', *AIAA J.* , V.8, No.11, pp. 2022-2030.

12. Fralich, R.W., (1963). ' Postbuckling Effects on the Flutter of Simply Supported Rectangular Panels at Supersonic Speeds ', *NASA Langley Research Center, TN-D-1615*.

13. Kobayashi, S., (1962). ' Flutter of Simply Supported Rectangular Panels in a Supersonic Flow ', *Trans. Japan Soc. Aero. Space Sci.* , V.5, No.8, pp. 79-89.

14. Kobayashi, S., (1962). 'Two-Dimensional Panel Flutter - I. Simply Supported Panel', *Trans. Japan Soc. Aero. Space Sci.* , V.5, No.8, pp. 90-102.

15. Kobayashi, S., (1962). ' Two-Dimensional Panel Flutter - II. Clamped Panel ', *Trans. Japan Soc. Aero. Space Sci.* , V.5, No.8, pp. 103-118.

16. Kobayashi, S. (1962). ' Flutter of Wings Subjected to Aerodynamic Heating ', *Trans. Japan Soc. Aero. Space Sci.*, V.5, No.7, pp. 57-68.

17. Voss, H.M., (1961). ' The Effect of an External Supersonic Flow on the Vibration Characteristics of Thin Cylindrical Shells ', *J. Aerospace Sciences* , V.28, No.12, Dec. 1961, pp. 945-956.

18. Evensen, D., and Olson, M.D., (1967). ' Nonlinear Flutter of a Circular Cylindrical Shell in Supersonic Flow ', *NASA Langley Research Center, TN-D-4265*.

19. Evensen, D.A., and Olson, M.D., (1968). ' Circumferentially Traveling Wave Flutter of a Circular Cylindrical Shell ', *AIAA J.* , V.6, No.8, pp. 1522-1527.

20. Olson, M.D., and Fung, Y.C., (1967). ' Comparing Theory and Experiment for the Supersonic Flutter of Circular Cylindrical Shells ', *AIAA J.* , V.5, No.10, pp. 1849-1856.

21. Gordon, J.T., and Atluri, S., (1973). ' Nonlinear Flutter of a Cylindrical Shell ', *Developments in Theoretical and Applied Mechanics(8th SECTAM)* , pp. 281-307, Catholic Univ. of America Press.

22. Dowell, E.H., (1966). ' Nonlinear Oscillations of a Fluttering Plate ', *AIAA J.*, V.4, No.7, pp. 1267-1275.

23. Dowell, E.H., (1967). ' Nonlinear Oscillations of a Fluttering Plate-II ', *AIAA J.*, V.5,

No.10, pp. 1856-1862.

24. Dowell, E.H., (1967). ' Nonlinear Analysis of the Flutter of Plates and Shells ', *Fluid-Solid Interaction Symposium*, ed. Joshua E. Greenspon, Pittsburgh, Nov., pp. 160-186.

25. Dowell, E.H., (1970). ' Panel Flutter : A Review of the Aeroelastic Stability of Plates and Shells ', *AIAA J.*, V.8, No.3, pp. 385-399.

26. Dowell, E. H., (1969). ' Nonlinear Flutter of Curved Plates ', *AIAA J.* , V.7, No.3, pp. 424-431.

27. Dowell, E. H., (1970). ' Nonlinear Flutter of Curved Plates, II ', *AIAA J.* , V.8, No.2, pp. 259-261.

28. Eastep, F.E., (1968), ' Nonlinear Oscillations of Elastic Panels in a Supersonic Nonviscous Airstream ', *AFOSR 68-1861*.

29. Eastep, F.E., and McIntosh, S.C., (1971). ' Analysis of Nonlinear Panel Flutter and Response Under Random Excitation or Nonlinear Aerodynamic Loading ', *AIAA J.*, V.9, No.3, pp. 411-418.

30. Dimantha, P.C., and Roorda, J., (1969). ' On the Domain of Asymptotic Stability of Nonlinear Nonconservative Systems ', *Appl. Sci. Res.* , V.20, pp. 272-288.

31. McIntosh, S.C., (1973). ' Effect of Hypersonic Nonlinear Aerodynamic Loading on Panel Flutter ', *AIAA J.* , V.11, No.1, pp. 29-32.

32. Friedmann, P., and Hanin, M., (1968). ' Supersonic Nonlinear Flutter of Orthotropic Panels with Arbitrary Flow Direction ', *Israel Journal of Technology*, V.6, No.1-2, pp. 46-57.

33. Dzygadlo, Z., (1970). ' Local Analysis of Nonlinear Forced Vibration of a Plate of Finite Length in Plane Supersonic Flow ', *Proc. Vibration Problems*, V.11 , No.4, pp. 353-368, Warsaw.

34. Morino, L., (1969). ' A Perturbation Method for Treating Nonlinear Panel Flutter Problems ', *AIAA J.*, V.7, No.3, pp. 405-411.

35. Smith, L.L., and Morino, L., (1976). ' Stability Analysis of Nonlinear Differential Autonomous Systems with Applications to Flutter ', *AIAA J.*, V.14, No.3, pp. 333-341.

36. Kuo, C.C., Morino, L., and Dugundji, J., (1972).' Perturbation and Harmonic Balance Methods for Nonlinear Panel Flutter ', *AIAA J.*, V.10, No.11, pp. 1479-1484.

37. Morino, L., and Kuo, C.C., (1971). ' Detailed Extension of Perturbation Method for Panel Flutter ', *ASRL TR-164-2* (March), Aeroelastic and Structures Res. Lab., Dept. of Aeronautics, MIT, Cambridge, Mass.

38. Kuo, C.C., Morino, L., and Dugundji, J., (1973). ' Nonlinear Interaction of Panel Flutter with Harmonic Forcing Excitation ', *AIAA J.*, V.11, No.4, pp. 419-420. See also *ASRL TR-159-5*.

39. Eslami, H., and Ibrahim, S.R., (1986). ' Nonlinear Flutter Analysis of Specially Orthotropic Panels ', *AIAA Paper 86-0900, 26th Structures, Structural Dynamics and Materials Conf.* , San Antonio, Texas, V.2, pp. 293-302.

40. Sipcic, S.R. and Morino, L., (1990). ' Dynamic Behavior of Fluttering Two-Dimensional Panels on an Airplane in Pull-Up Maneuver ', *AIAA J.*, V.29, No.8, pp. 1304-1312.

41. Sipcic, S. R., (1990). ' The Chaotic Response of a Fluttering Panel: The Influence of Maneuvering ', *Nonlinear Dynamics* , V.1, No.3, 243-264.

42. Yuen, S.W., and Lau, S.L., (1991). ' Effects of In-Plane Load on Nonlinear Panel Flutter by Incremental Harmonic Balance Method ', *AIAA J.* , V.29, No.9, pp. 1472-1479.

43. Weiliang, Y., and Dowell, E.H., (1991). ' Limit Cycle Oscillation of a Fluttering Cantilever Plate ', *AIAA J.*, V.29, No.11, pp. 1929-1936.

44. Dowell, E.H., (1982). ' Flutter of a Buckled Plate as an Example of Chaotic Motion of a Deterministic Autonomous System ', *J. Sound and Vibration*, V.85,No.3, pp. 333-344.

45. Dowell, E.H.,(1984). 'Observation and Evolution of Chaos for an Autonomous System', *J. Applied Mechanics*, V.51, pp. 664-673.

46. Seydel, R., (1988). *From Equilibrium to Chaos : Practical Bifurcation and Stability Analysis* , Elsevier, New York.

47. Thompson, J.M.T., and Stewart, H.B., (1986). *Nonlinear Dynamics and Chaos*, John Wiley, Great Britain.

48. Shiau, L.-C, and Lu, L.-T., (1992). ' Nonlinear Flutter of Two-Dimensional Simply

Supported Symmetric Composite Laminated Plates ', *J. Aircraft* , V.29, No.1, pp. 140-145.

49. Holmes, P.J., (1977). ' Bifurcations to Divergence and Flutter in Flow-induced Oscillations ', *J. Sound and Vibration* , V.53, No.4, pp. 471-503.

50. Holmes, P.J., and Marsden, J., (1978). ' Bifurcations to Divergence and Flutter in Flow-induced Oscillations: An Infinite Dimensional Analysis ', *Automatica* , V.14, No.4, pp. 367-384.

51. Holmes, P.J., (1981). ' Center Manifolds, Normal Forms and Bifurcation of Vector Fields with Application to Coupling between Periodic and Steady Motions ', *Physica* , V.2D, pp. 449-481.

52. Dowell, E.H., and Virgin, L.N., (1990). ' On Spatial Chaos, Asymptotic Modal Analysis, and Turbulence ', *J. Applied Mechanics* , V.57, No.4, pp. 1094-1097.

53. Zhao, L.C., and Yang, Z.C., (1990). ' Chaotic Motions of an Airfoil with Nonlinear Stiffness in Incompressible Flow ', *J. Sound and Vibration* , V.138, No.2, pp. 245-254.

54. Dixon, I.R., and Mei, C., (1991). 'Finite Element Analysis of Nonlinear Flutter of Composite Panels ', *AIAA Paper* 91-1173-CP, pp. 2002-2011.

55. Gray, C.E., Mei, C., and Shore, C.P., (1991). ' Finite Element Method for Large-Amplitude Two-Dimensional Panel Flutter at Hypersonic Speeds ', *AIAA J.* , V.29, No.2, pp. 290-298.

56. Dixon, I.R., and Mei, C., (1992). ' Nonlinear Futter of Rectangular Composite Panels under Uniform Temperature using Finite Elements ', *Nonlinear Vibrations* , eds. R.A. Ibrahim, N. Sri Namachchivaya, and A.K. Bajaj, DE-V.50/AMD-V.144, pp. 123-132, ASME, Anaheim, CA.

57. Tezak, E.G., Nayfeh, A.H., and Mook, D.T., (1982). ' Parametrically Excited Nonlinear Multidegree-Of-Freedom Systems with Repeated Natural Frequencies ', *J. Sound and Vibration* , V.85, No.4, pp. 459-472.

58. Tezak, E.G., (1979). ' Parametrically Excited Nonlinear Multi-Degree-Of-Freedom Systems', V.P.I. & S.U., Ph.D. dissertation, Blacksburg, VA.

59. Fu, F.C.L., and Nemat-Nasser, S., (1972). ' On the Stability of Steady-State Response

of Certain Nonlinear Dynamic Systems Subjected to Harmonic Excitations ', *Ingenieur-Archiv* , V.41, No.6, pp. 407-420.

60. Namachchivaya, N. Sri, and Malhotra, N., (1992). ' Parametrically Excited Hopf Bifurcation with Non-Semisimple 1:1 Resonance ', *Nonlinear Vibrations* , eds. R.A. Ibrahim, N. Sri Namachchivaya, and A.K. Bajaj, DE-V.50/AMD-V.144, pp. 29-46, ASME, Anaheim, CA.

61. Eckmann, J.-P., (1981). ' Roads to Turbulence in Dissipative Dynamical Systems ', *Reviews of Modern Physics* , V.53, No.4, Part 1, pp. 643-654.

62. Moon, F. C., (1987). *Chaotic Vibrations*, John Wiley, New York.

63. Farmer, J.D., Ott, E., and Yorke, J.A., (1983). 'The Dimension of Chaotic Attractors', *Physica* , V.7D, pp. 153-180.

64. Parker, T.S., and Chua, L.O., (1989). *Practical Numerical Algorithms for Chaotic Systems*, Springer-Verlag, New York.

65. Kaplan, J.L., and Yorke, J.A., (1978). ' Chaotic Behavior of Multidimensional Difference Equations ', *Lecture Notes in Mathematics* , V.730, Springer-Verlag, Berlin, 1979.

66. Grassberger, P., and Procaccia, I., (1983). ' Measuring the Strangeness of Strange Attractors ', *Physica* , V.9D, pp. 189-208.

67. Packard, N.H., Crutchfield, J.P., Farmer, J.D., and Shaw, R.S., (1980). 'Geometry from a Time Series', *Phys. Rev. Lett.* , V.45, pp. 712-715.

68. Froehling, H., Crutchfield, J.P., Farmer, D., Packard, N.H., and Shaw, R., (1981). ' On Determining the Dimension of Chaotic Flows ', *Physica* , V.3D, pp. 605-617.

69. Goldhirsch, I., Sulem, P.-L., and Orszag, S.A., (1987). ' Stability and Lyapunov Stability of Dynamical Systems: A Differential Approach and a Numerical Method ' , *Physica* , V.27D, pp. 311-337.

70. Berge, P., Pomeau, Y., and Vidal, C., (1984). *Order Within Chaos: Towards a Deterministic Approach to Turbulence*, Hermann & Wiley-Interscience, Paris.

71. Aboudi, J., Cederbaum, G., and Elishakoff, I., (1990). ' Dynamic Stability Analysis of Viscoelastic Plates by Lyapunov Exponents ', *J. Sound and Vibration* , V.139, No.3,

pp. 459-467.

72. Wolf, A., Swift, J.B., Swinney, H.L., and Vastano, J.A., (1985). ' Determining Lyapunov Exponents From a Time Series ', *Physica* , V.16D, pp. 285-317.

73. Shimada, I., and Nagashima, T., (1979). 'A Numerical Approach to Ergodic Problems of Dissipative Dynamical Systems', *Prog. of Theoretical Phys.* , V.61, No.6, pp. 1605-1616.

74. Benettin, G., Galgani, L., Giorgilli, A., and Streclyn, J.-M., (1980). 'Lyapunov Characteristic Exponents for Smooth Dynamical Systems and for Hamiltonian Systems; A Method for Computing All of Them. Part 2: Numerical Application', *Meccanica* , V.15, pp. 21-30.

75. Pezeshki, C., and Dowell, E.H., (1989). ' Generation and Analysis of Lyapunov Exponents for the Buckled Beam ', *Int. J. Non-linear Mech.* , V.24, No.2, pp. 79-97.

76. Swinney, H.L., (1983). ' Observations of Order and Chaos in Nonlinear Systems ', *Physica* , V.7D, pp. 3-15.

77. Newhouse, S., Ruelle, D., and Takens F., (1978). ' Occurrence of Strange Axiom A Attractors Near Quasi Periodic Flows on T^m, $m \geq 3$ ', *Commun. Math. Phys.* , V.64, pp. 35-40.

78. Grebogi, C., Ott, E., and Yorke, J.A., (1985). ' Attractors on an N-Torus. Quasiperiodicity versus Chaos ', *Physica* , V.15D, pp. 354-373.

79. Reddy, J.N., (1984). ' A Refined Nonlinear Theory of Plates With Transverse Shear Deformation ', *Int. J. Solids Structures*, V.20, Nos.9-10, pp. 881-896.

80. Librescu, L., and Schmidt, R., (1988). ' Refined Theories of Elastic Anisotropic Shells Accounting for Small Strains and Moderate Rotations ', *Int. J. Non-linear Mech.*, V.23, No.3, pp. 217-229.

81. Librescu, L., and Stein, M., (1991). ' A Geometrically Nonlinear Theory of Transversely Isotropic Laminated Composite Plates and Its Use in the Postbuckling Analysis ', *Thin-Walled Structures*, V.11, No.1-2, pp. 177-201.

82. Librescu, L., and Reddy, J.N., (1989). 'A Few Remarks Concerning Several Refined Theories of Anisotropic Composite Laminated Plates ', *Int. J. Eng. Sci.*, V.27, No.5, pp. 515-527.

83. Librescu, L., and Chang, M.Y., (1992). ' Imperfection Sensitivity and Postbuckling Behavior of Shear-Deformable Composite Doubly-Curved Shallow Panels ', *Int. J. Solids Structures*, Vol.29, No.9, pp. 1065-1083.

84. Librescu, L., and Chang, M.Y., (1993). ' Effects of Geometric Imperfections on Vibration of Compressed Shear Deformable Laminated Composite Curved Panels ', *Acta Mechanica*, Vol.96, pp. 203-224.

85. Nayfeh, A.H., and Balachandran, B., (1993). *Applied Nonlinear Dynamics: Analytical, Computational, and Experimental Methods*, John Wiley, New York.

86. Nayfeh, A.H., (1981). *Introduction to Perturbation Techniques*, Wiley-Interscience, New York.

87. Aprille, T.J., and Trick, T.N., (1972). ' A Computer Algorithm to Determine the Steady-State Response of Nonlinear Oscillators ', *IEEE Trans. on Circuit Theory*, V.CT-19, No.4, pp. 354-360.

88. Mees, A., (1981). *Dynamics of Feedback Systems*, Wiley-Interscience, Chichester, England.

VITA

Naresh K. Chandiramani was born in Bombay, India, on March 6, 1964, the son of the late Mr. Kotumal K. Chandiramani and Mrs. Padma K. Chandiramani. He graduated from The Scholar High School, Bombay, in December 1978 and then majored in science at the Jaihind and Basantsing Institute of Arts and Sciences. In August 1980, he joined the Indian Institute of Technology, New Delhi, with a major in Civil Engineering, and was awarded the degree of Bachelor of Technology in May 1985. He then came to the USA for his graduate education at Virginia Polytechnic Institute and State University, Blacksburg, where, after a brief stint in the Department of Civil Engineering, he joined the Department of Engineering Science and Mechanics. He received his Master of Science degree in December 1987 and his Doctor of Philosophy degree in July 1993. His major area of concentration is Structural Dynamics.

Naresh K. Chandiramani